University of Liege

Faculty of Applied Sciences

Attaching soft to hard:

A multimodal correlative investigation of the tendon-bone interface

Doctoral thesis conducted by

Alexandra Tits

with the aim of obtaining the degree of Doctor in Biomedical Engineering

Supervisor

Davide Ruffoni

Jury members

Liesbet Geris

Markus Hartmann

Jean-François Kaux

G. Harry van Lenthe

Cédric Schwartz

Academic Year 2022-2023

"J'apprends encore tous les jours.
Quand je n'apprendrai plus rien,
Je serai vieux."

"I still learn every day.
When I'll stop learning,
I'll be old."

Hubert Grooteclaes

Abstract

Joining dissimilar materials is a challenging and frequent requirement in nature as well as in engineering. Thanks to evolution and natural selection through millions of years, biological materials have probed different strategies to fulfill such task, hence becoming a source of inspiration and curiosity for a broad range of researchers. A fascinating example actually lies in the human body and is called the enthesis. This region is essential for the musculoskeletal system, ensuring efficient transitions at the interfaces between soft tissues and bones, often through a layer of fibrocartilage. Entheses therefore have a crucial role for the healthy functioning of our joints, yet they are much less investigated than single individual tissues such as tendon or bone. Limited regeneration abilities leading to poor clinical outcomes in case of reattachment surgeries, combined with injuries, inflammation and degenerative changes make entheses highly relevant in the clinical context.

In this thesis, we propose a multimodal correlative investigation of the tendon-bone interface, with the global aim to enrich the understanding of enthesis structure and properties. As biological system, the Achilles tendon insertion into calcaneus bone of adult rats is analyzed. This anatomical location does not only feature fibrocartilage at the enthesis, anchoring tendon to bone, but also another fibrocartilage, called periosteal, facilitating tendon sliding. The two tissues are adjacent but sustain distinct mechanical loading, and are therefore a valid model system to explore the impact of the mechanical environment on tissue properties at different hierarchical level.

Micro-computed tomography (micro-CT) at two different length scales, combined with histology and electron microscopy imaging, highlight specificities of tissue organization, microstructure and microporosity at enthesis and periosteal regions. We show that the insertion of the tendon occurs at a dedicated bony protrusion that also allows a direct loading transfer from the tendon to the plantar fascia without the involvement of other regions of the calcaneus bone. A strong structural anisotropy of bone vascular channels can be observed within the tuberosity, which is also a characteristic feature of fibrochondrocyte lacunae, forming highly aligned columns. At the enthesis, a high roughness of the interface connecting unmineralized to mineralized fibrocartilage is additionally observed. Periosteal fibrocartilage exhibits very different features: besides reduced waviness at the mineralizing interface, the tissue is more heterogeneous and displays an isotropic channel network together with randomly arranged fibrochondroycte lacunae.

To further explore structure-property relationships within enthesis and periosteal fibrocartilage at the material level, we combined nanoindentation with second harmonic generation (SHG) and quantitative backscattered electron imaging (qBEI), allowing to spatially correlate mechanical properties with mineralization and fibrous matrix organization. SHG images show that microstructural anisotropy is mirrored into highly aligned fibers at the insertion, further impacting the local mechanical behavior. Indeed, anisotropic regions are associated with a close spatial correspondence between mineral content and tissue modulus and a remarkably constant spatial profile within mineralized fibrocartilage towards bone. Those findings suggest that the enthesis fibrocartilage should provide high strength to sustain the tensile loading of the tendon. The more isotropic porosity of periosteal area is also reflected in the arrangement of the collagenous matrix. Indeed, the tissue displays an intricate fiber organization which results in a gradual increase in tissue modulus, probably to resist compressive loading. Despite their distinct spatial modulation of mechanical properties, both fibrocartilages are less mineralized than bone and yet quite efficient as they attain their stiffness with less calcium that bone would require. Finally, qBEI images show a considerable entanglement between fibrocartilage and bone at the interface to increase anchoring ability.

Using a confocal laser scanning microscope on stained samples, a connection is then revealed at the enthesis, between trabecular bone marrow space and fibrocartilage, through vasculature perforating the interface. This pathway provides a crosstalk between the osteocyte lacuno-canalicular network and fibrochondrocytes. Indeed, canaliculi are stopped at the cement line anchoring fibrocartilage to bone (or slightly before) but densely decorate the perforating subchondral channels, the latter further reaching the fibrochondrocytes. Those connections are much more evident at the enthesis than within the periosteal fibrocartilage, where they are practically absent.

In conclusion, our findings suggest that anisotropy and interdigitations are key features of the enthesis, and that preferentially oriented channels have a crucial role in bone-fibrocartilage crosstalk. The specificities of structure-property relationships of enthesis and periosteal fibrocartilage, also compared with underlying subchondral bone, demonstrate the versatility and efficiency of this tissue.

Several paths could be followed to extend our study. First, other species including humans, as well as other entheses, should be analyzed to determine how the strategies we highlighted vary with animal size and anatomical site (and corresponding loading). Finite-element models are currently developed to provide more insights into the biomechanical implications of our findings. Finally, it would be highly valuable to implement our procedure in medically relevant scenarios such as over or unloading of the entheses, inflammation and ageing to observe possible changes in enthesis structure and properties.

Résumé

Unir des matériaux fortement dissemblables est une nécessité fréquente mais complexe dans la nature ainsi qu'en ingénierie. Grâce à des millions d'années d'évolution et de sélection naturelle, les matériaux biologiques ont exploré de nombreuses stratégies afin de réaliser cette tâche, devenant ainsi une source d'inspiration et de curiosité pour une grande variété de chercheur·ses. Un exemple fascinant se trouve dans le corps humain et s'appelle l'enthèse. Cette région est indispensable au système musculosquelettique, assurant des transitions efficaces aux interfaces entre les tissus mous et les os, souvent par une couche de fibrocartilage. Les enthèses ont donc un rôle crucial dans le fonctionnement sain de nos articulations, et pourtant elles sont beaucoup moins étudiées que les tissus individuels tels que le tendon ou l'os. Des capacités de régénération limitées menant à de mauvais résultats cliniques en cas de chirurgie de réattachement, combinées à de potentielles lésions, de l'inflammation et des changements dégénératifs, rendent les enthèses très pertinentes dans un contexte clinique.

Dans cette thèse, nous proposons une étude multimodale corrélative de l'interface tendon-os, avec pour objectif global d'enrichir la compréhension scientifique de la structure et des propriétés des enthèses. Comme système biologique, l'insertion du tendon d'Achille dans l'os calcanéen de rats adultes est analysée. Ce site anatomique ne contient pas uniquement du fibrocartilage au niveau de l'enthèse, ancrant le tendon à l'os, mais également un autre fibrocartilage, appelé périostéal, facilitant le glissement du tendon. Les deux tissus sont adjacents mais sont soumis à des chargements mécaniques distincts, et représentent donc un modèle valide afin d'explorer l'impact de l'environnement mécanique sur les propriétés des tissus à différentes échelles hiérarchiques.

De la micro-tomographie assistée par ordinateur (micro-CT) à deux échelles distinctes, combinée à de l'histologie et de la microscopie électronique, ont mis en évidence les particularités de l'organisation, de la microstructure mais aussi de la microporosité des tissus à l'enthèse et dans la région périostéale. Nous montrons que l'insertion du tendon se produit dans une protubérance dédiée de l'os, ce qui permet également un transfert de charge direct du tendon vers le fascia plantaire, sans impliquer d'autres régions de l'os calcanéen. Une forte anisotropie structurelle des canaux vasculaires osseux peut être observée à l'intérieur de la tubérosité et est également une caractéristique des lacunes des fibrochondrocytes, formant des colonnes fortement alignées. À l'enthèse, une rugosité importante de l'interface connectant le fibrocartilage non-minéralisé et minéralisé est également observée. Le fibrocartilage périostéal possède des caractéristiques

très différentes : en plus d'une ondulation réduite à l'interface de minéralisation, le tissu est plus hétérogène, et présente une isotropie du réseau de canaux ainsi que des lacunes des fibrochondrocytes arrangées aléatoirement.

Afin d'explorer les relations structure-propriété dans le fibrocartilage de l'enthèse et périostéal en termes de matériau, nous avons combiné de la nanoindentation avec de la génération de deuxièmes harmoniques (SHG) et de l'imagerie quantitative par électrons rétrodiffusés (qBEI), permettant de corréler spatialement les propriétés mécaniques avec le niveau de minéralisation et l'organisation de la matrice fibreuse. Les images SHG montrent que l'anisotropie microstructurelle se reflète dans des fibres hautement alignées au niveau de l'insertion, impactant de surcroît le comportement biomécanique local. En effet, les régions anisotropiques sont associées à une correspondance spatiale proche entre le contenu minéral et le module tissulaire, ainsi qu'un profil spatial remarquablement constant depuis l'interface entre le fibrocartilage non-minéralisé et minéralisé. Ces résultats suggèrent que le fibrocartilage de l'enthèse doit surtout fournir une force élevée afin de supporter la charge de traction du tendon. La porosité plutôt isotropique de l'aire périostéale se reflète également dans l'arrangement de la matrice de collagène. En effet, le tissu présente une organisation fibreuse complexe résultant en une augmentation graduelle du module tissulaire, probablement pour résister à la charge compressive. Malgré une modulation spatiale spécifique de leurs propriétés mécaniques, les deux fibrocartilages sont moins minéralisés que l'os et pourtant efficaces : ils atteignent leur raideur avec moins de calcium que ce dont l'os aurait besoin. Finalement, les images qBEI démontrent un enchevêtrement considérable à l'interface entre le fibrocartilage et l'os, afin d'augmenter les capacités d'ancrage.

À l'aide de microscopie confocale à balayage laser sur des échantillons teintés, une connexion est révélée à l'enthèse entre la moelle osseuse trabéculaire et le fibrocartilage, via le système vasculaire perforant l'interface. Cette voie permet la communication entre le réseau lacuno-canaliculaire des ostéocytes et les fibrochondrocytes. En effet, les canalicules s'arrêtent à la ligne de cémentisation ancrant le fibrocartilage dans l'os (ou juste avant), mais ornent densément les canaux sous-chondraux perforants, ces derniers atteignant finalement les fibrochondrocytes. Ces connexions sont évidentes à l'enthèse, et beaucoup moins dans le fibrocartilage périostéal où elles sont quasiment absentes.

En conclusion, nos résultats suggèrent que l'anisotropie et les enchevêtrements sont des aspects clés de l'enthèse, et que les canaux préférentiellement orientés ont un rôle crucial dans la communication os-fibrocartilage. Les particularités des relations structure-propriété du fibrocartilage de l'enthèse et périostéal, également en comparaison avec l'os sous-chondral sous-jacent, démontrent la versatilité et l'efficacité de ce tissu.

Plusieurs chemins peuvent être empruntés afin d'étendre notre étude. Premièrement, d'autres espèces comme l'humain, ainsi que d'autres enthèses, devraient être analysées afin de déterminer comment les

stratégies que nous avons mises en évidence varient avec la taille de l'animal et le site anatomique (et son chargement correspondant). Des modèles aux éléments finis sont actuellement en développement afin de fournir davantage d'éclaircissements sur les implications biomécaniques de nos résultats. Finalement, il serait très enrichissant d'implémenter notre procédure dans des scénarios pertinents d'un point de vue clinique, comme par exemple la surcharge ou décharge de l'enthèse, de l'inflammation ou du vieillissement afin d'observer les potentiels changements dans la structure et les propriétés de l'enthèse.

Acknowledgements

Writing a PhD thesis interestingly incites you to take some time to reflect on what you achieved and recognize who helped and supported you to get there. This is a valuable and insightful exercise that I think we should practice more often. The last four years have been quite of a roller coaster: ups and downs, both emotionally and scientifically. But above everything else, I learned (almost) every day.

The relationship between a PhD student and a supervisor is particular. A "supervisor" lies somewhere between a boss, a mentor and a team colleague. I have been lucky that mine was a great combination of those. Thank you Davide for your unconditional support, your smart guidance and most importantly, your sensibility and understanding. We might have disagreed on a few things... But you have always been truly open to feedback and discussion and this a rare quality. To be pronounced with a strong Italian accent: *Let's put it like this*, you've shown me a great example of pure scientific curiosity and intellectual integrity: I hope to follow your path, wherever I go next. Thank you for the trust you put in me and the freedom you gave me, no matter how eccentric my side activities were and how much they invaded my working hours.

I would like to express my gratitude to all the great scientists that I have been lucky to collaborate with. First I want to thank Dr. Jean-François Kaux, Prof. Pierre Drion and Luc Duwez from the CHU University Hospital, for their advice and assistance regarding sample extraction. Thank you Luc for your patience and teaching, even though I was never perfectly well equipped. Jean-François, thank you for your support and for believing heartily in the collaboration between biomedical engineers and surgeons. I am thankful to Prof. Harry van Lenthe and the whole KULeuven team for welcoming me to the FIBEr lab and teaching me how to exploit the micro-CT machine. Thank you Harry for your continuous support and advice since day one of this PhD! I am highly grateful to Markus Hartmann and Stéphane Blouin from the LBIO: thank you again for your warm welcome during my research stay in Vienna and for inviting me to join your annual retreat. It has been a pleasure to learn the secrets of your beautiful qBEI images by your side. Thank you for your always smart opinion on my work - even despite my eccentric colorful qBEI scale bars! Thanks also to Petra Keplinger, Sonja Lueger and Phaedra Messmer from the LBIO for their assistance during sample preparation, data acquisition and evaluation of qBEI. Another special thanks for Chloe Jones and Sonja Jaeger for their caring and moral support during my stay: I hope we'll have that espresso martini to celebrate! I also want to show my profound appreciation to the Max Planck team, Prof. Richard Weinkamer and Dr. Max Rummler. Thank you Ricci for our great conversation during the walk and talk at the retreat:

your words still accompany my thoughts about how I want my life to look like. Thank you for being a strong reviewer to my work: yes I am still recovering from it :-), but above all beyond grateful to learn from you. I can see where Davide got his curiosity and integrity: thank you for passing along to him your humble dedication to science, which I hope to pursue and transmit myself.

Research can be overwhelming and sometimes lack of tangible short-term results. I have found balance by getting involved into several associations and committees. First and foremost, I have launched and developed the Pot'Ingé, an association raising awareness on ecological issues through a shared vegetable garden, conferences and workshops. I am deeply grateful to the other founders Sophie, Kathleen, Bertrand and François, but also to all the members that joined us since the beginning in 2019: Eva, Romin, the two Chloé's, Alexis, and all the others that became true friends. I am heartily wishing all the best for the future of the project: I hope to see the whole campus filled with vegetables in five years! I have also been involved in the ULiège PhD community, the "Réseau des Doctorant·es". I want to thank the incredible people that I've had the chance to exchange with and the projects we developed together: being a PhD student is more than doing a thesis, and it has been exciting and enriching to share that vision with all of you. A special thanks goes to Virginie Christophe: thank you for your kindness and the incredible faith you've always put in me. I have also been part of the European Society of Biomechanics student committee. There as well I have had the chance to meet researchers from all over the world that inspired me and somehow motivated me to keep doing this work. A special thanks to Aurélie Carlier, the chair of the student committee and a brilliant scientist: thank you for being one of my role models in a field still mainly populated by men. A last appreciation goes to the members of Youngster National Committee of Biomedical Engineering: thank you for the warm welcome in the team!

Final word, of course, goes to my close friends and family. I am extremely lucky to be surrounded by loving and caring persons. My "4/4" (pound cake is really an unfortunate translation), my two Marie's and Alice, my best friends since high school and I am sure forever: thank you for your infinite support, encouragement and understanding, no matter if you didn't really get everything I was doing (but that was before MT180 I hope!). Thank you Sophie, my "PhD sister": sharing this particular path with a friend that actually understands it has been an invaluable source of motivation. Thank you Sacha, my best dance partner: our dance classes and endless chatting sessions have been and still are one of my favorite highlights of each week. Finally, I want to mention my colleagues and now true friends, Astrid and Laura: thank you for showing me the excitement and happiness to share the office with such lovely and supporting colleagues. I am so proud to have been a part of your journey that I know for sure will be successful.

I certainly could not have made it without my two life pillars, my mom and sister. Our bond is hard to describe in words, but for sure I owe them a lot in everything I am and achieved today. Thank you mom for your incommensurable love, your infinite support and the faith you have in me. Thank you my Babou for being my best ally, for hearing my thoughts before I even speak (scary!), for standing closely by my side

no matter the distance between us. You both give me strength every day.

Ephkaristo daddy for blindly and heartily believing in me despite your distinctive sarcasm: you did add quite of a challenge but see, I did it. I hope you're proud up there.

I want to end with Bertrand, my love, my best friend, my life partner, my writing coach and honestly almost deserving co-authorship for this thesis. Sharing a life with you is a daily joy. Thank you for standing close to me day to day with unwavering faith in me. I can do anything with you by my side.

I should probably stop here, yet there are still so many other people that brought me the little joy or confidence that got me through the hard days: from an encouraging smile to an enriching conversation or for being without knowing an inspiring role model.

With all my heart, thank you all,

Alexandra
(Soon to be Dr. Tits, doesn't that sound amazing?)
January 2023

Contents

Contents

Chapter 1

Introduction

1.1 Thesis motivation

Nature is an infinite source of inspiration and curiosity for researchers, from material scientists to biologists, and also for engineers. The attachment of highly dissimilar materials provides fascinating illustrations of how certain species seamlessly build remarkable adaptation strategies to face such a challenging issue. Indeed, mismatches in stiffness, deformation mode and toughness are believed to trigger interface failure [1–3]. A well-known example of bimaterial attachment in nature is the beak of the jumbo squid that exhibits a 200-fold stiffness gradient between from the soft base, embedded within the buccal mass, to the very hard tip [4] (Fig. 1.1A). The latter is the result of a spatially controlled compositional gradient [4]. Mussel byssal threads enable the attachment of the soft body to hard surfaces in the rocky seashore [5] (Fig. 1.1B). Here again a gradient in stiffness is produced and regulated by a distribution of proteins with stiff and pliable domains [6].
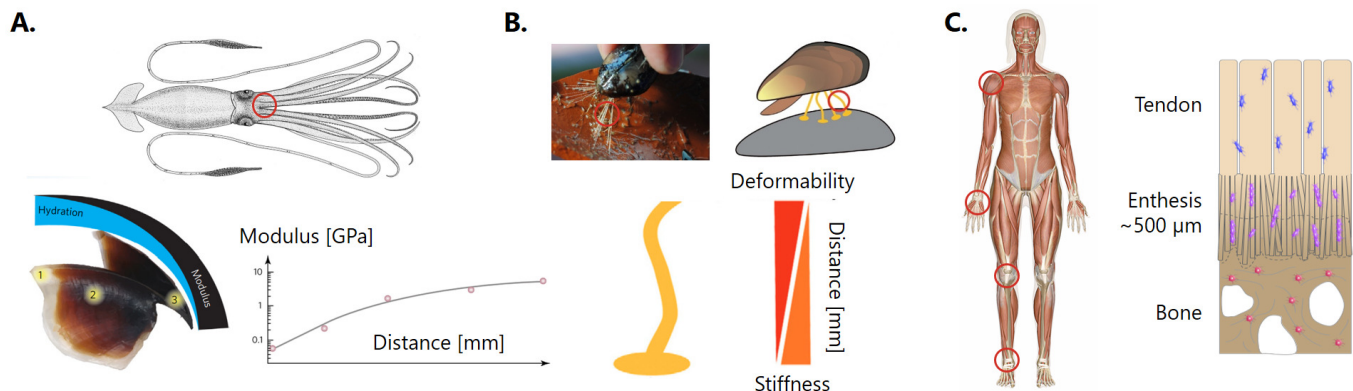
Figure 1.1: (A) Top: drawing of a whole giant squid. Bottom: illustration of hydration and stiffness gradients within a squid beak and resulting modulus increase with distance. (B) Top: picture and illustration of the mussel byssus threads. Bottom: Illustration of the gradient appearing within a single thread, being soft and flexible close to the mussel body and stiffer close to the rock surface. (C) Schematic representation of the enthesis at the tendon to bone insertion. Pictures adapted from [4, 5, 7], with permission.

A great material mismatch is also present within the human musculoskeletal system. Indeed, while the latter is a complex arrangement of several tissues (such as bone, muscle, tendon, ligament and cartilage), the whole system could not work properly without an additional component, often disregarded: the interfaces joining the different tissues. The insertion of tendons in bone, for example, is a challenging task given the strong differences between the two tissues in terms of composition, structure and material properties. The region dedicated to this integration is called enthesis and often comprises a layer of fibrocartilage to help bone to cope with loading from the tendon [8, 9] (Fig. 1.1C).

Contrarily to the squid beak and mussel threads that rely, as in many other biological mismatches, on macroscopic (tens of mm) range gradients [4, 6], the enthesis is spanning over a tiny region of only a few hundreds micrometers. This spatial constraint implies the development of multiple local strategies that in turn necessitate a multimodal analysis to be unraveled.

In addition to their scientific interest, entheses are of considerable relevance from a clinical viewpoint. As described more precisely throughout this thesis, they are indeed vulnerable to injuries and degenerative changes [10–16], and they suffer from limited regeneration abilities in case of reattachment surgery [17–22].

In this thesis, we focused on entheses and we decided to consider, as biological system, the Achilles tendon insertion into calcaneus bone of adult rats. This anatomical location presents, in both rats and adults, three distinct types of fibrocartilage [9]. At the insertion is found enthesis fibrocartilage, sandwiched between tendon and bone and mainly serving to insert the soft tissue. Sesamoid fibrocartilage lies on the tendon surface where it comes into contact with bone, whereas periosteal fibrocartilage covers the opposing bone surface (an illustration can be found in Fig. 5.1). In between periosteal and sesamoid fibrocartilages is located the retrocalcaneal bursa, a sort of cushion filled with fluid and fat [9]. Enthesis and periosteal fibrocartilages therefore offer the opportunity to explore contiguous tissues subjected to distinct mechanical loading. Indeed, enthesis region sustains mainly tensile loads from the tendon, whereas periosteal fibrocartilage facilitates tendon sliding during joint movements such as dorsiflexion, leading to a mixture of compressive and shear forces. Both fibrocartilages are first unmineralized, and then mineralized when approaching bone.

Building on the unique ability of bone to adapt its structure and material according to the local mechanical environment [23, 24], subchondral bone underlying both types of fibrocartilage should also be considered as an important player for proper soft tissue integration. Most studies targeting the enthesis directed their attention towards the interface between unmineralized and mineralized fibrocartilage, considered as the weakest link for transmitting forces [7, 25–28], while the other interface, between mineralized fibrocartilage and bone, is underconsidered. However, there is increased biomechanical and clinical evidence that mineralized fibrocartilage and underlying bone regions can also be the cause of failure [29–33]. We therefore hypothesize that they both have a crucial role in the anchoring and load transmission processes: this thesis proposes experimental tools combined with extensive analyses to unravel this role.

1.2 Outline of the thesis

Chapter 2 provides a short biological framework on bone and fibrocartilage. It also presents, in a concise manner, the basic physical principles of the material characterization techniques that are used throughout the thesis. The last section of this chapter reviews the insights that modeling and simulations, often in combination with experiments, have brought to the understanding of the tendon-bone interface complex.

Chapter 3, building on the provided background and literature review, introduces the main research aims of the thesis.

Chapters 4, 5 and 6 contain the core of the PhD work, exploring and characterizing mineralized fibrocartilage and the underlying subchondral bone using various, high-resolution and cutting-edge investigation techniques which are combined with advanced image processing and quantification tools. Three main aspects of the tissues, anticipated in the thesis aims (Chapter 3), are studied: their morphology (Chapter 4), their material and mechanical properties (Chapter 5) as well as their potential crosstalk (Chapter 6).

Chapter 7 provides the synthesis of the presented work, including the major findings of the thesis as well as the limitations. In the final part, perspectives for future research are suggested.

Chapter 8 presents two side projects for which techniques learned and exploited in this thesis have been applied to explore other biological materials: calcium carbonate biominerals and the mantis shrimp spike.

Bibliography

[1] Fernando A Cordisco et al. "Toughness of a patterned interface between two elastically dissimilar solids". In: *Engineering Fracture Mechanics* 96 (2012), pp. 192–208.

[2] K Fan et al. "Effects of toughness mismatch on failure behavior of Bi-material interfaces". In: *Procedia Engineering* 130 (2015), pp. 754–762.

[3] Andrea Schwartz and Stavros Thomopoulos. "The role of mechanobiology in the attachment of tendon to bone". In: *Structural Interfaces and Attachments in Biology*. Springer, 2013, pp. 229–257.

[4] YerPeng Tan et al. "Infiltration of chitin by protein coacervates defines the squid beak mechanical gradient". In: *Nature chemical biology* 11.7 (2015), pp. 488–495.

[5] John W.C. Dunlop, Richard Weinkamer, and Peter Fratzl. "Artful interfaces within biological materials". In: *Materials Today* 14.3 (2011), pp. 70–78.

[6] Matthew J Harrington and J Herbert Waite. "How nature modulates a fiber's mechanical properties: mechanically distinct fibers drawn from natural mesogenic block copolymer variants". In: *Advanced Materials* 21.4 (2009), pp. 440–444.

[7] Alexandra Tits and Davide Ruffoni. "Joining soft tissues to bone: Insights from modeling and simulations". In: *Bone Reports* 14 (2021), p. 100742.

[8] M Benjamin and JR Ralphs. "Fibrocartilage in tendons and ligaments—an adaptation to compressive load". In: *The Journal of Anatomy* 193.4 (1998), pp. 481–494.

[9] A Rufai, JR Ralphs, and M Benjamin. "Ultrastructure of fibrocartilages at the insertion of the rat Achilles tendon." In: *Journal of anatomy* 189.Pt 1 (1996), p. 185.

[10] Michael Benjamin et al. "Where tendons and ligaments meet bone: attachment sites ('entheses') in relation to exercise and/or mechanical load". In: *Journal of anatomy* 208.4 (2006), pp. 471–490.

[11] Michael Benjamin and Dennis McGonagle. "Histopathologic changes at "synovio–entheseal complexes" suggesting a novel mechanism for synovitis in osteoarthritis and spondylarthritis". In: *Arthritis & Rheumatism: Official Journal of the American College of Rheumatology* 56.11 (2007), pp. 3601–3609.

[12] Micheal Benjamin and Dennis McGonagle. "The anatomical basis for disease localisation in seronegative spondyloarthropathy at entheses and related sites". In: *The Journal of Anatomy* 199.5 (2001), pp. 503–526.

[13] M Benjamin, RN Tyers, and JR Ralphs. "Age-related changes in tendon fibrocartilage." In: *Journal of anatomy* 179 (1991), p. 127.

[14] HM Shaw and M Benjamin. "Structure–function relationships of entheses in relation to mechanical load and exercise". In: *Scandinavian journal of medicine & science in sports* 17.4 (2007), pp. 303–315.

[15] Sébastien Villotte and Christopher J Knüsel. "Understanding entheseal changes: definition and life course changes". In: *International Journal of Osteoarchaeology* 23.2 (2013), pp. 135–146.

[16] Pamela F Weiss. "Diagnosis and treatment of enthesitis-related arthritis". In: *Adolescent health, medicine and therapeutics* 3 (2012), p. 67.

[17] John Apostolakos et al. "The enthesis: a review of the tendon-to-bone insertion". In: *Muscles, ligaments and tendons journal* 4.3 (2014), p. 333.

[18] Daniel Lee John Bunker et al. "Tendon to bone healing and its implications for surgery". In: *Muscles, ligaments and tendons journal* 4.3 (2014), p. 343.

[19] Kathleen A Derwin et al. "Enthesis repair: challenges and opportunities for effective tendon-to-bone healing". In: *The Journal of Bone and Joint surgery. American Volume* 100.16 (2018), e109.

[20] Leesa M Galatz et al. "The outcome and repair integrity of completely arthroscopically repaired large and massive rotator cuff tears". In: *JBJS* 86.2 (2004), pp. 219–224.

[21] DT Harryman 2nd et al. "Repairs of the rotator cuff. Correlation of functional results with integrity of the cuff." In: *JBJS* 73.7 (1991), pp. 982–989.

[22] G Keene. "Arthroscopic reconstruction of the anterior cruciate ligament. A comparison of patellar tendon autograft and four-strand hamstring tendon autograft." In: *The American journal of sports medicine* 28.3 (2000), pp. 438–438.

[23] Carolin Lukas et al. "Mineralization kinetics in murine trabecular bone quantified by time-lapsed in vivo micro-computed tomography". In: *Bone* 56.1 (2013), pp. 55–60.

[24] Richard Weinkamer and Peter Fratzl. "Mechanical adaptation of biological materials—The examples of bone and wood". In: *Materials Science and Engineering: C* 31.6 (2011), pp. 1164–1173.

[25] L Rossetti et al. "The microstructure and micromechanics of the tendon–bone insertion". In: *Nature materials* 16.6 (2017), pp. 664–670.

[26] Helen H Lu and Stavros Thomopoulos. "Functional attachment of soft tissues to bone: development, healing, and tissue engineering". In: *Annual review of biomedical engineering* 15 (2013), p. 201.

[27] S Thomopoulos, GR Williams, and LJ Soslowsky. "Tendon to bone healing: differences in biomechanical, structural, and compositional properties due to a range of activity levels". In: *Journal of biomechanical engineering* 125.1 (2003), pp. 106–113.

[28] Stavros Thomopoulos et al. "Variation of biomechanical, structural, and compositional properties along the tendon to bone insertion site". In: *Journal of orthopaedic research* 21.3 (2003), pp. 413–419.

[29] James F Griffith et al. "Cruciate ligament avulsion fractures". In: *Arthroscopy: The Journal of Arthroscopic & Related Surgery* 20.8 (2004), pp. 803–812.

[30] SW Hamilton and PH Gibson. "Simultaneous bilateral avulsion fractures of the tibial tuberosity in adolescence: a case report and review of over 50 years of literature". In: *The Knee* 13.5 (2006), pp. 404–407.

[31] Jason Porr, Calin Lucaciu, and Sarah Birkett. "Avulsion fractures of the pelvis–a qualitative systematic review of the literature". In: *The Journal of the Canadian Chiropractic Association* 55.4 (2011), p. 247.

[32] Mikhail Golman et al. "Toughening mechanisms for the attachment of architectured materials: The mechanics of the tendon enthesis". In: *Science advances* 7.48 (2021), eabi5584.

[33] Claire Camy et al. "Effects of hindlimb unloading and subsequent reloading on the structure and mechanical properties of Achilles tendon-to-bone attachment". In: *FASEB Journal* 36.10 (2022).

Chapter 2

Background

The core of this chapter is a review of the current knowledge about the soft-tissue-to-bone interface and specifically how modeling and simulations are providing insights into one challenging and clinically relevant problem: the attachment of soft tissues to bone. Before presenting this review, some biological and material background are provided to permit a smooth reading of this thesis in view of its multidisciplinary character. The structure and development of bone and fibrocartilage are shortly described and then the techniques for characterizing mineralized tissue structure and composition that have been exploited are introduced.

2.1 Biological tissues

The functioning of the musculoskeletal system depends on the coordinated action of multiple tissues, and this coordinated action is partially ensured by entheses. They traditionally comprise four regions: the tendon, the unmineralized fibrocartilage, the mineralized fibrocartilage and the bone [1]. In this section, we provide elementary concepts related to bone and fibrocartilage, the tissues that will be investigated throughout this thesis.

2.1.1 Bone

Bone is one of the most essential organs in the human body, and forms the skeletal system of all vertebrates. Bones come in various shapes, sizes and mechanical properties, depending on their anatomical location and function. They share their vital functions to protect the inner organs, allow motion and storage of minerals. To accomplish such roles, they need to be simultaneously light and strong [2], thanks to a fine hierarchical structure down to the molecular level (as illustrated in Figure 2.1).

Bone is a hierarchical material

At the molecular level, bone is a composite material made of 30 % of organic matrix reinforced by 70 % mineral crystals. The organic matrix is mainly collagen type I, osteopontin, osteocalcin, and proteoglycans [3, 4]. Collagen type I molecule consists in a helix assembly of three polypeptide chains [5]. As illustrated in Figure 2.1, collagen molecules are then staggered periodically to form collagen fibrils [6]. At this level lie the inorganic minerals, hydroxyapatite particles, that deposit mainly within the collagen gap regions, but also outside fibrils [7]. Collagen fibrils assemble in fibers (or bundles), on the next level, which are subsequently organized into arrangements called lamellae (or sheets). At the macroscopic level, two types of bone can be distinguished: cortical and trabecular bone, differing at the microstructural scale [8]. In cortical bone, lamellae wrap in concentric layers around a central canal, forming a structure called osteon or Haversian system. While osteons are predominantly oriented parallel to the long axis of the bone, the orientation of collagen fibers within individual lamellae can differ [9]. Cortical bone is typically found at the outer layer of mature long bones, with a low porosity mainly due to blood vessels and cellular spaces [10]. Trabecular (or cancellous) bone is found in areas subjected to high compression, filling the cortical bone shell. It is much more porous and organized into a network of interconnected rods and plates called trabeculae. Usually there are no blood vessels inside the trabeculae, nutrition being provided by the bone marrow through diffusion [11]. Single trabecula consists of parallel lamellae, also referred to as bone packets, bounded by cement lines and mainly oriented parallel to trabecular surfaces [12].
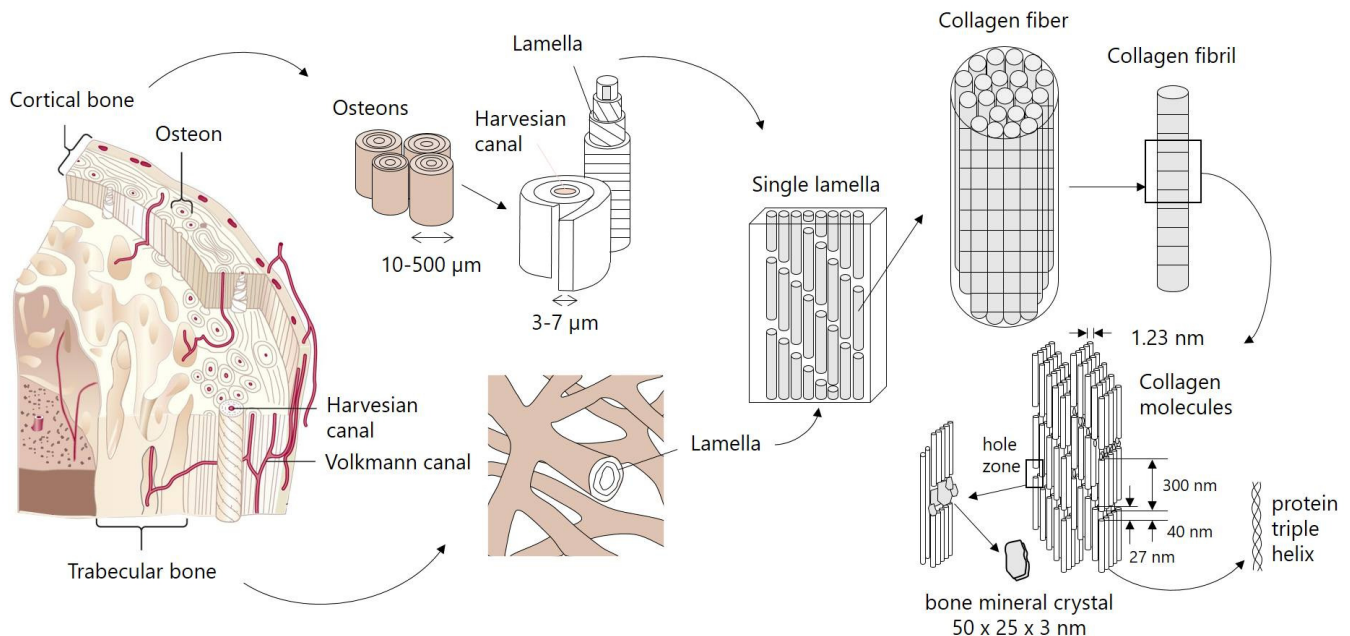
Figure 2.1: Schematic of the hierarchical structure of cortical and trabecular bone. The bone matrix consists of lamellae, organized in osteons or trabeculae. Each lamella consists of assembled fibers whereby each fiber is built of mineralized collagen fibrils. The latter is based on triple helical collagen type I molecules, assembling in a staggered arrangement including bone mineral crystals. Schemes inspired from [13], with permission.

Bone cells actively participate in remodeling and mineralization

One important feature of bone is its remodeling capacity, enabling it to adapt to changing external stimuli and to self-repair in case of damage [14, 15]. This remodeling process in enabled by the interaction of the four types of bone cells: osteoblasts, osteocytes, osteoclasts and bone lining cells, as illustrated in Fig. 2.2. Osteoclasts are cells responsible for bone resorption. Whenever they resorb bone, osteoblasts fill the cavities created by osteoclasts with osteoids, a matrix of non-mineralized bone that will be further mineralized afterwards. Then, osteoblasts differentiate either into osteocytes by integrating the bone matrix [16], or into bone lining cells (or else they die by apoptosis). The exact process of bone remodeling is slightly different in cortical and trabecular bone as they occur on different surfaces: at the intracortical/Haversian or at the endosteal/cancellous surfaces [17] (Fig. 2.2). Osteons are the product of remodeling in cortical bone as osteoclasts and osteoblasts burrow circular tunnels through bone matrix [18, 19]. In cancellous bone, bone is resorbed from the surface of trabeculae, forming discrete bone packets at the surface [20]. Bone packets are not deposited simultaneously. Mineralization increasing with time, their mineral content therefore may differ [21]. Rather than the tunnel of osteonal remodeling, trabecular bone packets have the shape of a half-cylinder (hemi-osteonal remodeling) [18, 22].
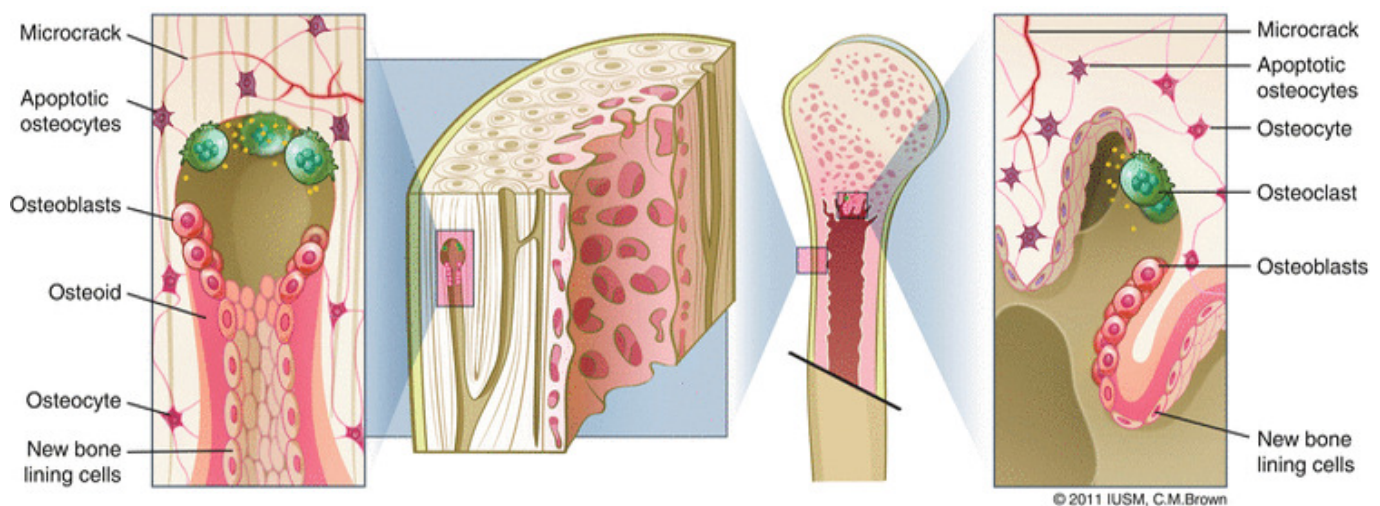
Figure 2.2: Osteonal and hemi-osteonal remodeling in cortical (left) and trabecular (right) bone, respectively. Picture from [17], with permission.

After differentiation from osteoblasts, osteocytes within the bone matrix also form their characteristic cell processes: the canaliculi (Fig. 2.3A). With the pores inside which osteocytes lie (the lacunae), they form an intricate network called the osteocyte lacuno-canalicular network (OLCN) [19] (Fig. 2.3B). The OLCN is dynamic as osteocytes are able to expand their dendrites to form new gap junctions [23]. Osteocytes are believed to have a variety of functions essential to bone health, including efficient transport (of nutrients and waste with blood vessels), signaling but also mechanosensation [24, 25]. Bone matrix deformations being too small to be directly sensed by bone cells [25], a strain amplification mechanism involving interstitial fluid was proposed [26], where load-induced fluid flow within the OLCN results in shear forces on the cell

surface that can be sensed by the osteocytes (Fig. 2.3B). Recent studies have also shown the importance of considering the OLCN topology for the prediction bone formation or resorption following mechanical stimuli [25].

Once osteoids, mainly consisting of unmineralized type I collagen fibrils, have been deposited by osteoblasts, the organic bone matrix has yet to be progressively, after some time lag, mineralized through the deposition of hydroxyapatite particles within and outside fibrils. Recent studies have highlighted the presence of a three-dimensional network of nanochannels [27], in addition to and much smaller than canaliculi (as shown in Fig. 2.3C), surrounding ellipsoidal domains [28] formed from apatite crystals in a process of coalescence analogous to powder sintering (Fig. 2.3D). Close interactions between those nanochannels, cells, collagen fibrils and minerals are central to the mineralization process [27, 29]. Mineralization of fibrils has been suggested to involve those nanochannels, through passive and/or active transport of mineral ions and/or mineral precursors by also interacting with presumptive extracellular matrix vesicles. Osteocyte canaliculi are believed to be part of the pathway by interacting with vesicles and providing further communication and conducting fluid [30, 31].

Bone development

There are two pathways that produce bone: intramembranous and endochondral, depending on the resulting bone produced. Flat bones of the skull, most of the cranial bones, and the clavicles arise from intramembranous ossification whereas the remainder of the axial skeleton and long bones develop from endochondral ossification, the latter involving an intermediate cartilage tissue [34]. Primary ossification occurs during embryonic development, whereas secondary ossification occurs after birth, at the end of long bones (epiphysis), but both follow the same process. Chondrocytes of hyaline cartilage (see section 2.1.2 below) first undergo hypertrophy and alter the matrix that they produce to allow calcification to start. Mineralization prevents nutrients to reach chondrocytes, which therefore leads them to apoptosis, and enable blood vessels to invade the area. Vasculature carries osteogenic cells (precursors of osteocytes and osteoblasts), enabling the osteoblasts to start building woven bone, a primary disordered bone type, on top of the remaining cartilage [35, 36]. This woven bone will later be remodeled into lamellar bone. The diaphysis of long bones is separated from the epiphysis by a growing zone of cartilage called growth, or epiphyseal, plate. This one is divided into several zones according to the stage of chondrocytes just mentioned: a resting zone, a proliferating zone (where new chondrocytes are produced), an hypertrophic zone and a calcification zone (Fig. 2.4). In humans, skeletal maturity is achieved between 18 to 25 years old [37]. At this age, cartilage has been entirely replaced by bone, resulting in a closing, or fusion, of the growth plate.

In addition to the longitudinal growth, bone cross-section also develops, width being essential to maintain strength [39]. During this process, called appositional growth, osteoclasts remove bone from the endosteum, at the internal surface of diaphysis, while osteoblasts produce new bone tissue on the external bone surface, beneath the periosteum.
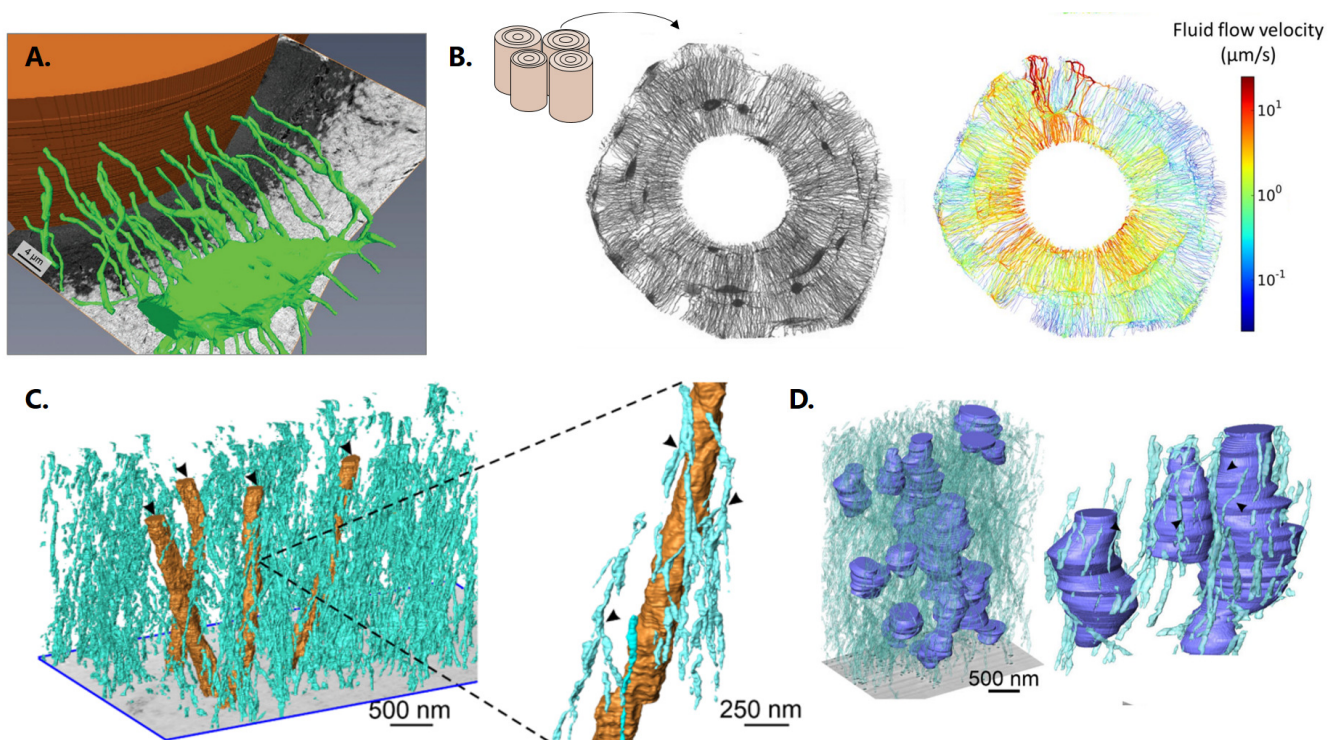
Figure 2.3: (A) Three-dimensional (3D) rendering from Focused Ion Beam Scanning Electron Microscope (FIB-SEM) backscattered electron images of an osteocyte lacuna and its canaliculi (green), and an Haversian canal (brown) within an osteon. Picture from [32]. (B) Projections of a typical 3D lacuno-canalicular network within an osteon from thresholded confocal microscopy image stacks, and corresponding fluid flow patterns in the network. In addition to the colorbar, edges with higher fluid flow velocity are rendered thicker. Pictures from [33]. (C) 3D reconstruction from FIB-SEM images, showing four canaliculi (brown, arrowheads) and the dense nanochannels (cyan) around them. Inset depicts a single canaliculus (brown) and its surrounding nanochannels (cyan), with its multiple branch nodes (arrow heads). (D) 3D rendering of the pillar- or columnar-shaped mineral domains (purple). Their diameter seems quite irregular and they are oriented in approximately the same direction, perpendicular to the image plane. Inset shows that the nanochannels closely follow the contours of the domains, and appear to define the pillar shape (arrowheads). Pictures from [27].
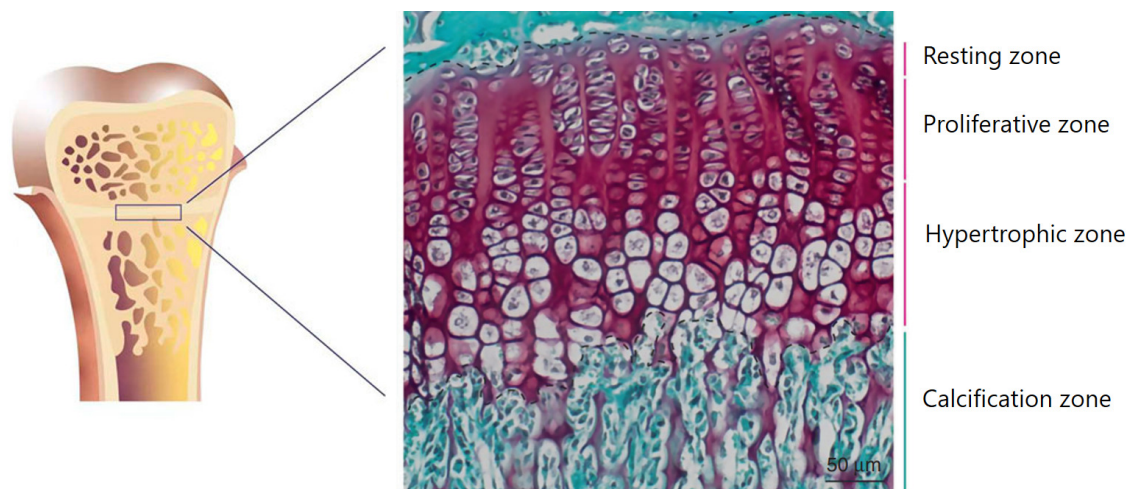
Figure 2.4: Histological images of a 30-day-old mouse epiphyseal cartilage (at the proximial tibia), stained with safranin O (red, cartilage) and fast green (green, bone and connective tissue). Picture from [38].

Unlike larger mammals, small animals such as rats undergo longitudinal growth throughout most of their life, their epiphyseal plate remaining open for a long time [40–45]. Moreover, they display little (in case of high-level fatigue loading, [46]) to no cortical remodeling [47]. Therefore, residues of endochondral ossification remain under the shape of highly mineralized cartilage islands [45].

2.1.2 Fibrocartilage

Cartilage is a highly versatile tissue

Cartilage is a resilient type of connective tissue, essential to the functioning of the musculoskeletal system. In mammals, it is classified in three main types: elastic cartilage, articular (hyaline) cartilage and fibrocartilage [48]. Cartilage is mainly composed of two cell types (chondrocytes and their precursor form, chondroblasts), collagen (mostly type II) and elastic fibers, as well as proteoglycans and glycosaminoglycan side chains [49]. Each specific type differs in relative amounts of constituents and functions. Articular cartilage is for example located within the joints, covering the ends of long bones and enabling joint motion while protecting bone from shocks. Elastic cartilage is, as suggested by its name, the most flexible type of cartilage and hence can be found in regions such as external ears or the larynx. Finally, but most importantly for this work, fibrocartilage is made of thick fibers, less flexible but efficient enough to permit the insertion of tendons and ligaments into bone at entheses [50]. This integrative tissue is also present at meniscal attachment to bone [51–53] .

Enthesis fibrocartilage development and fibrochondrocyte origin

Not all entheses exhibit a transitional fibrocartilage layer. Some insertions are called fibrous as they attach to bone directly through a fibrous tissue, similar to tendon mid substance. Fibrous entheses are generally found at insertion sites of stabilizing tendons, whereas fibrocartilaginous entheses are typically found at insertions of tendons where the insertion angle changes considerably during joint motion [54]. Fibrocartilage there comes in two forms: unmineralized at the tendon side and mineralized close to bone (Fig. 2.5).

But how is this transitional tissue formed? In recent years, studies investigating the formation of the embryonic attachment unit, the enthesis primordium, have shown that progenitors of the attachment unit express both specific chondrogenic (linked with cartilage development) and tenogenic (related to tendon generation) transcription factors [56, 57]. Those progenitors then further differentiate to chondrocytes forming bone on one side, in a process similar to endochondral ossification, or to tenocytes, which form the tendon on the other side, whereas the cells in between differentiate into specialized cells that eventually will form the enthesis [58–61]. Moreover, muscle-induced mechanical forces are necessary for the development of the enthesis (and other musculoskeletal components [62]), as the removal of muscle load has been shown to impair the formation of bone, fibrocartilage, and tendon at the developing enthesis [63].
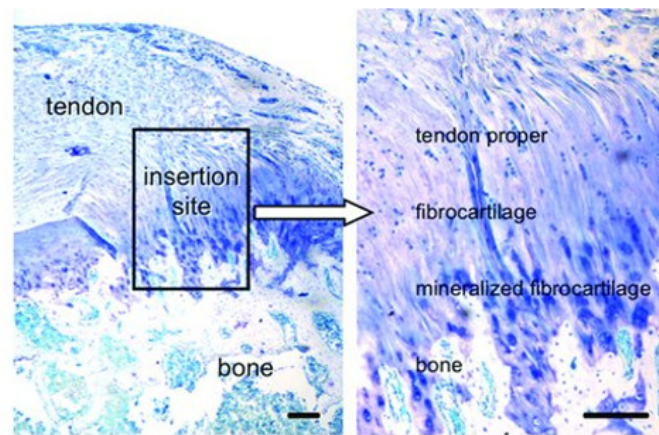
Figure 2.5: Rat supraspinatus tendon-humeral head bone insertion stained with toluidine blue, illustrating the transition between tendon and bone with a layer of fibrocartilage first unmineralized, then mineralized (paraformaldehyde fixed, paraffin embedded, 5 μm thin section). Picture from [55].

Postnatal enthesis cells have been termed fibrochondrocytes based on their histologic appearance as they display morphological features that are shared with tenocytes (elongated fibroblast-like tendon cells) and chondrocytes [63]. In order to better understand their identity, several studies have investigated the genes expressed by those cells and it has been found that they are able to activate a mixture of chondrocyte and tenocyte transcriptomes, under regulation of shared regulatory elements [61, 63–66] . This strategy allows to form a unique tissue without a dedicated genetic program regulating it [61].

2.2 Characterization techniques for mineralized tissues

The hierarchical structure of bone and biological tissues, combined with the multi-tissue character of the enthesis, require to exploit and correlate several characterization techniques to provide insights into its structure and function. The main techniques employed in the thesis and underlying physical principles are described here below.

2.2.1 Micro-computed tomography

The use of high-resolution micro-computed tomography (micro-CT) imaging to assess hard tissue morphology has grown immensely over the last years [67]. This non-destructive imaging technique is based on the transmission (with absorption) of X-ray beams through an object. As illustrated in Fig. 2.6, the basic components for a standard micro-CT scanner include an X-ray source, a collimator and some filters to control the beam, a sample holder and a detector. By rotating either the sample holder or the X-ray source and the detector, several projections are captured from different angles. These projections are then exploited to reconstruct the full volume using filtered back projection algorithms [68].

In bone and most mineralized biological tissues, the high amount of calcium (which has a rather elevated atomic number) leads to a considerable absorption, allowing to see those tissues easily on radiographs, especially given the contrast provided by the much lower atomic number of surrounding soft tissues [67]. The consequence is also that, in order to image those soft tissues, specific techniques of X-ray contrast-enhancing staining agents must be used. With the exception of some visualization on the tendon insertion location using a contrast agent (see Chapter 3), the majority of the micro-CT work of this thesis focuses on the mineralized portion of the enthesis, which therefore didn't require contrast enhancement techniques. Recent studies have revealed promising results for imaging muscles and collagen fibers from unmineralized tissues using cryogenic contrast-enhanced micro-CT [69].

One advantage of micro-CT is the range of resolutions that can be achieved, from whole bodies down to the tissue level [70]. Depending on sample size and scanner type, resolution can be as high as less than one micrometer.
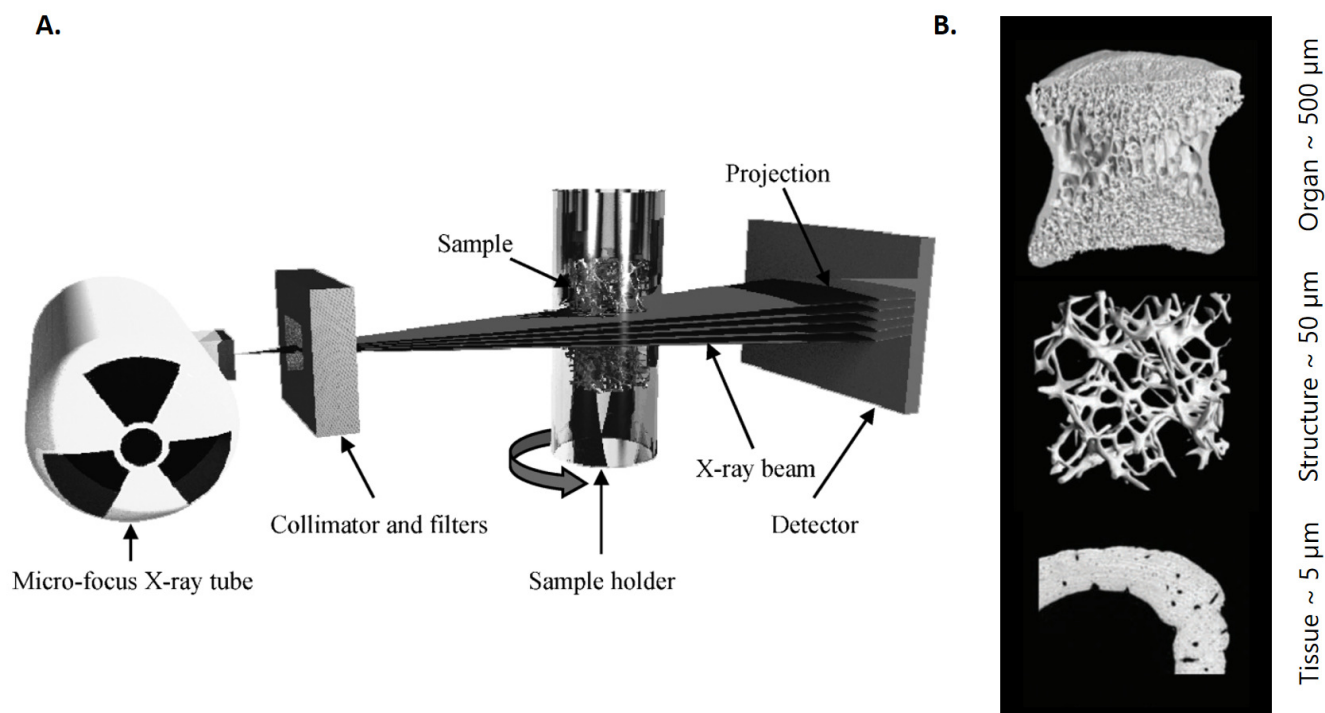
Figure 2.6: Key components for a standard micro-computed tomography (micro-CT) scanner (A) and schematic overview of hierarchical imaging obtained with micro-CT (B). Pictures from [70] and [71], with permission.

2.2.2 Confocal laser scanning microscopy

Conventional microscopy consists in sending light evenly on an entire sample placed in the focal plane, with lens(es) producing an enlarged image. In contrast, in order to reduce the influence of sample thickness and to improve optical resolution, a confocal microscope uses an additional lens, collecting scattered light,

followed by a pinhole to eliminate out-of-focus signal in front of the detector [72]. The focal plane and the pinhole are at "conjugate" planes of focus (hence the name *confocal*), which ensures that only the light emitted from the focal plane enters the pinhole [73]. This allows to change the plane of focus in z-direction and thus to obtain a stack of images from the entire sample. Additionally, as only one point in the sample is scanned at a time, scanning in xy direction line by line is achieved by scanning mirrors (as illustrated in Fig. 2.7).

An additional specificity of the confocal *laser scanning* microscope lies in the use of lasers of controllable wavelength as light source, enabling to exploit fluorescence imaging. Specific molecules, called fluorophores, are indeed able to emit photons of a specific wavelength after absorption of light of another defined wavelength. This process occurs through an intermediate high excited state of the molecule energy, emitting photons while returning to ground state. Because of the transitions between electronic states, the emitted photons have a lower energy, hence a higher wavelength. This shift enables to filter the incoming light from the fluorescent signal and improve image quality. In the context of this work, a staining method with a highly fluorescent rhodamine dye (rhodamine-6G) was used to visualize the lacuno-canalicular network [74, 75]. Due to its small molecular size, rhodamine-6G diffuses fast through samples and stains all internal surfaces of the porosities in the mineralized tissue including blood vessels, osteocyte lacunae and canaliculi [30, 76]. Example images from confocal laser scanning microscopy are shown in Fig. 2.7B.
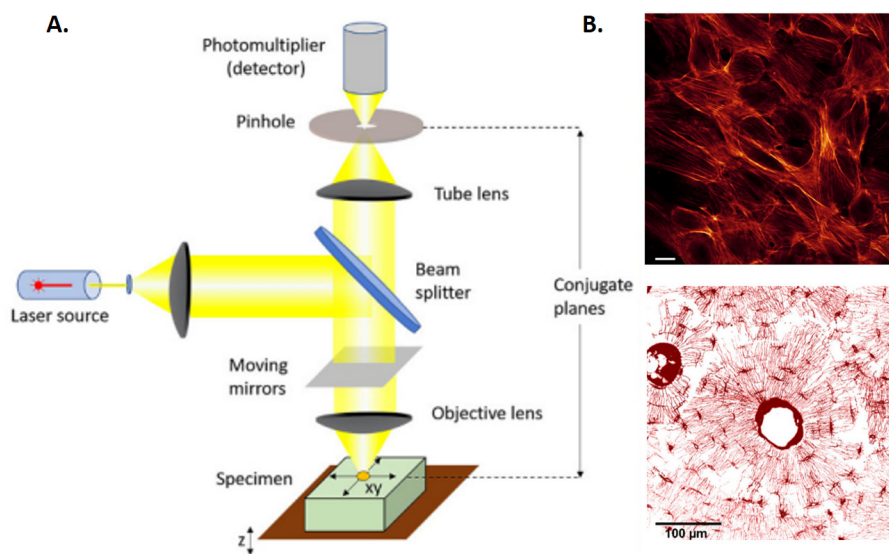
Figure 2.7: (A) Scheme of the components in a confocal laser scanning microscope (CLSM), as described in the text. (B) Example images from CLSM; coupling of two stainings enabling to visualize the filamentous actin forming the cytoskeleton of cells on a Petri dish (top, scale bar: 10 μm) and osteocyte lacuno-canalicular network in human long bone, surrounding the central Harvesian canal (bottom). Pictures from [73], with permission.

2.2.3   Second harmonic generation imaging

Harmonic generation is an optical effect in which k photons with the same frequency interact with a material and generate a new photon with k times the frequency of the initial photons, as schematized in Fig. 2.8A. Second harmonic generation (SHG) is a specific case in which two photons are involved ; and therefore the frequency is doubled [77]. Only specific types of material of able to produce SHG signal, the most important prerequisite condition being that at the molecular level, the material must have no center of symmetry [78]. Several biological tissues meet these requirements, including collagen type I and II, as well as myosin [79].

Using a laser able to generate intense light and specific filters, the emitted signal can be easily extracted as its frequency is twice the one of the excitation. To produce an efficient signal, molecules should be aligned within the image plane, as illustrated in Fig. 2.8B [80, 81]. The intensity of the signal also depends on the collagen concentration, the degree of order, the diameter of the fibrils [82] and the amount of cross linking of collagen [83]. SHG imaging is a powerful technique as it provides endogenous contrast for collagen without the need for staining, its main limitation being related to the proper quantification of the signal, which, given the confounded parameters of influence just mentioned, remains delicate [81].
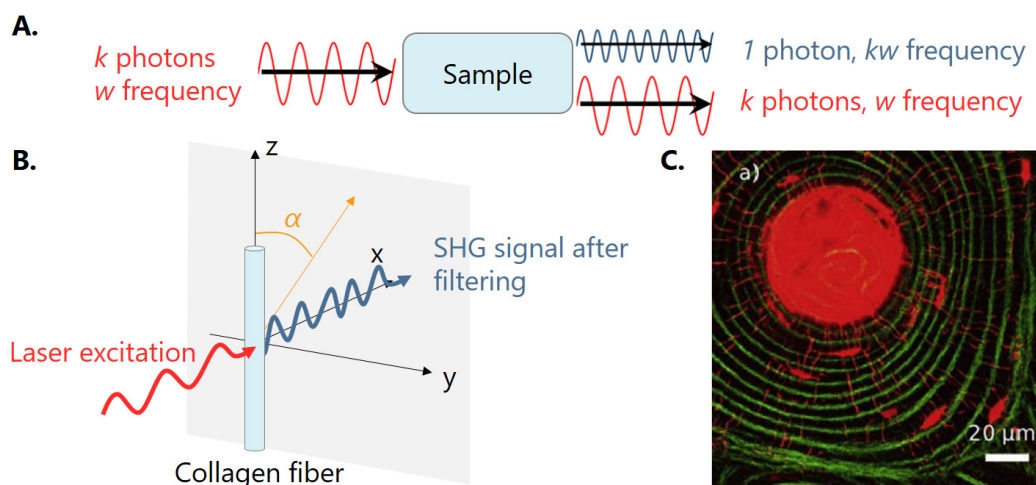
Figure 2.8: (A) Illustration of the harmonic generation principle. (B) Schematic of the optimal in-plane position of single collagen fiber relative to an applied laser excitation. The emitted second harmonic generation (SHG) signal after spectral filtering is shown in blue. Picture from [84]. (C) Example image of SHG imaging of collagen fibers (green), showing the concentric lamellae within an osteon. Red fluorescence signal denotes the lacuno-canalicular network, with a central Harvesian canal, imaged by confocal microscopy. Picture from [85], with permission.

2.2.4   Electron microscopy and quantitative backscattered electron imaging

Another way to visualize and characterize biological tissues is to exploit electrons rather than light. When a beam of electrons hits a sample, many interactions with atoms occur, producing various signals (see Fig.

2.9A), depending on the beam energy and the structure of the sample. Backscattered electrons (BEs) are electrons from the beam that are reflected back because they are elastically deviated by the atom nuclei (Fig. 2.9B). Therefore, BE signal is highly sensitive to the local atomic number Z: the higher the atomic number of the atoms hit by the beam, the higher the BE signal.

Due to its high amount and atomic number, calcium dominates the BE signal from bone and mineralized fibrocartilage. BE imaging can therefore be exploited to assess local calcium concentration. To make this signal quantitative and therefore correlate the BE image gray level (GL) to calcium percentage, a calibration and standardization procedure, developed by Roschger and colleagues, has to be followed [86]. This method is based on the experimental observation that for low atomic number (typically Z < 20), the dependence of BE on local atomic number is approximately linear, as shown in Fig. 2.9C. Therefore, the microscope is first calibrated with carbon and aluminum standards: image brightness and contrast are tuned to obtain a GL of 25 $\pm$ 1 for carbon and 225 $\pm$ 1 for aluminum. This allows to draw the calibration line and ensure that hydroxyapatite GL, of known mean atomic number, is 255. Secondly, the GL of osteoid, considered to contain 0 wt % of calcium, is measured experimentally. Knowing that pure hydroxyapatite is 39.86 wt % of calcium, those two points permit the definition of the standardization line, connecting calcium concentration and GL: Ca = 0.1733 GL - 4.332 [86].

As bone is constantly remodeling and incorporating minerals, bone calcification is heterogeneous and quantitative BE imaging (qBEI) provides a highly accurate (sub-micrometer resolution for a small penetration depth of $\sim 1\ \mu$m) technique to assess it; older tissue appearing brighter than new bone as shown Fig. 2.9D [21]. Bone mineralization density distribution (BMDD), computed as the calcium content frequency distribution of an area scanned by qBEI, can further be associated with bone turnover, mineralization kinetics and average tissue age, but also as a diagnostic tool or to assess the efficiency of a treatment (Fig. 2.9E). The main limitations of qBEI are that it requires a biopsy sample and proper polishing to avoid influence of crystal orientation at the surface, but also that instrumental parameters must be considered with care as they may contribute to contrast [87]. Quantitative comparisons between qBEI measurements are only valid when they are obtained with the same device and the with same experimental settings.

2.2.5 Nanoindentation

Nanoindentation has become a powerful technique for testing material micro- to nanomechanical properties, including the measurement of elastic modulus, hardness, stress–strain relationship or fracture toughness [90, 91]. Several studies have focused on hard tissues, but soft and viscoelastic biomaterial testing is also of growing interest.

In short, in a standard quasi-static test, a controlled load, or displacement, is applied and removed to a sample through a geometrically well-defined and nanoscale-radius indentation probe. The probe depth, or
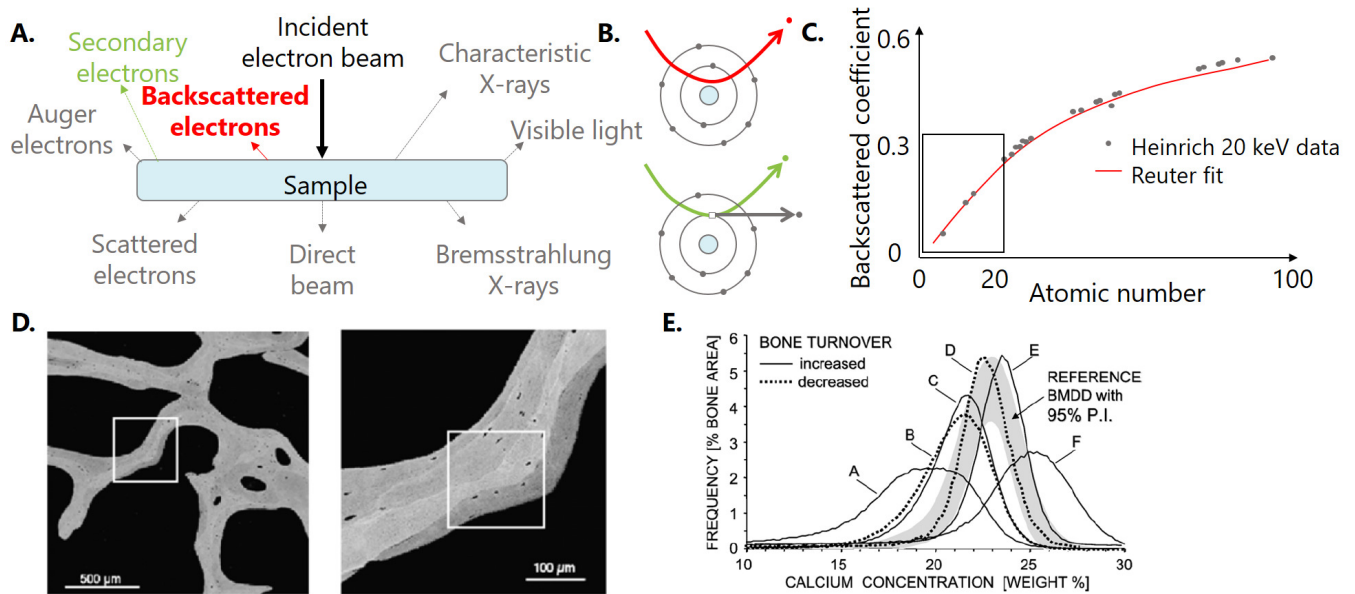
Figure 2.9: (A) Interactions from an incident electron beam hitting a sample. (B) Sketch of backscattered and secondary electron interaction with an atom: backscattered electrons interact only with the atom whereas secondary electrons cause the ejection of an inner-shell electron, causing the emission of either Auger electrons or X-rays. (C) Electron backscattered coefficient as a function of atomic number for pure elements: for small atomic number (< 20), the relationship can be approximated as linear. Picture from [88]. (D) Backscattered electron images of: trabecular features from a transiliac biopsy (left) and inset (rectangular white frame) of one trabecula with visible individual bone packets of distinct mineral content. (E) Bone mineral density distributions of healthy and diseased or treated bone. Pictures from [89], with permission.

load, is continuously measured so that the load-depth curve can be obtained, as illustrated in Fig. 2.10. The Oliver-Pharr method [92] proposes a model to extract indentation hardness (H) and reduced modulus (E_r) from this curve. First, the hardness is defined as $H = P_{max}/A$, where P_{max} is the peak indentation load and A the projected area at the corresponding contact depth h_c. The probe contact area has to be carefully calibrated prior to the measurements with fused quartz (or another standard sample) to provide accurate relationship between contact area and depth. Reduced modulus E_r is then extrapolated as: $E_r = \sqrt{\pi}S/2\sqrt{A}$, S being the initial unloading stiffness (as shown in Fig. 2.10). E_r is a combination of the elastic properties of the sample (Young's modulus E_s and Poisson's ratio ν_s) and of the typically (not always) diamond tip (Young's modulus E_t and Poisson's ratio ν_t). As E_t (around 1140 GPa) is typically much higher than E_t, reduced modulus can be expressed as:

$$\frac{1}{E_r} = \frac{1 - \nu_s^2}{E_s} + \frac{1 - \nu_t^2}{E_t} \approx \frac{1 - \nu_s^2}{E_s}. \tag{2.1}$$
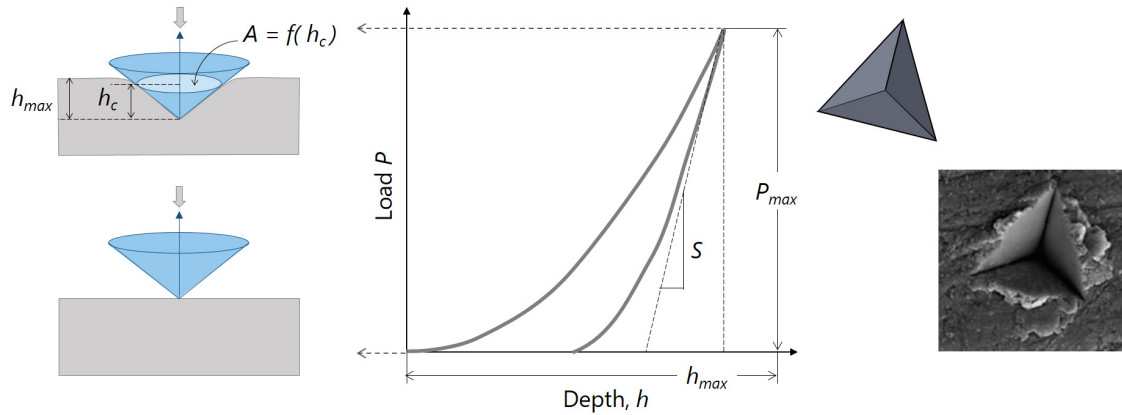
Figure 2.10: Typical load-depth nanoindentation curve and corresponding schematic of the tip indenting the sample (left), as well as illustration of an indent trace and scanning electron microscopy image of a real indent (right). Picture from [93], with permission.

Several precautions must be taken when performing nanoindentation measurements, especially regarding roughness and indent spacing. Sample surface roughness should be as low as possible, and the chosen maximum indentation depth is recommended to be 10 times this roughness [94, 95]. Moreover, due to inelastic deformation, the influence area of one indent is larger than the mark it creates on the surface. To avoid overlapping influence areas, the lateral spacing between indents should be at least three times the contact radius [96].

2.3 Insights from modelling and simulations

[a] Mechanics of Biological and Bioinspired Materials Laboratory, Department of Aerospace and Mechanical Engineering, University of Liège, Liège, Belgium.

ABSTRACT

Entheses are complex multi-tissue regions of the musculoskeletal system serving the challenging task of connecting highly dissimilar materials such as the compliant tendon to the much stiffer bone, over a very small region. The first aim of this review is to highlight mathematical and computational models that have been developed to investigate the many attachment strategies present at entheses at different length scales. Entheses are also relevant in the medical context due to the high prevalence of orthopedic injuries requiring the reattachment of tendons or ligaments to bone, which are associated with a rather poor long-term clinical outcome. The second aim of the review is to report on the computational works analyzing the whole tendon to bone complex as well as targeting orthopedic relevant issues. Modeling approaches have provided important insights on anchoring mechanisms and surgical repair strategies, that would not have been revealed with experiments alone. We intend to demonstrate the necessity of including, in future models, an enriched description of enthesis biomechanical behavior in order to unravel additional mechanical cues underlying the development, the functioning and the maintaining of such a complex biological interface as well as to enhance the development of novel biomimetic adhesive, attachment procedures or tissue engineered implants.

2.3.1 Introduction

The musculoskeletal system comprises not only different tissues such as muscle, tendon, ligament, cartilage and bone, serving diverse biological and biomechanical functions, but also many internal interfaces joining them. Although interfaces occupy only a small fraction of the overall tissue volume, they are crucial for the structural integrity and functioning of the musculoskeletal apparatus [97].

Interfaces are specialized regions facilitating load transmission between dissimilar tissues, which is a challenging task when the tissues being joined have a large mismatch in constitutive material behavior. From a mechanical viewpoint, a sharp transition in material properties can give rise to local high stresses at bi-material junctions [98]. As a consequence, upon repeated loading, contact failure at a level of stress lower than the strength of the two materials may happen [55]. In contrast with this well-accepted mechanical phenomenon, healthy musculoskeletal interfaces have the remarkable ability to sustain large forces (even higher than body weight) for several millions of loading cycles. This is the case of the interface anchoring

tendon (or ligament) to bone, called enthesis (Fig. 2.11A).

The tissues being joined at entheses have distinct composition, structure and biomechanical function (Fig. 2.11B) ([99]). Tendons are effective biological springs designed to sustain large tensile stresses: they have to be stiff enough to prevent excessive stretching when loaded by the muscles, but also somewhat compliant to bend around bones and to allow changes in joint position [100]. At the tissue level, the stress-strain curve of tendons is non-linear, with a characteristic J-shape where the stiffness increases with strain up to a Young's modulus of about 0.5–1.5 GPa (Fig. 2.11C). Although tendons show a heterogeneous mechanical response, strongly depending on the anatomical location and health status, they can be considered both fairly strong (tensile strength from 50 to 150 MPa) and extensible (failure strains up to 12–15%) [101]. The combination of these two properties results in a material with high toughness, which is approximately defined as the ability to absorb energy before failure. On the other side, bones have to face a more complex loading scenario featuring tensile, compressive, and shear stresses. They have to be very stiff to prevent excessive deformation under load but also as tough as possible to avoid fractures [47]. At the tissue level, bones have a different stress-strain behavior than tendons (Fig. 2.11C): they are much stiffer (Young's modulus of 15–25 GPa), roughly equally strong (tensile strength of 120–180 MPa) but much less deformable (failure strains of about 2–3%), resulting in smaller toughness.

Connecting two tissues with such dissimilar mechanical characteristics is not an easy task, as mismatches in stiffness, deformation mode and toughness can trigger interface failure [102–104]. Indeed, despite an extraordinary endurance, entheses are vulnerable to injuries [105], which may need surgical interventions. Rotator cuff tear is a frequent orthopedic problem occurring typically at the tendon insertion and often requiring the surgical reattachment of the soft tissue to the bone [106–109]. The rupture of the anterior cruciate ligament (ACL) is another common injury: even if ACL breaks more frequently at the mid-substance rather than at the enthesis, the ACL is often entirely replaced using grafts (ACL reconstruction), which need to be anchored to the bone and which require proper soft tissue to bone healing [110, 111]. There are many indications that the long term clinical outcome of reattachment and de novo anchoring procedures can be rather poor [111], one reason being the lack of proper enthesis regeneration and healing.

In contrast to other biological systems where dissimilar materials are joined using compositional gradients over a length scale of several millimeters (e.g., squid beak and byssus threads), which is much larger than the micrometer-size of the elementary building blocks [52, 112, 113], musculoskeletal tissues such as tendon and bone are attached over a very tiny transition region, spanning only a few hundreds of micrometers ([99]). This may require the combination of multiple mechanisms to provide entheses with adequate mechanical competence and failure resistance. Indeed, entheses are complex biological interfaces which appear either as fibrous or fibrocartilaginous, depending on the anatomical location and corresponding mechanical requirements [114]. In fibrous insertions, the soft tissue attaches to bone in a direct manner and in the presence of substantial fibrous connective tissue, as for example at the insertion between medial col-
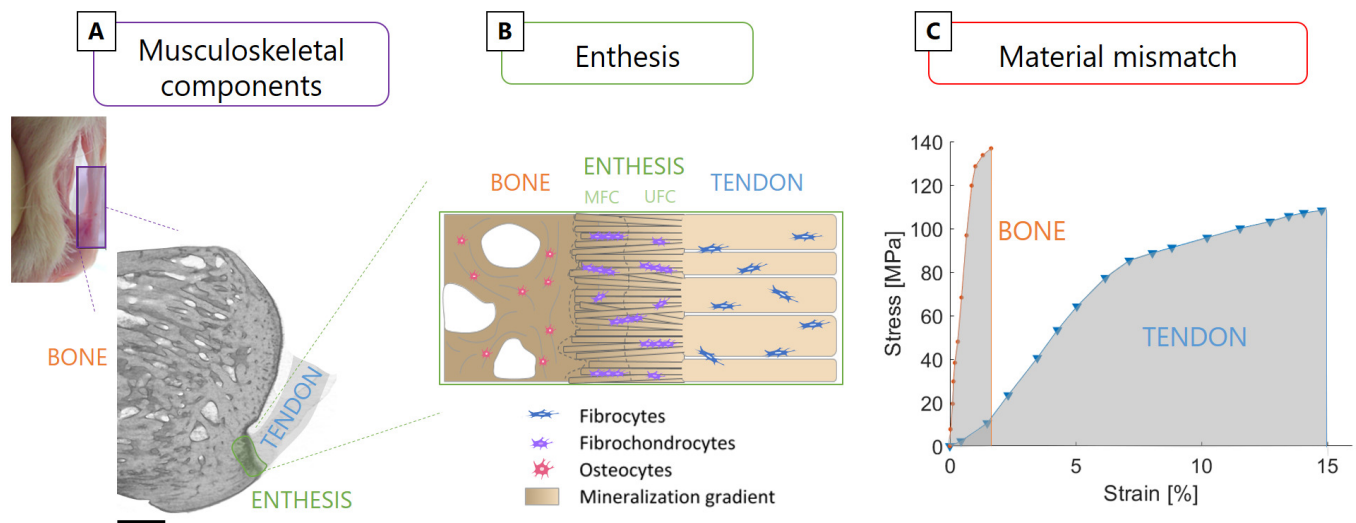
Figure 2.11: (A) Micro-computed tomography (micro-CT) reconstruction of a calcaneus bone-tendon complex (rat) highlighting the location of the enthesis at the posterior side of the bone. Scale bar: 500μm. (B) Schematic representation of the enthesis at the tendon to bone insertion comprising unmineralized fibrocartilage (UFC) and mineralized fibrocartilage (MFC). (C) Typical tissue level stress-strain behavior of bone and tendon, underlining mismatches in stiffness (bone is stiffer than tendon) and toughness (tendon is tougher than bone) that should be "resolved" at the interface. Figures modified from [118, 119],with permission.

lateral ligament and tibia, or deltoid tendon and humeral head [115]. Fibrocartilaginous entheses are more structured and have higher clinical relevance, as they are found at sites suffering from enthesis injuries and pathologies [1, 116]. In short, fibrocartilaginous entheses traditionally comprise four adjacent tissues (Fig. 2.11B): tendon (or ligament), unmineralized fibrocartilage (UFC), mineralized fibrocartilage (MFC) and bone. Tendons and ligaments have a highly ordered and aligned hierarchical structure, based on collagen type I molecules assembling in a staggered manner to form fibrils, which are then arranged in higher level structural patterns such as fibers and fascicles [11]. The cells responsible for the synthesis of the fibrous collagen-based matrix in this region are fibroblasts. The next region is UFC, which lacks the long range order of tendons and ligaments, but still presents parallel arrays of collagen fibrils embedded into a more random fibrous network [50, 117].

Fibrocartilage is mainly composed of collagen type I, II and III, together with aggrecan, a relatively large proteoglycan molecule. Before reaching bone, fibrocartilage gets reinforced by nanometer-sized mineral particles [120], and features an organic matrix mainly composed of collagen type II and X together with other cartilage-associated proteins [116, 121]. In histological sections, the interface between unmineralized and mineralized cartilage is clearly demarcated by a "tidemark", which coincides with the mineralization front. The main cells in charge of synthetizing the extracellular matrix of fibrocartilage are fibrochondrocytes. From a mechanobiological point of view, the presence of fibrocartilage at entheses is believed to be an adaptation to compressive loading [50]. The last zone is bone, with the basic building block being the mineralized collagen fibril, forming parallel arrays which are then arranged in different structural patterns at higher level of the hierarchical ladder [122]. In bone, the cells encased within the mineralized extracel-

lular matrix are the osteocytes, which are kept alive and communicate with each other thanks to an intricate canalicular network [123, 124]. The transitions in composition, mineralization and structural arrangement among the four regions are believed to occur in a gradual manner, which is a basic requirement to avoid dangerous stress localization. Nevertheless, such gradients are restricted to the micrometer length scale and the identification of additional strengthening and toughening strategies present at enthesis is a crucial step [125], not only to improve the understanding of the healthy tendon to bone insertion [126], but also to develop new approaches for treating enthesis injuries and ruptures [116].

There are several excellent studies focusing on different aspects of entheses: a good starting point are the works of Benjamin and colleagues, drawing the attention to the importance of entheses as complex "organs" at musculoskeletal interfaces and their related clinical disorders [1, 50, 114]. Thomopoulos and co-workers have performed extensive research on enthesis biomechanics, mechanobiology, development and healing, including the effects of unloading, well summarized in several papers [55, 104, 116, 127, 128]. Mechanoregulated molecular aspects of enthesis development have been also investigated and reviewed by Zelzer and colleagues [62, 129]. Various imaging modalities are available to characterize such a multi-tissue region at different length scales, both in the clinical context as well as in basic research, as discussed in [130]. A currently active research route is about repair and tissue engineering options for orthopedic interfaces, as presented in numerous reviews [108, 131–135]. Together with experimental approaches, modeling and simulations have been used as complementary tools to elucidate the structure-function relationship at entheses.

The main goal of the present review is to summarize mathematical and computational approaches that have been used, in close synergy with experiments, to characterize the biomechanical behavior of entheses at different hierarchical levels. We classify the modeling approaches in two categories: models which have been used to highlight, at specific length scales, the contribution of microstructural and compositional adaptations to improve anchoring properties (Section 2.3.2), and models of the whole soft tissue to bone complex which have been developed to evaluate overall load transfer mechanisms from soft tissue to bone as well as to answer orthopedic questions (Section 2.3.3). The review shall illustrate how the knowledge of the local mechanical environment can improve our understanding of this complex multi-tissue region as well as suggest new aspects deserving more consideration in future studies.

2.3.2 How to link microstructure and composition to mechanical properties?

This section presents modeling strategies which have been employed to investigate the mechanical role of specific compositional and microstructural features experimentally observed at entheses. Computational models, although idealized, allow the separation of the relative contributions of compositional and microstructural adaptations on the local mechanical behavior. Bones and tendons are both fibrous composite materials [11]: going from tendon to bone, the focus is first on the spatial variations in fiber architecture

Highlights

- The fibrous nature of tendon is preserved across the interface, with tendon fibers splaying and unravelling to anchor to bone. This generates a spatial variation in fiber architecture and orientation, with the degree of alignment decreasing whenapproaching bone.

- Collagen fibers are progressively reinforced by mineral crystals when crossing the interface between unmineralized and mineralized fibrocartilage. This reinforcement provides substantial stiffening to fibers only for mineral accumulation exceeding a percolation threshold.

- The complex interplay between fiber orientation and degree of mineralization results in a non-monotonic variation of tissue stiffness along the insertion, with the appearance of a compliant region having stiffness lower than tendon and bone.

- Interface roughness and interlocking between different sub-regions of the enthesis help to increase fracture toughness.

Limitations and outlooks

- The fibrous nature of the insertion suggests that discrete network models accounting for the individual collagen fibers could provide new insights into enthesis biomechanics, for example by elucidating the link between fiber architecture and local damage mechanisms at the sub-tissue scale.

- In addition to tissue stiffness, the spatial variation of other material properties such as viscoelasticity and strength should be characterized and interpreted based on fiber architecture and degree of mineralization.

- The role of internal interfaces and their complex interlocking patterns should be further investigated. A computational model comprising the interface between unmineralized and mineralized fibrocartilage and the one between mineralized fibrocartilage and bone could unravel new avenues to improve enthesis fracture toughness.

Table 2.1: Linking microstructure and composition to mechanical properties

(first paragraph). Then, the impact of mineral reinforcements - which appear starting from the transition region between UFC and MFC - is analyzed, highlighting the effect of reinforcements at different length scales (second paragraph). Surface roughness and interdigitations are present at the interface between UFC and MFC and also between MFC and bone. In the third paragraph, their biomechanical role is reviewed. Major insights and perspectives regarding those three main aspects are summarized in Table 2.1. In the present review, if not stated otherwise, we use collagen fibril to indicate a collection of self-assembled tropocollagen molecules, having diameter at the nanometer length scale (typical values reaching a few hundreds of nanometers) [100]. With collagen fiber, we indicate an assembly of several fibrils with an indicative final diameter up to several tens of micrometers.

Fiber architecture

Despite being based on the same type of collagen, an important difference between tendon and bone – in addition to the presence of mineral - is the arrangement of the collagen fibers. In tendon, fibers are

mainly parallel and fairly well aligned along a common direction, usually corresponding to the main axis of the tendon [6], with the degree of alignment even increasing when the tendon is loaded [11]. In bone, the orientation of the mineralized collagen fibers is more sophisticated, probably reflecting more complex mechanical requirements. Considering lamellar bone, for example, fibers can form either rotated plywood structures as in cortical bone [136] or parallel arrays following the local predominant orientation of trabeculae as in cancellous bone [12]. Common approaches to characterize quantitatively the orientation of collagen include: polarized light microscopy [137, 138], polarized Raman and Fourier-transform infrared spectroscopy (FTIR) [139–141], as well as x-ray-based techniques such as small angle x-ray diffraction [142, 143] . However, these methods are mainly restricted to two-dimension and current research is focusing on new strategies to derive orientation in three-dimension [8].

The spatial arrangement of collagen fibers at the interface between bone and soft tissues largely depends on the anatomical location and on the type of interface considered. At the interface between bone and articular cartilage, an abrupt change in fiber orientation has been reported (using x-ray scattering), with fibers arranged parallel to the interface from the bone side and perpendicular to the interface from the cartilage side [144]. Such arrangement is thought to favor a tight connection between bone and articular cartilage, preventing cartilage failure by reducing its later extension [144]. Conversely, at the connection between the supraspinatus tendon and the humerus (Fig. 2.12A), fibers tend to have a similar predominant direction (along the major axis of the tendon) which is maintained after crossing the interface, as measured with polarized light [138]. However, at the bony insertion, the frequency distribution of fiber orientation showed somewhat higher heterogeneity when compared to the tendon insertion (Fig. 2.12B), suggesting a less ordered arrangement. This observation was refined in another study focusing on the same anatomical location (i.e. shoulder joint). The angular deviation of fiber orientation, which is an indication of how well the fibers are aligned along a common direction, was measured with polarized light at adjacent sides along the tidemark between MFC and UFC (Fig. 2.12C, positions A to E), with the mineralized side of the tidemark showing significantly smaller angular deviation (Fig. 2.12D). The information of both studies on the rotator cuff were used to extrapolate the spatial evolution of the angular deviation from tendon to bone (Fig. 2.12E), by combining measurements done within tendon and bone (Fig. 2.12B) with measurements performed along the tidemark (Fig. 2.12C) [144]. Going from tendon to bone, the angular deviation increased of almost a factor of four, and reached a small peak before hitting the tidemark between UFC and MFC, hinting for a disordered region before entering into the mineralized tissue. Considering a different anatomical location (the knee joint) and a ligament-bone interface, high resolution two-dimensional (2D) spatial mapping of fiber orientation have been obtained at the femoral and tibial insertions of ACL combining polarized light and FTIR ([99, 145]. Results revealed a quite heterogeneous arrangement (as estimated by the area ratio of Amide I and II peak in the spectra) with collagen fibers in the ligament oriented predominantly perpendicular to the interface but changing the orientation when crossing fibrocartilage region and reaching bone with a more oblique organization (Fig. 2.12G and H). Overall, those studies suggest that collagen fibers are locally organized into parallel bundles also within fibrocartilage, corroborating previous

qualitative observations based on electron microscopy at the Achilles tendon enthesis [117], but most likely being less ordered than in tendon or bone.

Collagen fibers (and fibrils) are long and thin structural elements and, in the absence of mineral reinforcements, they are usually strong in tension and weak in compression [11]. Therefore, small changes in fiber orientation can have a large impact on the mechanical behavior. Indeed, the modulation of fiber orientation is a well-known approach used both in biological [136, 146] and in synthetic fibrous composites [147, 148], to finely tune the local mechanical behavior without modifying chemical composition. There are numerous experimental assessments of fiber organization at the soft tissue to bone interface ([99, 138, 144, 145, 149]; however, one challenge of the experimental works is that when crossing the interface between UFC and MFC, collagen gets reinforced with mineral crystals (as presented in the next section). It is therefore difficult to isolate the contribution of fibers orientation on the overall mechanical competence. This challenge can be overcome thanks to computational approaches.

Essentially, there are two main modeling strategies to link fiber arrangement with mechanical behavior: classical continuum structural mechanics approaches and discrete fiber network models. In the continuum mechanics frameworks [150–152], fibers are not explicitly modeled; instead, at each location, an elasticity tensor linking tissue stress with strain is derived based on averaged and simplified descriptors of fiber mechanical behavior, packing and orientation [152]. Usually, these models are computationally inexpensive and can capture fairly well the overall stress-strain behavior at the tissue level. The obtained constitutive relations can then be implemented into continuum level finite element (FE) models [153], therefore accounting for more complex geometries and heterogeneous tissues [150, 152].

However, continuum approaches cannot resolve mechanical events at the level of individual fibers (or at the fiber-matrix interface). Such information could be essential to understand the interaction between the fiber network and other elements such as cells and interfibrillar matrix or to account for failure at discrete attachment points where collagen fibers (or fiber bundles) anchor to bone [125]. Individual collagen fibers are explicitly considered in discrete fiber network approaches [154–160], which are computationally more demanding than continuum models and, therefore, smaller volumes of interest and length scales are usually investigated. Discrete fiber models have been adopted to characterize force transmission in collagen-based networks, and allow capturing complex coupling mechanisms among different deformation modes [157], which are not emerging when using continuum models. They are also useful in the presence of substantial reconfiguration of the network under load [158]. In the bone context, discrete fiber models have been used to investigate the link between the spatial organization and the fracture behavior of mineralized collagen fibrils [154, 161]. In contrast to the many computational works dealing with fibril arrangement in collagen-based tissues, models devoted to the investigation of fiber properties at the soft tissue to bone insertion are still rather sparse [55, 149, 150].
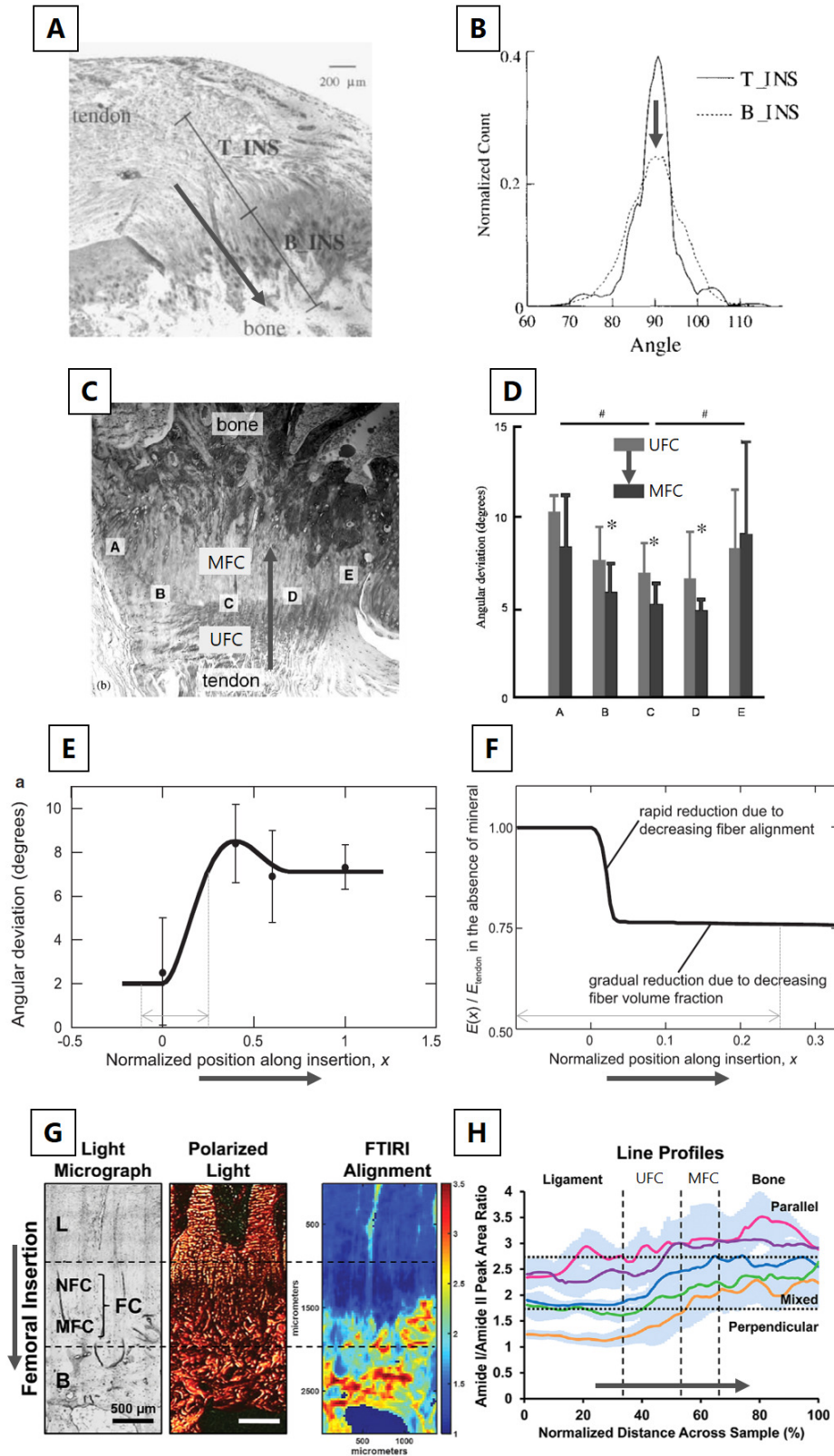
Figure 2.12

Figure 2.12: (A) Histological cross-section of the supraspinatus tendon to bone insertion (rat sample) showing the two regions used to measure orientation of collagen fibers with polarized light (T-INS: tendon end of the insertion, B-INS: bone end of the insertion). (B) Bell-like frequency distribution of collagen fibers orientation for the tendon insertion (T-INS) and the bony insertion (B-INS). Note that the 90∘ orientation lies along the main axis of the tendon. The distribution at the bone insertion shows a slightly higher heterogeneity. (C) Bright field microscopy of the supraspinatus insertion showing the regions (A–E) used for collagen orientation assessment on both sides of the tidemark (unmineralized fibrocartilage, UFC and mineralized fibrocartilage, MFC). (D) Resulting angular deviation measured with polarized light showing that fibers in the center (B–D) are more organized at the MFC compared to the UFC. (E) Spatial variation of angular deviation (which defines how well the fibers are aligned along a common direction) across the tendon (position 0) to bone (position 1) interface. Smaller values indicate higher alignment. (F) Spatial variation in elastic modulus computed with a continuum mechanics approach assuming the angular dispersion visualized in (C) and an ideal enthesis with no mineral. Decreasing fiber alignment causes a sudden and substantial drop in modulus. (G) Organization of collagen fibers across the anterior cruciate ligament (ACL) to bone insertion. Light micrograph (left) with the different tissues encounter at the enthesis (L: ligament, NFC: non-MFC, B: bone). Polarized light images (middle) of sections stained with Picrosirius red to highlight collagen arrangement and (left) corresponding FTIR spectroscopic maps (fiber orientation is color-coded as follows: blue perpendicular to interface; yellow: mixed orientation; red: parallel to interface). (H) Line profile analyses of spectroscopic maps for five samples (full line is the mean and shaded area shows standard deviation for each sample) revealing a clear transition in fiber organization. Bold grey arrows represent the tendon to bone direction. Figures modified from [138, 145, 149, 150], with permission.

The micromechanical consequences of the spatial variation in fiber orientation across the bone-tendon interface (at the shoulder joint) have been estimated using a continuum mechanics unit cell model, with fibers idealized as linear elastic transversally isotropic elements, together with additional assumptions on mineral accumulation within fibers and fiber three-dimensional (3D) orientation [149]. The local tissue elastic modulus was computed based on the experimentally assessed angular deviation of fiber orientation (Fig. 2.12E) and mineral volume fraction, at different spatial positions across the interface. Assuming a hypothetical enthesis without mineral, the elastic modulus showed a fairly large drop (about 25%) as soon as the angular deviation increased above 2.5 degrees (Fig. 2.12F). This behavior can be mechanically justified by a switching in the main deformation mode of the fibers from stretching to bending as the angular deviation increases.

To the best of our knowledge, there are no studies using discrete network models to characterize anchoring mechanisms at musculoskeletal interfaces. Nevertheless, recent experimental works have highlighted additional features of the fibrous collagen network at enthesis [125, 162, 163], which could be investigated with such approach. Rossetti and coworkers [125], using high resolution micro-computed tomography (micro-CT), confocal imaging and electron microscopy, revealed that tendon fibers "split" into an almost order of magnitude thinner interface fibers before inserting into calcaneus bone (Fig. 2.13A). The decrease in fiber diameter is accompanied by a splay out of interface fibers, with the anchoring to bone eventually taking place at discrete locations along a wavy interface. The transition in fibers geometry coincide with a switch in network composition from collagen type I to type II, as evidenced by confocal imaging of immunostained sections (Fig. 2.13B). From a mechanical viewpoint, the unravelling and splaying out of tendon fibers are advantageous mechanisms as they contribute to decrease stress concentration (by increasing attachment area) as well as stress edge singularities (by reducing the angle of force transmission at the interface) [55, 164, 165].

Furthermore, in situ mechanical testings, combined with multiscale confocal microscopy and advanced image processing to map the displacement field, revealed that at the interface, the group of fibers involved in the transmission of load from tendon to bone changes with the angle of force application. This phenomenon leads to an angle-dependent force redistribution, with dedicated fibers recruited at different stages and supporting different types of loads (e.g. shear, buckling or in-plane rotations), with the overall effect of increasing interface resilience [125]. Others have highlighted the 3D arrangement and the topology of the collagen network at the insertion between Achilles tendon and calcaneus bone using propagation-based phase-contrast micro-CT in combination with a fiber tracking algorithm, even resolving individual collagen fibers [162]. The study confirmed a smaller fiber cross-sectional area at the enthesis and revealed detailed aspects of fiber curving, branching and twisting before entering into bone (Fig. 2.13C and D). This novel microstructural information should be cast into computational models accounting for individual collagen fibers to elucidate their impact on the biomechanical behavior of the enthesis.

Mineral reinforcements

In mineralized tissues such as bone and fibrocartilage, the collagen fibrils are reinforced by nanometer-sized mineral crystals [11]. The relative arrangement between collagen and mineral is of paramount importance for the mechanical behavior of the mineralized collagen fibril. In mature bone, stiff mineral crystals are arranged in a staggered fashion within the collagenous matrix, with force transmitted to the mineral particles through shearing of the matrix, when the fibril is loaded in tension [166]. This mechanism is a universal construction principle common to other biological materials [167], which provides the composite with high stiffness (from the mineral) and high toughness (from the matrix) [11, 168]. Noteworthy, the same staggered arrangement between stiff and compliant building blocks is repeated at higher structural length scales in both bone and tendon, and has a profound influence on the deformation mechanisms [169].

The local distribution of mineral within a calcified tissue can be quantified experimentally with various techniques, the most common being: qBEI [170, 171], Raman and FTIR [140, 172], synchrotron radiation microcomputed tomography [173, 174] and, to some extent, desktop micro-CT (being aware of beam hardening artifacts which can alter the results) [175–177]. As a consequence of the biological processes of bone remodeling and mineralization, bone tissue is not uniformly mineralized but shows a characteristic distribution of mineral content, which can be analyzed with the help of mathematical models to extract information on the kinetics of mineral incorporation into the organic matrix in both trabecular [21, 178] as well as cortical [179] bone. Interestingly, although both tissues are made up of lamellar bone, the mineralization (and therefore the stiffening) process seems to proceed at distinct velocities, perhaps due to more complex microstructural differences than commonly believed [179].

Regarding entheses, mineral content and heterogeneity of MFC have been measured across multiple species and locations ([99, 120, 126, 145, 180, 181] however, details of the mineralization process of this tissue are less clear [59, 182, 183]. At the interface between unmineralized tissues and bone, the mineral content has

29

to increase from 0% to about 50% volume fraction and, consequently, biomechanically crucial questions that should be answered are: i) what is the width of the transition region between unmineralized and mineralized tissue? ii) how does the mineral content vary across this region? and iii) what is the corresponding behavior of the local mechanical properties (e.g. elastic modulus) in this region?

The width of the transition zone between UFC and MFC seems to be very tiny and, depending on species, anatomical location and assessment technique, ranges from about 10 to 120 μm ([99, 165, 182, 184, 185]. A slightly larger width (190 μm) has been observed at meniscal attachments ([52]), whereas at the bone-articular cartilage interface the mineral content shows a strong increase within a zone of only 20–40 μm [186]; others have even described a surprising smaller transition region, as small as 5 μm [96].

Considering the variation of mineral content across the interface, a pioneering work of Wopenka and colleagues described a fairly linear gradient at the mature rat supraspinatus to bone interface (Fig. 2.14A) [184], while subsequent investigations point towards steeper exponential (or even step-wise) variations, as measured at the ACL tibial and femoral insertion ([99, 145]. Analyzing developing entheses, the gradient between calcified and uncalcified enthesis seems to be present even before the appearance of fibrocartilage and, therefore, could be an intrinsic feature of the mineralization front associated with endochondral ossification [182]. Nevertheless, different spatial increase in mineral content from soft tissue to bone may also underline dissimilarities in the biomechanical requirements of the interfaces.

Finally, the connection of mineral gradients (and tissue composition) to local mechanical behavior is probably the most challenging question to answer. Experimentally, spatial mapping of local tissue elasticity at musculoskeletal interfaces has been obtained with nanoindentation [53, 181, 186], atomic force microscopy [96], confocal elastography [52], scanning acoustic microscopy [187] and micromechanical testing [125, 126, 185, 188]. In some cases, the mechanical information has been directly correlated with the mineral content [181, 186]). Despite the compositional and microstructural complexity of the enthesis, a gradient in the mineral content engenders a fairly similar graded transition in local elastic properties [96, 181] at the same time, viscous damping has an opposite trend and seems to vary across a broader region [51, 96]. Less evident is that the correlation between local stiffness and mineral content can be different in mineralized cartilage compared to bone. Indeed, mineralized (articular) cartilage requires a higher mineral content than bone to reach the same Young's modulus, most likely due to differences in the organic matrix [186]. Whether this is also the case for MFC is not known; however, a better understanding of the material behavior of MFC would be relevant, for example to improve the modeling of the deformation and fracture of such tissue.

A number of modeling and computational studies have characterized the role of mineral reinforcements at the soft tissue-bone interface. As nanoindentation is one of the most straightforward experimental approach to characterize the mechanical behavior of multi-tissue interfaces, it is worth mentioning a combined
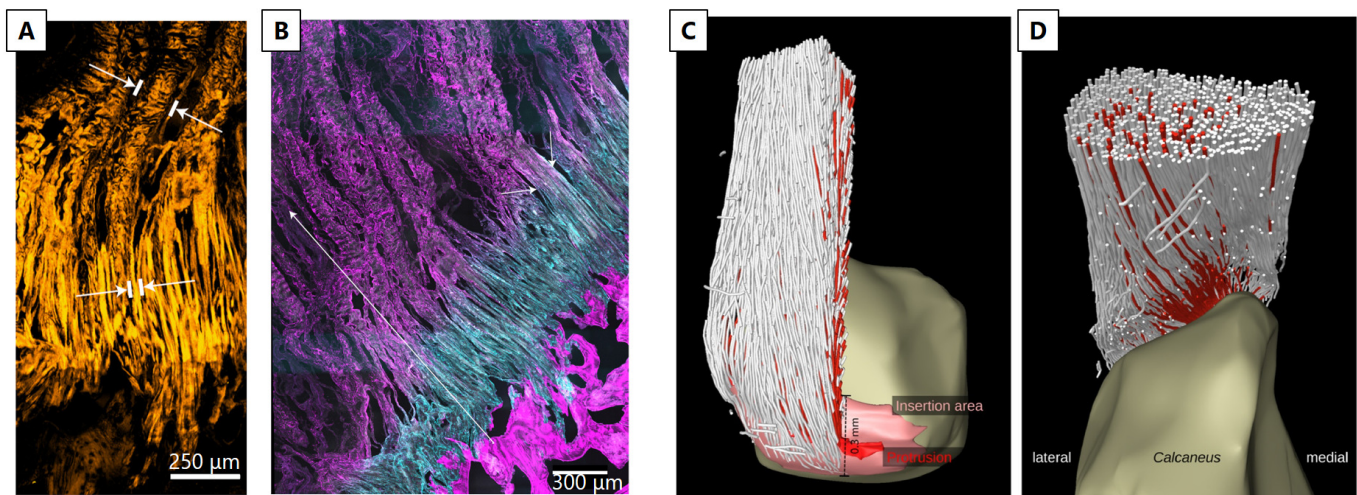
Figure 2.13: (A) Confocal microscopy image of tendon fibers unravelling into thinner interface fibers before attaching to bone. The white marks indicate fiber width. (B) Cryo-cut immunostained section imaged with confocal microscopy showing collagen type I (magenta) and II (cyan) fibers. Fiber composition changes within a 500μm thick region preceding bone. The transition in fiber composition coincides with the transition in fiber architecture (splaying and unravelling) as highlighted by the short white arrows. (C) and (D) show two different perspectives (posterior and superior) of the fibrous collagen network visualized in 3D using propagation-based phase-contrast micro-CT, which allows resolving and tracking the path of individual collagen fibers. The red color indicates fibers inserting into a specific region (protrusion) of the calcaneus bone. Figures modified from [125, 162], with permission.

experimental-computational work evaluating the ability of such technique to measure mechanical properties across two highly dissimilar materials [189]. FE models where used to investigate the relationship between the measured and the real spatial distribution of the elastic modulus across a graded bimaterial interface. The authors provided general guidelines to investigate mechanical properties variation in tissues with significant modulus heterogeneity, by demonstrating that the indenter size should be less than 10% of the expected length scale of the modulus variations. Translated to the context of interfaces between soft tissue and bone, assuming an interface width of 20 μm, current nanoindentation techniques should use probes smaller than 2 μm, which could make the quantification of the properties of tissues with stiffness of the order 10–100 MPa quite challenging [189]. This could be problematic not so much for the bone-tendon interface but more for bone-cartilage or bone-meniscal junctions.

Focusing on modeling studies, a number of micromechanical models have been developed for answering relevant research questions on i) the impact of mineral reinforcements on the biomechanical behavior of collagen at different length scales (from nano up to tissue level), ii) the role of gradients in mineral content on the elastic properties of partially mineralized collagen fibrils and fibers, and iii) the interplay between mineral reinforcements and fiber architecture for the overall tissue level properties across the entheses [149, 183, 190, 191].

One first fiber-level model was developed to predict the impact of mineral gradients on the local stiffening effect in partially mineralized collagen fiber [149]. The model assumed different idealized relative arrange-

ments of clusters of mineralized and unmineralized collagen at the micrometer length scale, including a "diffuse" model describing uniform mineralization, an "equiaxial" model representing non-uniform mineral accumulation and an "elongated" model where mineral clusters were non-uniformly distributed and also geometrically elongated along the fiber direction (Fig. 2.14D). The model was solved using a continuum mechanics framework in combination with FE analysis, and allowed computing the full tissue level stiffness tensor. At the percolation threshold, corresponding to the formation of a large uninterrupted cluster of mineral spanning the entire length of the collagen fiber, the stiffening effect of the mineral reinforcements increased substantially. The different mineral arrangements had an impact on the degree of mineralization needed to reach the percolation threshold.

To better capture the mechanisms of mineral accumulation at sub-micrometer length scales, Liu and co-workers proposed a framework for partially mineralized collagen fibrils accounting for differences in the initiation and sequence of mineralization [183]. Specifically, five distinct scenarios were considered, starting from a completely unmineralized collagen fibril (Fig. 2.14B). Model A: mineralization initiated at the gap region followed by extrafibrillar mineralization nucleating over the gap regions and spreading along the fibril; model B: like model A but extrafibrillar mineralization started from a single nucleation site on each fibril; model C: same as models A and B concerning initiation within the gap region, followed by random accumulation of mineral at the exterior of fibrils, with no subsequent growth of these accumulations; model D: random extrafibrillar accumulations of mineral preceding the mineralization of gap regions; model E: identical to model A except that it included mineralization of the overlap regions following the filling of the gap regions and prior to extrafibrillar mineralization. The (partially) mineralized fibrils were then included into higher hierarchical level fibers using additional assumptions and finite-element (FE) simulations. In addition to confirming the percolation threshold as a key factor for fiber stiffening, those models revealed how the specific sequence of mineralization could impact the degree of tissue stiffening: mineralization models which delayed the percolation of the mineral phase lead to a "slower" spatial gradient in tissue modulus. The collagen-mineral biocomposite has also been investigated in more general terms, considering micromechanical approaches developed for man-made composite materials containing multiple inclusions [190, 191]. This route was followed to estimate the elastic properties of an idealized soft collagen matrix reinforced by a high volume fraction of stiff mineral in the form of ellipsoidal inclusions [191]. The model was used to derive longitudinal and transverse elastic moduli of partially mineralized collagen fibers as a function of mineral content and showed good agreement with (computationally more expensive) approaches based on FE analysis [183].

In a similar context, a multiscale model based on homogenization procedures has been developed to include the contribution of several nano-, sub-micro- and microstructural features observed at the interface, on the effective anisotropic stiffness tensor of the tissue (Fig. 2.14F) [190]. The study, although based on different assumptions and following an alternative methodology, confirms the presence of a percolation threshold above which mineral accumulation within collagen can provide substantial stiffening.

Using some of the presented modeling strategies, the gradual transitions in mineral content can be combined with the reported angular deviation of the collagen fibers to derive the corresponding spatial variation of the overall tissue level elastic behavior across the interface [149, 183, 190]. Interestingly, all these studies have found a non-monotonic variation in tissue stiffness across the insertion, highlighting a compliant region with stiffness lower than both tendon and bone (Fig. 2.14C, E and G). Such counterintuitive behavior can be explained by the interplay between fiber alignment (which is reduced approaching the interface) and mineralization (which gradually increases and shows a significant contribution above the percolation threshold). Noteworthy, a compliant zone near the mineralized gradient has also been identified in experimental micromechanical tests of tendon-bone samples [125, 185] and is believed to enhance energy absorption, allowing higher local deformation [185]. The width and the depth (i.e. drop in modulus) of the compliant region described in several computational works depend on the chosen model parameters. A dominant factor influencing the size of the compliant belt seems to be the position of the mineralization front (i.e. representing the onset of the mineralization process) within the enthesis fibrocartilage [183, 190]. Based on the current literature, values for the relative width of the compliant zone could be estimated and ranged from 13% to 59% of the total length of the insertion region, depending on the relative position of the mineralization front (starting positions from 0% to 35% of the insertion width were considered) [149, 183, 190]. A fairly broad compliant attachment region (occupying a considerable width of the interface) has been deduced experimentally based on the local strain field (Fig. 2.14H and I) [125]. Details of the mineral accumulation within the collagen had only a minor impact on the size of compliant region (Fig. 2.14C). Additionally, the drop in modulus observed in the compliant band appears to be linked to the magnitude of the angular deviation of collagen fibers [149, 183, 190]. Depending on the interplay between the position of the mineralization front and the spatial variation in angular deviation, such drop may occur either in the vicinity of the tendon side (Fig. 2.14E) or very close to the tidemark, just before the mineralized fibrocartilage (Fig. 2.14C and G). The latter being in agreement with experiment findings and, most likely, corresponding to the transition from collagen type I to type II [125]. The minimum value of the tissue elastic modulus computed in the soft attachment region was estimated to range from about 14% to 23% of the longitudinal modulus of the tendon [149, 183, 190]. A higher modulus drop (i.e., a factor of 0.1 of the tendon modulus) has been assumed based on experimental measurements of the strain field at the interface (Fig. 2.14I) [125].

Overall, these findings suggest that the compliant region is a remarkable construction strategy of tendon to bone attachment, which deserves additional insights in future studies. Moreover, owing to the pivotal importance of mineral and collagen arrangements for the mechanical behavior of mineralized collagen fibrils [11], future modeling and computational works may still investigate mineral reinforcement aspects at the bone-soft tissue interface. For example, the staggered geometry seen in mature lamellar bone could be considered in combination with different mineral volume fractions, not only to characterize the corresponding elastic gradients but also to model deformation, failure and fracture behavior of such a transition zone.
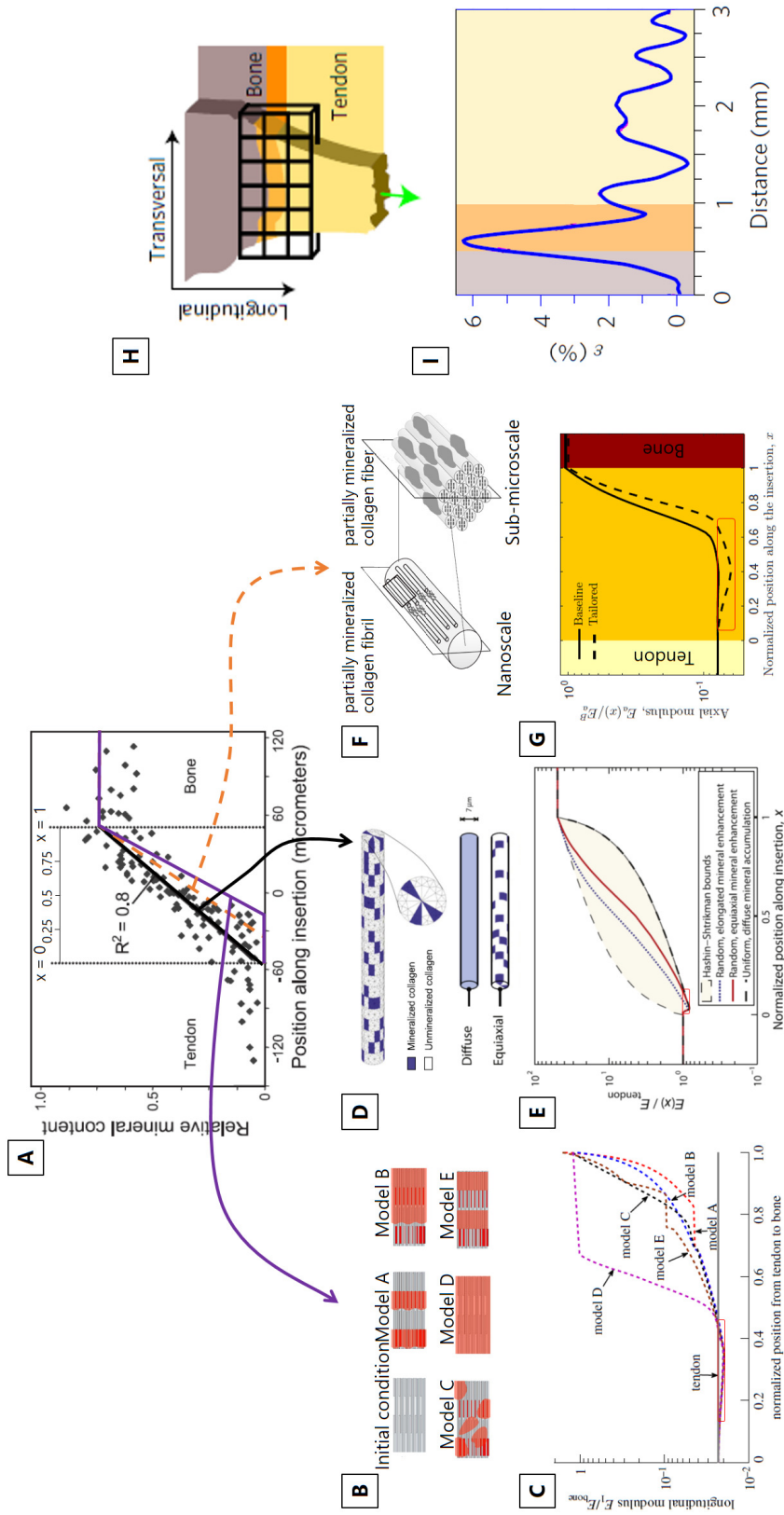
Figure 2.14: (A) Relative mineral content (estimated using Raman spectroscopy) across the tendon to bone insertion. The gradual increase in the mineral content occurs over a 120μm thick region and is well fitted by a linear function. (B) Micromechanical model of the mineralized collagen fibril at the sub-micrometer length scale with hypothetical scenarios for the mineralization process. (C) Corresponding spatial modulation of the longitudinal modulus along the tendon-bone interface, obtained considering a gradient starting at x ≈ 0.35 (purple line in A, x denotes the normalized position along the tendon-bone interface). Depending on the details of mineral nucleation and accumulation, different elasticity gradients could be derived. (D) Micromechanical model of a mineralized collagen fiber at the micrometer length scale, used to compute the elastic properties variation from tendon to bone assuming three different scenarios for the mineral distribution within the fiber. (E) Corresponding normalized modulus variation from tendon to bone, obtained considering a gradient starting at x ≈ 0 (black line in A): a small compliant zone with stiffness lower than tendon and bone is visible. (F) Representation of two specific steps of a multiscale approach, illustrating a partially mineralized collagen fibril and fiber. (G) Corresponding normalized axial modulus variation from tendon to bone. The full line is obtained considering a gradient starting in x ≈ 0, whereas the dashed line a gradient starting in x ≈ 0.2 (i.e., orange line in A). In agreement with previous models, the spatial delay in mineralization front induces a compliant region (highlighted by a red frame). (H) Micromechanical testing of enthesis samples (green arrow shows the applied deformation along the longitudinal direction). (I) Strain values at the enthesis: the high initial peak of the strain corresponds to a locally softer material. Figures modified from [125, 149, 183, 190], with permission.

Surface roughness and interlocking

The compositional and microstructural gradients highlighted in the previous sections are believed to smooth the transition in material properties from tendon to bone. Nevertheless, at the sub-millimeter length scale, it is still reasonable to identify interfacial regions between the different tissues present at the enthesis and to investigate their morphology. Specifically, there are two interfaces of interests: i) the transition between UFC and MFC, referred to as the tidemark or mineralization front; and ii) the one between MFC and bone. Those regions are experimentally accessible and have been visualized using various approaches such as histology [51, 192, 193], serial sectioning [194], quantitative backscattering electron imaging [144, 180, 181, 186] and micro-CT [162, 163]. There are two main features in common to these biological interfaces: a high roughness and the presence of interlocking mechanisms, as evidenced by the analysis of different entheses including the attachment of Achilles tendon into calcaneus [194], the insertion of the supraspinatus tendon into humeral head [192], and the meniscus-tibia interface [51] (Fig. 2.15A–C). The same is also true for the interface between mineralized articular cartilage and bone [96, 144, 186].

Joining two dissimilar materials through a patterned interface is indeed a well-known strategy to improve the failure resistance of bimaterial attachments, and numerous works have investigated this topic considering engineering materials [103, 195–198]. In this context, one interesting research question is about the relationship between the interface geometrical properties and the corresponding interfacial fracture toughness.

A possible way to approach this problem is firstly to reduce the complexity of interface roughness by assuming an idealized profile, described for instance by a sinusoidal function (which is characterized by two parameters: amplitude A and wavelength λ). Using computational fracture mechanics tools is then feasible to relate interface geometry to fracture behavior for different mismatches in material properties between the two solids being joined. Following such route, Cordisco and colleagues [103] have reported that roughness increases fracture toughness with respect to a flat interface but, as a function of the material mismatch, it exists a critical threshold of A/λ above which the cracking behavior switches from single to multiple crack propagation. This transition substantially reduces the toughening effect of the interface roughness. This is an interesting finding that could be used to interpret the morphology of biological interfaces. Assuming a ratio between the elastic modulus of bone and tendon of 10, the critical value of A/λ is about 0.5 [103].

Interestingly, roughness analysis at interface between UFC and MFC (specifically at the supraspinatus tendon to bone insertion) revealed that the aspect ratio of the interface waviness (defined as A/λ) follows an approximately normal distribution centered at 0.14 (Fig. 2.15D and E) [192], which is well below the 0.5 threshold. The measured surface roughness was further interpreted with an idealized 2D unit cell continuum mechanics approach [192]. The model was used to calculate the strength (peak load) and the toughness (approximated by the area under the force-displacement curve) of virtual bone-tendon interfaces as a function of the interface shape. The authors considered several bimaterial unit cells with the interface approximated

by a cosine wave characterized by varying amplitudes, which were assigned according to prescribed normal distributions at constant width and λ (Fig. 2.15D). The impact of the mean value and standard deviation of the distributions of the waviness (A/λ) on strength and toughness was estimated. Simulations showed that higher interface roughness and roughness heterogeneity both decreased the strength but increased the toughness of bimaterial attachments. There was a combination of A/λ and heterogeneity, for which the gain in toughness outweighs the loss in strength (Fig. 2.15F). The geometrical properties of the healthy bone-tendon interface seem to lie in that region, suggesting that not only a regular [103] but also a random wavy pattern can be an effective toughening mechanism at bimaterial interfaces [192].

A subsequent work has analyzed the extent and shape of the bone-tendon interface at the same anatomical location (shoulder joint) but across multiple species having large differences in size (ranging from mice to dogs) [165]. Interface roughness and interdigitations were well-preserved features across the considered species. In contrast to the attachment area, which showed an almost isometric scaling with muscle cross section (used as an estimation of the loading conditions), the geometrical parameters describing surface waviness (A and λ) did not change significantly with animal size. This could be explained by the fact that the increase in attachment area accompanying the increase in loading results in an almost constant interfacial stress, therefore minimizing the need to adapt interface shape [165]. A second reason may be that excessively large aspect ratios may become disadvantageous for interface fracture toughness [103].

Surface roughness is also a typical feature seen at the interface between MFC and bone. Milz and co-workers [194] analyzed the Achilles tendon insertion using serial sectioning and could reconstruct the 3D spatial morphology of the fibrocartilage-bone interface (Fig. 2.15A). They highlighted not only a rough surface but even the presence of a complex interlocking pattern which may be a fundamental strategy to improve attachment, for instance by providing increased resistance to shear loading. Considering the importance of surface morphology on the mechanical properties of bimaterial junctions, further modeling and computational studies should focus on this aspect. One possible research question could be the interplay between roughness and interlocking and the impact on the overall anchoring strength and toughness. Indeed, if roughness reduces attachment strength, this may be compensated by interlocking mechanisms. Additionally, a model comprising both interfaces (i.e. UFC/MFC and MFC/bone), with their specific morphologies, is still missing but could be helpful to better target the weakness of reattachment procedures, which fail to reproduce such complex interfacial shapes.

2.3.3 Modeling the whole bone-tendon construct: load transfer optimization and orthopedic related questions

The number of orthopedic injuries requiring the reattachment of tendons or ligaments to bone, together with the complexity of the surgical procedure and the poor long-term clinical outcome [116, 199], have triggered the development of computational models at the macroscopic length scale [150, 200–206]. These
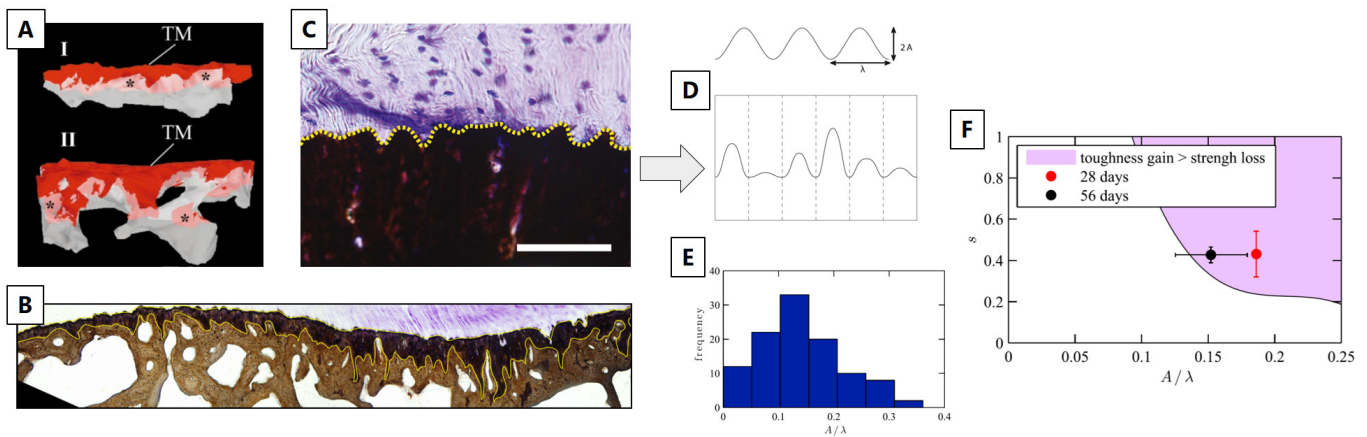
Figure 2.15: (A) Three-dimensional reconstructions (based on serial sectioning) of the interface between mineralized fibrocartilage (MFC, red) and the underlying bone (grey) in the proximal (I) and central (II) region of the Achilles tendon insertion. TM indicates the tidemark between unmineralized fibrocartilage (UFC) and MFC. (B) Roughness and interdigitations at the interface between meniscus and MFC (top) and MFC and bone (bottom). (C) Interface between mineralized (stained in black) and unmineralized (stained in purple) tissues at the supraspinatus tendon to bone insertion. The dotted line highlights the surface roughness, described in (D) as a sinusoidal wave with approximately the same wave length λ but varying amplitude A. (E) Interface waviness (defined as the ratio of A/λ) measured at the supraspinatus tendon to bone insertion in mice follows a quasi-normal distribution centered at 0.14. (F) Contour plot illustrating the region (shaded area) and the corresponding combination of roughness parameters (waviness A/λ and standard deviation s) for which the gain in toughness exceeds the loss in strength as predicted by the model in [192]. Symbols represent the physiological values of the roughness parameters measured experimentally. Figures modified from [51, 192, 194], with permission.

models differ from the approaches presented in the previous sections as they essentially try to investigate the mechanical behavior of the whole bone-soft tissue complex as well as to answer specific orthopedic-related questions. The key messages highlighted by those models, together with their shortcomings, are summarized in Table 2.2.

Macroscopic models of the tendon-bone system

In comparison with the vast literature on tissue and organ level models of bones, tendons and ligaments, computational works on the entire bone-soft tissue complex including details of the enthesis are still sparse. Nevertheless, such studies are essential as they provide a picture of the stress and strain transfer from tendon to bone in the presence of selected features of the enthesis, such as the shape of the attachment area [55], the local tissue anisotropy [150] or the transition in elastic properties [206].

Bimaterial junctions are known to be at risk of highly localized stresses, especially at the edge of the junction [55, 164]. One possible tissue level strategy to alleviate such high stresses it to optimize the shape of the attachment area. Firstly, it should be noticed that a substantial reduction of the angle between the two materials at the free edge of the attachment can be a first solution to decrease the peak stresses developed at the interface [55]. This may be a biomechanical motivation of the splay-out of collagen fibers observed experimentally at the bone-tendon interface (Fig. 2.13A–B) [125]. Peak stresses can also be reduced by

Highlights

- The shape of the supraspinatus insertion is optimized to alleviate peak stresses.

- Computational models illustrate the complexity of the rotator cuff with stresses heterogeneously distributed into non-trivial patterns.

- The stress level at the insertion increases substantially with arm abduction and in case of damage (tears).

- Reattachment procedures with transosseous sutures allow a uniform redistribution of contact pressure and reduce stress concentration.

Limitations and outlooks

- Limited amount of details on geometries and material properties are used in the macroscopic and organ scale models. Future work may focus on the progressive inclusion of features highlighted in Section 2.3.2, such as material gradients and interlocking at the insertion.

Table 2.2: Modeling the whole bone-tendon construct.

optimizing the gross morphology of the attachment area. Using an idealized continuum FE model in combination with a gradient-based shape optimization algorithm, it was shown that the shape of the bone-tendon insertion region can be optimized to practically eliminate peak stresses caused by mismatches in material properties. Besides, the optimized shape differed when comparing pristine entheses with reattached tendons through scar tissue ([55].

The gross shape of the insertion site at the millimeter level is undoubtedly an important parameter for the efficiency of the enthesis. A computational model combining the morphology of the attachment area with orientation-dependent mechanical behavior of the enthesis was developed by Thomopoulos and coworkers [150]. The authors modeled the supraspinatus tendon to bone complex using a 2D idealized continuum FE approach which captured, to some extent, the observed outward splay geometry of rat supraspinatus tendon insertion and accounted for the elastic anisotropy caused by locally different orientation of tendon fibers (Fig. 2.16A). Various scenarios were considered for the distribution of collagen orientation, including a random, a mechanically optimized and an experimentally based arrangement. The FE results, analyzed in terms of stress and strain concentrations (Fig. 2.16B), underlined that the spatial distribution of material anisotropy had a very large impact on the overall stress and strain transfer between tendon and bone. Furthermore, the physiological arrangement of collagen fibers at the enthesis seems to be dictated by multiple requirements such as reducing peak stresses, shielding the insertion splayed geometry and, at the same time, maximizing the stiffness along the main pulling direction of the tendon.

As seen in the first paragraph of Section 2.3.2, computational models of partially mineralized collagen fibers predict a decrease in elastic modulus at the insertion site to values lower than tendon and bone [149, 206].

To better understand the possible biomechanical reasons of such counterintuitive behavior, a tissue-scale biomechanical model was developed, describing essential geometrical features and loading conditions of the bone-tendon complex at the shoulder joint [206]. The model features three axisymmetric concentric cylinders, with an isotropic bone core encompassed by an orthotropic cylindrical tendon and with the bone-tendon interface described as a ring in between (Fig. 2.16C). Different material properties were assigned to the ring-like interface region, including unmineralized (like tendon), fully mineralized (like bone) and linearly graded transition from tendon to bone. The model was solved using a continuum structural mechanics approach and showed that, in all the considered scenarios, the radial stress increased and was from 40% to 90% higher than the applied external stress (Fig. 2.16D). Conversely, if local material properties within the interface region were allowed varying according to a numerical optimization scheme minimizing radial stress, the obtained distribution of elastic modulus showed a minimum value below that of tendon and bone (Fig. 2.16E). However, this happened at the expense of tangential stresses which increased to values above the applied stress. A similar approach was then used to demonstrate that the level of peak stresses at the shoulder joint is a much conserved feature across multiple species, despite the large variations in key anatomical characteristics of the enthesis [207].

Those results illustrate that interface anisotropy may be advantageous when connecting an orthotropic material to an isotropic one. Interestingly, such anisotropy can be caused by different factors, and this is a topic worth of comparison among the different modeling approaches, as anisotropy can have a large impact on stress concentration at bimaterial interfaces. For example, considering modeling approaches described in the second paragraph of Section 2.3.2, anisotropy can result from an intrinsic behavior of the basic constituents of the model (e.g., collagen fibers idealized as transversally isotropic elements) [183] or it can as well emerge from the shape and spatial arrangement of basic isotropic building blocks [190, 191].

Organ-scale models targeting orthopedic questions

Musculoskeletal injuries involving enthesis are a common clinical problem with an increased incidence in the aged population [208], and with related treatment strategies suffering from complications and, in some cases, high failure rates [199]. The most frequently injured locations include the knee and the shoulder joints. At the knee joint, ACL rupture often requires the replacement of the damaged ligament with biological or synthetic grafts [209]. Despite the fact that the surgical procedure is well-established, about 50% of the patients still experience pain one year post surgery [210] and have an increased probability (up to 50%) of suffering from osteoarthritis in the following years [211]. At the shoulder joint, the rotator cuff tear is a major cause of pain and instability [212]. The rotator cuff is a fairly complex joint featuring several muscles and tendons (Fig. 2.16). Due to the specific loading conditions and anatomical position, the supraspinatus tendon is the most frequently damaged soft tissue of the shoulder [101, 213, 214], being susceptible to partial or full-thickness tears [215–217]. Massive rotator cuff injuries may necessitate the reattachment of the tendon to the bony insertion with sutures: different surgical options are available [205] but, contrary to ACL repair, there is no consensus on a gold-standard management approach [204, 205].

Reattachment procedures are exposed to high risk of failure, with re-injury rates as high as 94% [199, 218]. Moreover, effects of unloading (e.g., due to disuse or paralysis) at the rotator cuff have been experimentally investigated [128] and revealed alterations across multiple length scales that could lead to increased risk of injury.

For those reasons, numerous clinical and biomechanical studies have focused on both healthy and damaged supraspinatus-humerus complex and, therefore, we will briefly review some computational models at this anatomical location, which have been developed with the overall goal of understanding the main biomechanical reasons for damage and failure as well as to improve treatment options [200–205].

### Simulations of healthy bone-tendon complex

One important research question which has been investigated with computational models of healthy bone-tendon complex is about the position and the magnitude of peak stresses during arm abduction [200, 201]. Using a fairly simple 2D approach with geometrical information based on magnetic resonance images, Wakabayashi and co-workers [201] developed a multi-tissue model, with the tendon fully bonded to the humeral head and with the presence of (frictionless) contact between tendon and bone , and rather simplified material properties. Starting from the arm at resting position (0° abduction), peak stresses were located at the contact region between tendon and bone, which happened away from the insertion location. Increasing the abduction angle, the highest stressed region moved towards the enthesis and reached it at about 60° abduction.

Such behavior was confirmed in a subsequent refined 3D model, based on computed tomography (CT) scans and including more anatomical details, such as the three major rotator cuff tendons and the middle fibers of the deltoid muscle (Fig. 2.17A–B) [200]. The authors also incorporated additional complexity in material definition, all soft tissues being modeled with non-linear material properties, and the possible interaction between bone and tendon surfaces during abduction was described by frictionless contact. The model confirmed a substantial increase of peak stresses with abduction, in particular closer to the insertion of the supraspinatus at anterior edge of the articular side (Fig. 2.17C–D). The results interestingly hinted for the presence of shear stresses caused by differences in the stress state across the tendon from the articular (highly loaded in tension) to the bursal (less loaded in tension) surface. Shear load in tendon might cause delamination, which could explain the partial-thickness tears often observed in that location [219, 220].
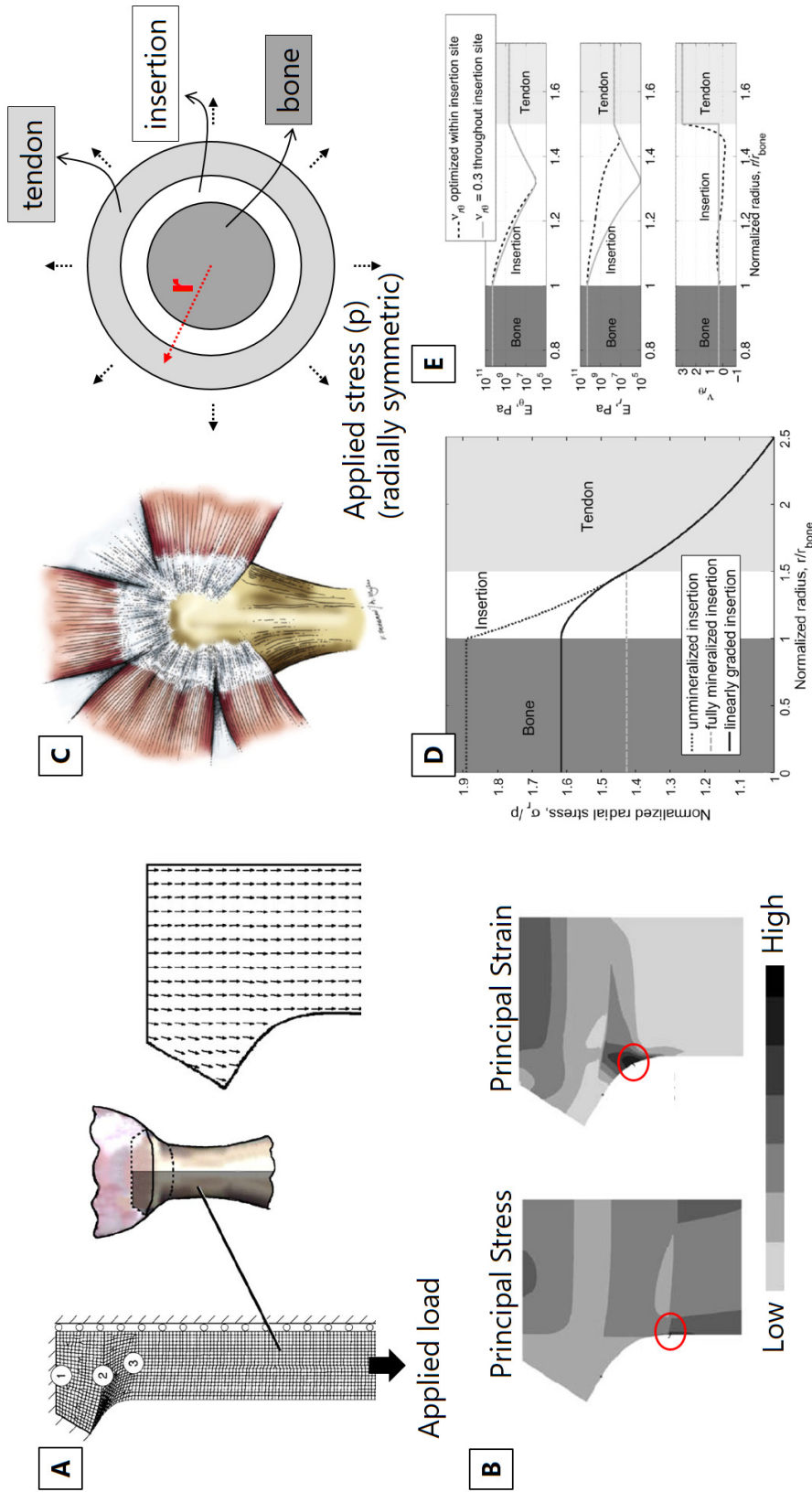
Figure 2.16: (A) Idealized FE model of the tendon-bone complex based on measured geometrical features at the rat shoulder. The numbers indicate: (1) the bone-mineralized cartilage interface, (2) the tidemark between mineralized fibrocartilage (MFC) and unmineralized fibrocartilage (UFC) and (3) the tendon. The right image shows one of the simulated scenarios for the local predominant orientation of collagen fibers, following the outward splay of interface region. (B) Simulated principal stress and strain. Peak values are localized beneath the outward splay of the tendon (as highlighted by the red circles). (C) Anatomical side view (left) and idealized model (right) of the bone-tendon system at the rotator cuff, showing the rotator cuff tendons wrapping around the humeral head. The axisymmetric idealized model comprises the bone, the bone-tendon interface and the tendon. Material properties of bone and tendon were fixed, whereas properties of the interface were allowed varying. The applied radial stress simulated muscle loading. (D) Variation of normalized radial stress (along the radial direction) for unmineralized (tendon like), fully mineralized (bone like), and linearly graded interface region. In all cases, stresses are substantially higher than the applied stress. This happens not only at the interface but also within the bone and the tendon. (E) Distribution of material properties (i.e., radial elastic modulus, tangential elastic modulus and Poisson ratio of the insertion) resulting from the minimization of radial stress. A compliant region (with stiffness lower than tendon and bone) appears at the interface. Allowing Poisson ratio to vary across the insertion has an effect only on the tangential modulus. Figures modified from [150, 206], with permission.

41
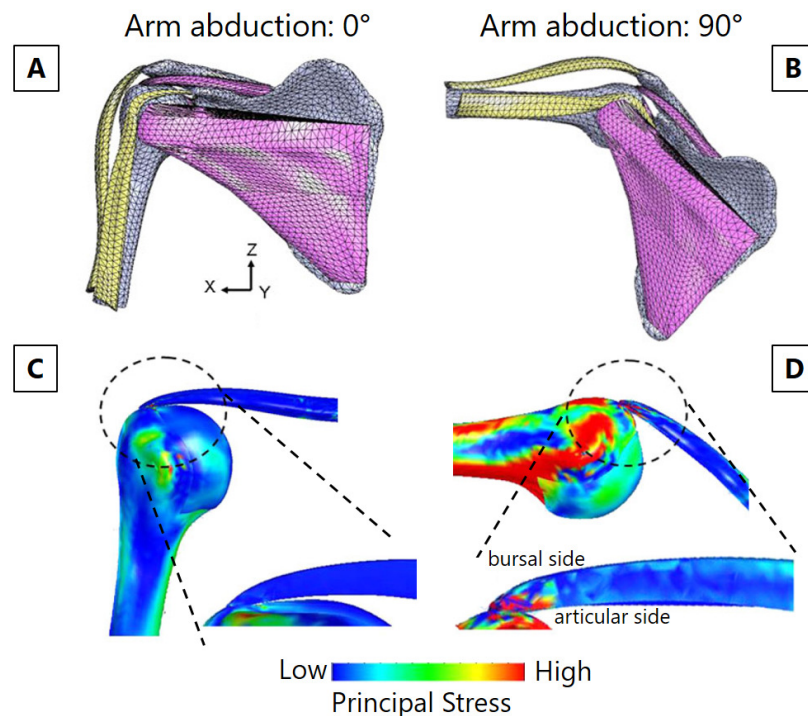
Figure 2.17: Three-dimensional FE model of a normal shoulder joint at (A) 0° and (B) 90° arm abduction. Corresponding surface distributions of maximum principal stress are shown in (C) and (D). The inserts show a sagittal cut through the anterior section and highlight the increase in stress caused by a lifted arm, especially at the articular side of the tendon, which might explain the observed high tear incidence at that location. Figures modified from [200], with permission.

Simulations of damaged bone-tendon complex and reattachment procedures

Computational models offer the possibility to elucidate the impact of damage (in the form of tears) on the overall mechanical competence of tendon-bone constructs. One clear advantage of virtual models is that different degrees of damage can be inserted in a controlled manner at selected locations and the detrimental role can be estimated [203, 204]. Sano and co-workers, for example, simulated partial-thickness tears on three different anatomical positions close to the tendon insertion (i.e., articular surface, bursal surface and tendon midsubstance) using a simplified 2D model of the supraspinatus-humerus complex [203]. Interestingly, inserting damage not only caused stress concentration around the damaged region, but also increased the level of stress at the bony insertion. Furthermore, the biomechanical impact of damage locations depended on arm position: at 0° abduction, damage on the bursal side was the worst-case scenario, whereas at 60° abduction, tears at the articular surface induced the highest stress.

A subsequent and extensive 3D study was conducted by Quental and co-workers [204], with virtual samples of the supraspinatus-humerus complex based on the Visible Human Project dataset [221]. The model included not only bone and tendon but also articular and enthesis fibrocartilage (Fig. 2.18A), assumed to behave like hyperelastic Neo-Hookean materials. Tears of increasing severity were introduced right at bone-tendon attachment by decreasing the insertion area at different locations (i.e., anterior, central and

posterior). The authors evaluated the impact of tears by monitoring the distributions of principal strains (Fig. 2.18B), as this quantity seems to correlate with damage propagation, at least in vitro [215]. Results indicated that tears located on the anterior side had a greater risk of propagation, as the volume of tendon tissue exceeding a typical tissue failure strain (assumed at 24.5% strain) was the highest (Fig. 2.18C). Overall this study represents a good example of how computational models can support and help the biomechanical interpretation of orthopedic observations.

Computational models have also been developed to investigate the impact of surgical approaches reattaching soft tissues to bone [202, 205]. Funokashi and co-workers performed an early study to compare different orthopedic reattachment strategies at the rotator-cuff humerus enthesis including a traditional double row fixation [222] and a surface holding repair technique either with transosseous sutures or with knotless anchors [202]. The authors performed experimental in vitro tests on bovine shoulders and developed simplified FE models to support the interpretation of the experimental findings, by characterizing the link between the reattachment options and the corresponding stress distribution in the tendon-bone complex. The surface-holding repair with transosseous sutures provided the most rigid fixation and also prevented the high stress concentration seen with the double-row repair. This could explain the improved failure resistance of such reattachment strategy observed in the experiments.

A subsequent computational work confirmed the biomechanical advantages of transosseous sutures (Fig. 2.19A) [205]. The authors simulated three different repair approaches (i.e., single row, double row and transosseous equivalent) now using a 3D model with a patient-specific geometry based on a CT scan (Fig. 2.19B). FE results showed that the transosseous equivalent suture lead to an increase in contact area and a more uniform distribution of contact pressure between tendon and bone (Fig. 2.19C), which are two factors linked with the effectiveness of rotator cuff repair [223].

Future continuum FE-based models targeting reattachment procedures could be enriched by including a more detailed description of entheses microstructure and biomechanical behavior as presented in Section 2.3.2. Clearly, it is highly challenging to bridge such a gap between the organ scale (relevant to address applied orthopedic questions) and the (sub-)micrometer level (suited to investigate basic anchoring strategies). To some extent, computational multiscale models could be helpful and may, for example, trigger the development of novel (biomimetic) adhesive [224], recapitulating for certain aspects the material behavior of healthy entheses.

2.3.4 Limitations and outlook

Entheses are essential players of the musculoskeletal system, which have the challenging task of attaching dissimilar tissues over a very tiny region. In this review, we have presented some key features allowing entheses to facilitate load transmission from soft tissues to bone (summarized in Table 2.3). In particular,
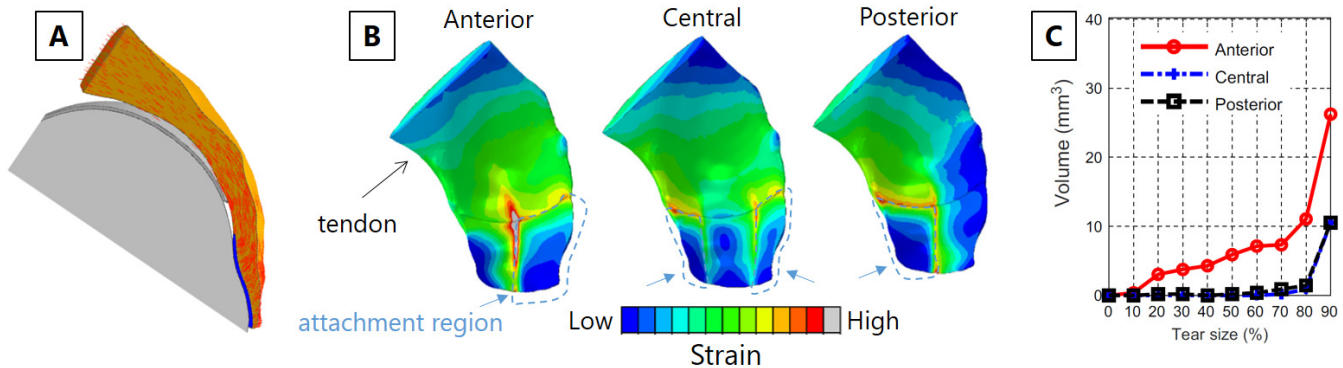
Figure 2.18: (A) Two-dimensional cross-sectional view of the computational model for the tendon-humerus complex featuring the humerus (light grey), the cartilage (grey), the fibrocartilage (blue), and tendon (orange). The predominant direction of selected tendon fibers is represented by red lines. (B) Illustration of the maximum principal strains computed for a 200 N load in a 50% damaged tendon-humerus complex with full-thickness tears on anterior, central or posterior location. (E) Corresponding volume of tendon tissue with strain above the failure threshold (estimated to be at 24.5%) as a function of tear size. Figures modified from [204], with permission.
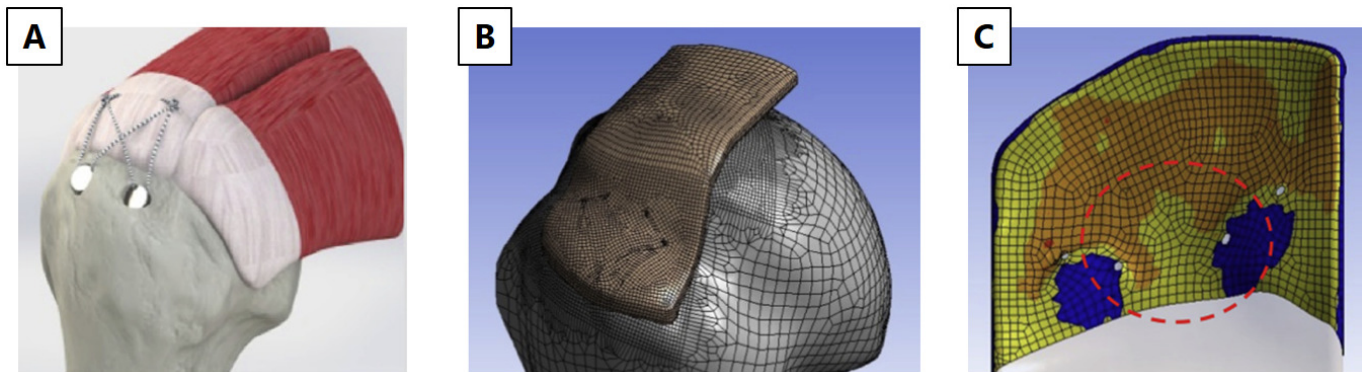
Figure 2.19: (A) Solid model for the FE analysis of the transosseous equivalent technique. (B) 3D mesh used in the simulations. (C) Qualitative maps of the supraspinatus-bone contact layout; orange represents the area in contact with a positive applied pressure. The free surfaces are in yellow, and the absence of any contact (device insertion areas) is shown in blue. Figures modified from [205], with permission.

we have highlighted the valuable contributions of modeling and computer simulations for the investigation of attachment strategies.

Models have provided insights into the structure-function relationship at entheses, which would not have been possible using experiments only. In general, models have the considerable advantage to be able to simulate scenarios that would be either impossible or costly to reproduce experimentally, such as assessing the mechanical impact of an individual feature (e.g., fiber alignment) or a gradual and controlled variation in a selected parameter (e.g., tendon tear size).

Considering Section 2.3.2 (reviewing the link between enthesis microstructure and composition to mechanical properties), one modeling approach still not much explored for the enthesis could be based on discrete network models, accounting for individual fibers (or fiber bundles) attaching to bone at discrete anchoring points. Although computationally expensive, such modeling route may reveal novel biomechanical aspects which are not captured when describing the enthesis as a continuum material. In analogy, discrete computational models of trabecular bone accounting for individual trabeculae have boosted our understating on deformation, failure and even mechanical adaptation of trabecular bone, by detailing mechanisms not easily evident with continuum modeling [225–229].

Furthermore, future models should target not only the local heterogeneous stress distribution but also failure aspects such as damage initiation and propagation. This could provide a broader picture on enthesis resilience and robustness to various loading conditions. Indeed, entheses may be designed by nature not only to minimize possible stress concentrations due to material mismatches, but also to cope with the unavoidable presence of damage.

Similarly to bone [230] and many other biological materials [11, 231], entheses may feature multiple toughening mechanisms at different length scales to hamper damage propagation. The presence of a compliant region with stiffness lower than tendon and bone is most likely one of such toughening strategies, deserving extra attention in future damage-based computational efforts. This is also a remarkable construction principle that may trigger the development of novel bioinspired adhesive to join strongly dissimilar materials. Finely tuned spatial variations in elastic modulus is only one aspect of the complex transition in material properties when going from tendon to bone, as the two tissues feature also different failure strain, fracture toughness, as well as viscoelastic behavior. Indeed, other material-level properties may also display a somewhat gradual transition across the enthesis, which need to be characterized by local experimental methods. Once known, these material parameters may then be cast into computational models going beyond linear elasticity to obtain a more realistic picture of the load transfer mechanism at the enthesis.

Computer simulations at the organ scale have allowed answering orthopedic relevant questions, with many studies focusing on the rotator cuff, as reviewed in Section 2.3.3. In general, organ scale models lack a de-

tailed description of the enthesis, probably due to the high computational cost needed to include micrometer level information on enthesis structure and material behavior. Depending on the specific research questions investigated with the model, a realistic representation of the enthesis may or may not be necessary. However, selecting and quantifying which aspects of the enthesis (e.g. spatial gradients, interlocking structure, compliant zone) should be included into organ level models may help to increase the ability of those studies to predict surgical outcomes.

From a mechanobiological viewpoint, musculoskeletal tissues have the remarkable ability to modify their structure in response to functional mechanical demands. Bone and tendon mechanobiology are well-established fields, which have seen important contributions coming from modeling and simulations. For instance, the knowledge of the local stress and strain at the tissue level obtained thanks to image-based microstructural FE analysis, combined with experimental information on bone remodeling, has allowed unravelling fundamental aspects on the mechanical control of bone regeneration [229, 232–234]. Enthesis mechanobiology is still a growing field and future in silico approaches should be used to compute the local mechanical environment at the cellular level, for instance during various stages of enthesis development, to elucidate the mechanical cues underlying the formation and the maintain of such a complex biological interface. Knowing the local mechanical environment within enthesis fibrocartilage and around fibrochondrocytes may also improve the understanding of the biomechanical factors contributing to enthesis degeneration.

Investigated feature	Paper	Studied enthesis & species	Approach of the study	Main findings
2.1 Fiber architecture	(Genin et al.,2009) [149]	Shoulder joint (rat supraspinatus tendon)	Continuum mechanics 3D unit cell model of a hypothetical enthesis without mineral	Angular deviation of fibers alone causes a drop of elastic modulus.
	(Rossetti et al.,2017) [125]	Ankle joint (pig Achilles tendon)	Experimental analysis combined with displacement field mapping	Tendon fibers are splaying and unravelling to anchor to bone. There is an angle-dependent force redistribution among fibers.
2.2 Mineral reinforcement	(Sartori and Stark, 2020)[162]	Ankle joint (mice Achilles tendon)	Experimental analysis combined with fiber tracking algorithm	Details aspects of fiber curving, branching and twisting before entering bone.
	(Wopenka et al.,2008) [235]	Shoulder joint (rat supraspinatus tendon)	Experimental assessment of mineral content across insertion	The variation of mineral content across the interface is fairly linear and occurs over a region of 120 μm.
	(Genin et al., 2009) [149]	Shoulder joint (rat supraspinatus tendon)	Continuum mechanics 3D unit cell model with different modes of mineralization	The resulting variation in tissue stiffness across insertion is highlighting a compliant region with a stiffness lower than tendon and bone
	(Liu et al., 2013) [183]	Idealized models based on data from shoulder joint (rat supraspinatus tendon)	Micromechanical 3D model of collagen stiffening based on nanoscale mineralization details (initiation and sequence)	Details of the mineralization process can have a large impact on tissue stiffening, notably on the spatial gradient rather than on the compliant region.
	(Aghaei et al., 2020)[190]	Idealized models based on generalized entheses data and data from shoulder joint (rat supraspinatus tendon)	Micromechanical continuum 3D model based on homogenization steps including nano-, sub-micro- and microstructural information	The width and modulus drop of the compliant region vary with the mineralization front position and the magnitude of the fibers angular deviation, respectively.
2.3 Surface roughness and interlocking	(Cordisco et al., 2012) [103]	General approach	Fracture mechanics tools applied on an idealized sinusoidal interface	Roughness increases toughness but there is a threshold above which multiple cracks start forming hence reducing toughness.
	(Hu et al., 2015) [192]	Shoulder joint (rat supraspinatus tendon)	Continuum mechanics 2D idealized bimaterial unit cell model	Geometrical properties of the interface lay in a region where the gain in toughness outweighs the loss in strength.
	(Milz et al., 2002) [194]	Ankle joint (human Achilles tendon)	Experimental analysis combined with 3D reconstruction of morphology	In addition to roughness, there is a complex interlocking pattern at the interface.
3.1 Load transfer optimization	(Liu et al., 2011) [55]	Shoulder joint (human supraspinatus tendon)	Continuum 2D FE model combined with a shape optimization algorithm	Shape of the insertion can be optimized to eliminate peak stresses.
	(Thomopoulos et al., 2006) [150]	Shoulder joint (rat supraspinatus tendon)	Continuum 2D FE model including local anisotropy and experimentally observed outward splay geometry.	Experimentally based arrangement reduces peak stress and shields the insertion splay while maximizing the stiffness.
	(Liu et al., 2012) [206]	Shoulder joint (human rotator cuff tendons)	Continuum 2D structural model combined with numerical optimization (minimizing radial stress)	Resulting elastic modulus of the interface has a minimum lower than tendon and bone (at the expense of tangential stress).
3.2 Peak stress regions (and link with tear)	(Inoue et al., 2013) [200]	Shoulder joint (human supraspinatus tendon)	2D simplified FE model with linear material properties	Peak stress move towards insertion with arm abduction.
	(Wakabayashi et al., 2003) [201]	Shoulder joint (human supraspinatus tendon)	3D FE model comprising non-linear material properties	Differences in stress state between both sides of the tendon with arm abduction can cause shear stress and therefore delamination tears
3.2 Damage and reattachment procedures	(Sano et al., 2006b) [203]	Shoulder joint (human supraspinatus tendon)	2D simplified FE model with partial thickness tears	Damage cause stress concentration around tears but also increase stress at the bony insertion. Stress state depends on arm abduction.
	(Quental et al., 2016)[204]	Shoulder joint (human supraspinatus tendon)	3D FE model including fibrocartilage modeling, with increasing size tears	Tears on the anterior side have a greater risk of propagation.
	(Funakoshi et al., 2008) [202]	Shoulder joint (bovine supraspinatus tendon)	2D FE model with three types of reattachment procedures	Surface holding repair with transosseous sutures prevents high stress concentration.
	(Mantovani et al., 2016) [205]	Shoulder joint (human supraspinatus tendon)	3D FE model with three types of reattachment procedures	Transosseus sutures lead to increased contact area and more uniform distribution of contact pressure.

Table 2.3: Computational and experimental findings regarding attachment strategies, load optimization mechanisms and overall biomechanical competence of tendon (and ligament) to bone junctions.

47

Bibliography

[1]   M. Benjamin et al. "Where tendons and ligaments meet bone: attachment sites ('entheses') in relation to exercise and/or mechanical load". English. In: *Journal of Anatomy* 4 (Apr. 2006), pp. 471–490.

[2]   Peter Fratzl et al. "Structure and mechanical quality of the collagen–mineral nano-composite in bone". In: *Journal of materials chemistry* 14.14 (2004), pp. 2115–2123.

[3]   Dieter Felsenberg. "Struktur und funktion des knochens: stützwerk aus kollagen und hydroxylapatit". In: *Pharmazie in unserer Zeit* 30.6 (2001), pp. 488–494.

[4]   Dick Heinegård and åke Oldberg. "Structure and biology of cartilage and bone matrix noncollagenous macromolecules". In: *The FASEB Journal* 3.9 (1989), pp. 2042–2051.

[5]   Michel Van Der Rest and Robert Garrone. "Collagen family of proteins". In: *The FASEB journal* 5.13 (1991), pp. 2814–2823.

[6]   P. Fratzl. "Collagen: Structure and Mechanics, an Introduction". In: *Collagen: Structure and Mechanics*. Ed. by Peter Fratzl. Boston, MA: Springer US, 2008, pp. 1–13. DOI: 10.1007/978-0-387-73906-9_1.

[7]   Natalie Reznikov et al. "Fractal-like hierarchical organization of bone begins at the nanoscale". In: *Science* 360.6388 (2018), eaao2189.

[8]   Marios Georgiadis, Ralph Müller, and Philipp Schneider. "Techniques to assess bone ultrastructure organization: orientation and arrangement of mineralized collagen fibrils". In: *Journal of The Royal Society Interface* 13.119 (June 2016), p. 20160088. (Visited on 04/22/2020).

[9]   Kilian E Stockhausen et al. "Collagen fiber orientation is coupled with specific nano-compositional patterns in dark and bright osteons modulating their biomechanical properties". In: *ACS nano* 15.1 (2021), pp. 455–467.

[10]   John D Currey and Ron Shahar. "Cavities in the compact bone in tetrapods and fish and their effect on mechanical properties". In: *Journal of Structural Biology* 183.2 (2013), pp. 107–122.

[11]   P. Fratzl and R. Weinkamer. "Nature's hierarchical materials". English. In: *Progress in Materials Science* 52.8 (Nov. 2007), pp. 1263–1334.

[12]   Natalie Reznikov et al. "The 3D structure of the collagen fibril network in human trabecular bone: Relation to trabecular organization". In: *Bone* 71 (Feb. 2015), pp. 189–195.

[13]   Jae-Young Rho, Liisa Kuhn-Spearing, and Peter Zioupos. "Mechanical properties and the hierarchical structure of bone". In: *Medical engineering & physics* 20.2 (1998), pp. 92–102.

[14]   Nicolas H Hart et al. "Mechanical basis of bone strength: influence of bone material, bone structure and muscle action". In: *Journal of musculoskeletal & neuronal interactions* 17.3 (2017), p. 114.

[15]   Alizae Marny Mohamed. "An overview of bone cells and their regulating factors of differentiation". In: *The Malaysian journal of medical sciences: MJMS* 15.1 (2008), p. 4.

[16]   Tamara A Franz-Odendaal, Brian K Hall, and P Eckhard Witten. "Buried alive: how osteoblasts become osteocytes". In: *Developmental dynamics: an official publication of the American Association of Anatomists* 235.1 (2006), pp. 176–190.

[17]   Christopher L. Newman and Matthew R. Allen. "Bone Remodeling". In: *Encyclopedia of Exercise Medicine in Health and Disease*. Ed. by Frank C. Mooren. Berlin, Heidelberg: Springer Berlin Heidelberg, 2012, pp. 140–143.

[18]   A Michael Parfitt. "Osteonal and hemi-osteonal remodeling: the spatial and temporal framework for signal traffic in adult human bone". In: *Journal of cellular biochemistry* 55.3 (1994), pp. 273–286.

[19]   Felix Repp et al. "Spatial heterogeneity in the canalicular density of the osteocyte network in human osteons". In: *Bone reports* 6 (2017), pp. 101–108.

[20]   A Michael Parfitt. *Quantum concept of bone remodeling and turnover: implications for the pathogenesis of osteoporosis*. 1979.

[21]   D. Ruffoni et al. "The bone mineralization density distribution as a fingerprint of the mineralization process". English. In: *Bone* 40.5 (May 2007), pp. 1308–1319.

[22] MA Hartmann et al. "Trabecular bone remodelling simulated by a stochastic exchange of discrete bone packets from the surface". In: *Journal of the mechanical behavior of biomedical materials* 4.6 (2011), pp. 879–887.

[23] Lynda F Bonewald. "Osteocytes as dynamic multifunctional cells". In: *Annals of the New York Academy of Sciences* 1116.1 (2007), pp. 281–290.

[24] Lynda F Bonewald. "The amazing osteocyte". In: *Journal of bone and mineral research* 26.2 (2011), pp. 229–238.

[25] Alexander Franciscus van Tol et al. "The mechanoresponse of bone is closely related to the osteocyte lacunocanalicular network architecture". In: *Proceedings of the National Academy of Sciences* 117.51 (2020), pp. 32251–32259.

[26] Sheldon Weinbaum, Stephan C Cowin, and Yu Zeng. "A model for the excitation of osteocytes by mechanical loading-induced bone fluid shear stresses". In: *Journal of biomechanics* 27.3 (1994), pp. 339–360.

[27] Tengteng Tang et al. "A 3D Network of Nanochannels for Possible Ion and Molecule Transit in Mineralizing Bone and Cartilage". In: *Advanced NanoBiomed Research* (2022), p. 2100162.

[28] Chiara Micheletti et al. "Bone Mineral Organization at the Mesoscale: A Review of Mineral Ellipsoids in Bone and at Bone Interfaces". In: *Acta Biomaterialia* (2022).

[29] Zhaoyong Zou et al. "Three-dimensional structural interrelations between cells, extracellular matrix, and mineral in normally mineralizing avian leg tendon". In: *Proceedings of the National Academy of Sciences* 117.25 (2020), pp. 14102–14109.

[30] Michael Kerschnitzki et al. "Architecture of the osteocyte network correlates with bone material quality". In: *Journal of bone and mineral research* 28.8 (2013), pp. 1837–1845.

[31] Cesare Ciani, Stephen B Doty, and Susannah P Fritton. "An effective histological staining process to visualize bone interstitial fluid space using confocal microscopy". In: *Bone* 44.5 (2009), pp. 1015–1017.

[32] Mahdi Ayoubi et al. "3D interrelationship between osteocyte network and forming mineral during human bone remodeling". In: *Advanced healthcare materials* 10.12 (2021), p. 2100113.

[33] Alexander F van Tol et al. "Network architecture strongly influences the fluid flow pattern through the lacunocanalicular network in human osteons". In: *Biomechanics and modeling in mechanobiology* 19.3 (2020), pp. 823–840.

[34] Grant Breeland, Margaret A Sinkler, and Ritesh G Menezes. "Embryology, bone ossification". In: *StatPearls [Internet]*. StatPearls Publishing, 2021.

[35] Hans-Peter Gerber et al. "VEGF couples hypertrophic cartilage remodeling, ossification and angiogenesis during endochondral bone formation". In: *Nature medicine* 5.6 (1999), pp. 623–628.

[36] Carolina A Moreira, David W Dempster, and Roland Baron. "Anatomy and ultrastructure of bone–histogenesis, growth and remodeling". In: *Endotext [Internet]* (2019).

[37] "Chapter 6 - Skeletal System Changes". In: *Functional Movement Development Across the Life Span (Third Edition)*. Ed. by Donna J. Cech and Suzanne "Tink" Martin. Third Edition. Saint Louis: W.B. Saunders, 2012, pp. 105–128.

[38] Andrei S Chagin and Phillip T Newton. "Postnatal skeletal growth is driven by the epiphyseal stem cell niche: potential implications to pediatrics". In: *Pediatric research* 87.6 (2020), pp. 986–990.

[39] Ego Seeman. "Periosteal bone formation—a neglected determinant of bone strength". In: *New England Journal of Medicine* 349.4 (2003), pp. 320–323.

[40] TJ Wronski et al. "Long-term effects of ovariectomy and aging on the rat skeleton". In: *Calcified tissue international* 45.6 (1989), pp. 360–366.

[41] Benjamin N Berg, Charles R Harmison, et al. "Growth, disease and aging in the rat." In: *Journal of gerontology* 12 (1957), pp. 370–377.

[42] Alden B Dawson. "Additional evidence of the failure of epiphyseal union in the skeleton of the rat. Studies on wild and captive gray Norway rats". In: *The Anatomical Record* 60.4 (1934), pp. 501–511.

[43] Alden B Dawson. "Further studies on epiphyseal union in the skeleton of the rat". In: *The Anatomical Record* 60.1 (1934), pp. 83–86.

[44] W Sontag. "Age-dependent morphometric alterations in the distal femora of male and female rats". In: *Bone* 13.4 (1992), pp. 297–310.

[45] Fiona Linnea Bach-Gansmo et al. "Calcified cartilage islands in rat cortical bone". In: *Calcified tissue international* 92.4 (2013), pp. 330–338.

[46] V Bentolila et al. "Intracortical remodeling in adult rat long bones after fatigue loading". In: *Bone* 23.3 (1998), pp. 275–281.

[47] John D. Currey. *Bones: structure and mechanics*. Princeton, N.J.: Princeton University Press, 2002.

[48] VC Mow, WY Gu, and FH Chen. "Structure and function of articular cartilage". In: *Basic orthopedic biomechanics and mechano-biology* 3 (2005), pp. 181–258.

[49] Javad Parvizi. *High yield orthopaedics E-Book*. Elsevier Health Sciences, 2010.

[50] M. Benjamin and J. R. Ralphs. "Fibrocartilage in tendons and ligaments–an adaptation to compressive load". eng. In: *Journal of anatomy* 193 (Pt 4).Pt 4 (1998), pp. 481–494.

[51] Adam C. Abraham and Tammy L. Haut Donahue. "From meniscus to bone: A quantitative evaluation of structure and function of the human meniscal attachments". In: *Acta Biomaterialia* 9.5 (May 2013), pp. 6322–6329.

[52] Alexander J. Boys et al. "Understanding the Stiff-to-Compliant Transition of the Meniscal Attachments by Spatial Correlation of Composition, Structure, and Mechanics". In: *ACS Applied Materials & Interfaces* 11.30 (July 2019), pp. 26559–26570.

[53] K.N. Hauch et al. "Nanoindentation of the insertional zones of human meniscal attachments into underlying bone". en. In: *Journal of the Mechanical Behavior of Biomedical Materials* 2.4 (Aug. 2009), pp. 339–347. (Visited on 02/08/2021).

[54] Megan L Killian. "Growth and mechanobiology of the tendon-bone enthesis". In: *Seminars in Cell & Developmental Biology*. Vol. 123. Elsevier. 2022, pp. 64–73.

[55] Yanxin Liu et al. "Mechanisms of Bimaterial Attachment at the Interface of Tendon to Bone". eng. In: *Journal of engineering materials and technology* 133.1 (Jan. 2011).

[56] Einat Blitz et al. "Tendon-bone attachment unit is formed modularly by a distinct pool of Scx-and Sox9-positive progenitors". In: *Development* 140.13 (2013), pp. 2680–2690.

[57] Yuki Sugimoto et al. "Scx+/Sox9+ progenitors contribute to the establishment of the junction between cartilage and tendon/ligament". In: *Development* 140.11 (2013), pp. 2280–2288.

[58] Neta Felsenthal et al. "Development of migrating tendon-bone attachments involves replacement of progenitor populations". In: *Development* 145.24 (2018), dev165381.

[59] Andrea G. Schwartz, Fanxin Long, and Stavros Thomopoulos. "Enthesis fibrocartilage cells originate from a population of Hedgehog-responsive cells modulated by the loading environment". In: *Development* 142.1 (2015), p. 196.

[60] Andrea G Schwartz, Leesa M Galatz, and Stavros Thomopoulos. "Enthesis regeneration: a role for Gli1+ progenitor cells". In: *Development* 144.7 (2017), pp. 1159–1164.

[61] Shiri Kult et al. "Bi-fated tendon-to-bone attachment cells are regulated by shared enhancers and KLF transcription factors". In: *Elife* 10 (2021), e55361.

[62] Neta Felsenthal and Elazar Zelzer. "Mechanical regulation of musculoskeletal system development". In: *Development* 144.23 (2017), p. 4271.

[63] Stavros Thomopoulos, Guy M Genin, and Leesa M Galatz. "The development and morphogenesis of the tendon-to-bone insertion What development can teach us about healing". In: *Journal of musculoskeletal & neuronal interactions* 10.1 (2010), p. 35.

[64] Chia-Feng Liu et al. "Spatial and temporal expression of molecular markers and cell signals during normal development of the mouse patellar tendon". In: *Tissue Engineering Part A* 18.5-6 (2012), pp. 598–608.

[65] Chia-Feng Liu et al. "A role for hedgehog signaling in the differentiation of the insertion site of the patellar tendon in the mouse". In: *PloS one* 8.6 (2013), e65411.

[66] Eva S Liu et al. "Molecular analysis of enthesopathy in a mouse model of hypophosphatemic rickets". In: *Development* 145.15 (2018), dev163519.

[67] Mary L Bouxsein et al. "Guidelines for assessment of bone microstructure in rodents using micro–computed tomography". In: *Journal of bone and mineral research* 25.7 (2010), pp. 1468–1486.

[68] LA Feldkamp, LC Davis, and JW Kress. "Optics InfoBase: Journal of the Optical Society of America A-Practical cone-beam algorithm". In: *JOSA A* (1984).

[69] Arne Maes et al. "Cryogenic contrast-enhanced microCT enables nondestructive 3D quantitative histopathology of soft biological tissues". In: *Nature communications* 13.1 (2022), pp. 1–14.

[70] Martin Stauber and Ralph Müller. "Micro-computed tomography: a method for the non-destructive evaluation of the three-dimensional structure of biological specimens". In: *Osteoporosis*. Springer, 2008, pp. 273–292.

[71] Ralph Müller. "Hierarchical microimaging of bone structure and function". In: *Nature Reviews Rheumatology* 5.7 (2009), pp. 373–381.

[72] Marvin Minsky. "Memoir on inventing the confocal scanning microscope". In: *Scanning* 10.4 (1988), pp. 128–138.

[73] Stéphane Blouin et al. "Confocal laser scanning microscopy—a powerful tool in bone research". In: *Wiener Medizinische Wochenschrift* 168.11 (2018), pp. 314–321.

[74] Andreas Roschger. "Quantitative analysis of local mineral content and composition during bone growth and remodeling". PhD thesis. Humboldt-Universität zu Berlin Berlin, 2015.

[75] Michael Kerschnitzki. "Bone material characteristics influenced by osteocytes". In: (2012).

[76] Michael Kerschnitzki et al. "Poorly ordered bone as an endogenous scaffold for the deposition of highly oriented lamellar tissue in rapidly growing ovine bone". In: *Cells Tissues Organs* 194.2-4 (2011), pp. 119–123.

[77] PA Franken et al. "Generation of optical harmonics". In: *Physical Review Letters* 7.4 (1961), p. 118.

[78] R Gauderon, PB Lukins, and CJR Sheppard. "Optimization of second-harmonic generation microscopy". In: *Micron* 32.7 (2001), pp. 691–700.

[79] Guy Cox et al. "3-dimensional imaging of collagen using second harmonic generation". In: *Journal of structural biology* 141.1 (2003), pp. 53–62.

[80] Isaac Freund, Moshe Deutsch, and Aaron Sprecher. "Connective tissue polarity. Optical second-harmonic microscopy, crossed-beam summation, and small-angle scattering in rat-tail tendon". In: *Biophysical journal* 50.4 (1986), pp. 693–712.

[81] Xiyi Chen et al. "Second harmonic generation microscopy for quantitative analysis of collagen fibrillar structure". In: *Nature protocols* 7.4 (2012), pp. 654–669.

[82] Ronald LaComb et al. "Phase matching considerations in second harmonic generation from tissues: effects on emission directionality, conversion efficiency and observed morphology". In: *Optics communications* 281.7 (2008), pp. 1823–1832.

[83] Vivien Lutz et al. "Impact of collagen crosslinking on the second harmonic generation signal and the fluorescence lifetime of collagen autofluorescence". In: *Skin Research and Technology* 18.2 (2012), pp. 168–179.

[84] Raghu Ambekar et al. "Quantifying collagen structure in breast biopsies using second-harmonic generation imaging". In: *Biomedical optics express* 3.9 (2012), pp. 2021–2035.

[85] Felix Repp et al. "Coalignment of osteocyte canaliculi and collagen fibers in human osteonal bone". In: *Journal of Structural Biology* 199.3 (2017), pp. 177–186.

[86] P Roschger et al. "Validation of quantitative backscattered electron imaging for the measurement of mineral density distribution in human bone biopsies". In: *Bone* 23.4 (1998), pp. 319–326.

[87] Markus A Hartmann et al. "Quantitative Backscattered Electron Imaging of bone using a thermionic or a field emission electron source". In: *Calcified Tissue International* 109.2 (2021), pp. 190–202.

[88] Joseph I Goldstein et al. "Backscattered electrons". In: *Scanning electron microscopy and X-ray microanalysis*. Springer, 2018, pp. 15–28.

[89] Paschalis Roschger et al. "Bone mineralization density distribution in health and disease". In: *Bone* 42.3 (2008), pp. 456–466.

[90] A B MANN. "9 - Nanoindentation". In: *Surfaces and Interfaces for Biomaterials*. Ed. by Pankaj Vadgama. Woodhead Publishing Series in Biomaterials. Woodhead Publishing, 2005, pp. 225–247.

[91] L.-H. He and M.V. Swain. "3.9 Microindentation". In: *Comprehensive Biomaterials II*. Ed. by Paul Ducheyne. Oxford: Elsevier, 2017, pp. 144–168.

[92] Warren Carl Oliver and George Mathews Pharr. "An improved technique for determining hardness and elastic modulus using load and displacement sensing indentation experiments". In: *Journal of materials research* 7.6 (1992), pp. 1564–1583.

[93] Shahrouz Amini et al. "The role of quasi-plasticity in the extreme contact damage tolerance of the stomatopod dactyl club". In: *Nature materials* 14.9 (2015), pp. 943–950.

[94] Eve Donnelly et al. "Effects of surface roughness and maximum load on the mechanical properties of cancellous bone measured by nanoindentation". In: *Journal of Biomedical Materials Research Part A: An Official Journal of The Society for Biomaterials, The Japanese Society for Biomaterials, and The Australian Society for Biomaterials and the Korean Society for Biomaterials* 77.2 (2006), pp. 426–435.

[95] MS Bobji and SK Biswas. "Estimation of hardness by nanoindentation of rough surfaces". In: *Journal of Materials Research* 13.11 (1998), pp. 3227–3233.

[96] Sara E Campbell, Virginia L Ferguson, and Donna C Hurley. "Nanomechanical mapping of the osteochondral interface with contact resonance force microscopy and nanoindentation". In: *Acta biomaterialia* 8.12 (2012), pp. 4389–4396.

[97] J. W. C. Dunlop, R. Weinkamer, and P. Fratzl. "Artful interfaces within biological materials". English. In: *Materials Today* 14.3 (Mar. 2011), pp. 70–78.

[98] R. Desmorat and F. A. Leckie. "Singularities in bi-materials: parametric study of an isotropic/anisotropic joint". In: *European Journal of Mechanics - A/Solids* 17.1 (Jan. 1998), pp. 33–52.

[99] Jeffrey P Spalazzi et al. "Quantitative mapping of matrix content and distribution across the ligament-to-bone insertion". In: *PLoS One* 8.9 (2013), e74349.

[100] A. A. Biewener. "Tendons and Ligaments: Structure, Mechanical Behavior and Biological Function". In: *Collagen: Structure and Mechanics*. Ed. by Peter Fratzl. Boston, MA: Springer US, 2008, pp. 269–284. DOI: 10.1007/978-0-387-73906-9_10.

[101] R. Bruce Martin, David B. Burr, and Neil A. Sharkey. "Mechanical Properties of Ligament and Tendon". In: *Skeletal Tissue Mechanics*. Ed. by R. Bruce Martin, David B. Burr, and Neil A. Sharkey. New York, NY: Springer New York, 1998, pp. 309–348. DOI: 10.1007/978-1-4757-2968-9_8.

[102] K. Fan et al. "Effects of Toughness Mismatch on Failure Behavior of Bi-Material Interfaces". In: *Procedia Engineering* 130 (Jan. 2015), pp. 754–762.

[103] Fernando A Cordisco et al. "Toughness of a patterned interface between two elastically dissimilar solids". In: *Engineering Fracture Mechanics* 96 (2012), pp. 192–208.

[104] Andrea Schwartz and Stavros Thomopoulos. "The Role of Mechanobiology in the Attachment of Tendon to Bone". In: *Structural Interfaces and Attachments in Biology*. Ed. by Stavros Thomopoulos, Victor Birman, and Guy M. Genin. New York, NY: Springer New York, 2013, pp. 229–257. DOI: 10.1007/978-1-4614-3317-0_11.

[105] HM Shaw and M Benjamin. "Structure–function relationships of entheses in relation to mechanical load and exercise". In: *Scandinavian journal of medicine & science in sports* 17.4 (2007), pp. 303–315.

[106] Teun Teunis et al. "A systematic review and pooled analysis of the prevalence of rotator cuff disease with increasing age". In: *Journal of Shoulder and Elbow Surgery* 23.12 (Dec. 2014), pp. 1913–1921.

[107] Simon M. Gianotti et al. "Incidence of anterior cruciate ligament injury and other knee ligament injuries: A national population-based study". In: *Journal of Science and Medicine in Sport* 12.6 (Nov. 2009), pp. 622–627.

[108] Sahishnu Patel et al. "Integrating soft and hard tissues via interface tissue engineering". In: *Journal of Orthopaedic Research* 36.4 (2018), pp. 1069–1077.

[109] Luciano A Rossi et al. "Current concepts in rotator cuff repair techniques: Biomechanical, functional, and structural outcomes". In: *Orthopaedic journal of sports medicine* 7.9 (2019).

[110] Stephen Lyman et al. "Epidemiology of anterior cruciate ligament reconstruction: trends, readmissions, and subsequent knee surgery". In: *JBJS* 91.10 (2009), pp. 2321–2328.

[111] Asheesh Bedi et al. "Effect of early and delayed mechanical loading on tendon-to-bone healing after anterior cruciate ligament reconstruction". In: *The Journal of Bone and Joint Surgery. American volume.* 92.14 (2010), p. 2387.

[112] Ali Miserez et al. "The Transition from Stiff to Compliant Materials in Squid Beaks". In: *Science* 319.5871 (2008), p. 1816.

[113] Matthew J. Harrington and J. Herbert Waite. "How Nature Modulates a Fiber's Mechanical Properties: Mechanically Distinct Fibers Drawn from Natural Mesogenic Block Copolymer Variants". In: *Advanced Materials* 21.4 (Jan. 2009), pp. 440–444. (Visited on 04/13/2020).

[114] Michael Benjamin et al. "The skeletal attachment of tendons—tendon 'entheses'". In: *Comparative Biochemistry and Physiology Part A: Molecular & Integrative Physiology* 133.4 (2002), pp. 931–945.

[115] John Apostolakos et al. "The enthesis: a review of the tendon-to-bone insertion". eng. In: *Muscles, ligaments and tendons journal* 4.3 (2014), pp. 333–342.

[116] H. H. Lu and S. Thomopoulos. "Functional attachment of soft tissues to bone: development, healing, and tissue engineering". English. In: *Annu Rev Biomed Eng* 15 (2013), pp. 201–26.

[117] A. Rufai, J. R. Ralphs, and M. Benjamin. "Ultrastructure of fibrocartilages at the insertion of the rat Achilles tendon". eng. In: *J Anat* 189 (Pt 1).Pt 1 (Aug. 1996). Edition: 1996/08/01, pp. 185–91.

[118] Wolfgang Wagermaier, Klaus Klaushofer, and Peter Fratzl. "Fragility of bone material controlled by internal interfaces". In: *Calcified tissue international* 97.3 (2015), pp. 201–212.

[119] Geoffroy Nourissat et al. "Mesenchymal Stem Cell Therapy Regenerates the Native Bone-Tendon Junction after Surgical Repair in a Degenerative Rat Model". In: *PLOS ONE* 5.8 (2010), e12248.

[120] Kristofer D. Sinclair et al. "Characterization of the Anchoring Morphology and Mineral Content of the Anterior Cruciate and Medial Collateral Ligaments of the Knee". In: *The Anatomical Record* 294.5 (May 2011), pp. 831–838. (Visited on 06/23/2020).

[121] Andrew D Waggett et al. "Characterization of collagens and proteoglycans at the insertion of the human Achilles tendon". In: *Matrix Biology* 16.8 (1998), pp. 457–470.

[122] Richard Weinkamer and Peter Fratzl. "Solving conflicting functional requirements by hierarchical structuring—Examples from biological materials". In: *MRS Bulletin* 41.9 (2016), pp. 667–671.

[123] Richard Weinkamer, Philip Kollmannsberger, and Peter Fratzl. "Towards a connectomic description of the osteocyte lacunocanalicular network in bone". In: *Current Osteoporosis Reports* 17.4 (2019), pp. 186–194.

[124] Pascal R. Buenzli and Natalie A. Sims. "Quantifying the osteocyte network in the human skeleton". In: *Bone* 75 (June 2015), pp. 144–150.

[125] L. Rossetti et al. "The microstructure and micromechanics of the tendon-bone insertion". In: *Nat Mater* 16.6 (June 2017), pp. 664–670.

[126] K. L. Moffat et al. "Characterization of the structure-function relationship at the ligament-to-bone interface". English. In: *Proceedings of the National Academy of Sciences of the United States of America* 105.23 (June 2008), pp. 7947–7952.

[127] Kathleen A. Derwin et al. "Enthesis Repair: Challenges and Opportunities for Effective Tendon-to-Bone Healing". eng. In: *The Journal of bone and joint surgery. American volume* 100.16 (2018), e109–e109.

[128] Alix C Deymier et al. "The multiscale structural and mechanical effects of mouse supraspinatus muscle unloading on the mature enthesis". In: *Acta biomaterialia* 83 (2019), pp. 302–313.

[129] Elazar Zelzer et al. "Tendon-to-bone attachment: From development to maturity". In: *Birth Defects Research Part C: Embryo Today: Reviews* 102.1 (2014), pp. 101–112.

[130] Alistair Bannerman, Jennifer Z. Paxton, and Liam M. Grover. "Imaging the hard/soft tissue interface". In: *Biotechnology Letters* 36.3 (Mar. 2014), pp. 403–415.

[131] Edward D. Bonnevie and Robert L. Mauck. "Physiology and Engineering of the Graded Interfaces of Musculoskeletal Junctions". In: *Annual Review of Biomedical Engineering* 20.1 (June 2018), pp. 403–429. (Visited on 06/23/2020).

[132] Alexander J. Boys et al. "Next generation tissue engineering of orthopedic soft tissue-to-bone interfaces". In: *MRS Communications* 7.3 (2017). Edition: 10/03, pp. 289–308.

[133] Ryan C. Locke, Adam C. Abraham, and Megan L. Killian. "Orthopedic Interface Repair Strategies Based on Native Structural and Mechanical Features of the Multiscale Enthesis". In: *ACS Biomaterials Science & Engineering* 3.11 (Nov. 2017), pp. 2633–2643.

[134] Nancy Lee, Jennifer Robinson, and Helen Lu. "Biomimetic strategies for engineering composite tissues". In: *Current Opinion in Biotechnology* 40 (Aug. 2016), pp. 64–74.

[135] Isabel Calejo, Raquel Costa-Almeida, and Manuela E. Gomes. "Cellular Complexity at the Interface: Challenges in Enthesis Tissue Engineering". In: *Cell Biology and Translational Medicine, Volume 5: Stem Cells: Translational Science to Therapy*. Ed. by Kursad Turksen. Cham: Springer International Publishing, 2019, pp. 71–90. DOI: `10.1007/5584_2018_307`.

[136] W Wagermaier et al. "Spiral twisting of fiber orientation inside bone lamellae". In: *Biointerphases* 1.1 (2006), pp. 1–5.

[137] Timothy G. Bromage et al. "Circularly polarized light standards for investigations of collagen fiber orientation in bone". In: *The Anatomical Record Part B: The New Anatomist* 274B.1 (Sept. 2003), pp. 157–168. (Visited on 04/22/2020).

[138] Stavros Thomopoulos et al. "Variation of biomechanical, structural, and compositional properties along the tendon to bone insertion site". In: *Journal of orthopaedic research* 21.3 (2003), pp. 413–419.

[139] Leonardo Galvis et al. "Polarized Raman Anisotropic Response of Collagen in Tendon: Towards 3D Orientation Mapping of Collagen in Tissues". In: *PLOS ONE* 8.5 (2013), e63518.

[140] M. Kazanci et al. "Bone osteonal tissues by Raman spectral mapping: Orientation–composition". In: *Journal of Structural Biology* 156.3 (Dec. 2006), pp. 489–496.

[141] X. Bi et al. "A novel method for determination of collagen orientation in cartilage by Fourier transform infrared imaging spectroscopy (FT-IRIS)". In: *Osteoarthritis and Cartilage* 13.12 (Dec. 2005), pp. 1050–1058.

[142] O. Paris et al. "Analysis of the hierarchical structure of biological tissues by scanning X-ray scattering using a micro-beam". eng. In: *Cellular and molecular biology (Noisy-le-Grand, France)* 46.5 (July 2000), pp. 993–1004.

[143] Craig Boote, Sally Dennis, and Keith Meek. "Spatial mapping of collagen fibril organisation in primate cornea—an X-ray diffraction investigation". In: *Journal of Structural Biology* 146.3 (June 2004), pp. 359–367.

[144] I Zizak et al. "Characteristics of mineral particles in the human bone/cartilage interface". In: *Journal of structural biology* 141.3 (2003), pp. 208–217.

[145] Dovina Qu et al. "Compositional mapping of the mature anterior cruciate ligament-to-bone insertion". In: *Journal of Orthopaedic Research* 35.11 (Nov. 2017), pp. 2513–2523. (Visited on 06/05/2020).

[146] A Daxer and P Fratzl. "Collagen fibril orientation in the human corneal stroma and its implication in keratoconus". In: *Investigative Ophthalmology & Visual Science* 38.1 (1997), pp. 121–129. (Visited on 05/05/2020).

[147] Laura Zorzetto and Davide Ruffoni. "Wood-inspired 3D-printed helical composites with tunable and enhanced mechanical performance". In: *Advanced Functional Materials* 29.1 (2019), p. 1805888.

[148] D. Hull and T. W. Clyne. *An Introduction to Composite Materials*. 2nd ed. Cambridge Solid State Science Series. Cambridge: Cambridge University Press, 1996. DOI: `10.1017/CBO9781139170130`.

[149] Guy M. Genin et al. "Functional grading of mineral and collagen in the attachment of tendon to bone". eng. In: *Biophysical journal* 97.4 (2009), pp. 976–985.

[150] Stavros Thomopoulos et al. "Collagen fiber orientation at the tendon to bone insertion and its influence on stress concentrations". In: *Journal of Biomechanics* 39.10 (Jan. 2006), pp. 1842–1851.

[151] Gerald A Zickler et al. "Finite element modeling of the cyclic wetting mechanism in the active part of wheat awns". In: *Biointerphases* 7.1 (2012), p. 42.

[152] T. Christian Gasser, Ray W. Ogden, and Gerhard A. Holzapfel. "Hyperelastic modelling of arterial layers with distributed collagen fibre orientations". In: *Journal of The Royal Society Interface* 3.6 (Feb. 2006), pp. 15–35. (Visited on 05/08/2020).

[153] Davide Ruffoni and Harry van Lenthe. "Finite element analysis in bone research: a computational method relating structure to mechanical function". en. In: Comprehensive Biomaterials. Elsevier, 2011.

Bibliography

[154] Yaohui Wang and Ani Ural. "Mineralized collagen fibril network spatial arrangement influences cortical bone fracture behavior". In: *Journal of biomechanics* 66 (2018), pp. 70–77.

[155] Shoubin Dong et al. "A three-dimensional collagen-fiber network model of the extracellular matrix for the simulation of the mechanical behaviors and micro structures". In: *Computer Methods in Biomechanics and Biomedical Engineering* 20.9 (July 2017), pp. 991–1003.

[156] Byoungkoo Lee et al. "A Three-Dimensional Computational Model of Collagen Network Mechanics". In: *PLOS ONE* 9.11 (2014), e111896.

[157] Ehsan Ban et al. "Strong triaxial coupling and anomalous Poisson effect in collagen networks". In: *Proceedings of the National Academy of Sciences* 116.14 (2019), p. 6790.

[158] Hailong Wang et al. "Long-range force transmission in fibrous matrices enabled by tension-driven alignment of fibers". In: *Biophysical journal* 107.11 (2014), pp. 2592–2603.

[159] Lijuan Zhang et al. "A coupled fiber-matrix model demonstrates highly inhomogeneous microstructural interactions in soft tissues under tensile load". In: *Journal of biomechanical engineering* 135.1 (2013), p. 011008.

[160] William J. Richardson et al. "Potential strain-dependent mechanisms defining matrix alignment in healing tendons". In: *Biomechanics and Modeling in Mechanobiology* 17.6 (Dec. 2018), pp. 1569–1580.

[161] P. De Falco et al. "Staggered Fibrils and Damageable Interfaces Lead Concurrently and Independently to Hysteretic Energy Absorption and Inhomogeneous Strain Fields in Cyclically Loaded Antler Bone". In: *ACS Biomaterials Science & Engineering* 3.11 (Nov. 2017), pp. 2779–2787.

[162] J. Sartori and H. Stark. "Tracking tendon fibers to their insertion - a 3D analysis of the Achilles tendon enthesis in mice". In: *Acta Biomater* 120 (Jan. 2021). Edition: 2020/05/20, pp. 146–155.

[163] Julian Sartori et al. "Three-dimensional imaging of the fibrous microstructure of Achilles tendon entheses in Mus musculus". In: *Journal of Anatomy* 233.3 (Sept. 2018), pp. 370–380. (Visited on 06/17/2020).

[164] R. G. Balijepalli et al. "Numerical simulation of the edge stress singularity and the adhesion strength for compliant mushroom fibrils adhered to rigid substrates". In: *International Journal of Solids and Structures* (May 2016), pp. 160–171.

[165] Alix C. Deymier-Black et al. "Allometry of the Tendon Enthesis: Mechanisms of Load Transfer Between Tendon and Bone". In: *Journal of Biomechanical Engineering* 137.11 (2015), pp. 111005–111005–8.

[166] I. Jäger and P. Fratzl. "Mineralized collagen fibrils: a mechanical model with a staggered arrangement of mineral particles". In: *Biophys J* 79.4 (Oct. 2000), pp. 1737–46.

[167] Baohua Ji and Huajian Gao. "Mechanical properties of nanostructure of biological materials". In: *Journal of the Mechanics and Physics of Solids* 52.9 (Sept. 2004), pp. 1963–1990.

[168] H. Gao et al. "Materials become insensitive to flaws at nanoscale: lessons from nature". In: *Proc Natl Acad Sci U S A* 100.10 (May 2003), pp. 5597–600.

[169] Himadri S. Gupta et al. "Cooperative deformation of mineral and collagen in bone at the nanoscale". eng. In: *Proceedings of the National Academy of Sciences of the United States of America* 103.47 (2006). Edition: 11/09, pp. 17741–17746.

[170] P. Roschger et al. "Bone mineralization density distribution in health and disease". English. In: *Bone* 42.3 (Mar. 2008), pp. 456–466.

[171] C. Lukas et al. "The Heterogeneous Mineral Content of Bone-Using Stochastic Arguments and Simulations to Overcome Experimental Limitations". English. In: *Journal of Statistical Physics* 144.2 (July 2011), pp. 316–331.

[172] Eleftherios P. Paschalis, Richard Mendelsohn, and Adele L. Boskey. "Infrared Assessment of Bone Quality: A Review". In: *Clinical Orthopaedics and Related Research®* 469.8 (Aug. 2011), pp. 2170–2178.

[173] S. Nuzzo et al. "Quantification of the degree of mineralization of bone in three dimensions using synchrotron radiation microtomography". English. In: *Medical Physics* 29.11 (Nov. 2002), pp. 2672–2681.

[174] B. Borah et al. "Long-term risedronate treatment normalizes mineralization and continues to preserve trabecular architecture: Sequential triple biopsy studies with micro-computed tomography". In: *Bone* 39.2 (Aug. 2006), pp. 345–352.

[175] C. Lukas et al. "Quantification of the interplay between mineralization and remodeling in trabecular bone assessed by in vivo micro-computed tomography". -. In: vol. 48. GREECE Athens NY New York: Elsevier Science Inc, May 2011, S205–S205.

[176] Maleeha Mashiatulla, Ryan D. Ross, and D. Rick Sumner. "Validation of cortical bone mineral density distribution using micro-computed tomography". In: *Bone* 99 (June 2017), pp. 53–61.

[177] Lisa Bounoure et al. "The Role of the Renal Ammonia Transporter Rhcg in Metabolic Responses to Dietary Protein". en. In: *Journal of the American Society of Nephrology* 25.9 (2014), pp. 2040–2052.

[178] D. Ruffoni et al. "Effect of temporal changes in bone turnover on the bone mineralization density distribution: A computer simulation study". English. In: *Journal of Bone and Mineral Research* 23.12 (Dec. 2008), pp. 1905–1914.

[179] Chloé Lerebours et al. "Mineral density differences between femoral cortical bone and trabecular bone are not explained by turnover rate alone". In: *bioRxiv* (2020), p. 2020.06.08.141036.

[180] Jill E. Shea, Rhett K. Hallows, and Roy D. Bloebaum. "Experimental confirmation of the sheep model for studying the role of calcified fibrocartilage in hip fractures and tendon attachments". In: *The Anatomical Record* 266.3 (Mar. 2002), pp. 177–183. (Visited on 06/18/2020).

[181] Virginia L. Ferguson, Andrew J. Bushby, and Alan Boyde. "Nanomechanical properties and mineral concentration in articular calcified cartilage and subchondral bone". en. In: *Journal of Anatomy* 203.2 (Aug. 2003), pp. 191–202. (Visited on 02/08/2021).

[182] Andrea G. Schwartz et al. "Mineral Distributions at the Developing Tendon Enthesis". In: *PLOS ONE* 7.11 (2012), e48630.

[183] Yanxin Liu et al. "Modelling the mechanics of partially mineralized collagen fibrils, fibres and tissue". eng. In: *Journal of the Royal Society, Interface* 11.92 (2013), pp. 20130835–20130835.

[184] Brigitte Wopenka et al. "The tendon-to-bone transition of the rotator cuff: a preliminary Raman spectroscopic study documenting the gradual mineralization across the insertion in rat tissue samples". In: *Applied spectroscopy* 62.12 (2008), pp. 1285–1294.

[185] A. C. Deymier et al. "Micro-mechanical properties of the tendon-to-bone attachment". eng. In: *Acta Biomater* (Jan. 2017). Edition: 2017/01/16.

[186] H.S. Gupta et al. "Two different correlations between nanoindentation modulus and mineral content in the bone–cartilage interface". en. In: *Journal of Structural Biology* 149.2 (Feb. 2005), pp. 138–148. (Visited on 02/08/2021).

[187] Hirotaka Sano, Yoshifumi Saijo, and Shoichi Kokubun. "Non-mineralized fibrocartilage shows the lowest elastic modulus in the rabbit supraspinatus tendon insertion: Measurement with scanning acoustic microscopy". In: *Journal of Shoulder and Elbow Surgery* 15.6 (Nov. 2006), pp. 743–749.

[188] Johnathan L. Sevick et al. "Fibril deformation under load of the rabbit Achilles tendon and medial collateral ligament femoral entheses". In: *Journal of Orthopaedic Research* 36.9 (Sept. 2018), pp. 2506–2515. (Visited on 06/28/2020).

[189] O. E. Armitage and M. L. Oyen. "Indentation across interfaces between stiff and compliant tissues". In: *Acta Biomater* (Jan. 2017).

[190] A. Aghaei et al. "Assessing the effective elastic properties of the tendon-to-bone insertion: a multiscale modeling approach". In: *Biomechanics and Modeling in Mechanobiology* (Oct. 2020).

[191] Fatemeh Saadat et al. "Effective elastic properties of a composite containing multiple types of anisotropic ellipsoidal inclusions, with application to the attachment of tendon to bone". In: *Journal of the Mechanics and Physics of Solids* 82 (2015), pp. 367–377.

[192] Yizhong Hu et al. "Stochastic interdigitation as a toughening mechanism at the interface between tendon and bone". eng. In: *Biophysical journal* 108.2 (2015), pp. 431–437.

[193] Can Dai et al. "Regional fibrocartilage variations in human anterior cruciate ligament tibial insertion: a histological three-dimensional reconstruction". In: *Connective Tissue Research* 56.1 (Jan. 2015), pp. 18–24.

[194] S Milz et al. "Three-dimensional reconstructions of the Achilles tendon insertion in man". In: *Journal of Anatomy* 200.2 (2002), pp. 145–152.

[195] Francesco Caimmi and Andrea Pavan. "An experimental evaluation of glass–polymer interfacial toughness". In: *Engineering fracture mechanics* 76.18 (2009), pp. 2731–2747.

[196] Edwin Hernandez et al. "Toughness amplification in copper/epoxy joints through pulsed laser micro-machined interface heterogeneities". In: *Scientific reports* 7.1 (2017), pp. 1–12.

[197] Won-Seock Kim et al. "Evaluation of mechanical interlock effect on adhesion strength of polymer–metal interfaces using micro-patterned surface topography". In: *International Journal of Adhesion and Adhesives* 30.6 (2010), pp. 408–417.

[198] Qizhou Yao and Jianmin Qu. "Interfacial versus cohesive failure on polymer-metal interfaces in electronic packaging—effects of interface roughness". In: *J. Electron. Packag.* 124.2 (2002), pp. 127–134.

[199] L. M. Galatz et al. "The outcome and repair integrity of completely arthroscopically repaired large and massive rotator cuff tears". English. In: *Journal of Bone and Joint Surgery-American Volume* 86a.2 (Feb. 2004), pp. 219–224.

[200] Atsushi Inoue et al. "Nonlinear stress analysis of the supraspinatus tendon using three-dimensional finite element analysis". In: *Knee Surgery, Sports Traumatology, Arthroscopy* 21.5 (May 2013), pp. 1151–1157.

[201] Ikuko Wakabayashi et al. "Mechanical environment of the supraspinatus tendon: a two-dimensional finite element model analysis". In: *Journal of Shoulder and Elbow Surgery* 12.6 (Nov. 2003), pp. 612–617.

[202] Tadanao Funakoshi et al. "In vitro and finite element analysis of a novel rotator cuff fixation technique". In: *Journal of Shoulder and Elbow Surgery* 17.6 (Nov. 2008), pp. 986–992.

[203] Hirotaka Sano, Ikuko Wakabayashi, and Eiji Itoi. "Stress distribution in the supraspinatus tendon with partial-thickness tears: An analysis using two-dimensional finite element model". In: *Journal of Shoulder and Elbow Surgery* 15.1 (Jan. 2006), pp. 100–105.

[204] C. Quental et al. "Full-thickness tears of the supraspinatus tendon: A three-dimensional finite element analysis". In: *Journal of Biomechanics* 49.16 (Dec. 2016), pp. 3962–3970.

Bibliography

[205] Matteo Mantovani et al. "A 3D finite element model for geometrical and mechanical comparison of different supraspinatus repair techniques". In: *Journal of Shoulder and Elbow Surgery* 25.4 (2016), pp. 557–563. (Visited on 02/04/2020).

[206] Y. X. Liu et al. "Bi-material attachment through a compliant interfacial system at the tendon-to-bone insertion site (vol 44, pg 83, 2012)". English. In: *Mechanics of Materials* 49 (June 2012), pp. 100–100.

[207] Fatemeh Saadat et al. "The concentration of stress at the rotator cuff tendon-to-bone attachment site is conserved across species". In: *Journal of the mechanical behavior of biomedical materials* 62 (2016), pp. 24–32.

[208] Ken Yamaguchi et al. "The demographic and morphological features of rotator cuff disease: a comparison of asymptomatic and symptomatic shoulders". In: *JBJS* 88.8 (2006), pp. 1699–1704.

[209] James F. Heming, Jason Rand, and Mark E. Steiner. "Anatomical Limitations of Transtibial Drilling in Anterior Cruciate Ligament Reconstruction". In: *The American Journal of Sports Medicine* 35.10 (Oct. 2007), pp. 1708–1715. (Visited on 02/10/2020).

[210] G Keene. "Arthroscopic reconstruction of the anterior cruciate ligament. A comparison of patellar tendon autograft and four-strand hamstring tendon autograft". In: *The American journal of sports medicine* 28.3 (2000), p. 438.

[211] David Simon et al. "The Relationship between Anterior Cruciate Ligament Injury and Osteoarthritis of the Knee". eng. In: *Advances in orthopedics* 2015 (2015). Edition: 2015/04/19, pp. 928301–928301.

[212] Mufaddal Mustafa Gombera and Jon K. Sekiya. "Rotator cuff tear and glenohumeral instability : a systematic review". eng. In: *Clinical orthopaedics and related research* 472.8 (2014), pp. 2448–2456.

[213] Spencer P. Lake et al. "Effect of fiber distribution and realignment on the nonlinear and inhomogeneous mechanical properties of human supraspinatus tendon under longitudinal tensile loading". In: *Journal of orthopaedic research : official publication of the Orthopaedic Research Society* 27.12 (2009), pp. 1596–1602.

[214] Nigel Palastanga, Derek Field, and Roger Soames. *Anatomy and human movement: structure and function*. Vol. 20056. Elsevier Health Sciences, 2006.

[215] Nelly Andarawis-Puri, Eric T. Ricchetti, and Louis J. Soslowsky. "Rotator cuff tendon strain correlates with tear propagation". In: *Journal of Biomechanics* 42.2 (Jan. 2009), pp. 158–163.

[216] Christoph Engelhardt et al. "Effect of partial-thickness tear on loading capacities of the supraspinatus tendon: a finite element analysis". In: *Computer Methods in Biomechanics and Biomedical Engineering* 19.8 (June 2016), pp. 875–882.

[217] James Thunes et al. "The effect of size and location of tears in the supraspinatus tendon on potential tear propagation". In: *Journal of biomechanical engineering* 137.8 (2015).

[218] DT Harryman 2nd et al. "Repairs of the rotator cuff. Correlation of functional results with integrity of the cuff." In: *JBJS* 73.7 (1991), pp. 982–989.

[219] Heui-Chul Gwak et al. "Delaminated rotator cuff tear: extension of delamination and cuff integrity after arthroscopic rotator cuff repair". In: *Journal of Shoulder and Elbow Surgery* 24.5 (2015), pp. 719–726.

[220] Satoshi Iwashita et al. "Characteristics of the patients with delaminated rotator cuff tear". In: *SICOT-J* 4 (2018).

[221] Victor Spitzer et al. "The visible human male: a technical report". In: *Journal of the American Medical Informatics Association* 3.2 (1996), pp. 118–130.

[222] Pol E Huijsmans et al. "Arthroscopic rotator cuff repair with double-row fixation". In: *JBJS* 89.6 (2007), pp. 1248–1257.

[223] Yilihamu Tuoheti et al. "Contact area, contact pressure, and pressure patterns of the tendon-bone interface after rotator cuff repair". In: *The American journal of sports medicine* 33.12 (2005), pp. 1869–1874.

[224] Evangelos I Avgoulas et al. "Adhesive-based tendon-to-bone repair: failure modelling and materials selection". In: *Journal of the Royal Society Interface* 16.153 (2019), p. 20180838.

[225] Ji Wang et al. "Trabecular plates and rods determine elastic modulus and yield strength of human trabecular bone". In: *Bone* 72 (2015), pp. 71–80.

[226] Davide Ruffoni, R Müller, and G Harry van Lenthe. "Mechanisms of reduced implant stability in osteoporotic bone". In: *Biomechanics and modeling in mechanobiology* 11.3 (2012), pp. 313–323.

[227] Manfred M Maurer et al. "Does mechanical stimulation really protect the architecture of trabecular bone? A simulation study". In: *Biomechanics and modeling in mechanobiology* 14.4 (2015), pp. 795–805.

[228] John WC Dunlop et al. "New suggestions for the mechanical control of bone remodeling". In: *Calcified tissue international* 85.1 (2009), pp. 45–54.

[229] Friederike A Schulte et al. "Local mechanical stimuli regulate bone formation and resorption in mice at the tissue level". In: *PloS one* 8.4 (2013), e62172.

[230] Hajar Razi et al. "Damage tolerance of lamellar bone". In: *Bone* 130 (2020), p. 115102.

[231] Wei Huang et al. "Multiscale toughening mechanisms in biological materials and bioinspired designs". In: *Advanced Materials* 31.43 (2019), p. 1901561.

[232] Patrik Christen et al. "Bone remodelling in humans is load-driven but not lazy". In: *Nature communications* 5.1 (2014), pp. 1–5.

[233] Zihui Li et al. "Mechanical regulation of bone formation and resorption around implants in a mouse model of osteopenic bone". In: *Journal of the Royal Society Interface* 16.152 (2019), p. 20180667.

[234] Hajar Razi et al. "Aging leads to a dysregulation in mechanically driven bone formation and resorption". In: *Journal of Bone and Mineral Research* 30.10 (2015), pp. 1864–1873.

[235] Brigitte Wopenka et al. "The tendon-to-bone transition of the rotator cuff: a preliminary Raman spectroscopic study documenting the gradual mineralization across the insertion in rat tissue samples". In: *Applied spectroscopy* 62.12 (2008), pp. 1285–1294.

Chapter 3

Specific aims of the thesis

The global aim of this thesis is to explore the structure and the properties of mineralized fibrocartilage and of the underlying subchondral bone at the Achilles tendon insertion into calcaneus bone. Those tissues are involved in transmitting forces produced by the tendon insertion and sliding during motion. Two specific locations are compared: the enthesis and the periosteal areas. Those regions are subjected to different mechanical loading: tensile forces at enthesis and a combination of shear and compressive forces at the periosteal side. Through this thesis, an effort has been made to illustrate how high-resolution characterization techniques can be used to assess a multi-tissue region such as the fibrocartilage-bone complex. All the tools are carefully explained and guidelines are provided in each chapter to align with this objective. Three more specific aims were defined:

Aim I: Quantify microstructure and microporosity within mineralized fibrocartilage and underlying subchondral bone

This research aim is the main content of the published paper presented in Chapter 4. Specifically, we use micro-computed tomography (micro-CT) at two different length scales combined with histology and electron microscopy imaging to shed light on tissue organization, microstructure (trabecular bone morphology and interface roughness) and microporosity (fibrochondrocyte lacunae and subchondral bone channels) at enthesis and periosteal regions.

Aim II: Unravel structure-property relationships within enthesis and periosteal mineralized fibrocartilage, using subchondral bone as a reference tissue

To tackle this aim, a multimodal investigation at the same tissue locations is achieved in the paper presented in Chapter 5. Specifically, we combine nanoindentation with second harmonic generation (SHG) and quantitative backscattered electron imaging (qBEI) to spatially correlate mechanical properties with mineralization and fibrous matrix organization. As the proposed material characterization techniques are mainly limited to two dimensions, we considered both longitudinal and transverse cross-sections to address

tissue anisotropy and provide three-dimensional insights.

Aim III: Explore mineralized fibrocartilage-bone crosstalk and subchondral bone functional nanoporosity

Confocal laser scanning microscope on stained samples allows to visualize and investigate the osteocyte lacuno-canalicular network behavior close to the interface with fibrocartilage. As staining infiltrates throughout all the accessible pores, it can also be exploited (in combination with previously used techniques such as micro-CT, qBEI and SHG) to track communication pathways between bone and mineralized fibrocartilage. This work is reported in Chapter 6.

Chapter 4

Local anisotropy in mineralized fibrocartilage and subchondral bone beneath the tendon-bone interface

[a] Mechanics of Biological and Bioinspired Materials Laboratory, Department of Aerospace and Mechanical Engineering, University of Liège, Liège, Belgium ; [b] Chemical Engineering Department, University of Liège, Liège, Belgium ; [c] Ludwig Boltzmann Institute of Osteology, Hanusch Hospital of OEGK and AUVA Trauma Centre Meidling, 1st Medical Department Hanusch Hospital, Vienna, Austria ; [d] Department of Physical Medicine and Sports Traumatology, University of Liège and University Hospital of Liège, Liège, Belgium ; [e] Experimental Surgery unit, GIGA & Credec, University of Liege, Liege, Belgium ; [f] Auckland Bioengineering Institute and Department of Engineering Science, University of Auckland, New Zealand ; [g] Department of Mechanical Engineering, KU Leuven, Leuven, Belgium.

ABSTRACT

The enthesis allows the insertion of tendon into bone thanks to several remarkable strategies. This complex and clinically relevant location often features a thin layer of fibrocartilage sandwiched between tendon and bone to cope with a highly heterogeneous mechanical environment. The main purpose of this study was to investigate whether mineralized fibrocartilage and bone close to the enthesis show distinctive three-dimensional microstructural features, possibly to enable load transfer from tendon to bone. As a model, the Achilles tendon-calcaneus bone system of adult rats was investigated with histology, backscattered electron imaging and micro-computed tomography. The microstructural porosity of bone and mineralized fibrocar-

tilage in different locations including enthesis fibrocartilage, periosteal fibrocartilage and bone away from the enthesis was characterized. We showed that calcaneus bone presents a dedicated protrusion of low porosity where the tendon inserts. A spatially resolved analysis of the trabecular network suggests that such protrusion may promote force flow from the tendon to the plantar ligament, while partially relieving the trabecular bone from such a task. Focusing on the tuberosity, highly specific microstructural aspects were highlighted. Firstly, the interface between mineralized and unmineralized fibrocartilage showed the highest roughness at the tuberosity, possibly to increase failure resistance of a region carrying large stresses. Secondly, fibrochondrocyte lacunae inside mineralized fibrocartilage, in analogy with osteocyte lacunae in bone, had a predominant alignment at the enthesis and a rather random organization away from it. Finally, the network of subchondral channels inside the tuberosity was highly anisotropic when compared to contiguous regions. This dual anisotropy of subchondral channels and cell lacunae at the insertion may reflect the alignment of the underlying collagen network. Our findings suggest that the microstructure of fibrocartilage may be linked with the loading environment. Future studies should characterize those microstructural aspects in aged and or diseased conditions to elucidate the poorly understood role of bone and fibrocartilage in enthesis-related pathologies.

4.1   Introduction

A crucial requirement of the musculoskeletal apparatus is the transmission of forces from tendons to bone. This can be a challenging task owing to the strong differences in composition, structure and material behavior between the soft tissue and the hard mineralized bone, making connecting regions vulnerable to high stresses, which may trigger failure upon repeated loading [1]. Consequently, the integration of tendons into bone often occurs through a specialized multi-material region called enthesis, which comprises fibrocartilage as an intermediate tissue to mitigate the incompatibilities between the two materials [2].

Entheses are traditionally subdivided into four contiguous regions: the tendon, the unmineralized fibrocartilage, the mineralized fibrocartilage and the bone. The inclusion of tendon and bone in the definition of entheses highlights the absence of a well-defined interface among these tissues [3]. From a compositional point of view, in contrast to tendon and bone, which are fibrous tissues based on collagen type I, enthesis fibrocartilage features a higher content of collagen type II and proteoglycans [4, 5]. The latter, having a high affinity for water, are believed to provide fibrocartilage with improved resistance to compression [2]. The transition from tendon to unmineralized fibrocartilage is characterized by a large decrease in the diameter of the tendon fibers, which branches into smaller interface fibers in fibrocartilage [5, 6]. Fibrocartilage fibers are somewhat less aligned along the tendon direction [7] and splay out [5], resulting in a broader attachment area. Before reaching bone, the fibrocartilage matrix gets reinforced by mineral crystals [8]. Rather than being flat, the interface between unmineralized and mineralized fibrocartilage is fairly wavy [9, 10] and the junction between mineralized fibrocartilage and bone is highly interlocked [2, 11]. Such compositional and architectural modifications are considered remarkable adaptation strategies to improve the endurance and
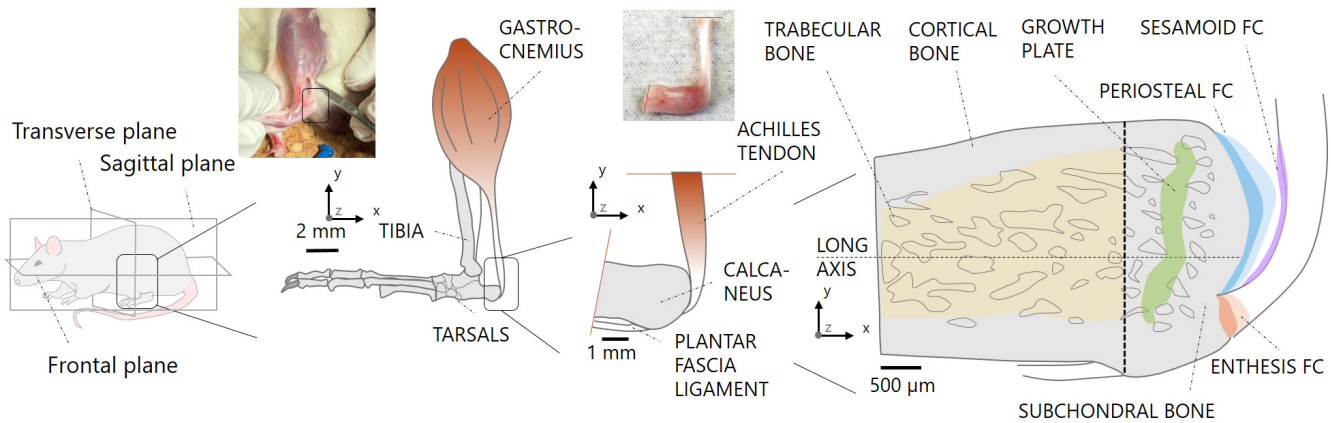
Figure 4.1: Schematic overview of the ankle joint. Several anatomical details and the different types of fibrocartilage required for joint functioning are highlighted. In addition to enthesis and periosteal fibrocartilage (FC), the tendon surface close to the enthesis is covered by a layer of sesamoid fibrocartilage, likely to protect the tendon by providing resistance against compressive and shear stresses coming from the contact with the bone. Unmineralized and mineralized fibrocartilages are shown in light and dark colors, respectively. Pictures of the tendon-bone construct were taken during sample extraction.

the robustness of entheses, enabling the transmission of loads even higher than body weight for millions of loading cycles [5, 9, 12–17].

Despite a finely tuned and unique biomechanical behavior, entheses are of considerable clinical relevance for several reasons. They are vulnerable to overuse injuries [3, 18], rheumatic pathologies [19–21] and degenerative changes [22, 23]. Some of these conditions seem to be more prevalent in entheses subjected to intense mechanical loading [3], and there is probably a relationship (yet poorly understood) between the highly heterogeneous local mechanical environment at the enthesis and the likelihood to develop enthesopathies [24]. Enthesis pathologies such as enthesitis are more complex to treat than pure tendon or bone lesions due to their histological and biomechanical characteristics and should be included into a potential general inflammatory context.

From an orthopedic perspective, tendon traumatic or acute injuries, even if they do not directly involve the attachment region, often require the surgical reattachment of the soft tissue to the bone. However, the enthesis, unlike bone and to some extent tendon, has slow and limited regeneration ability [25–27]. As a consequence, surgical treatments can have a rather poor long-term outcome [28–31]. Furthermore, there is strong biomechanical and clinical evidence that failure can occur not only at the soft side of the enthesis but also within the subchondral bone beneath the insertion [32], and even in the bone far away from the attachment region [33–35]. Those facts highlight the central role of bone in the anchoring process.

Bone has the unique ability to reorganize its structure and material properties according to the local mechanical environment [36, 37]. Over the last years, many in vivo mechanobiological experiments have shown that tissue level mechanical forces are able to drive local bone formation and resorption [29, 38–42], leading to reconfigurations of cortical and trabecular bone morphology. In aged conditions or following implant insertion, the bone mechanosensory machine is disturbed, causing a decreased mechanoresponsiveness [43, 44], which may lead to bone loss. Although less understood, there are suggestions that even the mineralization process [37], the orientation of the vascular canals [45, 46], the shape and arrangement of the osteocyte lacunae [47, 48] and, at smaller length scales, the organization of the osteocyte canalicular network [49, 50] may mirror the loading environment. The bone beneath the enthesis has the critical biomechanical task of receiving loads from the tendon and redistributing them away from the attachment point. Surprisingly, only little efforts have been made to characterize bone properties near insertions. Therefore, the main purpose of this study is to investigate bone microstructure close to the enthesis at multiple length scales, from whole bone down to cell lacunae. Such characterization is needed to improve our knowledge of bone adaptation close to soft tissue attachments, with perspectives on orthopedics and regenerative medicine.

As a biological system, the Achilles tendon insertion into calcaneus bone is considered (Fig. 4.1). At this anatomical location, bone is bordered with two types of fibrocartilage [51, 52]: the enthesis fibrocartilage, enabling the attachment of tendon into bone, and the periosteal fibrocartilage, which covers the bone surface above the insertion and facilitates the sliding between tendon and bone during joint movement (e.g. dorsiflexion). Here, we assume that bone shows distinctive features to cope with tendon loading, which are not present in regions away from the insertion. Specifically, we hypothesize that bone microstructure and microporosity beneath enthesis fibrocartilage differs from bone located below periosteal fibrocartilage, reflecting a distinct mechanical environment. Our core investigation is based on micro-computed tomography (micro-CT) at two different length scales, combined with advanced image processing. As entheses are complex regions comprising different tissues [18, 53], we used histology and backscattered electron imaging (BEI) to complement the micro-CT analysis with biological information on tissue type, location and organization. We performed a spatially resolved analysis of trabecular bone when approaching the enthesis. Then, we characterized the arrangement of subchondral channels and fibrochondrocyte lacunae within bone and fibrocartilage, respectively. Finally, we measured the local roughness of the interface anchoring unmineralized to mineralized fibrocartilage.

4.2   Materials and methods

4.2.1   Sample preparation, histology, backscattered electron imaging and micro-CT

Achilles tendon-calcaneus bone samples (n = 7) were carefully extracted from the posterior legs of 3-month-old male Sprague–Dawley rats (Fig. 4.1). Animal weight was 450 g $\pm$ 50 g and samples were available

at the Liège University Hospital (CHU) in the framework of a sample organ donation program approved by the Animal Ethics Committee of the University of Liège (ULg IACUC-21-2340). The procedure was performed in accordance with relevant guidelines and regulations and reported in compliance with the AR-RIVE guidelines. After extraction, two samples were prepared for histology. Tendon-bone specimens were fixed in 70 % ethanol, dehydrated (baths of increasing ethanol concentration of 80–90–100 %, 24 h each) and degreased by acetone. Subsequently, samples were embedded in poly-methylmethacrylate (PMMA). Sections with a thickness of approximately 3 μm were cut from the blocks with a hard tissue microtome (Leica SM2500, Nussloch, Germany) and stained either with Giemsa or with Goldner trichrome to distinguish fibrocartilage from bone. The sections were then visualized with a light microscope, also using polarized light (Axiophot, Zeiss, Oberkochen, Germany) equipped with a digital camera (Axiocam HRc, Zeiss). The rest block was used to perform BEI with 20 kV (Field Emission SEM Supra40, Zeiss) to distinguish mineralized from non-mineralized tissue. At the same time, the remaining five samples used for micro-CT imaging were dried overnight at room temperature directly after extraction and then glued on a custom three-dimensional printed support. Whole tendon-bone specimens were first scanned with micro-CT at a nominal isotropic voxel size of 5 μm. In brief, the machine (Skyscan 1272, Bruker, Belgium) was operated at tube voltage of 60 kV and current of 166 μA, in combination with a 0.25 mm thick aluminum filter. The samples were rotated over 180 ° with a rotation step of 0.2 ° (corresponding to 900 projections), with an exposure time of 2000 ms and a frame averaging of 4, leading to a scan time of approximately 3 h.

Following the first scan at the whole bone level, samples were fixed (70 % ethanol, 24 h) and dehydrated (baths of increasing ethanol concentration of 80–90–100 %, 24 h each) before subsequent embedding in epoxy resin (EpoThin 2 Resin, Buehler, Germany). The size of the samples along the cranio-caudal direction (Fig. 4.1) was reduced by performing a transverse cut with a manual saw, to enable scanning at a higher magnification of a smaller bone region adjacent to the periosteal and enthesis fibrocartilages. Samples were embedded to facilitate cutting and to minimize motion artifacts which can hamper image quality when scanning at high resolution and long scanning time. Embedded bone samples were then imaged with the same micro-CT machine at a nominal isotropic resolution of 1.25 μm, using a 0.5 mm aluminum filter combined with voltage and current of 55 kV and 181 μA, respectively. Again 900 projections were acquired with an exposure of 6000 ms and frame averaging of 2, for a scan duration of about 10 h per sample. Images were reconstructed using a filtered back projection algorithm, including ring artifact reduction and beam hardening correction [54], as implemented in the reconstruction software of the scanner (NRecon v.1.7.5.2, Skyscan).

4.2.2 Image processing and quantitative morphometry

Image alignment and segmentation

The reconstructed three-dimensional images of the whole tendon-bone complex were cropped along the transverse plane right before the medullar cavity (Fig. 4.2a). The virtual bones were then aligned along

their three principal axes of inertia using BoneJ (v.1.4.3), a module of ImageJ (v.1.52a) [55, 56]. Following this procedure, a distinct bony protrusion (referred as tuberosity) was revealed at the tendon attachment site, particularly evident when looking at sagittal sections (i.e., XY plane in Fig. 4.2b). The high-resolution scans were also aligned along the principal axes of inertia and slightly rotated in the sagittal plane so that the tuberosity of the low- and high-resolution images were co-aligned (Supplementary Fig. S4.1). To define the overall three-dimensional extent of the tuberosity, several consecutive cross-sections in the XY sagittal plane were inspected for anatomical landmarks in relation to the presence of the tendon, which was visible in the low-resolution scans (Supplementary Fig. S4.1): the tuberosity was considered to start as soon as it generated an angle of 100 ° with the superior periosteal region, and to end when there was no protrusion evident anymore on the plantar side of the bone (Fig. 4.2b). All subsequent image processing procedures were done using Matlab (R2018a; The Mathworks, USA), CTAn (v1.19.4.0, Skyscan) and Avizo (v.9.2.0, ThermoFisher Scientific).

Before segmentation and quantitative analysis, images were smoothed with a three-dimensional Gaussian filter (square kernel 1.5 radius, 0.65 standard deviation). Filtering of raw micro-CT data is often required prior to segmentation to remove inherent signal noise. Gaussian filters are frequently used as they allow noise removal while keeping a satisfying contrast between bone and background [57]. Considering the good signal-to-noise ratio of our micro-CT measurements, only a limited amount of filtering was necessary. Fig. S4.2 recapitulates the impact of Gaussian blurring on noise reduction with representative cross sections of the micro-CT images at 1.25 μm and 5 μm voxel size. In both cases, all microstructural features of interest were well-preserved. After filtering, images were binarized using a global threshold calculated with Otsu's method [58], as implemented in CTAn. This is an iterative algorithm ideal for bimodal distributions of gray values which possess a valley between the two peaks [59]. It finds a threshold that maximizes the difference in mean values while minimizing the variance between voxels classified as bone and background. A graphical explanation of Otsu's method is provided in Fig. S4.3.

Tuberosity and trabecular bone analysis

The bony tuberosity and the trabecular network were investigated using mainly the lower resolution (i.e. 5 μm) scans, analyzed with the software CTAn. The tuberosity was virtually separated from the remaining bone along an oblique plane, as illustrated in Fig. 4.2b. This region was quantified by measuring the overall tissue volume (i.e., tuberosity tissue volume, T.TV) and the orientation (T.θ, T.ϕ). Those angles describe the orientation of the tuberosity with respect to the principal axes of inertia of the bone (Fig. 4.2c). Additionally, the high-resolution scans were used to measure the tuberosity porosity (T.Po).

The segmentation of the trabecular compartment from the remaining bone was performed using a customized multistep procedure: firstly, the bones were cropped in the transverse direction to remove the growth plate. Then, a sequence of morphological operators, including despeckling, closing and erosion, was applied to exclude the cortical bone layer [60]. The trabecular bone morphology was quantified with
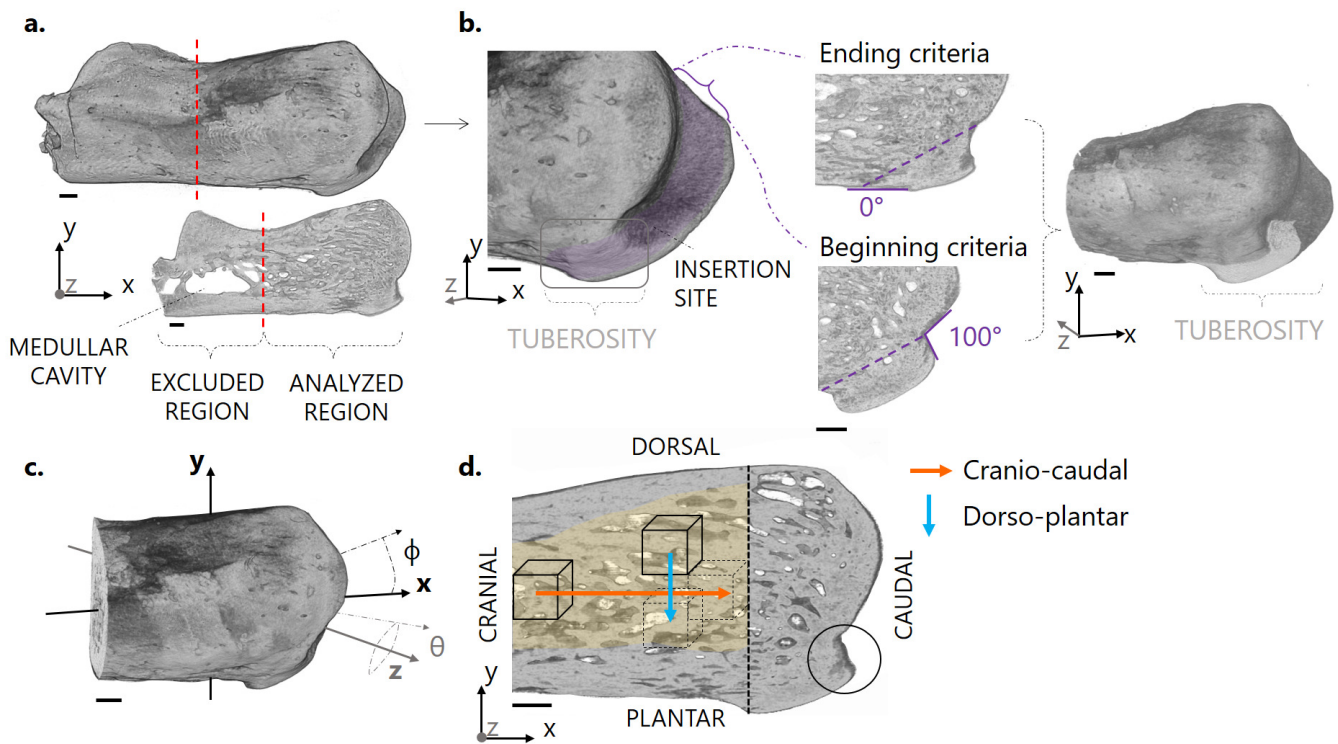
Figure 4.2: Image segmentation and reference coordinate system. (**a**) Three-dimensional rendering and typical sagittal section of a reconstructed and realigned calcaneus bone at 5 μm resolution. The cutting plane (red dashed lines) demarcates the analyzed region. (**b**) Cropped bone with a close up on the insertion site. The cross-sections considered for the tuberosity analysis are highlighted in purple. The anatomical landmarks to identify the tuberosity in the sagittal plane are also illustrated, together with the cutting orientation (dashed lines) used for the segmentation of the tuberosity. (**c**) Representation of the spherical coordinate system with the azimuthal (ϕ) and polar (θ) angles used to define the orientation of microstructural features. (**d**) Illustration of the cubic volumes of interest defined for the spatially resolved analysis of the trabecular network (the analyzed trabecular compartment is highlighted in yellow). Cubes were displaced along two directions: cranio-caudal (orange arrow) and dorso-plantar (blue arrow). Scale bars: 500 μm.

the software CTAn according to standard guidelines [57], with the following parameters: bone volume fraction (BV/TV), trabecular thickness (Tb.Th), trabecular separation (Tb.Sp), and degree of anisotropy (DA). The latter was computed by fitting the mean intercept length (MIL) tensor with an ellipsoid and considering 1 minus the ratio between the smallest and the biggest eigenvalues, such that anisotropic and isotropic microstructures are defined by DA = 1 and DA = 0, respectively. The trabecular network was further characterized with a local spatially resolved analysis [61], by defining cubic volumes of interest (VOI) marching along the cranio-caudal and the dorso-plantar directions (Fig. 4.2d). The size of each VOI was 0.75 mm (side length), so that about five trabeculae were included in each direction, to provide a spatially resolved and reliable estimation of trabecular architecture[57]. Starting from the most cranial region, the cube was displaced in steps of 0.375 mm (i.e., half of the side length) along the bone longitudinal axis of inertia and following the cranio-caudal direction (x-direction, Fig. 4.2d) until the growth plate. Seven locations were covered, for a total length of 3 mm. Spatial variations along the dorso-plantar direction (y-direction, Fig. 4.2d) were probed using marching cubes moving vertically, again in steps of 0.375 mm. Here, owing to the smaller dimensions of the calcaneus, only the most caudal locations were considered: two parallel sets of three regions could be analyzed, covering a length of 1.5 mm. Each cube contained only trabecular bone as ensured by simultaneous visualization of the three mutually perpendicular planes (Dataviewer, v.1.5.3.4, Skyscan). Within each VOI, the following local morphometric parameters were computed: BV/TV, Tb.Th, Tb.Sp, DA and preferred orientations (Pref.Or.θ and Pref.Or.ϕ). The latter were computed by considering the orientation of the MIL eigenvector with the smallest eigenvalue, which is an indication of the predominant spatial orientation of the trabeculae [62]. The two angles (Pref.Or.θ and Pref.Or.ϕ) were computed with respect to the principal axes of the bone [63, 64].

Bone microporosity: subchondral channels and fibrochondrocyte lacunae

Bone microporosity was analyzed based on the high-resolution (i.e., 1.25 μm voxel size) scans and considering three distinct locations (Fig. 4.3): (I) the tuberosity region where tendon attaches to bone and encompassing the entire bony tuberosity and including mineralized (enthesis) fibrocartilage; (II) a periosteal region found on the caudal side of the calcaneus above the tuberosity and comprising subchondral bone covered with mineralized (periosteal) fibrocartilage; and (III) a cortical bone region situated beneath the bone surface away from the enthesis and lacking fibrocartilage. Those regions were identified in all samples based on approximately the same positions. The characterization of microporosity in subchondral bone and mineralized cartilage was conducted in CTAn (Fig. 4.3). The main contributor of microporosity in mineralized cartilage are fibrochondrocyte lacunae. In addition to (osteocyte) lacunae, the subchondral plate microporosity includes both vascular and avascular channels [65, 66]. The former contain blood vessels while the latter are extensions of the marrow space and contain marrow cells and fat. As there is some overlapping in the dimensions of those features, a segmentation based on size is not feasible. Therefore, subchondral plate pores, other than lacunae, will be called subchondral channels [65]. Histology suggested that the majority of subchondral channels within the tuberosity and in the side region encloses blood vessels ("Results" section).
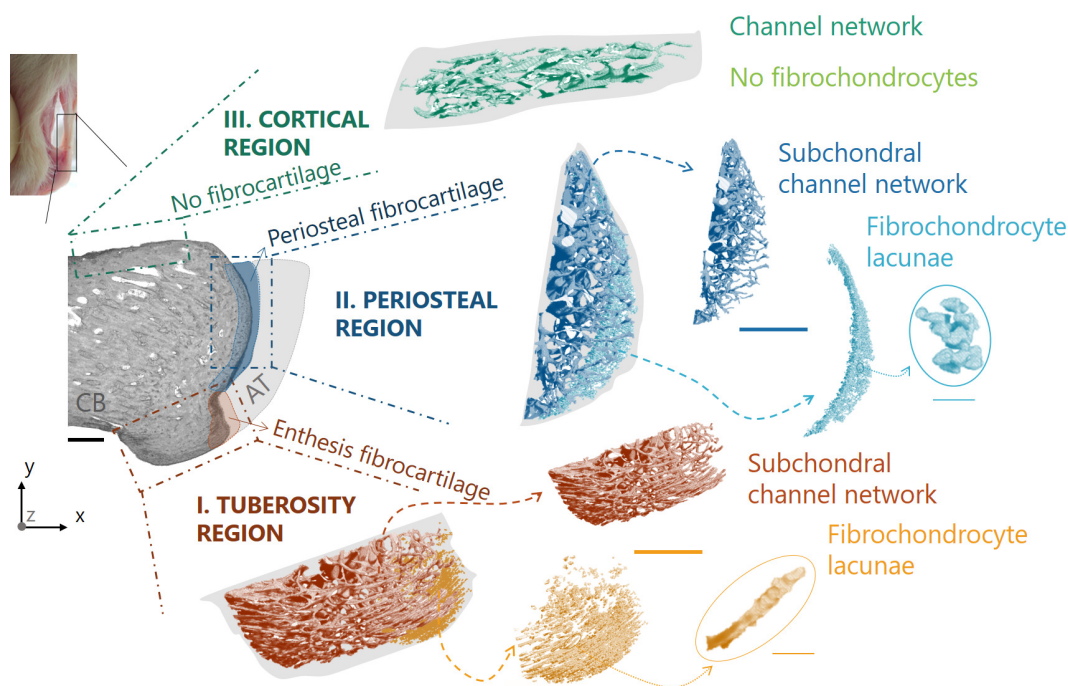
Figure 4.3: Representation of the three regions of interest defined for the analysis of bone microporosity along with three-dimensional renderings of the extracted subchondral channel network and fibrochondrocyte lacunae. The shaded gray area represents the considered tissue volume within each region. CB calcaneus bone, AT Achilles tendon. Scale bars: 500 μm (bold), 50 μm (thin).

The network of subchondral channels was extracted with the following procedure: a preliminary erosion operator (removing a layer of 125 μm in thickness) was applied to Region I and II to remove mineralized fibrocartilage. Then, a sweep method discarded all but the largest object. Bone porosity was highlighted by inverting the image, and then classified using a despeckle filter: objects with an area smaller than 20 pixels (i.e., corresponding to a diameter of about 6 μm in two-dimensional cross-sections), were considered to be either noise or osteocyte lacunae [46, 67, 68]. Finally, another sweep operator was applied to keep only the connected porosity, therefore ensuring to extract the subchondral channel network without interruptions.

A similar algorithm was used to segment the fibrochondrocyte lacunae, now focusing on the layer of mineralized fibrocartilage discarded in the previous analysis. Here, instead of keeping the largest connected component, pores were thresholded and only objects between 1000 and 30,000 μm^3 were considered to be fibrochondrocyte lacunae [69–71]. The upper threshold ensures that also large aggregates of fibrochondrocytes, which are a known feature of fibrocartilage [72], were included in the analysis while excluding bigger objects (channels). Nevertheless, manual object removal was still necessary for some samples because of unconnected channel parts entering the region of interest. Renderings of the cell lacunae and channel network (Fig. 4.3; Supplementary Videos) were generated using CTVox (v.3.3.0, Skyscan) and CTVol (v.2.3.2.1, Skyscan).

69

The three-dimensional architecture of the channel network was quantified using both global and local morphometry. The global analysis was conducted in CTAn with a model-independent approach as done for trabecular bone [73]. The extracted global parameters included: total channel volume (Ch.V), channel volume density (Ch.V/TV), mean channel diameter (Ch.Dm), mean channel spacing (Ch.Sp), and degree of anisotropy (Ch.DA). The channel network was further characterized by a local analysis resolving individual channels. For that purpose, a Euclidean distance-ordered sequential homotopic thinning [74] was applied to reduce the network to a one voxel thick skeleton without modifying the network topology. The voxels of the skeleton were then classified topologically as "branch" or "junction" [75]. The connected components of voxels marked as "junctions" were used as endpoints of the channels whereas the connected component of voxels classified as "branches" defined individual channels. All voxels belonging to an individual channel in the skeletonized image retained information on the corresponding Euclidean distance at that position, which can be interpreted as the local thickness of the channel in the original image. This measurement, along with channel connectivity, constituted the raw data used for the local channel morphometry. For each channel, the following local parameters were considered: channel length (Ch.L), channel diameter (Ch.Dm), channel connectivity (Ch.Conn), channel aspect ratio (Ch.ρ = Ch.Dm/Ch.L), and channel orientations (Ch.θ and Ch.ϕ). The two angles, polar (θ) and the azimuthal (ϕ), define a unit vector connecting the endpoints of a channel (Fig. 4.6). Since the channel network is an undirected graph structure, channel orientations were then mapped on an arbitrary half unit sphere by imposing that -90 $°$ $< \theta <$ 90 $°$ and 0 $°$ $< \phi <$ 180 $°$. Such constrains ensure that, for example, an angle of 10 $°$ is equivalent to an angle of 100 $°$ around the z-axis (Fig. 4.6). Channel skeletonization and processing were performed using ad hoc scripts developed in-house [76] and integrated in Avizo.

The fibrochondrocyte lacunae and lacuna aggregates were characterized in CTAn using first global measurements, followed by a local analysis. Global parameters included total lacuna volume (L.V), lacuna volume density (L.V/TV), lacuna number (L.N) and lacuna number density (L.N/TV). Local three-dimensional measurements on individual lacunae comprised lacuna sphericity (L.Sph) and lacuna orientations (L.θ and L.ϕ). The sphericity was computed as the ratio of the surface area of an equivalent volume matched sphere to the surface area of the object (e.g., L.Sph = 1 indicates a perfectly spherical lacuna) [77]. Orientations were assessed by fitting each lacuna with an ellipsoid and by considering the orientation of the main axis of the ellipsoid with respect to the principal axes of the bone. Orientations were characterized by two angles in a spherical coordinate system - polar (θ) and the azimuthal (ϕ) - considering the same hemisphere and reference system used for the channels (Fig. 4.7).

Surface roughness
Surface roughness was measured on the high-resolution scans (1.25 μm voxel size) following a two-dimensional procedure [78, 79] implemented in Matlab. Three different regions of interest, previously defined for the analysis of bone microporosity, were considered (Fig. 4.7). Specifically, a rectangular mask (437.5 μm x 625 μm) was applied to extract the bone surface at (I) the interface between mineralized and

unmineralized enthesis fibrocartilage located at the bony tuberosity; (II) the interface between mineralized and unmineralized periosteal fibrocartilage at the caudal side of the calcaneus; and (III) the bone surface (not covered by fibrocartilage) away from the enthesis and located on the dorsal side of the bone. For each sample, 10 sagittal cross-sections equally spaced about 30 μm apart, were studied for a total of 150 locations. In region (III), 6 masks (out of 50) were excluded because of the presence of blood vessels entering the bone (Supplementary Fig. S4.10). Surface profiles were defined based on contour voxels in the segmented micro-CT images. A mean reference surface was generated by approximating the extracted contour line with a 5th order polynomial. This choice ensures to account for the overall surface shape while avoiding the incorporation of local roughness caused for example by arrested fibrochondrocytes [80]. Surface height was computed as the shortest (Euclidean) distance from the reference line and roughness was measured as the root mean square deviation of the height profile from the mean line [79]. As the extraction of the bone contour is affected by the threshold, a sensitivity analysis was conducted to ensure that the main findings are robust against the specific value used to segment the bone (Supplementary Fig. S4.11).

4.2.3 Statistics

Statistically significant differences in the morphological parameters of trabecular bone, in the global descriptors of the subchondral channel network and in the surface roughness, were investigated using a two-sample Student's t test. Normality was checked by a Kolmogorov–Smirnov test, and variance using a two-sample F test. If one of those criteria was not met, a Mann–Whitney U test was employed. Significant differences in the three-dimensional orientation of channels and lacunae at the sites of interest were assessed with a non-parametric two-sample and two-dimensional Kolmogorov–Smirnov test, based on the Peacock algorithm [81]. This test determines whether two datasets are drawn from the same continuous distribution (without any assumption on the type of distribution). p values smaller than 0.05 were considered significant. The statistical analysis was done in Matlab (using the statistics toolbox and Central File Exchange) [82].

4.3 Results

4.3.1 Histology and backscattered electron imaging

As Giemsa stains proteoglycans, it allows to differentiate fibrocartilage from bone. In Fig. 4.4a, fibrocartilage appears in dark violet and bone in light pink. This staining highlighted the locations of periosteal (light blue asterisk) and enthesis (light pink asterisk) fibrocartilages on the caudal portion of the calcaneus. The histological analysis also revealed an intricate pattern of interdigitations at the insertion region, with fingers of fibrocartilage deeply inserting into subchondral bone. The periosteal region, in comparison, showed a smoother interface between fibrocartilage and bone. The growth plate zone could also be identified thanks to the presence of several cartilage inclusions. Likewise, cartilage islands were also found in other locations away from the growth plate, and they are a well-known feature of unremodeled rat bone [83]. Fig. 4.4b

shows an overview of a Goldner stained section at a similar location. This stain colors bone mineralized matrix in green, non-mineralized tissue, such as osteoid, in red, and erythrocytes in bright orange. Fig. 4.4c shows a cross section analyzed with BEI at a similar location, enabling to distinguish mineralized and un-mineralized areas. A magnified view in Fig. 4.4e highlights the high heterogeneity of the insertion region. Avascular subchondral trabecular pores containing marrow space (black arrows) could be observed. Smaller cavities were also detected close to the fibrocartilage layer, probably filled with osteoid and erythrocytes (white arrows). Both avascular and vascular channels are known features of the subchondral bone plate and mineralized cartilage [65]. A reddish band, approximately 50 μm away from bone and corresponding to the end of the mineralized area in BEI, demarcates mineralized from non-mineralized cartilage, as is illustrated in Fig. 4.4d. Fig. 4.4f,g present a magnified view on the cell population at the fibrocartilage insertions. First, the presence of fibrocartilage is confirmed by the observation of roundish fibrochondrocytes at both sites (white circles), yet of different arrangement. At the enthesis, they formed columns while the periosteal chondrocytes did not show specific organization. Osteocytes, much smaller and less round than fibrochon-drocytes, could also be spotted at the bone side (black circles).

In Fig. 4.4h, a polarized light microscopy image of the entire caudal portion of the calcaneus (including enthesis and periosteal region) is reported. A qualitative examination revealed a bright signal at the insertion (light pink asterisk) while the periosteal area remained dark (light blue asterisk), suggesting a different alignment of the collagen fibers in the two regions. Fig. S4.4 provides additional similar histological images performed on a different sample.

4.3.2 Tuberosity

The Achilles tendon inserts into the caudal portion of the calcaneus at a marked bony tuberosity, comprising not only mineralized fibrocartilage but also a large portion of subchondral bone, with a total tissue volume T.TV of 0.57 mm^3 $\pm$ 0.05 mm^3. The tuberosity had quite a low porosity (T.Po = 14.84 % $\pm$ 2.16 %, mea-sured at 1.25 μm voxel size) indicating that plate-like subchondral cortical bone prevailed over subchondral trabecular bone [84, 85]. The protrusion also had a clear global orientation with respect to the inertia axes of the calcaneus, being fairly well aligned along the sagittal plane, as implied by the polar angle T.θ of 94.79 ° $\pm$ 1.5 °, and pointing upwards in the direction of the tendon, with an inclination (azimuthal angle T.ϕ) of 21.26 ° $\pm$ 3.57 ° (Fig. 4.2c).

4.3.3 Trabecular morphology and spatially resolved analysis

The trabecular bone in the caudal region of the rat calcaneus was rather dense (BV/TV = 62.08 % $\pm$ 3.3 %) with the trabeculae being not particularly thick (Tb.Th = 103.5 μm $\pm$ 4.87 μm) but quite packed (Tb.Sp = 98.7 μm $\pm$ 9.15 μm). Overall, the trabecular network was also fairly anisotropic (DA = 0.48 $\pm$ 0.05). Those values are in line with previous studies on rat trabecular bone [84].
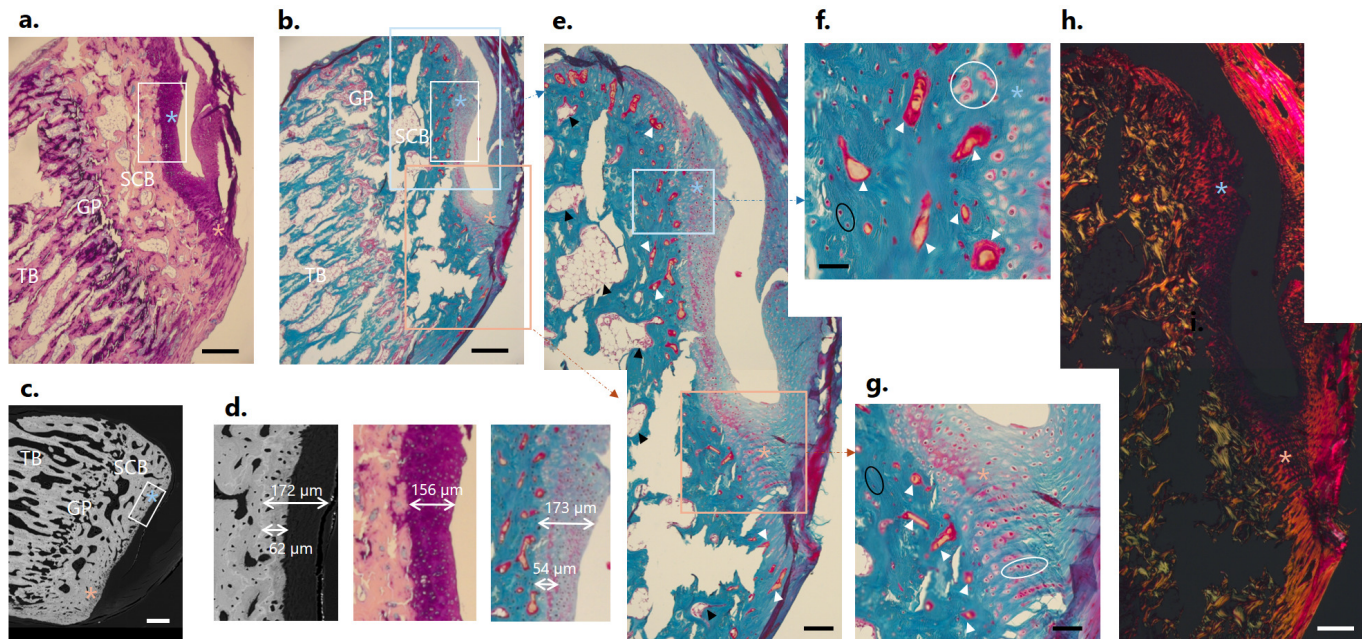
Figure 4.4: Histological and backscattered electron imaging (BEI) analysis from two sagittal sections stained with Giemsa and Goldner. Bright field light microscopy images of a thin section stained with Giemsa (**a**) and Goldner trichrome (**b**) at a similar location, as well as BEI (**c**), highlighting the areas of interest: trabecular bone (TB), growth plate (GP), subchondral bone (SCB), as well as periosteal fibrocartilage (light blue asterisk) and enthesis fibrocartilage (light pink asterisk). Scale bars: 250 μm. (**d**) Zoom from white frames in (a–c) on the periosteal fibrocartilage with BEI, Giemsa and Goldner, respectively, suggesting a thickness of the mineralized layer of about 50 μm corresponding to the reddish band in Goldner image. (**e**) Magnifications of light blue and pink frames from (**b**) illustrating some subchondral trabecular pores (black arrows) and subchondral vascular channels (white arrows). Scale bar: 100 μm. (**f**) Magnified view from frame in (**e**), revealing chondrocytes arrangement in fibrocartilage (white circle), as well as osteocytes in bone (black circle) and subchondral vascular channels (white arrows). Scale bar: 25 μm. (**g**) Magnified view at the insertion, from frame in (**e**), showing the column-like organization of chondrocytes, in close vicinity with osteocytes (black circle) and subchondral vascular channels (white arrow). Scale bar: 50 μm. (**h**) Polarized light microscopy corresponding to images in (**e**) suggesting a high degree of alignment of collagen fibers at the insertion. Scale bar: 100 μm.

Local spatial variations in trabecular microarchitecture were investigated to assess whether bone microstructure away from the highlighted tuberosity shows distinct patterns, which could be related to tendon attachment. The architectural descriptors were characterized along the cranio-caudal (CC) and the dorso-plantar (DP) directions (Fig. 4.5a,b). Quantitative assessment of trabecular microstructure along the cranio-caudal direction highlighted significant variations ($p < 0.05$) when approaching the growth plate for some morphological parameters (Fig. 4.5c,d). For example, BV/TV increased from 54.5 to 64.4 % with a slope of about 4 %/mm, mostly due to a decrease in trabecular spacing, with trabecular thickness being practically constant. The local predominant azimuthal orientation (Pref.Or.ϕ) of the trabecular network changed from about -19.5 ° to -5 ° when going closer to the growth plate, meaning that the trabeculae pointed initially towards the tuberosity and then rotated to align along with the cranio-caudal direction. The polar angle Pref.Or.θ did not show significant variations and stayed around 90°, suggesting that the trabecular network was parallel to the sagittal plane. Changes in trabecular orientation were accompanied by a significant increase of about 20 % in the degree of anisotropy (from 0.44 to 0.52, $p < 0.05$). Despite the presence of the tendon insertion and related tuberosity, almost none of the trabecular parameters showed significant differences when comparing dorsal versus plantar locations (Fig. 4.5e,f). Only the polar angle (Pref.Or.θ) significantly increased, indicating that plantar trabeculae were slightly more co-aligned with the sagittal plane.

4.3.4 Subchondral channel network

Although belonging to the same bone and being adjacent to each other, the three regions introduced to study bone microporosity (Fig. 4.3; Supplementary Videos S1, S2, S3) showed large differences in the subchondral channel network, as highlighted by the global morphological analysis (Table 4.1). Subchondral bone beneath periosteal fibrocartilage (Region II) had the highest Ch.V and Ch.V/TV, followed by the tuberosity (Region I) and cortical bone (Region III). In the latter, Ch.V/TV was about 42 % smaller than in the tuberosity ($p < 0.01$). The high channel density in the two regions beneath fibrocartilage (i.e. Region I and II) was due to fewer but larger and more separated channels in comparison with cortical bone. Interestingly, the three regions had strong dissimilarities in the degree of anisotropy, with the insertion site (Region I) showing Ch.DA more than a factor of two higher than at the periosteal site (Region II), and only 26 % smaller than within cortical bone (Region III).

To gain more insight in the arrangement of the channel network, a local analysis resolving individual channels was performed (Fig. 4.6). By knowing the local orientation of each channel (expressed as two angles Ch.θ and Ch.ϕ, Fig. 4.6a,b), two-dimensional heat maps of the channel orientation were obtained for each region of interest (Fig. 4.6c; Supplementary Fig. S4.7). The maps, generated by binning channel angles within a 20° interval, highlighted a strong anisotropy for the tuberosity and the cortical regions, in striking difference with respect to the more isotropic subchondral bone beneath periosteal fibrocartilage. In particular, channels within the tuberosity had a preferred orientation (corresponding to the maximum in the
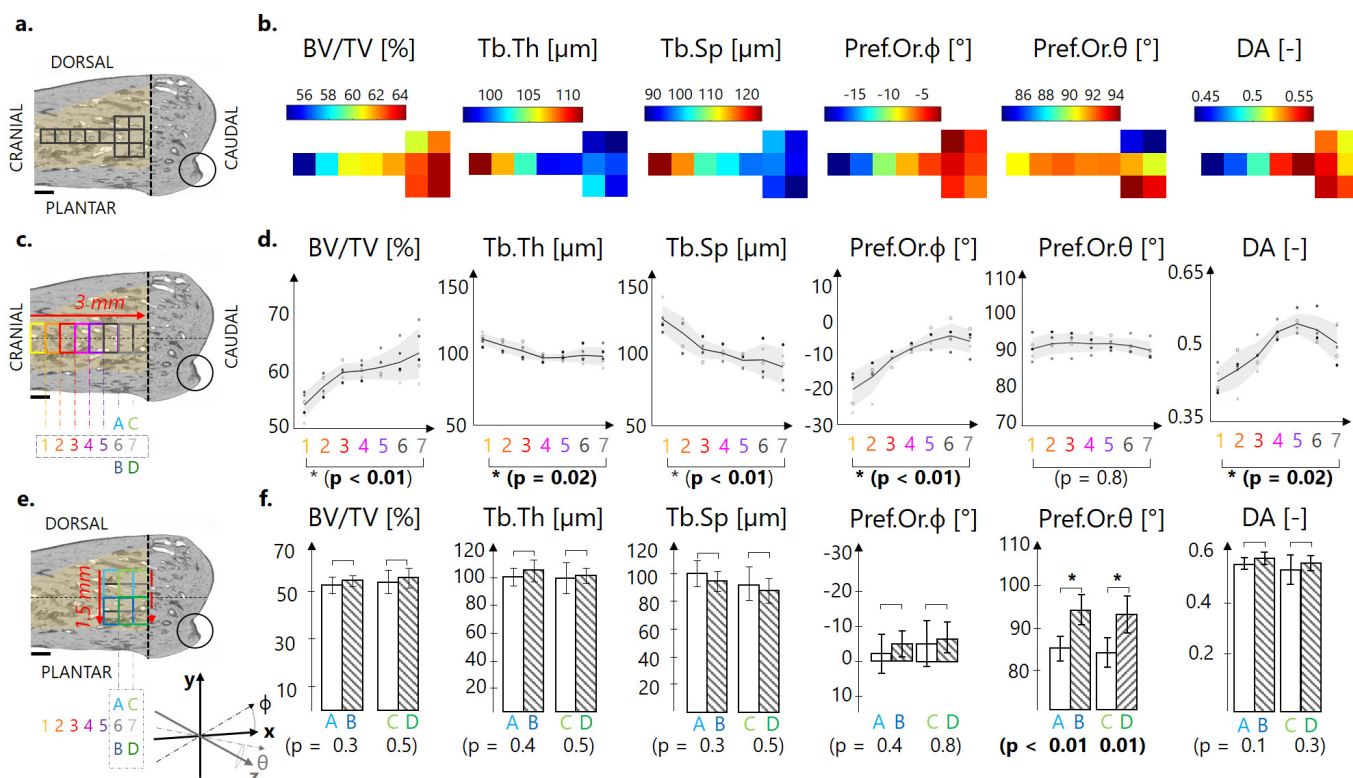
Figure 4.5: Three-dimensional spatially resolved analysis of trabecular bone architecture (the analyzed trabecular compartment is highlighted in yellow). (**a**) Overview of the central part of the regions of interest (black squares), with the analyzed parameters color-coded in (B). (**b**) Spatial evolution of bone microstructural parameters along the cranio-caudal (CC) and the dorso-plantar (DP) directions. (**c**) Illustration of the volumes of interest (VOI) for the CC investigation at 7 consecutive positions (i.e., 1, ..., 7). (**d**) Spatial evolution of morphometric parameters along the CC direction showing significant variations in BV/TV, Tb.Sp and Pref.Or.ϕ when comparing the two extremities (i.e., positions 1 and 7). (**e**) Illustration of the VOI for the DP investigation considering 2 dorsal (A and C) and 2 plantar (B and D) locations. (**f**) Comparison of trabecular parameters averaged within dorsal and plantar regions revealing significant changes only for Pref.Or.θ. Scale bars: 500 μm. Statistically significant p values (p<0.05) are shown in bold.

| Parameters	Tuberosity (Region I)	p(I-II)	Periosteal (Region II)	p(II-III)	Cortical (Region III)	p(I-III)
Subchondral channel parameters						
Ch.V (mm^3)	0.025 ± 0.01	**0.02**	0.05 ± 0.02	**< 0.01**	0.01 ± 0.003	**< 0.01**
Ch.V/TV (%)	6.21 ± 1.72	**0.02**	10.80 ± 2.22	**< 0.01**	3.84 ± 0.80	**< 0.01**
Ch.Dm (μm)	36.85 ± 15.92	0.15	50.36 ± 3.88	**0.02**	21.87 ± 2.69	**< 0.01**
Ch.Sp (μm)	100.51 ± 4.84	0.09	106.25 ± 2.16	**0.02**	121.83 ± 3.95	**0.03**
Ch.DA (–)	0.56 ± 0.03	**< 0.01**	0.21 ± 0.06	**< 0.01**	0.71 ± 0.02	**< 0.01**
Fibrochondrocyte lacuna parameters						
L.V (mm^3)	0.005 ± 0.0006	**< 0.01**	0.0078 ± 0.001		-	
L.V/TV (%)	2.24 ± 0.4	0.2	2.86 ± 0.7		-	
L.N (–)	1415 ± 256.6	**< 0.01**	2555 ± 230.6		-	
L.N/TV (/mm^3)	$274,845 \pm 38,719$	0.056	$329,447 \pm 22,090$		-	

Table 4.1: Global morphometric parameters used to characterize bone microporosity. Values are mean $\pm$ standard deviation. Statistically significant p values (p < 0.05) are shown in bold. Ch.V total channel volume, Ch.V/TV channel volume density, Ch.Dm mean channel diameter, Ch.Sp mean channel separation, Ch.DA channel degree of anisotropy, L.V total lacuna volume, L.V/TV lacuna volume density, L.N lacuna number, L.N/TV lacuna number density

heat map) characterized by Ch.ϕ = 10.6 ° ± 8.6 ° and Ch.θ = 81.8 ° ± 3 °. A polar angle Ch.θ close to 90 ° indicates that channels were rather parallel to the sagittal plane (XY plane in Fig. 4.6), yet somewhat oriented towards the lateral side of the calcaneus. The positive azimuthal angle Ch.ϕ underlines that channels pointed upwards (dorsally) in the direction of the tendon. The three regions had heat maps significantly different from each other, as indicated by a two-dimensional Kolmogorov–Smirnov test (p < 0.01, Supplementary Table S4.1). The channels were further classified, according to their aspect ratio Ch.ρ, into three groups: thick (Ch.$\rho \geq 1$), slender (0.1 < Ch.ρ < 1) and extremely slender (Ch.$\rho \leq 0.1$) channels. Frequency distributions of Ch.ϕ were obtained in the different regions and for the three groups (Fig. 4.6d). In the tuberosity, all distributions showed a clear peak but different peak positions and widths. Considering extremely slender channels, located predominantly on the Achilles tendon insertion side of the tuberosity (Fig. 4.6b), the most frequent azimuthal orientation was 45 % higher than that of less slender channels, indicating an increased tilt pointing towards the attachment region. Additionally, they also showed a somewhat reduced orientation heterogeneity as indicated by a narrower peak. In the cortical bone region, the frequency distributions peaked at Ch.ϕ = 2 ° both for thick and slender channels, indicating a preferential longitudinal arrangement (i.e. along the cranio-caudal axis), independently of the channel aspect ratio. A clearly different behavior was observed within subchondral bone beneath periosteal fibrocartilage, where channels had a fairly random (isotropic) orientation.

Furthermore, frequency distributions of channel length, diameter and connectivity in the different regions showed similar bell-shaped patterns with channels in the tuberosity having the tendency to be thinner and more branched in comparison with the cortical region (Supplementary Fig. S4.5). One additional distinct feature of the tuberosity common to all analyzed bones was the presence of a rather big central channel branching into smaller channels at an almost right angle when reaching the tuberosity (Supplementary Fig. S4.6).

4.3.5   Fibrochondrocyte lacunae

Three-dimensional visualization of lacunar porosity (Fig. 4.7) revealed that fibrochondrocyte lacunae formed specific aggregates depending on the considered location (Fig. 4.7b; Supplementary Videos S4, S5): at the mineralized enthesis fibrocartilage covering the most caudal part of the tuberosity, lacunae piled up to form elongated columnar structures, whereas at the mineralized periosteal fibrocartilage bordering subchondral bone, lacunae aggregated into three-dimensional clusters. Global morphometric parameters (Table 4.1) indicated that the two mineralized fibrocartilages had similar lacuna volume density and lacuna number density. At the individual level, pore sphericity was negatively correlated with pore volume, suggesting that small lacunae were consistently the most spherical ones (Supplementary Fig. S4.8). To target the specific arrangement of lacunar aggregates, the orientation analysis was restricted to pores of low sphericity (i.e., L.Sph < 0.6). Two-dimensional heat maps of lacuna orientation (L.θ and L.ϕ) showed strong and statistically significant differences (p < 0.01, Supplementary Table S4.2) between the two re-
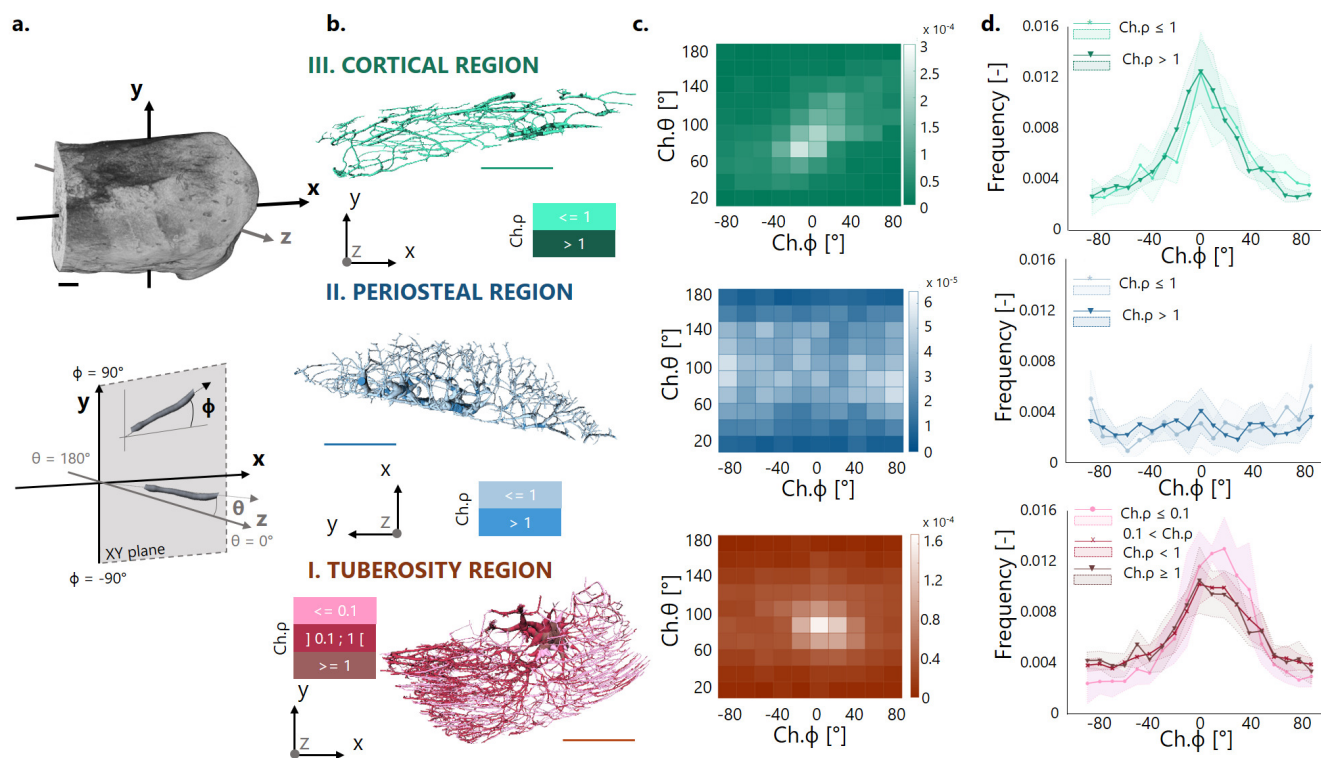
Figure 4.6: Tree-dimensional local analysis of the subchondral channel network at the three sites of interest based on the high-resolution micro-CT scans. (**a**) Representation of the spherical coordinate system with the azimuthal (ϕ) and polar (θ) angle defining the orientation of the channels. (**b**) Illustration of extracted channel network skeletonized to resolve individual channels, which are classified and colored according to the aspect ratio as thick, slender and extremely slender. (**c**) Representative two-dimensional heat maps of channel orientation, revealing a specific pattern for each region. Dataset relative to one animal and data normalized to unit volume. (**d**) Frequency distributions (normalized to unit area) of the azimuthal angle (Ch.ϕ) describing the orientation of the channel in the XY sagittal plane for the entire dataset. Channels are classified according to the aspect ratio as thick, slender and extremely slender. Data reported as mean value (thick lines) with standard deviation (shaded areas). Scale bars: 500 μm.

gions (Fig. 4.7c; Supplementary Fig. S4.9). Fibrochondrocyte lacunae forming columns located at the tuberosity were well oriented at an azimuthal angle of L.ϕ = 31.1 ° ± 4.4 ° (Fig. 4.7d), indicating that the columns pointed towards the tendon insertion site with a characteristic inclination. Rows corresponding to the biggest aggregates seemed to be located on the plantar side of the tuberosity (Fig. 4.7b). In the mineralized periosteal fibrocartilage, lacunar orientation was much less anisotropic, with azimuthal angles in the range 0 ° to 30 ° being almost equally likely. As for the channels, the polar angle L.θ within enthesis fibrocartilage was close to 80 ° (L.θ = 79.1 ° ± 1.8 °), highlighting a somewhat lateral arrangement of the lacuna columns and likely reflecting the predominant polar orientations of the tuberosity (Fig. 4.7d).

4.3.6 Roughness

Roughness was significantly different (p < 0.01) among the three analyzed surfaces (Fig. 4.8). Mean roughness (expressed as root mean square P$_q$) at the interface between mineralized and unmineralized enthesis fibrocartilage (present at the tuberosity) was 65 % higher than at the interface between mineralized and unmineralized periosteal fibrocartilage (covering subchondral bone), and 172 % higher than at the outer cortical bone surface. The latter was also significantly less rough (about -39 %) than the regions of bone covered by mineralized periosteal fibrocartilage. Those results were robust against the threshold value considered for roughness computation (Supplementary Fig. S4.11).

4.4 Discussion

In this work, we have analyzed microstructure and microporosity of bone and mineralized fibrocartilage at a clinically relevant location, where the Achilles tendon is attached to the calcaneus bone in rats. This region is highly heterogeneous and features different mineralized tissues such as the thin and irregular mineralized fibrocartilage layer, the dense subchondral plate, the porous subchondral trabecular bone and, after the growth plate, the trabecular compartment. To highlight different functional aspects of those regions, we have characterized either the microstructure (Figs. 4.5, 4.8) or the microporosity (Figs. 4.6, 4.7). Specifically, dense tissues such as the mineralized fibrocartilage and the subchondral plate were analyzed in terms of microporosity whereas the highly porous trabecular bone region and the irregular interface between mineralized and non-mineralized fibrocartilage were characterized in terms of microstructure. Although, in humans, this region suffers from overuse injuries, rheumatic pathologies and fractures, it has been much less investigated than tendon or bone [3].

In addition to the clinical relevance, the calcaneus bone presents attractive features for investigating mechanobiological questions. Firstly, it solves the clear biomechanical task of transmitting the tendon force to the ankle joint and, in analogy with a cantilever beam, the dorsal side is prevalently loaded in compression while the plantar side is loaded in tension [86]. In case of off-axis loading, shear strains may also be present [87]. Due to this fairly simple loading condition, the calcaneus has been used to characterize material and
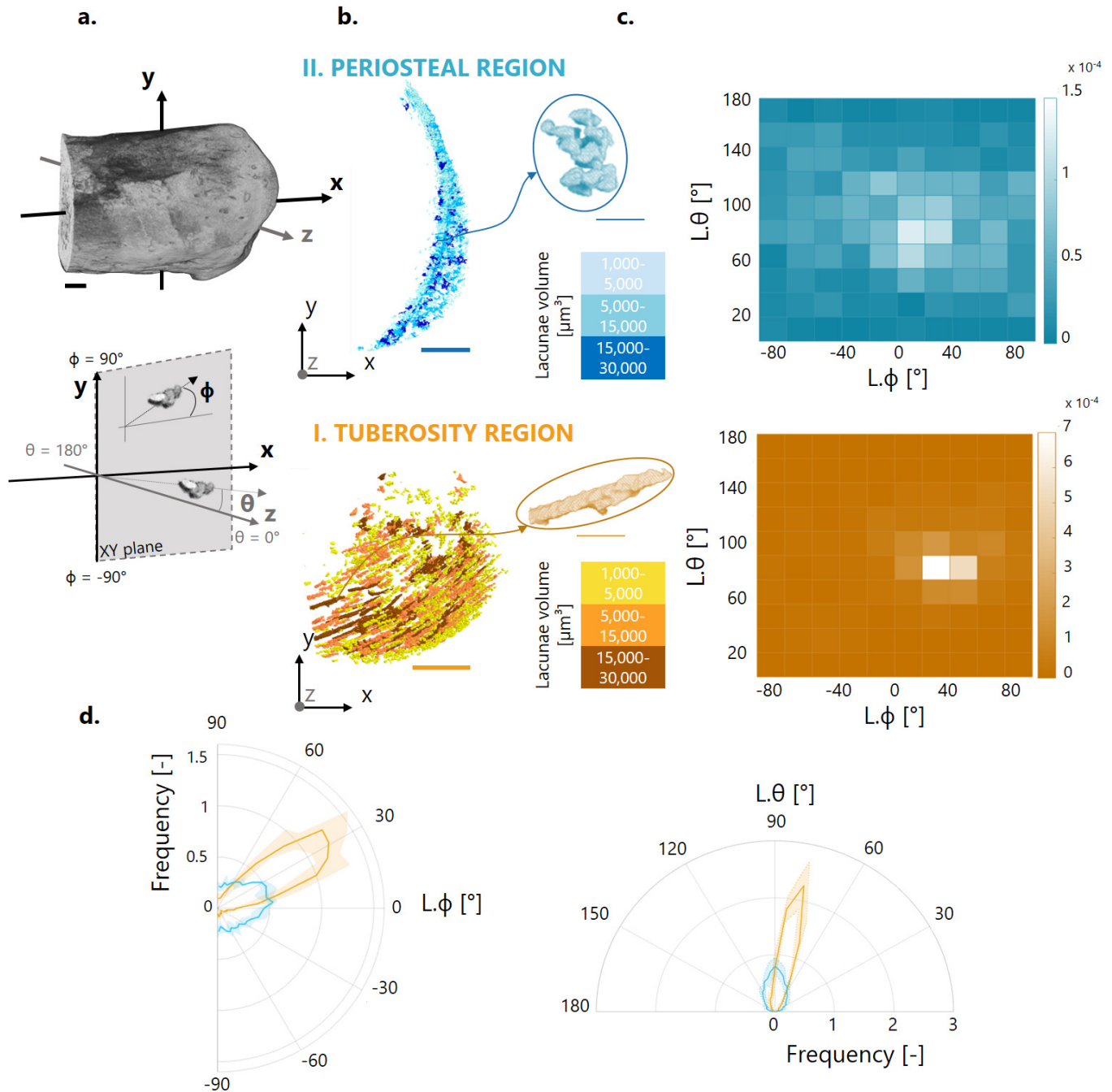
Figure 4.7: Tree-dimensional local analysis of the fibrochondrocyte lacunae within the two locations of interest and based on the high-resolution micro-CT scans. (**a**) Representation of the spherical coordinate system with the azimuthal (ϕ) and polar (θ) angles defining the orientation of the lacunar porosity. (**b**) Illustration of extracted lacuna aggregates for the two regions of interest. Lacunae are classified and colored according to their volume as small, intermediate and big. (**c**) Representative two-dimensional heat maps of lacuna orientation, revealing a clear preferred orientation at the insertion. Dataset relative to one animal and data normalized to unit volume. (**d**) Circular plots of the azimuthal angle (describing the orientation of the pores in the XY sagittal plane) and of the polar angle (depicting the orientation with respect to the z-axis) for the entire dataset. Data reported as mean value (thick lines) with standard deviation (shaded areas). Plots are normalized to unit area. Scale bars: 500 μm (thick) and 50 μm (thin).
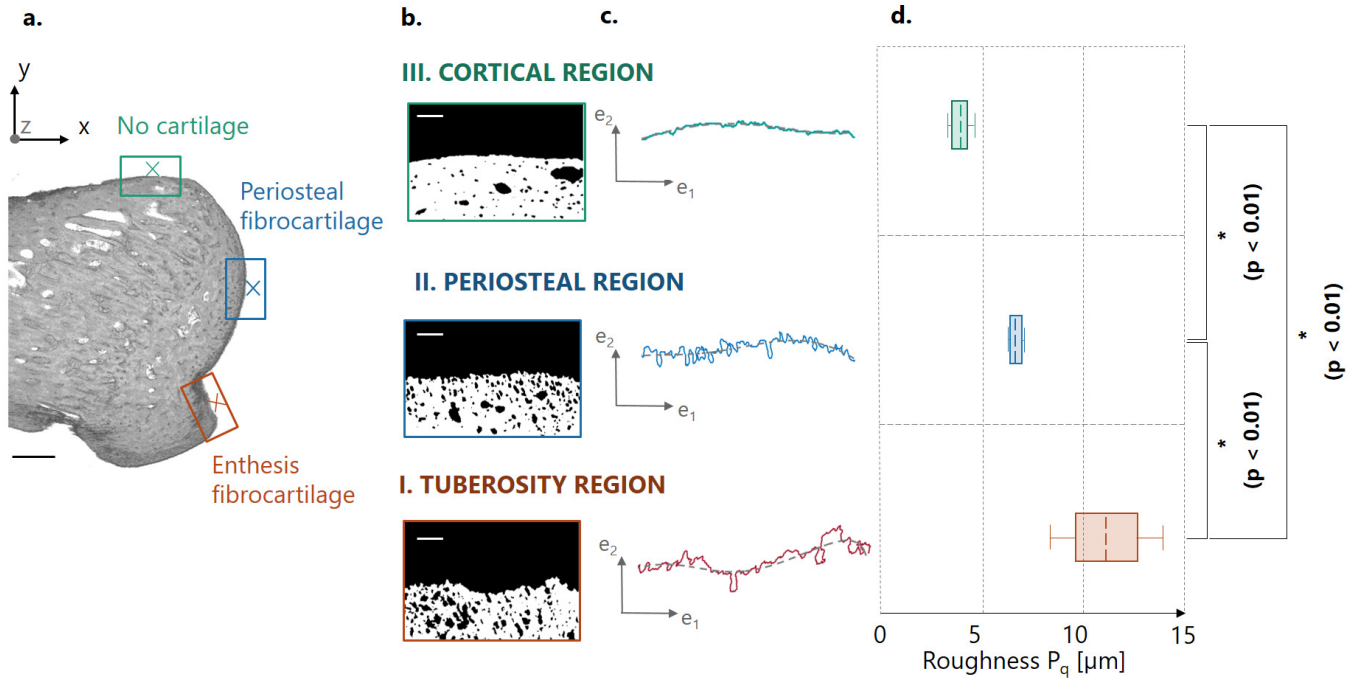
Figure 4.8: Roughness of the interface profile line based on the high-resolution micro-CT scans. **(a)** Regions of interest (ROI) on a representative bone cross section. **(b)** ROI after extraction and binarization. **(c)** The full line represents surface profile whereas the dashed line shows the reference line used to compute the roughness. e1 and e2 are local direction vectors. **(d)** Surface roughness (expressed as root mean square P_q) calculated in the three ROI including the interface between mineralized and unmineralized enthesis fibrocartilage (I. Tuberosity region), the interface between mineralized and unmineralized periosteal fibrocartilage (II. Periosteal region) and the outer cortical bone surface (III. Cortical region). Box plots extends from 25 to 75th percentiles and whisker bars covers the full data range. The dashed line represents the mean value. Scale bars: 500 μm (in A, black), 100 μm (in B, white). Statistically significant p values (p < 0.05) are shown in bold.

architectural adaptation to mechanical forces in different species [87–90]. Moreover, the bone receives the load from the tendon at a well-localized region, thus offering the additional opportunity to investigate local adaptation strategies of the mineralized tissues close to the insertion site.

Here, we have found that the calcaneus bone of rats presents a dedicated protrusion, referred to as tuberosity, to anchor (part of) the tendon. The existence of a specialized bony region at the enthesis is common to other bones [91], and plays a role in joint functioning. For example, at the Achilles tendon insertion in humans, the caudal tuberosity of the calcaneus is assumed to increase the lever arm of the tendon, thus providing a biomechanical advantage [3]. The tuberosity is also a possible indicator of muscle activity: from a mechanobiological point of view, a pronounced tuberosity may reflect increased muscle loading. For this reason, bony tuberosities have been investigated in the archeological context to learn about physical activities of past populations [92]. Noteworthy, tendon fibers attaching at the tuberosity of calcaneus bone (in mice) have a different arrangement than the surrounding fibers. This suggests that the protrusion could experience a different loading condition than nearby bone [6].

To further investigate the role of the tuberosity in load transfer, we have performed a spatially resolved analysis of the calcaneus trabecular microstructure, which revealed gradients when moving towards the growth plate along the cranio-caudal direction but not when approaching the tuberosity along the dorso-plantar direction. The presence of microstructural gradients in the trabecular network -especially in porosity- may serve to mitigate stress incompatibilities when transitioning from the more compliant trabecular region to the stiff cortical bone [93]. This is a known feature of long bones [61, 94]. However, the lack of significant changes in trabecular architecture along the dorso-plantar direction, despite moving closer to the tendon insertion, suggests that the tuberosity may facilitate the "force flow" from the Achilles tendon to the plantar fascia ligament, somewhat relieving the trabecular network from such task. Additional mechanical analysis, for example based on microstructural finite element simulations [95, 96], should be performed to confirm this assumption.

The caudal calcaneus features three types of fibrocartilage, of which two are contiguous but with specific biomechanical functions and developmental origin: enthesis fibrocartilage, anchoring tendon to bone, originates from the cartilage rudiment of the calcaneus and has analogies with the growth plate that is formed during endochondral ossification [91], whereas periosteal fibrocartilage, facilitating tendon sliding and protecting bone, arises from the calcaneal perichondrium [51, 72]. Owing to their tasks, the two tissues are subjected to distinct loading conditions. Enthesis fibrocartilage should prevalently accommodate the large tensile force of the tendon, with local compressive and shear strains emerging at the interface [5, 37, 53]. The periosteal fibrocartilage should sustain overall compressive and shear loading [72], likely of smaller magnitude than enthesis fibrocartilage. By comparing the mineralized regions of enthesis and periosteal fibrocartilage, we have found large dissimilarities in surface roughness and microstructural porosity.

Firstly, the roughness of the interface between mineralized and unmineralized tissues, caused by the mineralization front and by the arrested fibrochondrocytes, is the highest at the tuberosity. From a mechanical point of view, introducing surface pattering in the form of random roughness or controlled interdigitations is a well-known strategy to increase the fracture resistance of bi-material junctions [9, 97, 98]. At the tendon-bone attachment there are actually two interfaces of interest: the transition between unmineralized and mineralized fibrocartilage, referred to as the tidemark or mineralization front, and the one gluing mineralized fibrocartilage to bone (often featuring a thin interlayer, called cement line). Clearly, the roughness characterized in this work is at the mineralization front, yet both interfaces are far from being flat: the interface between mineralized fibrocartilage and bone probably shows the highest roughness caused by deep interdigitations between the two mineralized tissues [99, 100]. Interface waviness is a general feature of the attachment between bone and soft tissues, including tendon, ligament, cartilage and meniscus [6, 11, 13, 101]. At the tendon insertion, roughness is well conserved across different species but does not seem to increase much with animal size and muscle loading, perhaps because higher loading is often accompanied by a larger attachment area, resulting in a fairly constant interfacial stress with no requirement to adapt surface properties [12]. Nevertheless, we observed significant differences when comparing roughness between enthesis and periosteal location, possibly because the former has to sustain higher stresses. Others have also found differences in roughness between the two bundles of the ACL attaching to the tibia, which may reflect site-specific biomechanical requirements [99]. The roughness profiles measured here may be combined with computational models [9, 102] to estimate their impact on interface strength and fracture behavior [9].

In the two mineralized fibrocartilages, we also found specific arrangements of fibrochondrocyte lacunae, which formed clusters having distinct shapes and orientations. Similar to osteocytes, fibrochondrocytes live buried in the challenging environment of the mineralized matrix. In bone, the arrangement of the osteocytes is not fully random but reflects the three-dimensional organization of the collagen matrix [103] and is influenced by the local mechanical environment [47, 104, 105] as well as by systemic factors such as aging [106] and diseases [107]. Although fibrocartilage does not have the same remodeling ability than bone, the same considerations may hold (at least partially) for the fibrochondrocyte lacunae. Mechanical loading has been shown to be necessary for the growth and maturation of the enthesis [108–110], but also plays a critical role for interface healing [109]. During development, the whole process of chondrocyte proliferation, hypertrophy and bone formation is tightly regulated by biological signals and influenced by applied load [110, 111]. For example, a specific population of cells probably linked to the regulation of enthesis development, has been identified at the fibrocartilaginous enthesis as early as in perinatal period. Some hallmarks of these cells seem to be influenced by muscle loading [110]. From a mechanobiological point of view, enthesis development and healing are intimately connected with local mechanical cues. Likewise, the organization of mature tissues at enthesis may mirror the local mechanical environment. At the attachment region, although varying in orientation with gait cycle and motion, a rather clear and localized predominant loading condition is provided by the tendon, and this is where the lacunae exhibit the highest alignment,

also as a possible way to minimize dangerous stress localization around those large pores. This may also be the case for the highly aligned subchondral channels. Looking outside the mammalian musculoskeletal system, chondrocytes within mineralized cartilage of rays also show pronounced spatial organization and orientation, perhaps reflecting differences in the local loading environment [71]. The spatial organization of fibrocartilage cells may mirror the arrangement of the underlying collagen network. Indeed, in enthesis fibrocartilage, collagen fibrils assemble into parallel bundles with the cells forming elongated column-like structures sandwiched in between those bundles; conversely, in periosteal fibrocartilage, collagen exhibits a more disordered and interwoven network and cells tend to be more rounded and less ordered [51, 112, 113].

In addition to cell lacunae, we have also shown that the channel network inside the tuberosity is strongly anisotropic: channels were fairly well oriented along a predominant direction pointing towards the attachment region and differing from the disposition of a control cortical bone location, as well as from the organization of channels at the periosteal location, which were more randomly arranged. Bone adaptation to mechanical loading has been extensively investigated at the organ and tissue level, but much less at the level of the subchondral channel network. However, there is evidence that loading affects channel orientation even in primary cortical bone as immobilized bones show more radially oriented channels than loaded bones [46]. Here, we have highlighted that tendon loading may as well have an impact on the three-dimensional organization of the channel network. Finally, collagen fiber alignment has been shown to regulate (in vitro) the formation and alignment of the vascular network [114]. These mechanisms may play a role at the tuberosity as well. That being said, it should be kept in mind that entheses are known to be highly heterogeneous and anatomical site-dependent tissues, mainly because of specific and varying loading environments: for example, the anterior cruciate ligament shows structural and mechanical differences when comparing its femoral and the tibial insertions [13].

Turning to the limitations of this work, we have analyzed a limited number of samples. However, the central aim of our study was not to perform a comparison between groups, which would have required a larger number of animals, but to investigate specific locations within the same bone, likely undergoing dissimilar loading conditions. As we considered bones of laboratory rodents, all having the same age and raised in the same environment, the biological variability was strongly limited. Moreover, we characterized micrometer level features and the considered set of samples allowed extracting and analyzing about 46,000 channels and 20,000 lacunae, obtaining results which were not only statistically significant but also had fairly low standard deviations (as visually evidenced by the Supplementary Videos). In an effort to reduce the number of animals exploited, many studies aiming at comparing several sites within the same bone rather than intergroup comparisons, are based on a limited number of samples [6, 61, 71, 115].

Besides the similarities between humans and rodents in terms of bone architecture [116], ankle anatomy and physiology, the main advantage of analyzing murine calcanei is their small size, allowing to measure at high-resolution (around 1 μm) a large bone region comprising the entire tuberosity, subchondral bone and

mineralized fibrocartilages (enthesis and periosteal). However, it should be noted that our analysis does not allow distinguishing lacunae closer than the micro-CT resolution. While the grouping of fibrochondrocytes at the tendon insertion has been well documented [72], the existence of aggregates within periosteal fibrocartilage has been less explored. Nevertheless, considering the limited communication possibilities among fibrochondrocytes within the mineralized matrix, having cells very close to each other may facilitate the exchange of information.

Finally, the enthesis is a complex multi-tissue system and in this work, we have focused on the mineralized regions as they display a clear microstructural porosity which can be connected with the loading environment. Other complementary aspects of the unmineralized region of the enthesis may be investigated using, for example, contrast enhanced micro-CT [6].

In conclusion, this study has demonstrated that close to the tendon insertion site, bone as well as mineralized fibrocartilage exhibit specific microstructural features, including a strong anisotropy and interdigitations which should be considered when designing future tissue engineering replicates of the bone-tendon system or in the context of novel re-attachment strategies. Future studies, considering for instance aged or diseased animals, could exploit our approach to investigate how microstructural aspects are impacted by tissue degeneration, addressing the complex and poorly understood interplay between bone and fibrocartilage in enthesis related pathologies.

4.5   Supplementary material

Supplementary videos can be found in the online version of the paper here: https://doi.org/10.1038/s41598-021-95917-4.
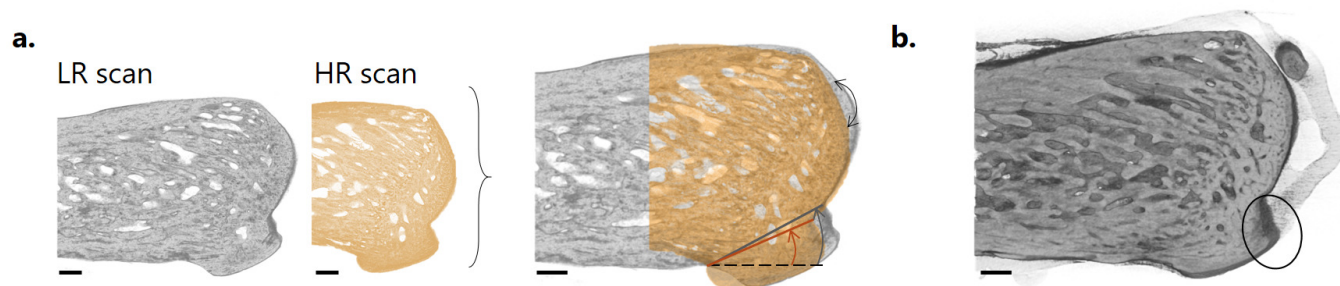
Figure S4.1: . Image alignment and tendon visualization. (**a**) Co-alignment procedure between the low resolution (LR, 5 μm voxel size) and the high resolution (HR, 1.25 μm voxel size) scans based on the orientation of the tuberosity. (**b**) Visualization of the Achilles tendon inserting into the bone at the tuberosity, obtained measuring bone-tendon samples in air (without embedding) and after a manual threshold highlighting the soft tissues. Scale bars: 500 μm.
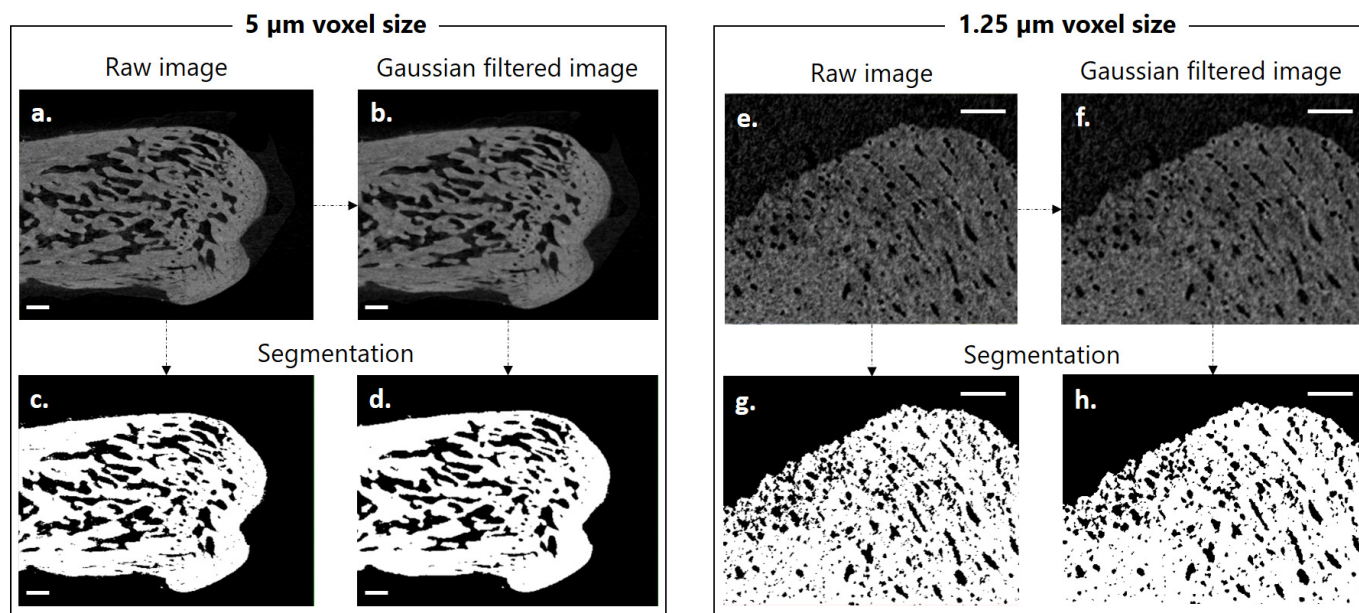
**Figure S4.2:** Gaussian filtering and binarization on representative cross-sections of the 5 μm and 1.25 μm scans. Filtering allows to remove image noise causing dot-like artifacts in the binarized data. As those tiny features were not considered in our analysis, and as we did relative comparisons among different regions of the same bone, we expect filtering not to impact our main findings. Scale bars: (a-d) 500 μm; (e-h) 100 μm.
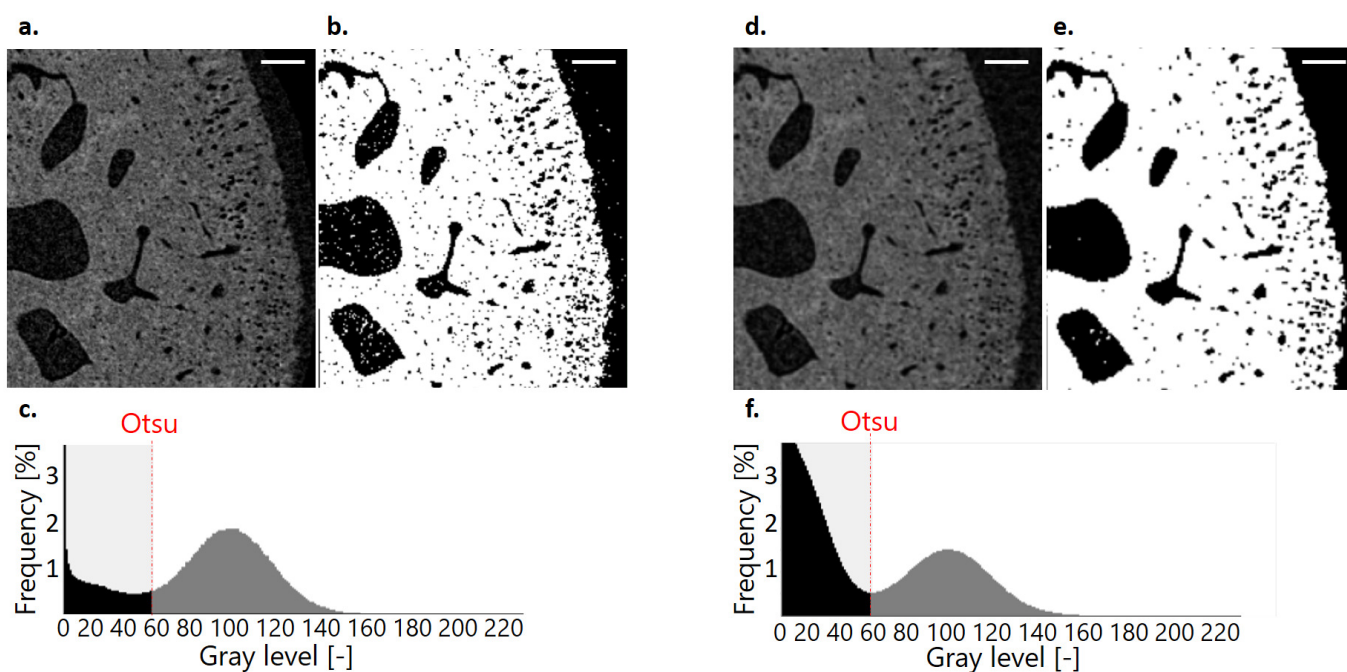
Figure S4.3: Illustration of Otsu's threshold on the original cross-section (a-c) and after filtering (d-f). Filter enhances the histogram bimodality, ensuring the efficiency of Otsu's algorithm to segment foreground from background voxels [59]. Scale bars: 100 μm.

Tuberosity (*Region I*)	θ_{T1}, ϕ_{T1}	θ_{T2}, ϕ_{T2}	θ_{T3}, ϕ_{T3}	θ_{T4}, ϕ_{T4}	θ_{T5}, ϕ_{T5}
p(I-II)	$2.5\ 10^{-71}$	$1\ 10^{-60}$	$1.2\ 10^{-55}$	$2.7\ 10^{-36}$	$2.5\ 10^{-37}$
Periosteal (*Region II*)	θ_{S1}, ϕ_{S1}	θ_{S2}, ϕ_{S2}	θ_{S3}, ϕ_{S3}	θ_{S4}, ϕ_{S4}	θ_{S5}, ϕ_{S5}
p(II-I)	$1.4\ 10^{-37}$	$3.4\ 10^{-46}$	$3.3\ 10^{-47}$	$1\ 10^{-71}$	$5.8\ 10^{-56}$
Cortical (*Region III*)	θ_{C1}, ϕ_{C1}	θ_{C2}, ϕ_{C2}	θ_{C3}, ϕ_{C3}	θ_{C4}, ϕ_{C4}	θ_{C5}, ϕ_{C5}
p(III-I)	$1.8\ 10^{-12}$	$1\ 10^{-18}$	$2.7\ 10^{-20}$	$7\ 10^{-74}$	$2.9\ 10^{-24}$
Tuberosity (*Region I*)	θ_{T1}, ϕ_{T1}	θ_{T2}, ϕ_{T2}	θ_{T3}, ϕ_{T3}	θ_{T4}, ϕ_{T4}	θ_{T5}, ϕ_{T5}

Table S4.1: Results of the two-sample two-dimensional Kolmogorov-Smirnov tests comparing the distributions of channel orientation among the three sites of interest.
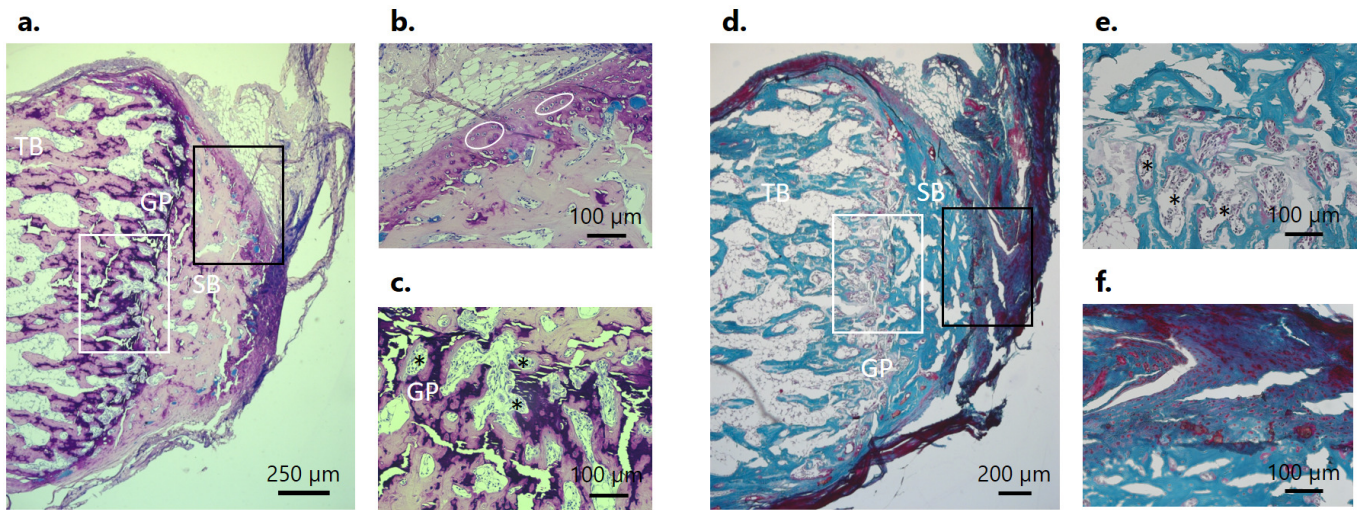

Figure S4.4: Histological analysis from two sagittal sections stained with Giemsa and Goldner. TB, GP and SB denote trabecular bone, growth plate and subchondral bone, respectively. The orientation of the cutting plane is slightly different as for the sample reported in Fig. 2. (**a**) Bright field light microscopy images of a thin section stained with Giemsa. The black and the white frames show the regions depicted with higher magnification in (**b**) and (**c**), respectively. (**b**) Magnified view highlighting a region at the growth plate, with cartilage inclusions (dark violet) and crowded with cells (black asterisks). (**c**) Zoom in the cartilage region (violet), with some chondrocytes circled in white. (**d**) Bright field light microscopy images of a thin section stained with Goldner. The black and the white frames show the regions depicted with higher magnification in (**e**) and (**f**), respectively. (**e**) Magnified view of the growth plate highlighting how active the region is: black asterisks show surfaces covered with cells, probably osteoblasts. (**f**) Zoom in the cartilage region: the darker area is less (or not) mineralized.

Tuberosity (*Region I*)	θ_{T1}, ϕ_{T1}	θ_{T2}, ϕ_{T2}	θ_{T3}, ϕ_{T3}	θ_{T4}, ϕ_{T4}	θ_{T5}, ϕ_{T5}
p(I-II)	$2.1\ 10^{-74}$	$9.2\ 10^{-69}$	$4\ 10^{-77}$	$5\ 10^{-42}$	$5\ 10^{-89}$
Periosteal (*Region II*)	θ_{S1}, ϕ_{S1}	θ_{S2}, ϕ_{S2}	θ_{S3}, ϕ_{S3}	θ_{S4}, ϕ_{S4}	θ_{S5}, ϕ_{S5}

Table S4.2: Results of the two-sample two-dimensional Kolmogorov-Smirnov tests comparing the distributions of fibrochondrocyte lacuna orientation between the two sites of interest.
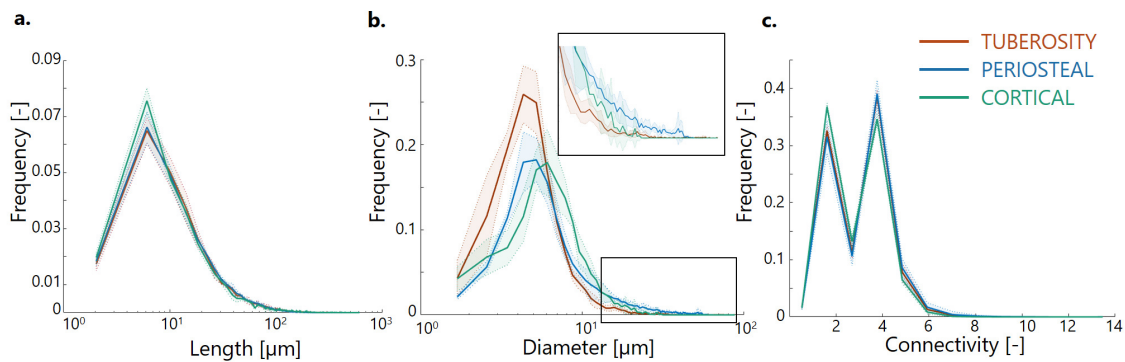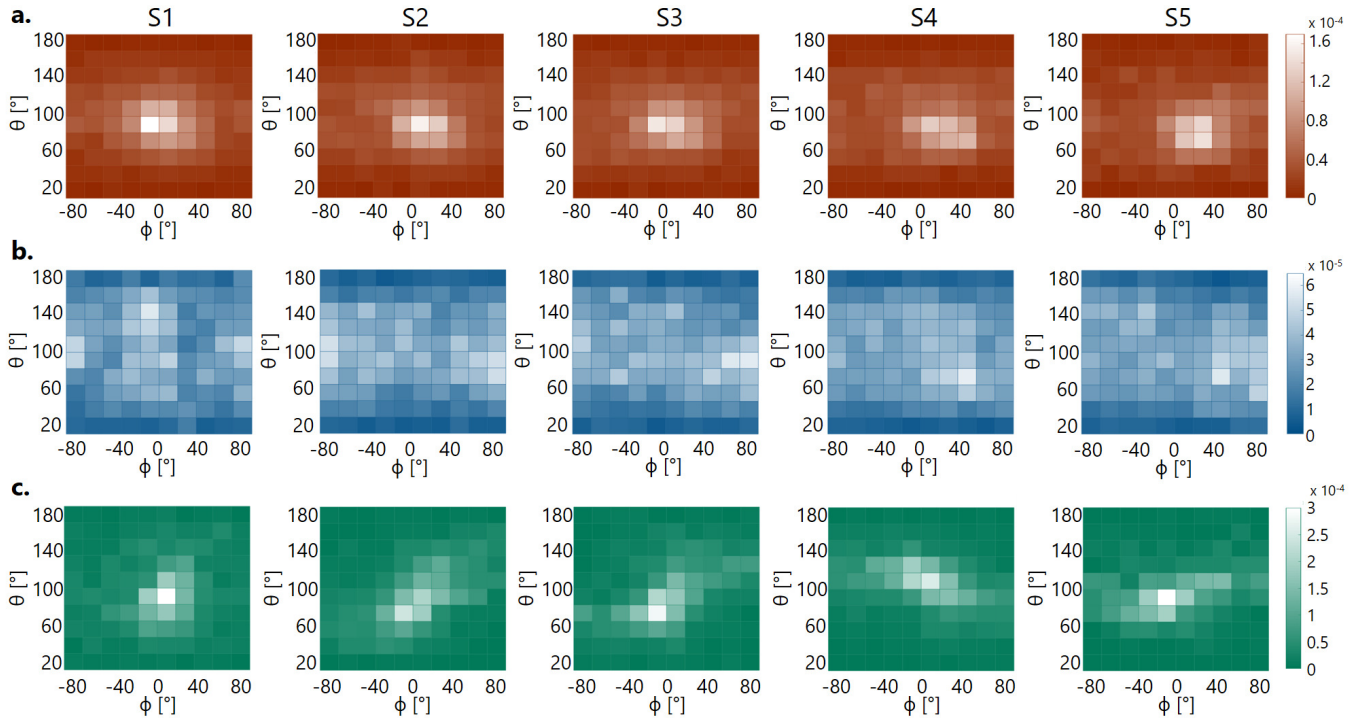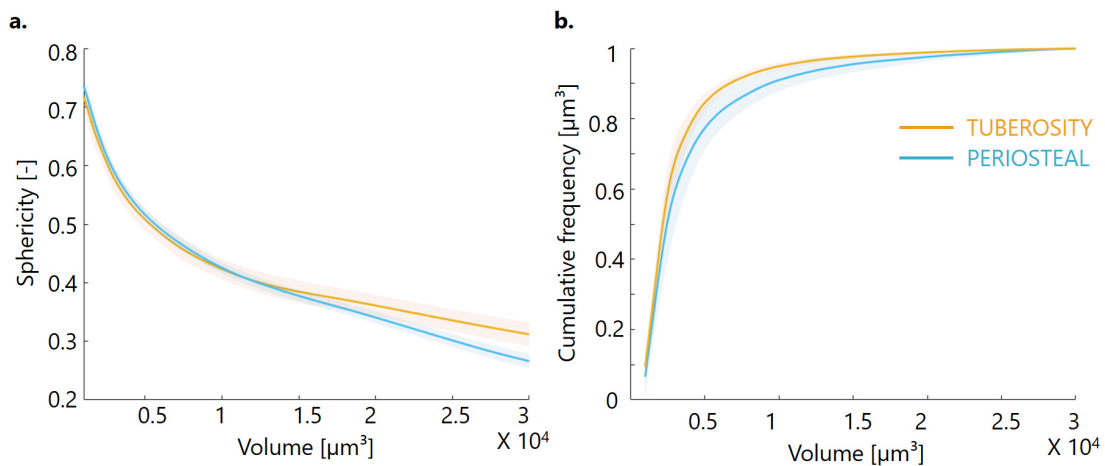
Figure S4.5: Three-dimensional local analysis of the channel morphology at the three sites of interest based on the high resolution micro-CT scans. Frequency distributions (normalized to unit area) of the channel length (**a**), diameter (**b**) and connectivity (**c**) for the entire dataset. Data reported as mean value (thick lines) with one standard deviation interval (shaded area).
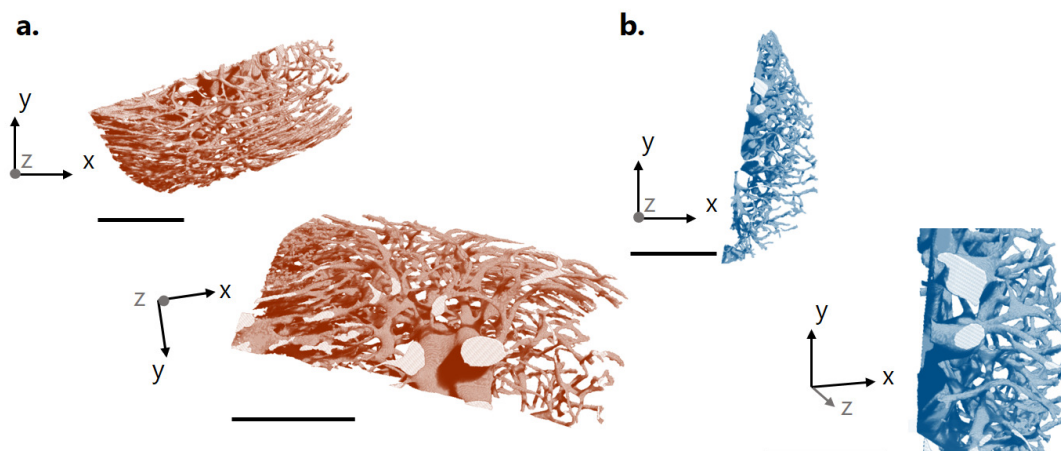

Figure S4.6: Illustration of large blood vessels entering the bone and spreading into smaller vessels for two sites of interest based on the high resolution micro-CT scans. In the tuberosity region (**a**), a big central blood vessel unravels into smaller and slender channels arranged like "butterfly" wings. The periosteal bone region (**b**) exhibits intermediate-sized channels lacking a clear predominant orientation. Scale bars: 500 μm.

Figure S4.7: Three-dimensional local analysis of the channel orientation at the three sites of interest based on the high resolution micro-CT scans. Two-dimensional heat maps of channel orientation for the whole dataset, confirming specific patterns for each region: the tuberosity (**a**) and the cortical bone (**c**) exhibit strong anisotropy whereas the periosteal bone (**b**) is rather isotropic. Data normalized to unit volume.


Figure S4.8: Three-dimensional local analysis of the lacunar sphericity at the two sites of interest based on the high resolution micro-CT scans. (**a**) Evolution of lacuna sphericity with volume reveals a strong decreasing trend with minor differences between the two sites and only for fairly large volumes. (**b**) Cumulative frequency distribution (normalized to unit area) of lacunae volume showing a sharper transition from small to high volume aggregates within the tuberosity. Data reported for the whole dataset as mean value (thick lines) with one standard deviation interval (shaded area).
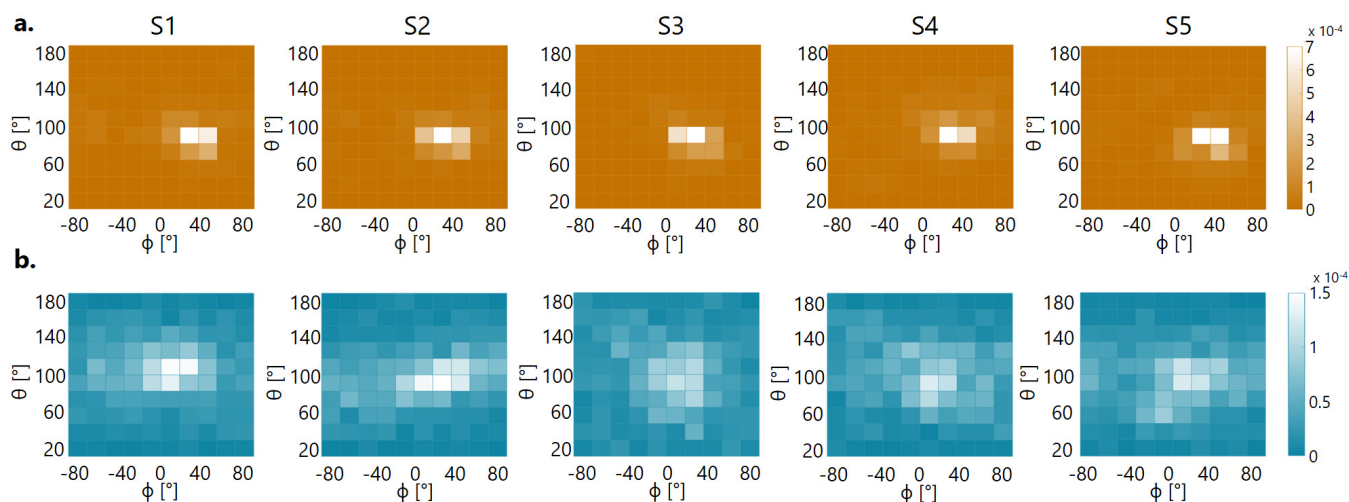
Figure S4.9: Three-dimensional local analysis of the lacunar porosity orientation at the two sites of interest based on the high resolution micro-CT scans. Representative two-dimensional heat maps of lacuna orientation for the whole dataset, confirming a clear preferred orientation at the insertion (**a**) compared to the periosteal region (**b**). Data normalized to unit volume.
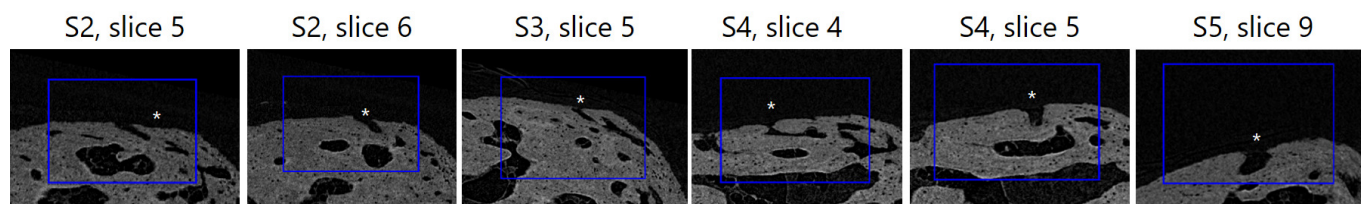
Figure S4.10: Roughness of the interface profile line based on the high resolution micro-CT scans. Illustration of the discarded regions for the roughness analysis because of blood vessels entering the bone.
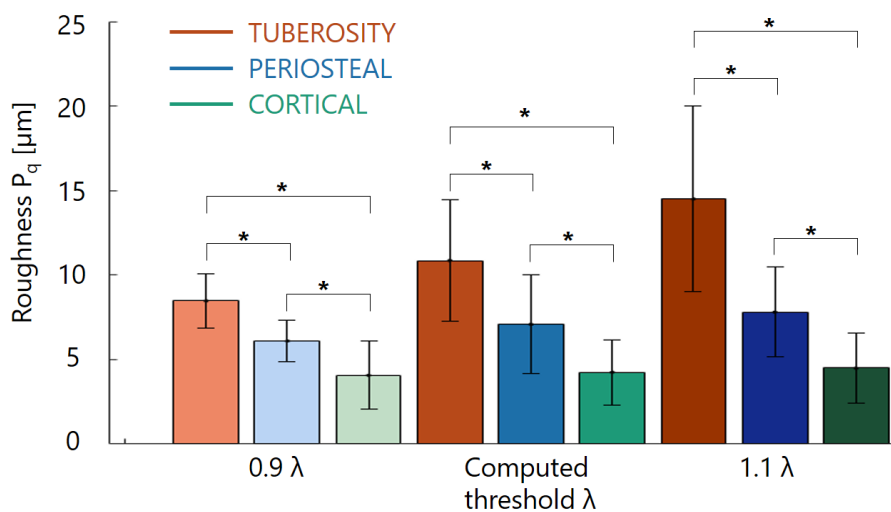
Figure S4.11: Sensitivity analysis on the threshold value for roughness computation, conducted for one representative animal (S1). Threshold variation of $\pm 10\%$ does not influence the statistically significant difference between the three regions of interest.

Bibliography

[1]   Helen H Lu and Stavros Thomopoulos. "Functional attachment of soft tissues to bone: development, healing, and tissue engineering". In: *Annual review of biomedical engineering* 15 (2013), p. 201.

[2]   M Benjamin and JR Ralphs. "Fibrocartilage in tendons and ligaments—an adaptation to compressive load". In: *The Journal of Anatomy* 193.4 (1998), pp. 481–494.

[3]   Michael Benjamin et al. "Where tendons and ligaments meet bone: attachment sites ('entheses') in relation to exercise and/or mechanical load". In: *Journal of anatomy* 208.4 (2006), pp. 471–490.

[4]   Andrew D Waggett et al. "Characterization of collagens and proteoglycans at the insertion of the human Achilles tendon". In: *Matrix Biology* 16.8 (1998), pp. 457–470.

[5]   L Rossetti et al. "The microstructure and micromechanics of the tendon–bone insertion". In: *Nature materials* 16.6 (2017), pp. 664–670.

[6]   Julian Sartori and Heiko Stark. "Tracking tendon fibers to their insertion–a 3D analysis of the Achilles tendon enthesis in mice". In: *Acta Biomaterialia* 120 (2021), pp. 146–155.

[7]   Stavros Thomopoulos et al. "Collagen fiber orientation at the tendon to bone insertion and its influence on stress concentrations". In: *Journal of biomechanics* 39.10 (2006), pp. 1842–1851.

[8]   Jeffrey P Spalazzi et al. "Quantitative mapping of matrix content and distribution across the ligament-to-bone insertion". In: *PLoS One* 8.9 (2013), e74349.

[9]   Yizhong Hu et al. "Stochastic interdigitation as a toughening mechanism at the interface between tendon and bone". In: *Biophysical journal* 108.2 (2015), pp. 431–437.

[10]   Alix C Deymier-Black et al. "Allometry of the tendon enthesis: mechanisms of load transfer between tendon and bone". In: *Journal of biomechanical engineering* 137.11 (2015).

[11]   Adam C Abraham and Tammy L Haut Donahue. "From meniscus to bone: a quantitative evaluation of structure and function of the human meniscal attachments". In: *Acta biomaterialia* 9.5 (2013), pp. 6322–6329.

[12]   Alix C Deymier et al. "Micro-mechanical properties of the tendon-to-bone attachment". In: *Acta biomaterialia* 56 (2017), pp. 25–35.

[13]   Kristen L Moffat et al. "Characterization of the structure–function relationship at the ligament-to-bone interface". In: *Proceedings of the national academy of sciences* 105.23 (2008), pp. 7947–7952.

[14]   Guy M Genin et al. "Functional grading of mineral and collagen in the attachment of tendon to bone". In: *Biophysical journal* 97.4 (2009), pp. 976–985.

[15]   Johnathan L Sevick et al. "Fibril deformation under load of the rabbit Achilles tendon and medial collateral ligament femoral entheses". In: *Journal of Orthopaedic Research®* 36.9 (2018), pp. 2506–2515.

[16]   A Aghaei et al. "Assessing the effective elastic properties of the tendon-to-bone insertion: a multiscale modeling approach". In: *Biomechanics and Modeling in Mechanobiology* 20.2 (2021), pp. 433–448.

[17]   Alexandra Tits and Davide Ruffoni. "Joining soft tissues to bone: Insights from modeling and simulations". In: *Bone Reports* 14 (2021), p. 100742.

[18]   HM Shaw and M Benjamin. "Structure–function relationships of entheses in relation to mechanical load and exercise". In: *Scandinavian journal of medicine & science in sports* 17.4 (2007), pp. 303–315.

[19]   Micheal Benjamin and Dennis McGonagle. "The anatomical basis for disease localisation in seronegative spondyloarthropathy at entheses and related sites". In: *The Journal of Anatomy* 199.5 (2001), pp. 503–526.

[20]   Michael Benjamin and Dennis McGonagle. "Histopathologic changes at "synovio–entheseal complexes" suggesting a novel mechanism for synovitis in osteoarthritis and spondylarthritis". In: *Arthritis & Rheumatism: Official Journal of the American College of Rheumatology* 56.11 (2007), pp. 3601–3609.

[21] Pamela F Weiss. "Diagnosis and treatment of enthesitis-related arthritis". In: *Adolescent health, medicine and therapeutics* 3 (2012), p. 67.

[22] M Benjamin, RN Tyers, and JR Ralphs. "Age-related changes in tendon fibrocartilage." In: *Journal of anatomy* 179 (1991), p. 127.

[23] Sébastien Villotte and Christopher J Knüsel. "Understanding entheseal changes: definition and life course changes". In: *International Journal of Osteoarchaeology* 23.2 (2013), pp. 135–146.

[24] Constantinos N Maganaris et al. "Biomechanics and pathophysiology of overuse tendon injuries". In: *Sports medicine* 34.14 (2004), pp. 1005–1017.

[25] John Apostolakos et al. "The enthesis: a review of the tendon-to-bone insertion". In: *Muscles, ligaments and tendons journal* 4.3 (2014), p. 333.

[26] Daniel Lee John Bunker et al. "Tendon to bone healing and its implications for surgery". In: *Muscles, ligaments and tendons journal* 4.3 (2014), p. 343.

[27] Kathleen A Derwin et al. "Enthesis repair: challenges and opportunities for effective tendon-to-bone healing". In: *The Journal of Bone and Joint surgery. American Volume* 100.16 (2018), e109.

[28] DT Harryman 2nd et al. "Repairs of the rotator cuff. Correlation of functional results with integrity of the cuff." In: *JBJS* 73.7 (1991), pp. 982–989.

[29] Leesa M Galatz et al. "The outcome and repair integrity of completely arthroscopically repaired large and massive rotator cuff tears". In: *JBJS* 86.2 (2004), pp. 219–224.

[30] G Keene. "Arthroscopic reconstruction of the anterior cruciate ligament. A comparison of patellar tendon autograft and four-strand hamstring tendon autograft." In: *The American journal of sports medicine* 28.3 (2000), pp. 438–438.

[31] David Simon et al. "The relationship between anterior cruciate ligament injury and osteoarthritis of the knee". In: *Advances in orthopedics* 2015 (2015).

[32] James F Griffith et al. "Cruciate ligament avulsion fractures". In: *Arthroscopy: The Journal of Arthroscopic & Related Surgery* 20.8 (2004), pp. 803–812.

[33] R Cole Beavis, Kevin Rourke, and Charles Court-Brown. "Avulsion fracture of the calcaneal tuberosity: a case report and literature review". In: *Foot & ankle international* 29.8 (2008), pp. 863–866.

[34] SW Hamilton and PH Gibson. "Simultaneous bilateral avulsion fractures of the tibial tuberosity in adolescence: a case report and review of over 50 years of literature". In: *The Knee* 13.5 (2006), pp. 404–407.

[35] Jason Porr, Calin Lucaciu, and Sarah Birkett. "Avulsion fractures of the pelvis–a qualitative systematic review of the literature". In: *The Journal of the Canadian Chiropractic Association* 55.4 (2011), p. 247.

[36] Richard Weinkamer and Peter Fratzl. "Mechanical adaptation of biological materials—The examples of bone and wood". In: *Materials Science and Engineering: C* 31.6 (2011), pp. 1164–1173.

[37] Carolin Lukas et al. "Mineralization kinetics in murine trabecular bone quantified by time-lapsed in vivo micro-computed tomography". In: *Bone* 56.1 (2013), pp. 55–60.

[38] Friederike A Schulte et al. "Local mechanical stimuli regulate bone formation and resorption in mice at the tissue level". In: *PloS one* 8.4 (2013), e62172.

[39] Patrik Christen et al. "Bone remodelling in humans is load-driven but not lazy". In: *Nature communications* 5.1 (2014), pp. 1–5.

[40] Floor M Lambers et al. "Trabecular bone adapts to long-term cyclic loading by increasing stiffness and normalization of dynamic morphometric rates". In: *Bone* 55.2 (2013), pp. 325–334.

[41] Vee San Cheong et al. "Bone remodelling in the mouse tibia is spatio-temporally modulated by oestrogen deficiency and external mechanical loading: A combined in vivo/in silico study". In: *Acta Biomaterialia* 116 (2020), pp. 302–317.

[42] Zihui Li, Ralph Müller, and Davide Ruffoni. "Bone remodeling and mechanobiology around implants: Insights from small animal imaging". In: *Journal of Orthopaedic Research®* 36.2 (2018), pp. 584–593.

[43] Hajar Razi et al. "Aging leads to a dysregulation in mechanically driven bone formation and resorption". In: *Journal of Bone and Mineral Research* 30.10 (2015), pp. 1864–1873.

[44] Zihui Li et al. "Mechanical regulation of bone formation and resorption around implants in a mouse model of osteopenic bone". In: *Journal of the Royal Society Interface* 16.152 (2019), p. 20180667.

[45] Isaac Vorster Pratt and David Michael Lane Cooper. "A method for measuring the three-dimensional orientation of cortical canals with implications for comparative analysis of bone microstructure in vertebrates". In: *Micron* 92 (2017), pp. 32–38.

[46] Hayley M Britz et al. "The effects of immobilization on vascular canal orientation in rat cortical bone". In: *Journal of anatomy* 220.1 (2012), pp. 67–76.

[47] René FM van Oers, Hong Wang, and Rommel G Bacabac. "Osteocyte shape and mechanical loading". In: *Current osteoporosis reports* 13.2 (2015), pp. 61–66.

[48] Haniyeh Hemmatian et al. "Mechanical loading differentially affects osteocytes in fibulae from lactating mice compared to osteocytes in virgin mice: possible role for lacuna size". In: *Calcified tissue international* 103.6 (2018), pp. 675–685.

Bibliography

[49]   Petar Milovanovic and Björn Busse. "Inter-site variability of the human osteocyte lacunar network: implications for bone quality". In: *Current osteoporosis reports* 17.3 (2019), pp. 105–115.

[50]   Alexander Franciscus van Tol et al. "The mechanoresponse of bone is closely related to the osteocyte lacunocanalicular network architecture". In: *Proceedings of the National Academy of Sciences* 117.51 (2020), pp. 32251–32259.

[51]   A Rufai, M Benjamin, and JR Ralphs. "Development and ageing of phenotypically distinct fibrocartilages associated with the rat Achilles tendon". In: *Anatomy and embryology* 186.6 (1992), pp. 611–618.

[52]   A Rufai, JR Ralphs, and M Benjamin. "Structure and histopathology of the insertional region of the human Achilles tendon". In: *Journal of orthopaedic research* 13.4 (1995), pp. 585–593.

[53]   Ryan C Locke et al. "Strain distribution of intact rat rotator cuff tendon-to-bone attachments and attachments with defects". In: *Journal of biomechanical engineering* 139.11 (2017).

[54]   Lee A Feldkamp, Lloyd C Davis, and James W Kress. "Practical cone-beam algorithm". In: *Josa a* 1.6 (1984), pp. 612–619.

[55]   Michael Doube et al. "BoneJ: free and extensible bone image analysis in ImageJ". In: *Bone* 47.6 (2010), pp. 1076–1079.

[56]   Caroline A Schneider, Wayne S Rasband, and Kevin W Eliceiri. "NIH Image to ImageJ: 25 years of image analysis". In: *Nature methods* 9.7 (2012), pp. 671–675.

[57]   Mary L Bouxsein et al. "Guidelines for assessment of bone microstructure in rodents using micro–computed tomography". In: *Journal of bone and mineral research* 25.7 (2010), pp. 1468–1486.

[58]   Nobuyuki Otsu. "A threshold selection method from gray-level histograms". In: *IEEE transactions on systems, man, and cybernetics* 9.1 (1979), pp. 62–66.

[59]   Josef Kittler and John Illingworth. "On threshold selection using clustering criteria". In: *IEEE transactions on systems, man, and cybernetics* 5 (1985), pp. 652–655.

[60]   Bruker. "MicroCT method note: Automated trabecular and cortical bone selection". In: ().

[61]   Peter Saparin et al. "Structural adaptation of trabecular bone revealed by position resolved analysis of proximal femora of different primates". In: *The Anatomical Record: Advances in Integrative Anatomy and Evolutionary Biology* 294.1 (2011), pp. 55–67.

[62]   Bruker. "Bruker MicroCT method note: Anisotropy, Mean Intercept Length (MIL) and stereology calculation in CT Analyser (MN031-1)". In: ().

[63]   WJ Whitehouse. "The quantitative morphology of anisotropic trabecular bone". In: *Journal of microscopy* 101.2 (1974), pp. 153–168.

[64]   TP Harrigan and RW Mann. "Characterization of microstructural anisotropy in orthotropic materials using a second rank tensor". In: *Journal of Materials Science* 19.3 (1984), pp. 761–767.

[65]   Sami Kauppinen et al. "3D morphometric analysis of calcified cartilage properties using micro-computed tomography". In: *Osteoarthritis and cartilage* 27.1 (2019), pp. 172–180.

[66]   JOHN M Clark. "The structure of vascular channels in the subchondral plate." In: *Journal of anatomy* 171 (1990), p. 105.

[67]   Paolo E Palacio-Mancheno et al. "3D assessment of cortical bone porosity and tissue mineral density using high-resolution μCT: effects of resolution and threshold method". In: *Journal of Bone and Mineral Research* 29.1 (2014), pp. 142–150.

[68]   Cesare Ciani, Stephen B Doty, and Susannah P Fritton. "An effective histological staining process to visualize bone interstitial fluid space using confocal microscopy". In: *Bone* 44.5 (2009), pp. 1015–1017.

[69]   Peter G Bush, Constantinos A Parisinos, and Andrew C Hall. "The osmotic sensitivity of rat growth plate chondrocytes in situ; clarifying the mechanisms of hypertrophy". In: *Journal of cellular physiology* 214.3 (2008), pp. 621–629.

[70]   Andrew C Hall. "The role of chondrocyte morphology and volume in controlling phenotype—implications for osteoarthritis, cartilage repair, and cartilage engineering". In: *Current Rheumatology Reports* 21.8 (2019), pp. 1–13.

[71]   Júlia Chaumel et al. "Co-aligned chondrocytes: zonal morphological variation and structured arrangement of cell lacunae in tessellated cartilage". In: *Bone* 134 (2020), p. 115264.

[72]   A Rufai, JR Ralphs, and M Benjamin. "Ultrastructure of fibrocartilages at the insertion of the rat Achilles tendon." In: *Journal of anatomy* 189.Pt 1 (1996), p. 185.

[73]   David ML Cooper et al. "Quantitative 3D analysis of the canal network in cortical bone by micro-computed tomography". In: *The Anatomical Record Part B: The New Anatomist: An Official Publication of the American Association of Anatomists* 274.1 (2003), pp. 169–179.

[74]   Chris Pudney. "Distance-ordered homotopic thinning: a skeletonization algorithm for 3D digital images". In: *Computer vision and image understanding* 72.3 (1998), pp. 404–413.

[75] Grégoire Malandain, Gilles Bertrand, and Nicholas Ayache. "Topological segmentation of discrete surfaces". In: *International journal of computer vision* 10.2 (1993), pp. 183–197.

[76] Erwan Plougonven. "3D image analysis and visualisation modules for Avizo". In: *chemeng.uliege.be/ep-avizo* ().

[77] Hakon Wadell. "Volume, Shape, and Roundness of Rock Particles". In: *The Journal of Geology* 40.5 (1932), pp. 443–451.

[78] Magdalena Rajczakowska, Damian Stefaniuk, and Maciej Sobótka. "Roughness analysis of the "invisible" surface by means of X-ray micro-CT". In: ().

[79] Greet Kerckhofs et al. "High-resolution microfocus X-ray computed tomography for 3D surface roughness measurements of additive manufactured porous materials". In: *Advanced Engineering Materials* 15.3 (2013), pp. 153–158.

[80] HS Gupta et al. "Two different correlations between nanoindentation modulus and mineral content in the bone–cartilage interface". In: *Journal of structural biology* 149.2 (2005), pp. 138–148.

[81] John A Peacock. "Two-dimensional goodness-of-fit testing in astronomy". In: *Monthly Notices of the Royal Astronomical Society* 202.3 (1983), pp. 615–627.

[82] D Muir. "kstest_2s_2d (x1, x2, alpha)". In: *MATLAB Central File Exchange* ().

[83] A Shipov et al. "Unremodeled endochondral bone is a major architectural component of the cortical bone of the rat (Rattus norvegicus)". In: *Journal of structural biology* 183.2 (2013), pp. 132–140.

[84] Pei-Yu Hsu et al. "Cortical bone morphological and trabecular bone microarchitectural changes in the mandible and femoral neck of ovariectomized rats". In: *PloS one* 11.4 (2016), e0154367.

[85] HM Britz et al. "3D visualization and quantification of rat cortical bone porosity using a desktop micro-CT system: a case study in the tibia". In: *Journal of microscopy* 240.1 (2010), pp. 32–37.

[86] Bettina M Willie et al. "Bone adaptation: Safety factors and load predictability in shaping skeletal form". In: *Bone* 131 (2020), p. 115114.

[87] John G Skedros et al. "Advancing the deer calcaneus model for bone adaptation studies: ex vivo strains obtained after transecting the tension members suggest an unrecognized important role for shear strains". In: *Journal of Anatomy* 234.1 (2019), pp. 66–82.

[88] John G Skedros, Steve C Su, and Roy D Bloebaum. "Biomechanical implications of mineral content and microstructural variations in cortical bone of horse, elk, and sheep calcanei". In: *The Anatomical Record: An Official Publication of the American Association of Anatomists* 249.3 (1997), pp. 297–316.

[89] STEVEN C Su et al. "Loading conditions and cortical bone construction of an artiodactyl calcaneus". In: *Journal of Experimental Biology* 202.22 (1999), pp. 3239–3254.

[90] Andrew A Biewener et al. "Adaptive changes in trabecular architecture in relation to functional strain patterns and disuse". In: *Bone* 19.1 (1996), pp. 1–8.

[91] Michael Benjamin et al. "The skeletal attachment of tendons—tendon 'entheses'". In: *Comparative Biochemistry and Physiology Part A: Molecular & Integrative Physiology* 133.4 (2002), pp. 931–945.

[92] Ksenija Djukić et al. "A microarchitectural assessment of the gluteal tuberosity suggests two possible patterns in entheseal changes". In: *American Journal of Physical Anthropology* 172.2 (2020), pp. 291–299.

[93] John WC Dunlop, Richard Weinkamer, and Peter Fratzl. "Artful interfaces within biological materials". In: *Materials Today* 14.3 (2011), pp. 70–78.

[94] Yankel Gabet et al. "Trabecular bone gradient in rat long bone metaphyses: mathematical modeling and application to morphometric measurements and correction of implant positioning". In: *Journal of bone and mineral research* 23.1 (2008), pp. 48–57.

[95] Davide Ruffoni et al. "High-throughput quantification of the mechanical competence of murine femora—a highly automated approach for large-scale genetic studies". In: *Bone* 55.1 (2013), pp. 216–221.

[96] Davide Ruffoni and G. H. van Lenthe. "Comprehensive Biomaterials". In: *Elsevier Science* (2010).

[97] Fernando A Cordisco et al. "Toughness of a patterned interface between two elastically dissimilar solids". In: *Engineering Fracture Mechanics* 96 (2012), pp. 192–208.

[98] Francesco Caimmi and Andrea Pavan. "An experimental evaluation of glass–polymer interfacial toughness". In: *Engineering fracture mechanics* 76.18 (2009), pp. 2731–2747.

[99] Lei Zhao, Ashvin Thambyah, and Neil D Broom. "A multi-scale structural study of the porcine anterior cruciate ligament tibial enthesis". In: *Journal of anatomy* 224.6 (2014), pp. 624–633.

[100] S Milz et al. "Three-dimensional reconstructions of the Achilles tendon insertion in man". In: *Journal of anatomy* 200.2 (2002), pp. 145–152.

[101]   Virginia L Ferguson, Andrew J Bushby, and Alan Boyde. "Nanomechanical properties and mineral concentration in articular calcified cartilage and subchondral bone". In: *Journal of Anatomy* 203.2 (2003), pp. 191–202.

[102]   Finn Donaldson et al. "Modeling microdamage behavior of cortical bone". In: *Biomechanics and modeling in mechanobiology* 13.6 (2014), pp. 1227–1242.

[103]   Michael Kerschnitzki et al. "The organization of the osteocyte network mirrors the extracellular matrix orientation in bone". In: *Journal of structural biology* 173.2 (2011), pp. 303–311.

[104]   Aviral Vatsa et al. "Osteocyte morphology in fibula and calvaria—is there a role for mechanosensing?" In: *Bone* 43.3 (2008), pp. 452–458.

[105]   Yasmin Carter et al. "Variation in osteocyte lacunar morphology and density in the human femur—a synchrotron radiation micro-CT study". In: *Bone* 52.1 (2013), pp. 126–132.

[106]   Haniyeh Hemmatian et al. "Age-related changes in female mouse cortical bone microporosity". In: *Bone* 113 (2018), pp. 1–8.

[107]   Steven M Tommasini et al. "Changes in intracortical microporosities induced by pharmaceutical treatment of osteoporosis as detected by high resolution micro-CT". In: *Bone* 50.3 (2012), pp. 596–604.

[108]   Stavros Thomopoulos et al. "Decreased muscle loading delays maturation of the tendon enthesis during postnatal development". In: *Journal of Orthopaedic Research* 25.9 (2007), pp. 1154–1163.

[109]   Stavros Thomopoulos. "The Role of Mechanobiology in the Attachment of Tendon to Bone." In: *IBMS BoneKEy* 8.6 (2011).

[110]   Andrea G Schwartz, Fanxin Long, and Stavros Thomopoulos. "Enthesis fibrocartilage cells originate from a population of Hedgehog-responsive cells modulated by the loading environment". In: *Development* 142.1 (2015), pp. 196–206.

[111]   Andrea G Schwartz et al. "Mineral distributions at the developing tendon enthesis". In: *PloS one* 7.11 (2012), e48630.

[112]   Diego Pulzatto Cury et al. "Structural and ultrastructural characteristics of bone-tendon junction of the calcaneal tendon of adult and elderly wistar rats". In: *PLoS One* 11.4 (2016), e0153568.

[113]   Benedicto de Campos Vidal, Eli Heber M Dos Anjos, and Maria Luiza S Mello. "Optical anisotropy reveals molecular order in a mouse enthesis". In: *Cell and tissue research* 362.1 (2015), pp. 177–185.

[114]   Michael G McCoy et al. "Collagen fiber orientation regulates 3D vascular network formation and alignment". In: *ACS Biomaterials Science & Engineering* 4.8 (2018), pp. 2967–2976.

[115]   Felix Repp et al. "Spatial heterogeneity in the canalicular density of the osteocyte network in human osteons". In: *Bone reports* 6 (2017), pp. 101–108.

[116]   Pramod B Voleti, Mark R Buckley, and Louis J Soslowsky. "Tendon healing: repair and regeneration". In: *Annual review of biomedical engineering* 14 (2012), pp. 47–71.

Chapter 5

Structural and functional heterogeneity of mineralized fibrocartilage at the Achilles tendon-bone insertion

Adapted from: Alexandra Tits [a], Stéphane Blouin [b], Maximilian Rummler [c], Jean-François Kaux [d], Pierre Drion [e], G. Harry van Lenthe [f], Richard Weinkamer [c], Markus A Hartmann [b], Davide Ruffoni [a], *Structural and functional heterogeneity of mineralized fibrocartilage at the Achilles tendon-bone insertion*, under review in Acta Biomaterialia.

[a] Mechanics of Biological and Bioinspired Materials Laboratory, Department of Aerospace and Mechanical Engineering, University of Liège, Liège, Belgium ; [b] Ludwig Boltzmann Institute of Osteology at Hanusch Hospital of OEGK and AUVA Trauma Centre Meidling, 1st Medical Department Hanusch Hospital, Vienna, Austria ; [c] Department of Biomaterials, Max Planck Institute of Colloids and Interfaces, 14476 Potsdam, Germany ; [d] Department of Physical Medicine and Sports Traumatology, University of Liège and University Hospital of Liège, Liège, Belgium ; [e] Experimental Surgery unit, GIGA & Credec, University of Liege, Liege, Belgium ; [f] Department of Mechanical Engineering, KU Leuven, Leuven, Belgium.

ABSTRACT

A demanding task of the musculoskeletal system is the attachment of tendon to bone at entheses. This region often presents a thin layer of fibrocartilage (FC), mineralized close to the bone and unmineralized close to the tendon. Mineralized FC deserves increased attention, owing to its crucial anchoring task and involvement in enthesis pathologies. Here, we analyzed mineralized FC and subchondral bone at the Achilles tendon-bone insertion of rats. This location features enthesis FC anchoring tendon to bone and sustaining tensile loads, and periosteal FC facilitating bone-tendon sliding with accompanying compressive and shear forces. Using a correlative multimodal investigation, we evaluated potential specificities in mineral content, fibers organization and mechanical properties of enthesis and periosteal FC. Both tissues had a lower degree

of mineralization than subchondral bone, yet used the available mineral very efficiently: for the same local mineral content, they had higher stiffness and hardness than bone. We found that enthesis FC was characterized by highly aligned mineralized collagen fibers even far away from the attachment region, whereas periosteal FC had a rich variety of fiber arrangements. Except for an initial steep spatial gradient between unmineralized and mineralized FC, local mechanical properties were surprisingly uniform inside enthesis FC while a modulation in stiffness, independent from mineral content, was observed in periosteal FC. We interpreted these different structure-property relationships as a demonstration of the high versatility of FC, providing high strength at the insertion (to resist tensile loading) and a gradual compliance at the periosteal surface (to resist contact stresses).

STATEMENT OF SIGNIFICANCE

Mineralized fibrocartilage (FC) at entheses facilitates the integration of tendon in bone, two strongly dissimilar tissues. We focus on the structure-function relationships of two types of mineralized FC, enthesis and periosteal, which have clearly distinct mechanical demands. By investigating them with multiple high-resolution methods in a correlative manner, we demonstrate differences in fiber architecture and mechanical properties between the two tissues, indicative of their mechanical roles. Our results are relevant both from a medical viewpoint, targeting a clinically relevant location, as well as from a material science perspective, identifying FC as high-performance versatile composite.

5.1   Introduction

Cartilage is a highly versatile tissue essential to the functioning of the musculoskeletal system. Articular (hyaline) cartilage and fibrocartilage (FC) are two types of cartilage present in mammals, which share the same constituents but in different proportions and arrangements depending on the anatomical location and mechanical function [1]. Cartilage is found at mechanically challenging locations to cope with tasks that bone alone cannot solve. The end of the bones that articulates in a joint, for example, is covered by a layer of unmineralized articular cartilage, followed by a thin region of mineralized cartilage, and then subchondral bone. Thanks to a sophisticated interplay between extracellular matrix and water, combined with consecutive layers of varying collagen orientation, the millimeter-thick unmineralized articular cartilage provides lubrication and resistance to contact stresses [2]. At the same time, with only a few hundreds of micrometers in thickness, mineralized cartilage must ensure a proper anchoring between cartilage and bone [3].

Similarly, at the insertion of tendons and ligaments into bone, particularly when the insertion angle changes considerably during joint movement, FC is present [4]. This integrative tissue is also found at meniscal attachment to bone [5–7]. In analogy with articular cartilage, FC comes in two forms: unmineralized FC (uFC) close to tendon/ligament and mineralized FC (mFC) close to bone. Like bone and tendon, FC is a

highly fibrous tissue but composed of a mixture of collagen type II and III (rather than collagen type I) and proteoglycans [8, 9]. In mFC, the fibrous matrix gets reinforced by mineral crystals and anchors to bone [10]. Knowing that bimaterial attachments are at risk of stress localization [11], the interface between uFC and mFC is considered the weakest link in the force transmission from tendon to bone, and it has received considerable attention. A fine tuning of composition and hierarchical organization across the interface provides enthesis with high mechanical efficiency, allowing the transmission of large forces for many years [9, 12–15]. mFC away from the interface and even the underlying (subchondral) bone have been investigated less. This is unfortunate as these regions may also be the cause of attachment failure, especially following a (high) monotonic loading event [16] or when the physiological loading conditions are altered [17]. Furthermore, studies on articular cartilage have underlined key structure-property relationships contributing to anchoring cartilage to bone [3, 18–20].

In this work, we exploited high-resolution material characterization methods to detect the effect of mechanical loading on the structure and mechanical properties of mFC at the micrometer length scale. Specifically, we analyzed the Achilles tendon-calcaneus bone enthesis in rats, one of the most used animal model to investigate enthesis diseases [21] [22] and the musculoskeletal system in general, especially tendons [23, 24], given its similarities with humans. Two types of FC can be found there, each with different mechanical loading conditions: enthesis FC anchors tendon to bone, therefore sustains predominantly tensile loads, whereas periosteal FC facilitates tendon sliding and bone-tendon contact with accompanying compressive and shear forces. In a previous work, we highlighted a strong anisotropy of the microstructural porosity (fibrochondrocyte lacunae and channel network) within enthesis mFC (E-mFC), with pores strongly oriented towards the tendon insertion [25]. Here, we combine nanoindentation with quantitative backscattered electron imaging (qBEI) and second harmonic generation (SHG) imaging on the same locations, to spatially correlate mechanical properties with mineral content and matrix organization, considering both longitudinal and transverse directions to address the inherent anisotropy of the tissue.

5.2 Materials and methods

5.2.1 Sample preparation

Achilles tendon-calcaneus bone samples were extracted from the posterior legs of 3-month-old male Sprague-Dawley rats (n = 3, weight of 402 ± 31.2 g) and stored in 70 % ethanol. Animals were available at the Liège University Hospital in the framework of an organ donation program (ethical approval: ULg-IACUC-21-2340). Samples were prepared to expose representative cross-sections of the tendon-bone insertion. Following dehydration and embedding in polymethyl methacrylate (PMMA), samples were cut along the sagittal plane (Fig. S5.1) with a diamond saw (Buehler Isomet 1000). Sample surface was ground with sandpaper until the tendon-bone insertion at the calcaneal tuberosity was spotted. A final polishing step using a diamond suspension (grain size down to 1 μm, Logitech PM5) completed the sample preparation.

After performing qBEI, SHG imaging and biomechanical analysis on the sagittal sections, the same samples were cut along the transverse plane and polished, such that two-mutually perpendicular cross-sections could be characterized for each sample.

5.2.2 Quantitative backscattered electron imaging

To quantify the mineral content, qBEI [26] was performed on carbon-coated samples with a Field Emission Scanning Electron Microscope (FESEM, Supra40, Zeiss) [27]. The measurements were performed at 20 kV with a working distance of 10 mm and a scan speed of 90 s per frame [27]. The intensity of the electrons backscattered from a thin (i.e., about 1-2 μm in thickness) surface layer is mainly determined by the local calcium concentration [26]. To allow a quantitative assessment of calcium content, the FESEM was calibrated with carbon and aluminum standards. Images were acquired at a magnification of 130x, yielding a nominal isotropic pixel size of 0.88 μm, and considering a 1024 $\times$ 768 pixel window. By stitching together adjacent measurements recorded with a 5 % spatial overlap, the entire sample surface was characterized. The gray level (GL) images were translated into spatial maps of the mineral content expressed as calcium weight percentage via:

$$\text{Ca [wt\%]} = -4.332 + 0.1733 \times \text{GL} \tag{5.1}$$

Before further quantification, the following pre-processing steps were performed with the software CTAn (v1.19.4.0, Skyscan). First, bone and mFC were manually segmented following the interface between the two tissues (see black dashed line in Fig. 5.1). To minimize boundary effects [28], a 1 pixel erosion operator was applied. Signals from the embedding resin and non-mineralized tissues were removed by setting a minimum threshold for the mineral content (5.2 wt %). Individual unconnected pixels were also discarded. The mineralization maps highlighted the presence of several highly mineralized regions, especially in the trabecular compartment (Fig. S5.3). In a previous work we have shown that these are cartilaginous inclusions of high mineral content [25], which have been also observed in rat cortical bone [29, 30]. The highly mineralized islands were discarded from the present analysis by setting an upper threshold of 29.5 wt % (determined by visual inspection). The mineralization maps were then summarized into mineralization density frequency distributions and normalized to unit area. The following five parameters were introduced to characterize the resulting histograms [28]: Ca_{mean} (average Ca concentration), Ca_{peak} (most frequent Ca concentration), Ca_{width} (full width at half maximum), Ca_{low} and Ca_{high}. The last two parameters describe the amount of low and high mineralized regions, corresponding to areas mineralized below the 5th percentile and above the 95th percentile of a reference distribution. Here, the histogram of subchondral bone adjacent to mFC was taken as reference, with $\text{Ca}_{\text{low}} = 22$ and $\text{Ca}_{\text{high}} = 27.3$ wt %. These values were then used to compute the area below Ca_{low} and above Ca_{high} on mFC distributions.

5.2.3 Second harmonic imaging

To visualize the arrangement of collagen fibrils, SHG imaging was used [31, 32]. In this nonlinear light scattering process, a strong SHG signal is usually generated by regions with densely packed collagen fibrils, preferentially arranged parallel to the imaging plane. Conversely, if collagen fibrils are oriented out of the image plane, no signal should be detected [33–35]. In between these two scenarios, intermediate intensities are measured depending on several factors including collagen charge density and out-of-plane orientation. Second harmonic imaging was performed using a SP8 confocal microscope (Leica Microsystems, Wetzlar, Germany) with a 40x oil immersion objective (HC PL APO 40×/1.30 OIL) without using the pinhole, corresponding to a nominal isotropic pixel size of 379 nm. A Mai-Tai high performance Ti:Sa Laser (Spectra-Physics, Milpitas, CA, USA) operating in pulse mode at a wavelength of 910 nm was used, and the backward direction signal was detected at 450-460 nm. Several windows of 1024 x 1024 pixels were analyzed and stitched together such that exactly the same regions were characterized by both qBEI and SHG.

5.2.4 Nanoindentation and data processing

The polished PMMA-embedded samples were mechanically characterized by nanoindentation (Triboindenter TI 950, Bruker, US) to measure indentation modulus and hardness. The nanoindenter was equipped with a Berkovich diamond probe (50 nm tip radius) and a displacement controlled trapezoidal load function was used (8-20-8 s), with a maximum displacement of 500 nm. The average surface roughness of the mineralized tissues, measured by scanning 20 μm x 20 μm regions with the tip of the nanoindenter at 2 μN contact force, was 15.5 ± 6.7 nm. The indentation depth was well above the recommended threshold of 10 times the surface roughness [36, 37]. Due to inelastic deformation, the lateral spacing between indents should be at least three times the contact radius [19], or 4.2 μm in our setting. A spacing of 6 μm was chosen here and several indentation grids (for a total of about 3000 indents) were performed on regions across the bone-mFC interface, selected on both enthesis and periosteal areas with the help of the qBEI maps (Fig. S5.4). The probe contact area was calibrated with fused quartz and the obtained load-depth curves were analyzed with the Oliver-Pharr method [38], to extract indentation hardness (H) and reduced modulus (E_r). The nanoindentation grids were then superimposed on the qBEI maps through a manual registration procedure. This allowed to classify indents as belonging to mFC or bone, as well as to discard indents falling within cracks or holes (Fig. S5.4). To correlate the mineral content with the local mechanical properties (E_r and H), the calcium concentration was averaged over a 4 x 4 pixel region centered around each indent. This size can be considered representative of the elastic field probed by the indent at 500 μm depth [19]. To assess the spatial evolution of the mechanical properties when entering the mineralized tissues, the shortest distance (Euclidean) of each indent from the mineralized surface was computed (Fig. S5.4). In soft tissues, especially close to the interface with mineralized tissues, only a limited number of indents could be considered due to high roughness. As for the mineral content, histograms of reduced modulus and hardness were calculated and characterized by similar parameters. Low and high values for elastic modulus and hardness

were calculated considering the corresponding distributions of subchondral bone (i.e., $E_{r, low}$ = 17.5 and
$E_{r, high}$ = 25.5 GPa; H_{low} = 0.55 and H_{high} = 0.79 GPa) and were used for calculating areas below these limits
on the mFC distributions.

5.2.5 Statistical methods

We used statistical analysis for two purposes: to compare the mean mineralization needed to reach specific
tissue modulus and hardness values (Fig. S5.3b and S5.8d) as well as to compare properties between sagit-
tal and transverse sections (Fig. 5.6). We applied a two-sample Student's t-test with normality checked by
a Kolmogorov-Smirnov test and homoscedasticity by a two-sample F-test. If one of those criteria was not
met, a Mann-Whitney U-test was employed. P-values smaller than 0.05 were considered significant. Me-
chanical properties-mineral content relationships were evaluated with a two-parameter exponential model
and nonlinear regression was used to determine the values of the parameters. The statistical analysis was
performed in Matlab (statistics toolbox) [39] and SigmaPlot (nonlinear regressions).

5.3 Results

5.3.1 Qualitative observations on mineral content and fiber organization

A qualitative observation of the qBEI images highlights several features of the mineralization pattern. The
layer of mFC at both periosteal and insertion sites is often demarcated from bone by a thin, very irregu-
lar and highly mineralized interphase which, in analogy with the interphase bordering osteons, is named
cement line (dashed black line in Fig. 5.1b, c). Some regions of bone appear as fully encircled by mFC
even up to hundreds of micrometers away from the interface (highlighted by closed lines Fig. 5.1c and
Fig. S5.6a). These isolated "islands" in 2D sections are most likely interconnected in 3D, making the con-
nection between mFC and bone highly interdigitated. At the insertion site, the mFC layer is thicker and
shows bigger interdigitations than at the periosteal side (also shown for the other samples in Fig. S5.5). The
interface between uFC and mFC is also fairly rough, but at a smaller length scale, with interface roughness
dominated by arrested fibrochondrocytes and by the irregular mineralization front. Overall, mFC exhibits
high porosity at the micrometer length scale due to numerous fibrochondrocyte lacunae, in agreement with
a previous investigation [25]. In some locations, former tidemarks, indicating previous interfaces between
uFC and mFC [18, 40], are detectable (see arrows in Fig. S5.6b).

SHG images provide qualitative insights into fiber organization. Similar to mineralization, an overall het-
erogeneity is observed (Fig. 5.1d and S5.7). At the insertion and especially towards the inferior side of
the tuberosity (Fig. 5.1f), the SHG signal is very strong and rather uniform, suggesting highly aligned
(in-plane) collagen fibers, connecting almost continuously the Achilles tendon with the plantar fascia, at-
taching on the opposite side of the tuberosity. In contrast, periosteal mFC (P-mFC, Fig. 5.1e) shows a more
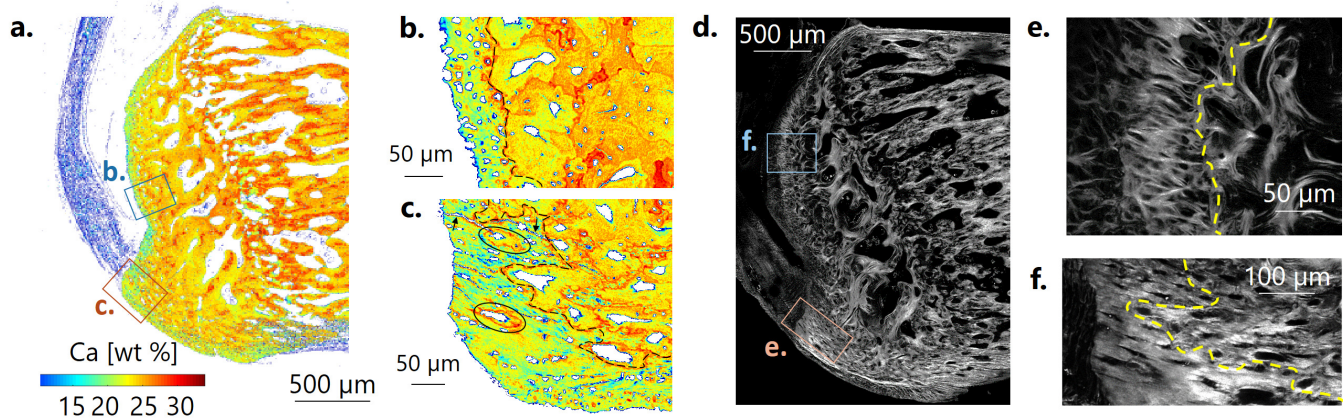
Figure 5.1: (a) Mineralization pattern from quantitative backscattered electron imaging (qBEI) and (d) corresponding fiber organization from second harmonic generation (SHG) imaging. Magnified views of qBEI data at (b) periosteal and (c) enthesis regions. Black dashed lines indicate the interface between mineralized fibrocartilage (mFC) and bone used to segment the different regions. Black closed lines (ellipse shaped) denote bone regions fully encircled by mFC, and arrows emphasize long cracks entering E-mFC. Magnified views of SHG images highlighting the specificities of (e) periosteal and (f) enthesis locations. The yellow dashed line represents the interface between mFC and bone, detected by superimposing SHG and qBEI images.

heterogeneous SHG signal with fibers appearing interwoven and following a tortuous path around the many pores present there, somewhat resembling tree roots. At the interface between mFC and bone (highlighted by the dashed yellow line in Fig. 5.1e, f), a continuous fiber arrangement is observed at the insertion site (Fig. 5.1f). Conversely, at the periosteal region, fibers of mFC tend to reach the interface at an almost right angle, whereas (some) fibers from the bone side are oriented parallel to the interface and follow the cement line (Fig. 5.1e). Overall, the SHG signal in bone is markedly different from mFC: thick regions of lamellar bone are recognizable, whereas other areas show a more diffuse signal (Fig. S5.3), indicating less ordered endochondral bone.

5.3.2 Quantitative global assessment of mineral content and biomechanical properties

Quantitative global assessment of mineral content, reduced modulus and hardness are introduced here as analysis of frequency distributions, computed within three different regions of interest: E-mFC, P-mFC and subchondral bone (Fig. 5.2, S5.2 and corresponding parameters in Tables S5.1, S5.2). Considering the different spatial resolutions of qBEI and nIND, for a "fair" comparison between mineralization and mechanical properties distributions, histograms of calcium content (Fig. 5.2) were based on average values around indents (distributions from the entire regions can be found in Fig. S5.2). Of high interest is that both E-mFC and P-mFC have mineralization distributions shifted towards lower mineral content with respect to subchondral bone (Fig. 5.2a), reflected in a decrease in Ca_{mean} of 10 % for both mFC. In agreement with a lower mineral content, the frequency distribution of reduced modulus (Fig. 5.2b) and hardness (Fig. 5.2c) are also shifted towards lower values, indicating that E-mFC and P-mFC are less stiff and hard than
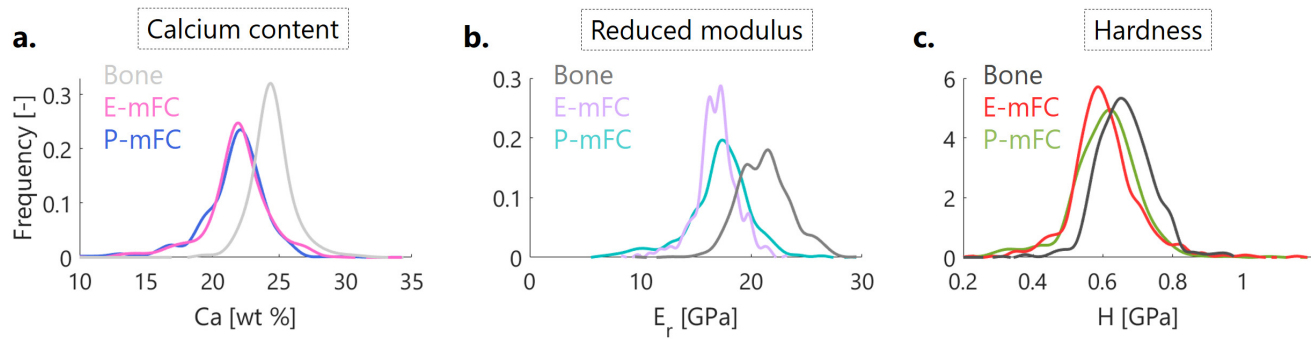
Figure 5.2: Frequency distributions of (a) calcium content, (b) reduced modulus and (c) hardness according to tissue type and location. Data shown as smoothed splines considering all indentation points on sagittal sections.

subchondral bone, with higher differences observed in reduced modulus (decrease in $E_{r, \text{mean}}$ of 20 % and in H_{mean} of 8 % for both types of mFC). While mineralization distributions of E-mFC and P-mFC are very similar, some differences are present in the distributions of the mechanical properties: the frequency distribution of reduced modulus of E-mFC is characterized by a higher and narrower peak with respect to P-mFC.

5.3.3 Relationship between mineral content and mechanical properties

The degree of mineralization is associated with mechanical properties in Fig. 5.3. Despite the increased scatter, calcium content is an important variable in explaining the variations in tissue modulus (Fig. 5.3a) and in hardness (Fig. S5.8c), as confirmed by the two-parameter exponential fit (Table S5.3). In Fig. 5.3b the reduced modulus was binned in the range 14-24 GPa (bin width of 2 GPa), and the corresponding average calcium required to reach each specific elastic modulus was computed. Statistical comparisons of calcium content within each bin reveals that subchondral bone requires a slightly higher mineral content than mFC to reach a specific stiffness level (a similar behavior is observed for hardness, Fig. S5.8d). No difference is present when comparing the two FCs. This is a central finding on the composition-mechanical property relations of the analyzed tissues. Our results can be further interpreted considering a staggered model for mineral packing in an organic matrix as proposed by Jäger and Fratzl [41] (see Appendix), and previously used also to investigate mineralized cartilage [18, 42]. The model provides a functional relationship between tissue elastic modulus and mineral content (expressed as mineral volume fraction), allowing to explore the role of different parameters, such the aspect ratio of mineral crystals (ϱ in Fig. 5.3a). The model indicates that subchondral bone and mFC, although having different mineral content and organic matrix lie on similar contour lines.

5.3.4 Mineralization gradients across the unmineralized-mineralized interface

To characterize the local gradients in mineral content across the unmineralized-mineralized interface, the high resolution of qBEI images (i.e. 0.88 μm pixel size) was exploited. The spatial variation of calcium
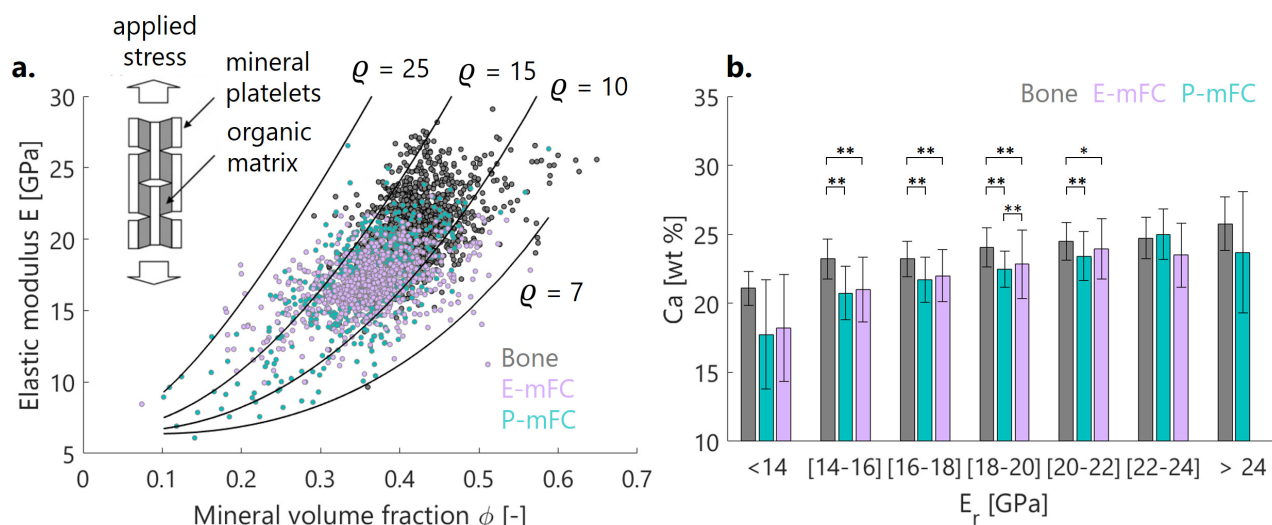
Figure 5.3: (a) Experimental modulus-mineral volume fraction relations (all indents are pooled) and comparison with predictions of a staggered model (contour lines) as a function of the mineral platelets aspect ratio ϱ [18, 41]. The schematic represents the staggered model, where an applied external stress induces shear stresses which are transferred from the gray organic matrix to the white mineral platelets. (b) Averaged calcium content values for mFC and bone providing reduced moduli ranging from 14 to 24 GPa. ** $P < 0.01$, * $P < 0.05$.

content measured along several probed lines perpendicular to the interface was fitted with a sigmoid function (Table S5.4). Based on the fitting function, the transition width was defined as the difference between 0.5 % and 99.5 % height. As illustrated in Fig. 5.4, the interface between unmineralized and mineralized tissues in both FCs exhibits a gradual increase in mineralization, occurring over a 14 μm width transition region. In comparison, when entering bone from resin (avoiding regions of low mineral content, probably indicating active modeling site), a much steeper gradient is found, i.e. transition width of 7 μm. Moreover, the plateau values of the sigmoid away from the interface are very similar in the two FCs (21.3 wt % and 21.4 wt % at enthesis and periosteal regions) and are about 18 % lower than in bone (25.3 wt %).

5.3.5 Spatial analysis of mineral content, fiber organization and mechanical properties

To gain further insight into the structure-function relationship of mFC, compositional (qBEI) and mechanical (nanoindentation) data were plotted as a function of the distance from uFC, spanning the entire thickness of the mFC layer and reaching subchondral bone (Fig. 5.5 and S5.8a, b). Representative indentation lines are presented and interpreted with the help of qBEI and SHG maps of the very same locations (Fig. 5.5a-d). At the insertion (Fig. 5.5a, b), the probed regions typically show a strong and uniform SHG signal: in this case, the reduced modulus follows calcium content very closely and, within E-mFC, a flat profile of both Ca and E_r is observed. Conversely, at P-mFC (Fig. 5.5 c, d) the SHG is highly heterogeneous, highlighting a complex interwoven fiber arrangement. Although mineral content profiles are flat, an unexpected gradual increase in mineral content spanning the entire P-mFC region is detected. By pooling all individual measurements (approximately 3000 indents), despite the rather large scatter, one can still notice a different
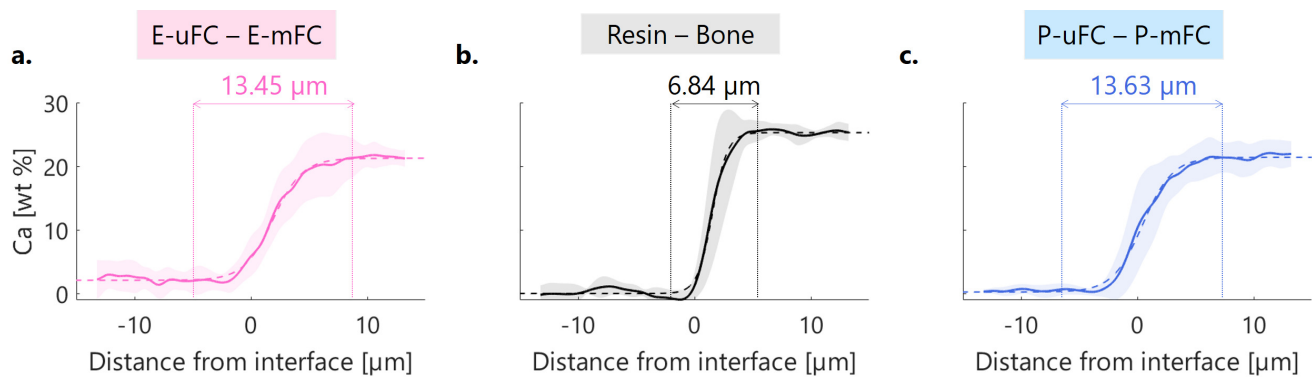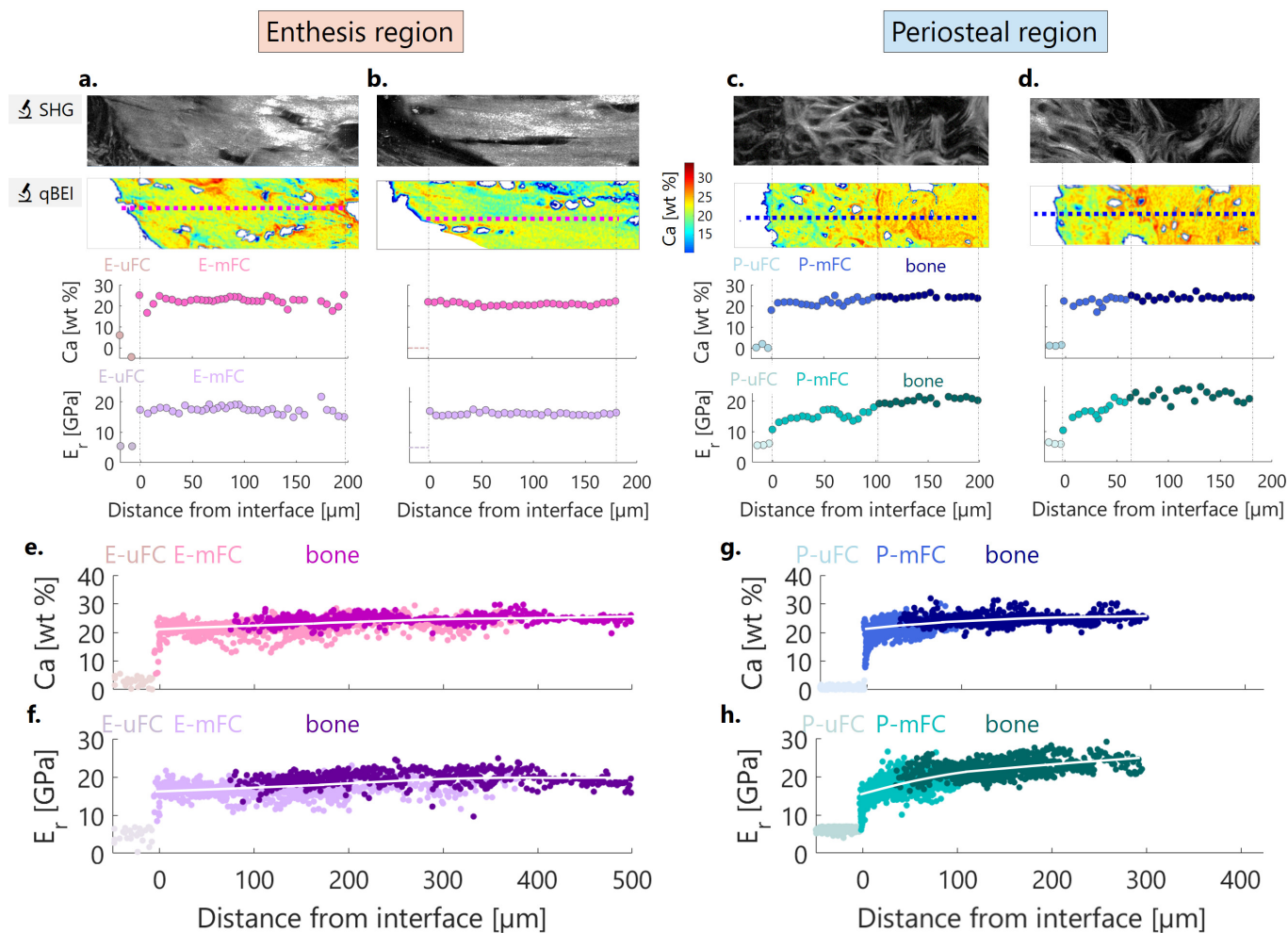
Figure 5.4: Spatial evolution of calcium content when entering mineralized tissues from unmineralized regions. (a) Transition from enthesis unmineralized FC (E-uFC) to enthesis mFC (E-mFC). (b) Transition from resin and bone (no FC is present here). (c) Transition from periosteal unmineralized FC (P-uFC) to periosteal mFC (P-mFC). Data shown as average (thick line) and standard deviation interval (shaded areas) over 10 profile lines per region, with the sigmoid fit (dashed line) and corresponding transition width.

spatial modulation of mechanical properties at enthesis (Fig. 5.5e, f) with respect to periosteal (Fig. 5.5g, h) regions. A qualitative similar trend is observed for hardness (Fig. S5.8a, b). The irregular mFC-bone interface has an impact on these plots, as points from bone and mFC have some overlapping, especially at the enthesis, where long "fingers" of bone enter mFC.

5.3.6 Orthogonal sections and three-dimensional implications of structural anisotropy

Orthogonal sections (perpendicular to the already analyzed sagittal planes) were prepared to investigate material anisotropy. To a first approximation, in sagittal sections, mineralized collagen fibers lie parallel to the analyzed surface meaning that nanoindentation is performed along the transverse axis of the fibers. The opposite is true for orthogonal sections, which expose fibers roughly perpendicular to the analyzed surface, thus being tested along their longitudinal axis. As illustrated in Fig. 5.6, E-mFC has highly heterogeneous and location-specific mineralization patterns, with higher mineral content observed in the central regions anchoring the tendon (visible in the sagittal section) in comparison to the periphery of the attachment (visible in the transverse section). The corresponding frequency distributions of mineral content are reported and quantified in Fig. S5.9. SHG images reveal how a strong signal in the sagittal section, indicating highly aligned fibers, becomes a very weak signal in the adjacent transverse plane, confirming that the fibers are now oriented perpendicular to the imaging section. Several indents (n = 21) placed inside mFC on virtually the same locations but belonging to the two orthogonal planes highlight the anisotropic biomechanical character of mFC at the enthesis: higher modulus (10.7 %, p < 0.01) and hardness (6.3 %, p = 0.04) are measured when indenting in the transverse plane (i.e. more aligned with the mineralized collagen fibers) with respect to the longitudinal plane. Conversely, an opposing trend is detected in the mineral content around the indents between the two planes.

Figure 5.5: Spatial modulation of mineral content, fiber organization and mechanical properties. SHG signal, region-matching qBEI maps and representative line scans of calcium content (Ca) and reduced modulus (Er), measured along the dotted line shown on qBEI maps at (a, b) E-mFC and (c, d) P-mFC. Evolution of Ca and E_r for all measured points as a function of the distance from the interface between uFC and mFC. Locally weighted scatter plot smoothing (LOWESS) lines help to visualize the trends (smoothing factor of 0.8).
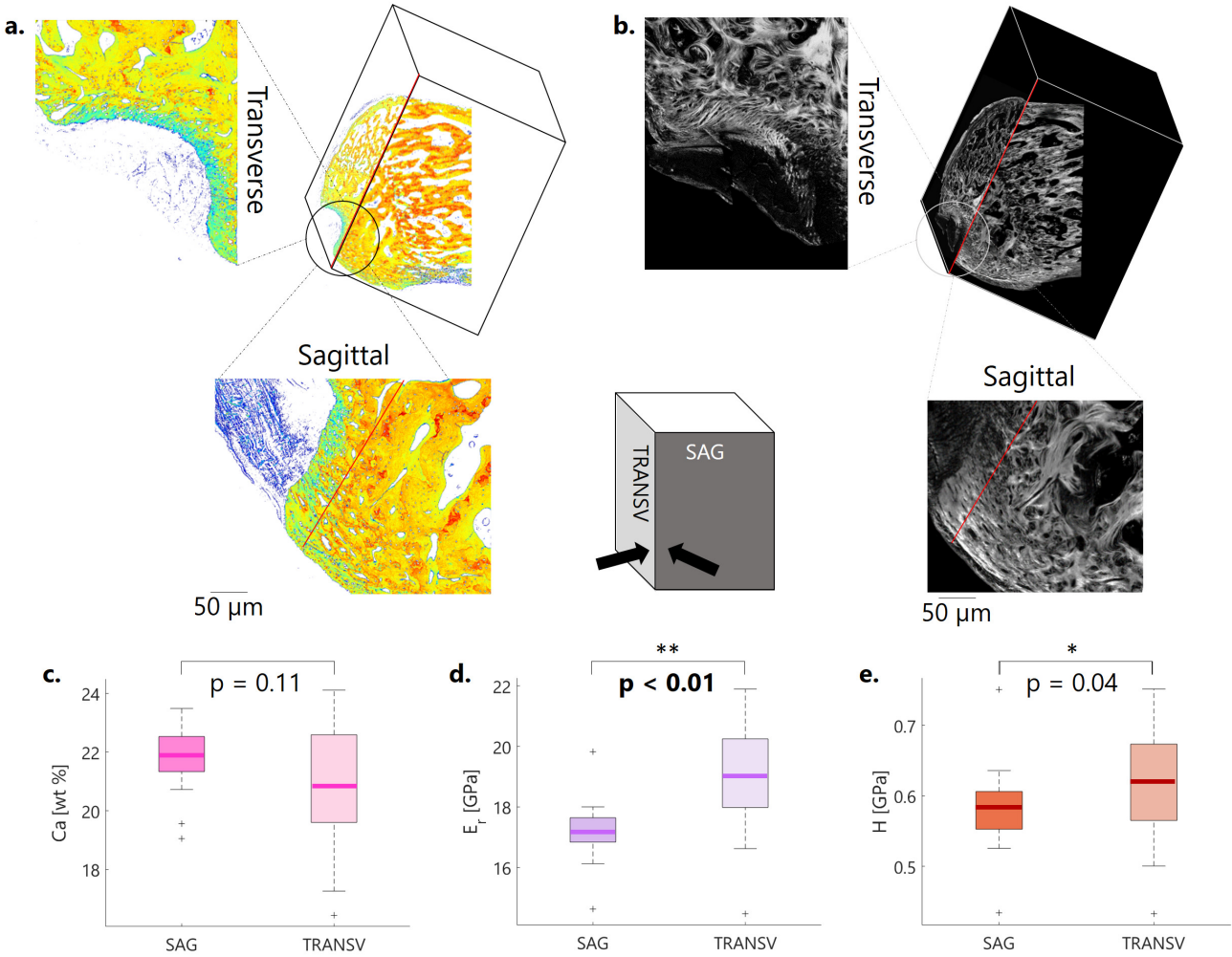
Figure 5.6: Mineralization, fiber organization and material properties measured on E-mFC considering two mutually orthogonal planes. Sagittal and transverse (a) qBEI maps and (b) SHG images. Box plots showing (c) calcium content, (d) reduced modulus and (e) hardness for a set of indentation points (n = 21) selected on adjacent locations within E-mFC on both planes. Boxes range from the 25th to the 75th percentiles. Points positioned more than one interquartile length away from the boxes were considered outliers and plotted individually (+). Whiskers extend till to the most extreme data point which is not an outlier. Thick lines represent the mean value. ** P < 0.01, * P < 0.05.

5.4 Discussion

Combining multiple high-resolution techniques at the same locations, we investigated two types of mFC that are contiguous but fulfill different tasks and the underlying subchondral bone. We explored whether differences in mechanical loading and microstructural porosity [25] are also reflected at the material level. We found that mFC is globally less mineralized and, consequently, less stiff and hard than subchondral bone. Despite these differences, mFC uses mineral reinforcements in a very efficient manner: it needs a smaller fraction of calcium than subchondral bone to reach the same local tissue stiffness and hardness. We uncovered differences between E- and P-mFC in fiber arrangements and spatial modulation of mechanical properties: while a similar compositional gradient is present at the interface between uFC and mFC at both locations, we found that local mechanical properties are fairly uniform inside enthesis FC (which shows highly aligned fibers) while an additional stiffness gradient, independent from mineral content, is observed in periosteal FC (where fiber organization is very heterogeneous).

Considering mineral content, a similar trend (i.e. mFC less mineralized than bone) was reported at the tendon insertions of the greater trochanter in 6–8-month-old rats [40]. At the same location, larger animals (sheep, 3–5 years old) and humans (59–64 years old) seem to have an opposite behavior [40]. Moving to calcified articular cartilage, a higher mineralization level than in bone was measured at human patellae [18] and femoral heads [43]. Conversely, at femoral heads of smaller animals (i.e., 6-month-old rabbit) no significant difference was found [19]. In mineralized tissues, the measured degree of mineralization depends on several factors including the extracellular matrix [3, 18], the presence of nanochannels [44], the mineralization kinetic (i.e. the speed of increase in mineral content) [45, 46], the turnover rate (i.e. the remodeling speed of the tissue) [47] and the modality of ion/precursor transport to the mineralizing sites [48–50]. An explanation of the higher calcium content of calcified cartilage may be the larger extrafibrillar space occupied by water in unmineralized cartilage, which is then replaced by minerals in calcified cartilage [51]. However, this does not clarify our findings. Unlike larger mammals, small animals have a relatively long skeletal maturation: growth in rats is often not completed before 35 weeks of age [52]. At the end of postnatal development, the enthesis is considered matured tissue [53]. Yet, during growth, portions of the tendon are replaced by unmineralized cartilage, the latter getting mineralized (as evident from the former tidemarks, Fig. S5.6b) and older calcified cartilage is (at least partially) remodeled into subchondral bone [54]. This may explain the lower degree of mineralization of cartilage found in growing rodents.

When compared to bone, mFC is on average more compliant and less hard, in agreement with a lower mineral content (Fig. 5.2). Analyzing Ca-Er relationship (Fig. 5.3) allowed two main conclusions. First, using a staggered model for mineral packing in an organic matrix [41] provided a good fit to the mineralization-modulus relation, with both FCs and subchondral bone lying on similar contour lines. This indicates that the aspect ratio of mineral platelets is comparable in both tissues. Second, subchondral bone shows a higher mineral content than mFC to reach a specific stiffness level. This is in contrast with previous results on hu-

man (articular) calcified cartilage by Gupta and colleagues [18]. The authors considered the organic matrix (type II collagen in cartilage and type I in bone) as a possible reason for different mechanical properties, perhaps due to changes in the mineral-collagen packing. Recently, more evidence is supporting the active role of the collagen matrix in introducing pre-stresses in mineralized tissue. Such pre-stresses depend on specifics of the collagen matrix and crucially influence the mechanical tissue properties [55, 56]. Mineral collagen packing in FC may be different than in articular cartilage owing to a different mixture of collagen type II and III [8, 9].

Fiber architecture is a key player for the mechanical efficiency of enthesis. Previous studies have focused on fiber arrangement, particularly when approaching the enthesis from the soft-tissue side [6, 9, 16, 57–60]. Although collagen fibers run continuously across the transition zone between tendon/ligament and FC, they feature several microstructural modifications coinciding with a compositional switch from pure collagen type I to a combination of collagen type II and III. Data from Achilles tendon insertions indicate that tendon fibers branch into much thinner interface fibers, spread out and enter FC [9, 58]. Within FC, fibers seem to be less aligned than in tendons [61] and ligaments [62]. Characterizations of fiber deformation (considering Achilles tendon and rotator cuff insertions) suggest that different groups of fibers are loaded depending on the angle of remote force application [9, 16, 63], allowing the enthesis to resist substantial and continuous changes regarding the direction of tendon force.

Here, we complemented current knowledge by following fibers inside mFC and subchondral bone, considering two mutually orthogonal planes. A central finding for the interpretation of our result is a very strong SHG signal within enthesis FC (Fig. 5.1 and S5.7), likely indicating a high alignment of mineralized collagen fibers. Investigation of the transverse direction confirms fiber anisotropy, with a weak SHG as expected when fibers are perpendicular to the imaging plane (Fig. 5.6). Fiber arrangement has a pivotal impact on the local mechanical behavior. At E-mFC where fibers are highly aligned, spatial variations of tissue modulus (and hardness) mirrored very closely the behavior of calcium content: except for a steep gradient across the interface between unmineralized and mineralized tissues, mineral content, elastic modulus and hardness had a remarkably constant profile (Fig. 5.5). At odds with this behavior is the overall increase of elastic modulus inside P-mFC, not accompanied by variations in mineral content (Fig. 5.5). Fiber architecture is probably responsible for this discrepancy: P-mFC has fibers spreading out, branching, intertwining and showing curved paths going around pores (Fig. 5.1). Despite these dissimilarities, the two FCs have a comparable behavior across the transition between unmineralized and mineralized tissues.

Using high-resolution (sub-micrometer) qBEI, we observed a steep gradient in mineral content occurring within less than 14 μm (Fig. 5.4), with no differences between enthesis and periosteal regions. Localized compositional gradients are well-known features of enthesis. Depending on anatomical location and measuring techniques, the width of the unmineralized-to-mineralized transition zone ranges from about 10 to 100 μm [10, 12, 53, 64–67]. Experimental and computational works have linked compositional to mechani-

cal gradients [68–71]. Although restricted to an extremely small region, the mechanical modulations should help solve stress and strain incompatibilities between soft and hard tissues [11, 72], enhancing failure resistance at the insertion site [16, 66]. Assuming that the interfacial material gradient is devoted to reducing stress concentration, the question arises if the different structure-property relationship observed in the two mFC reflect different functional requirements. Using a simple 2D model of staggered mineral crystals glued together by an elastoplastic protein matrix (details in Appendix), the "tunability" in stiffness, strength and energy absorption as a function of mineral volume fraction can be estimated (Fig. A5.1). Increasing mineralization of collagen fibers enhances stiffness and strength but decreases energy absorption. Overall, our finding suggests that E-mFC needs to be strong along the prevalent pulling direction of the tendon. To a first approximation, a strong material should have highly aligned fibers and should not include components with low mineral content (and low strength) as they may dominate the overall failure strength (assuming a serial arrangement with the applied load [73]). Such high strength may, however, come at the expenses of toughness. Although we did not perform a fracture study, long parallel cracks likely resulting from sample preparation, were mainly observed inside E-mFC rather than in P-mFC (Fig. 5.1c), further suggesting that the high anisotropy is probably aiming at enhancing tensile strength rather than toughness. P-mFC is a way more heterogeneous material, showing an intricate fiber organization and a gradual increase in tissue modulus. While material heterogeneity may favor damage resistance [74], the elastic modulus gradient should allow to resist compressive loading of the tendon (pressing against the bone during joint rotation) in a progressive manner, to avoid potentially high stresses which may harm both tissues.

Concerning limitations, it should be noted that tissues were tested dehydrated, although we are aware that hydration has a large impact on the local mechanical properties [75, 76]. Indenting dehydrated bones typically lead to an overestimation of reduced modulus and hardness [18]. However, to perform a correlative analysis, we had to follow preparation protocols enabling different techniques on the same samples. Being mainly interested in relative differences between mineralized tissues and locations, we would expect dehydration to have a comparable impact on those tissues. Our mechanical analysis was restricted to reduced modulus and hardness. Possible ways to explore post-yield behavior could rely on nanoindentation stress-strain curves [77], micropillar compression [78], or a combination of nanoindentation with finite element modeling [78, 79]. The required lateral spacing between indents imposes a constraint on the spatial resolution of nanoindentation, which is much lower than the sub-micrometer resolution of qBEI and SHG. While we could characterize very well the spatial increase in mineral content occurring across the unmineralized-mineralized interface, we could not measure the corresponding mechanical gradients in such detail. As the spatial modulation of calcium content was similar when entering mFC in the two locations (Fig. 5.4), we do not consider this as a critical limitation. In principle, a substantial increase in the lateral resolution of the mechanical characterization could be obtained using modulus mapping [80] or with contact resonance force microscopy [19].

Considering SHG, we did not attempt a quantification of the SHG signal as this would require additional

assumptions on fiber packing and phase matching [33]. In view of the striking differences of fiber arrangement between enthesis and periosteal regions, we judged that a qualitative analysis of SHG images was sufficient for our investigation.

Finally, our research strategy was to perform extensive characterization of a limited number of samples, rather than testing more samples to a lesser extent. Limiting the number of animals (compatible with the study aims) is also in line with the global effort to reduce animal usage in experimental research. The present multimodal approach can be used to investigate medically relevant scenarios, considering for example the impact on mFC of over or unloading [81], inflammation mimicking enthesopathies, or ageing. These studies would need a larger number of samples.

5.5   Conclusions

The combination of nanoindentation, qBEI and SHG imaging provided powerful insights into the structure and functioning of FC. We highlighted that E-mFC and P-mFC are mechanically efficient tissues attaining their stiffness and hardness by using less mineral than bone would require. The two FCs had different fibers organization and spatial modulation of mechanical properties. Spatially constant tissue modulus and hardness, combined with highly aligned collagen fibers were observed at enthesis FC, mirroring the previously detected microstructural anisotropy [25]. We hypothesize that such construction strategy enhances strength at the tendon insertion. Our work demonstrates the adaptability, versatility and efficiency of FC in helping bone to cope with challenging mechanical tasks.

Acknowledgements

Appendix

Assuming a staggered composite model with elastic-brittle mineral crystals glued together by a ductile elasto-plastic protein matrix, the elastic modulus E_C as a function of the mineral volume fraction φ is given by [41]:

$$E_C = \varphi \frac{E_M}{\kappa} + (1 - \varphi)E_p \tag{5.2}$$

$$\kappa = 1 + \frac{1-\varphi}{\varphi}\frac{4}{\varrho^2}\frac{E_M}{G_p} \tag{5.3}$$

With the Young's modulus of hydroxyapatite E_m = 100 GPa, the shear modulus of the organic protein matrix $G_p = \gamma E_p$, where $\gamma \approx 0.4$, and the Young's modulus of the organic protein matrix E_p = 5 GPa. The mineral platelets aspect ratio ϱ was allowed to vary from 10 to 20. To connect calcium content with mineral volume fraction, one can use the following relationships [82]:

$$\varphi = \frac{HA}{HA + (1 - HA)\left(\frac{\rho_{HA}}{\rho_{org}}\right)} \tag{5.4}$$

$$HA = 2.5066\, Ca_{mean} \tag{5.5}$$

With hydroxyapatite density $\rho_{HA} = 3.18$ g cm^{-3} and organic matrix density $\rho_{org} = 1.47$ g cm^{-3}.

The model further assumes that beyond a critical shear stress τ_p^* the matrix flows plastically. In in the staggered arrangement the stress on the mineral particles σ_m and the shear stress inside the protein matrix τ_p are linked by:

$$\tau_p = \frac{2}{\varrho}\sigma_m \tag{5.6}$$

Therefore, if τ_p^* is smaller than the fracture stress of the brittle mineral σ_m^f (according to Eq. 5.6), the matrix will flow before the mineral crystals can break. Here, we assumed σ_m^f = 100 MPa and $\tau_{p}^{*} = G_p\, \eta_p^\gamma$ with η_p^γ =0.8 % being the critical yield shear strain at which the protein matrix starts plastic flow (likely due to breaking of ionic bonds [82]). Strength is measured as the maximum stress reached by the staggered protein-mineral composite at the end of the elastic region right before plastic flow, according to:

$$\sigma_C^{max} = E_C\,\varepsilon_C = E_C\,\varepsilon_m = E_C\,\frac{\kappa\rho}{E_m}\tau_p^* \tag{5.7}$$

Toughness is estimated at the area under the overall stress-strain curve of the composite. Once the matrix starts to flow, the stress in the staggered composite does not increase but the strain does, till the matrix reaches its fracture shear strain η_p^f = 8 %. The maximum strain on the composite at the end of the plastic flow of the protein matrix is given by:

$$\varepsilon_C^{max} = \varepsilon_m + \frac{2}{\varrho}\frac{1-\varphi}{\varphi}\eta_p^f = \frac{\kappa\rho}{2E_m}\tau_p^* + \frac{2}{\varrho}\frac{1-\varphi}{\varphi}\eta_p^f \tag{5.8}$$
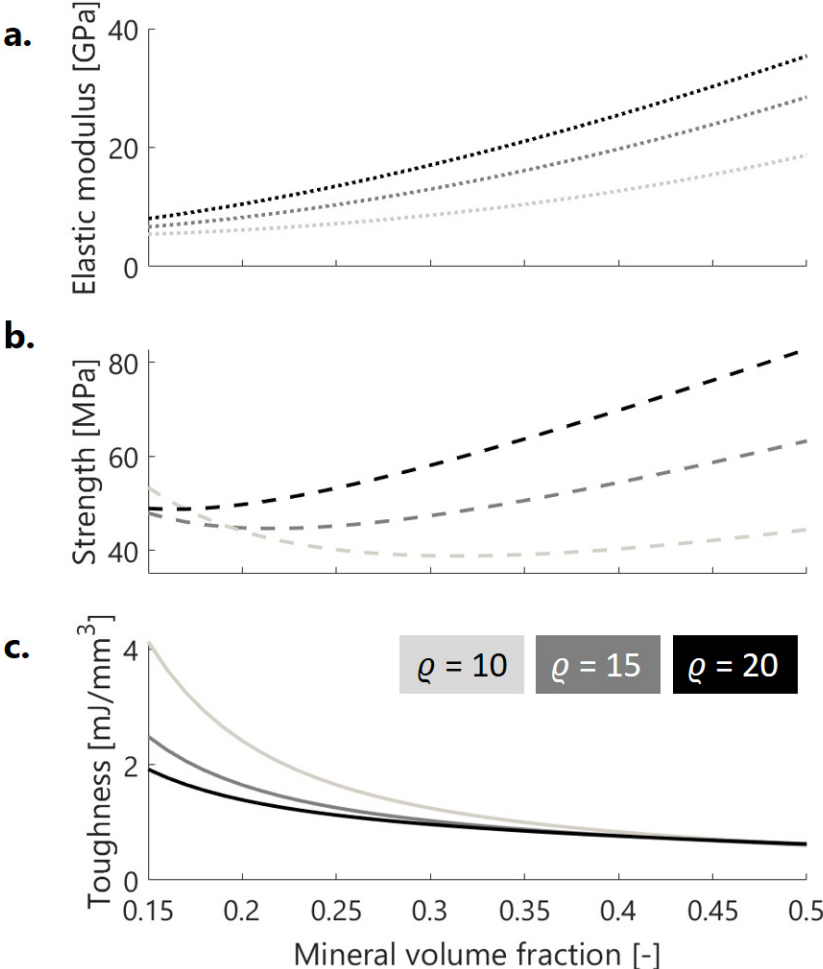
Figure A5.1: Modulation of (a) elastic modulus, (b) strength and (c) toughness as a function of the mineral volume fraction and for several mineral aspect ratios ϱ, as estimated by a staggered composite model.

# 5.6 Supplementary material (Figures and Tables)
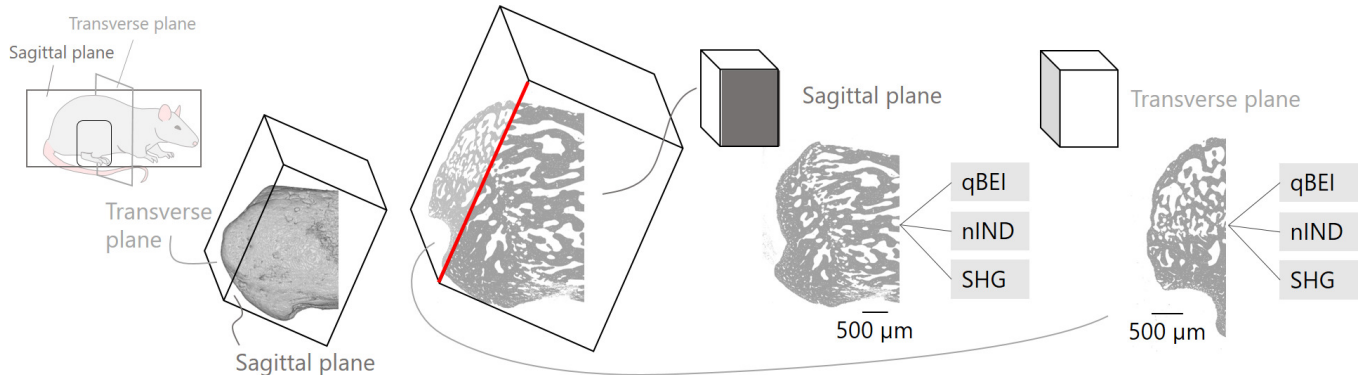
Figure S5.1: Schematic of the sagittal and transverse planes on a representative sample, and corresponding investigation techniques: qBEI (quantitative backscattered electron imaging), nIND (nanoindentation), SHG (second harmonic generation).
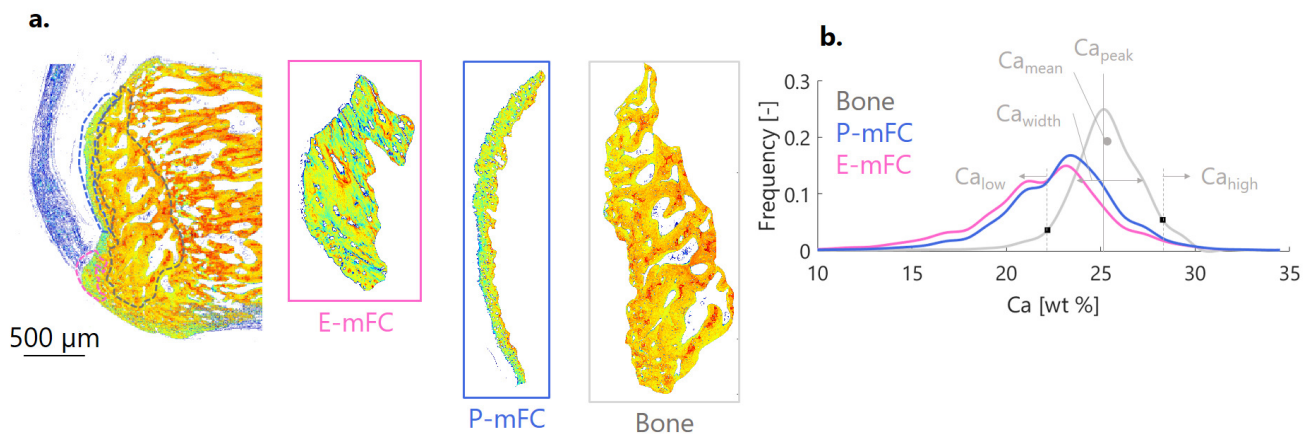
Figure S5.2: (a) qBEI maps and regions of interest used to measure the mineral content of the entire enthesis mineralized fibrocartilage (E-mFC), periosteal mFC (P-mFC) and subchondral bone regions, on a representative sample. (b) Frequency distributions of calcium content.
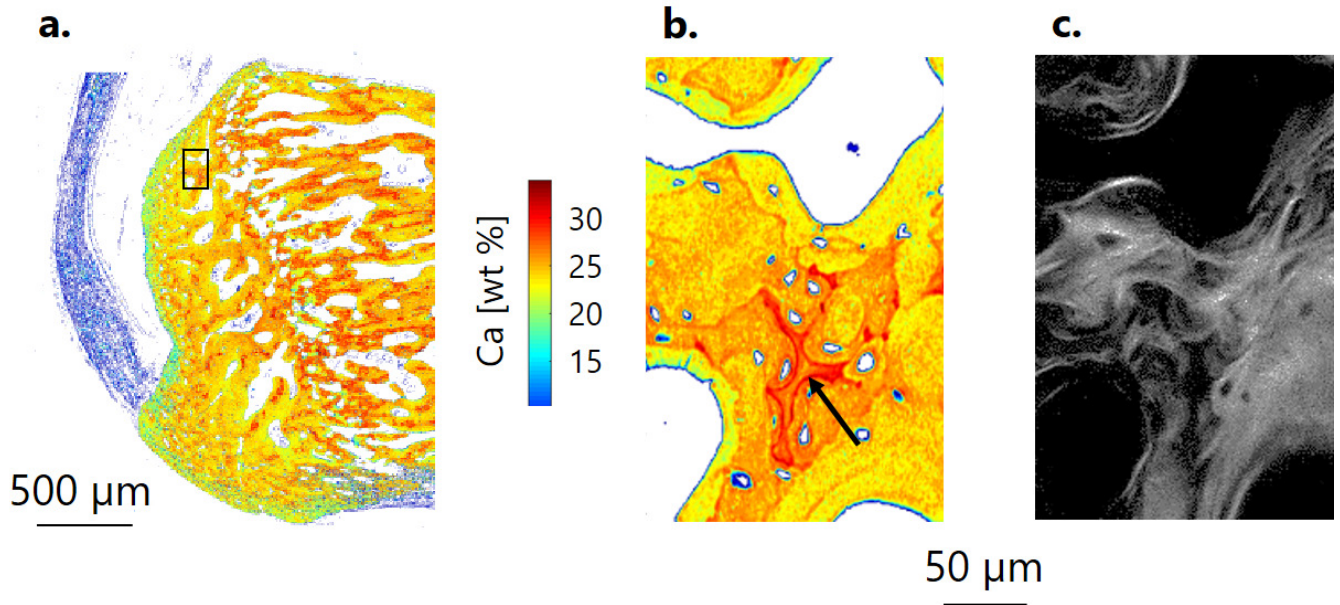
Figure S5.3: Illustration of a cartilaginous inclusion in bone probably formed during endochondral ossification and not removed by remodeling [1, 2]. The high mineral content is clearly visible in qBEI as indicated with a black arrow (a) and it is reflected into a blurry SHG signal (b), likely indicating less ordered endochondral bone.
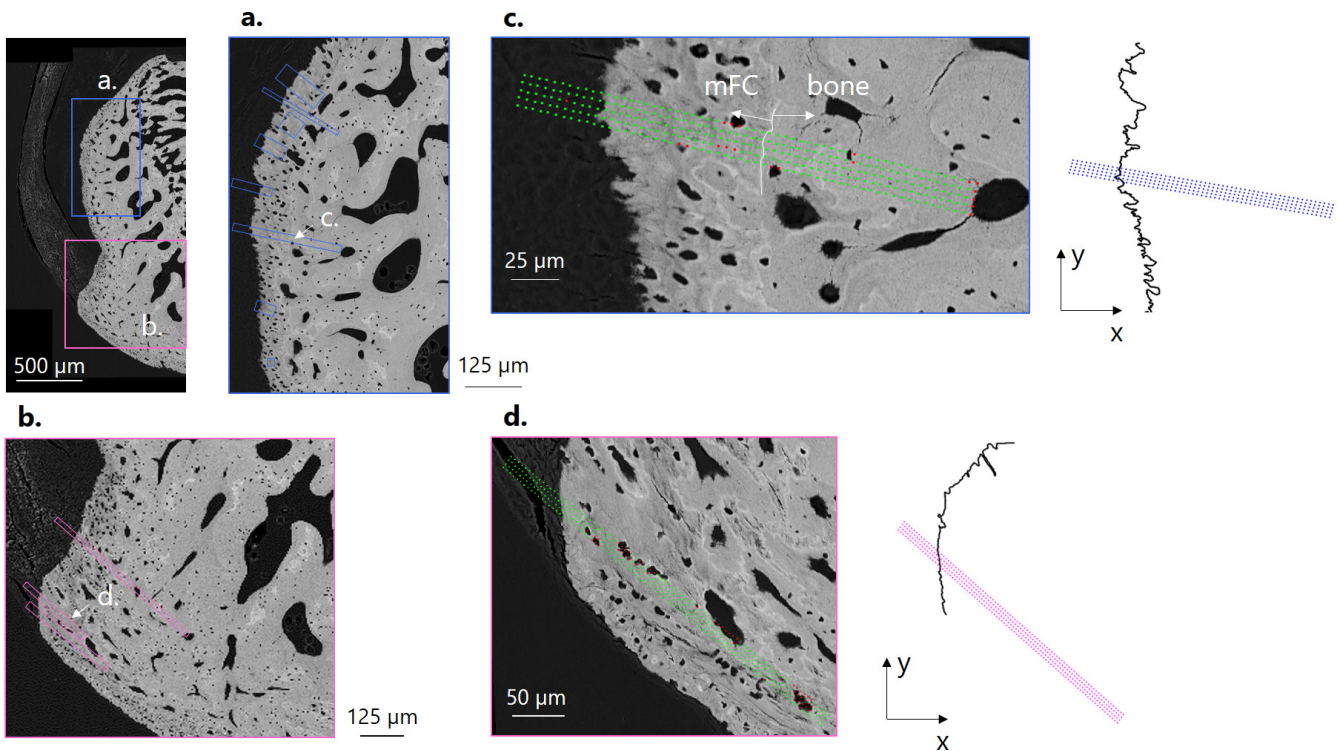

Figure S5.4: Overview of several nanoindentation grids on a representative sample at the periosteal (a) and enthesis (b) region. Close-up on typical scanning grids at the periosteal (c) and enthesis (d) region, showing the rejected indents in red and the accepted ones in green, as well as the resulting contour extraction of the interface between unmineralized fibrocartilage (uFC) and mFC for distance-to-surface measurement.
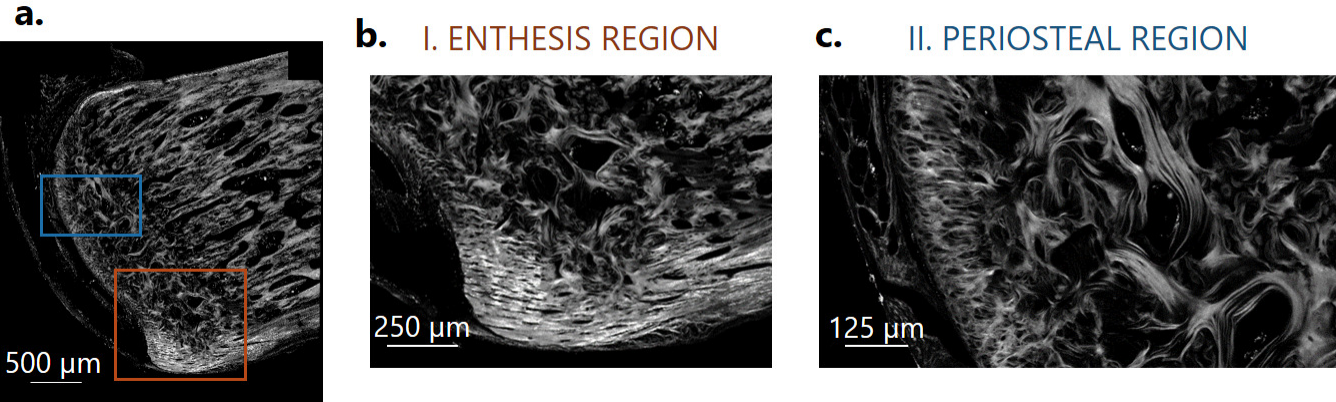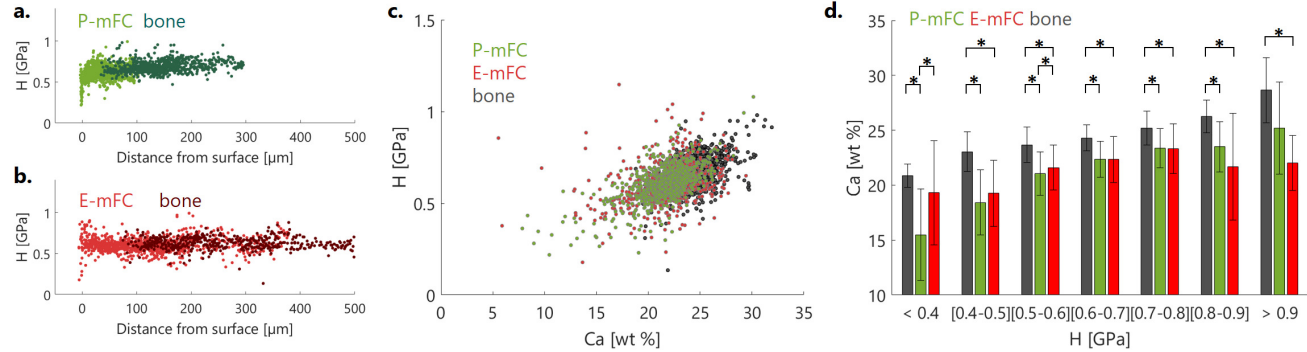
I. ENTHESIS REGION   II. PERIOSTEAL REGION
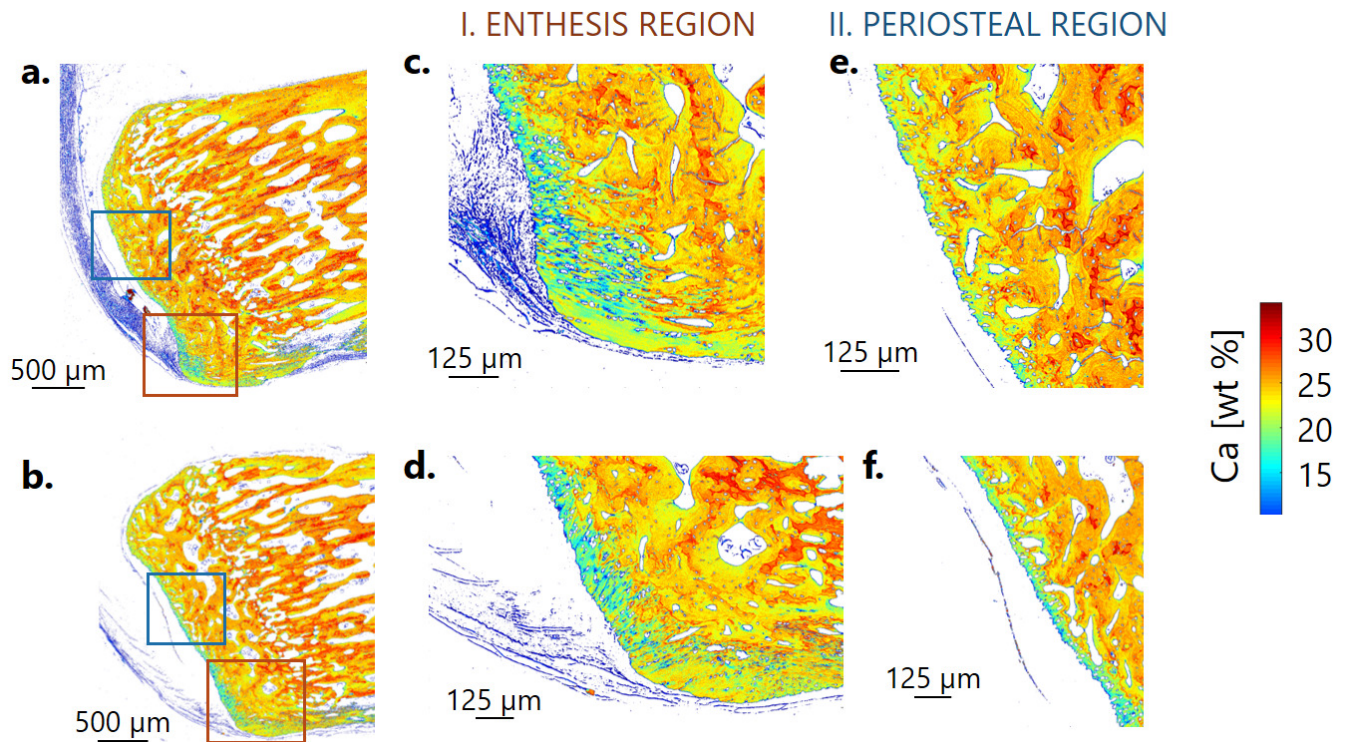
Figure S5.5: Full qBEI overviews (a and b) and close-up on the regions of interest including enthesis and periosteal locations for the measured samples not shown in the main manuscript. As in one sample (bottom row) the tuberosity could not be clearly spotted and, consequently, both mFC layers were very thin, the sample was not considered for further quantitative analysis.
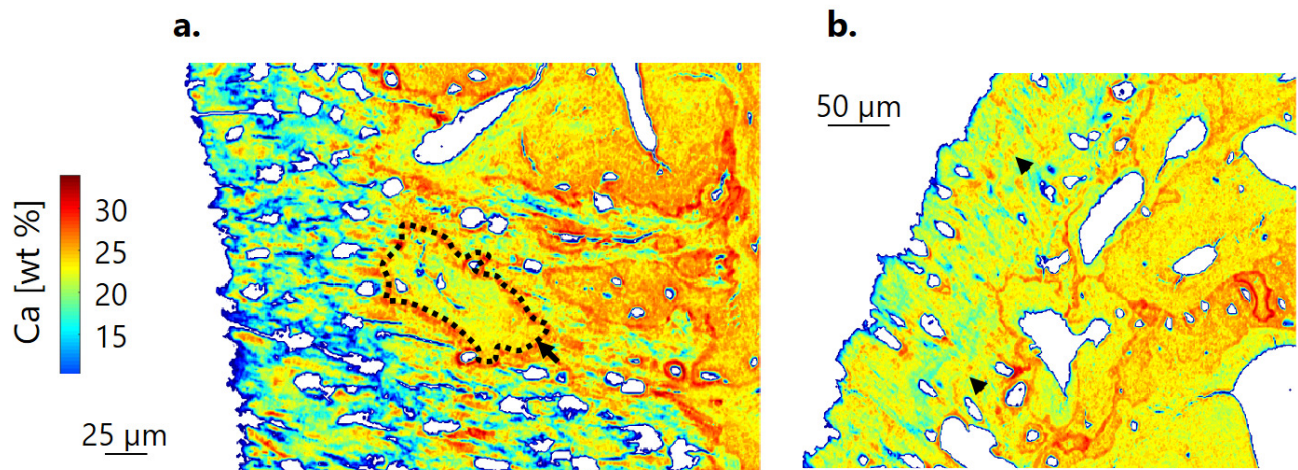

Figure S5.6: Characteristic features on qBEI images. (a) Bone island (contoured in black, and indicated by the black arrow) within periosteal FC. (b) Former tidemarks (black arrows) within periosteal FC.

Figure S5.7: Full SHG overview (a), and inset into the (b) enthesis and (c) periosteal areas, for the second sample not shown in the main manuscript.

Figure S5.8: (a, b) Spatial evolution of hardness (H) at (a) periosteal and (b) enthesis region. (c) Hardness as a function of local calcium weight percentage in mFC and bone at periosteal and enthesis region. (d) Averaged calcium content values for mineralized cartilage and bone needed to obtain hardness ranging from 0.4 to 0.9 GPa (bin width 0.1 GPa) * $P < 0.05$.
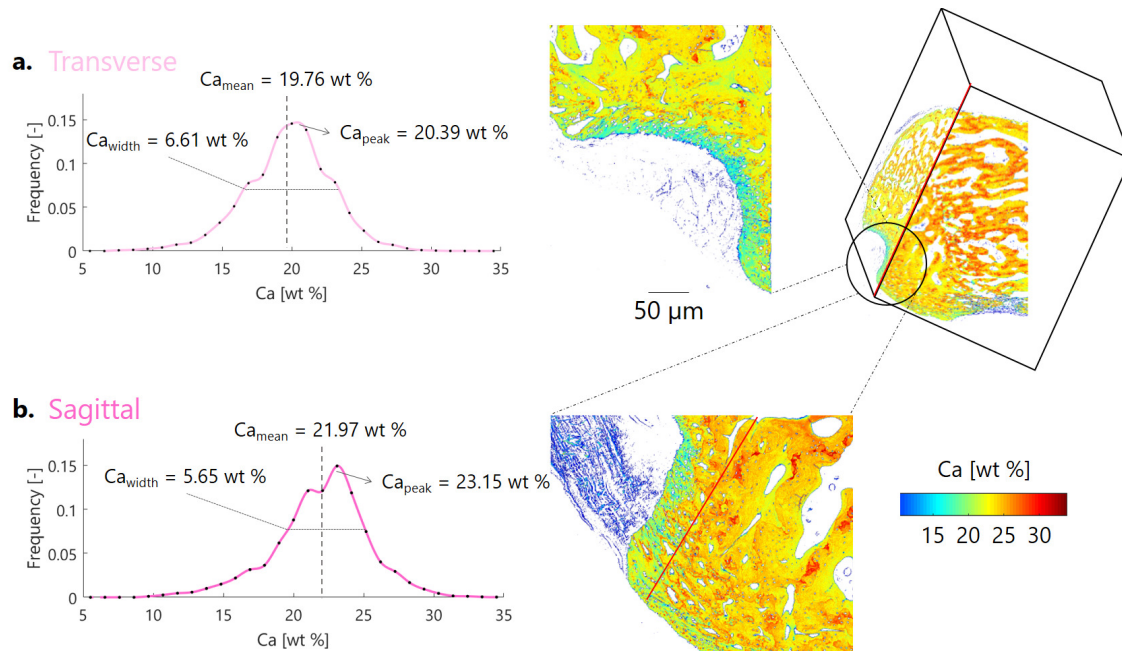
Figure S5.9: Frequency distributions of calcium content for transverse (a) and sagittal (b) enthesis mFC measured based on the entire tissue region, and represented using a smoothing spline.

Parameter	Bone (Region I)	Δ(I-II)	Periosteal mFC (Region II)	Δ(II-III)	Insertional mFC (Region III)	Δ(I-III)
Mineralization properties (based on pixels around the indent location)						
Ca_{mean} [% wt]	24.49	-9.76 %	22.11	-1.18 %	21.85	-10.78 %
Ca_{peak} [% wt]	24.36	-11.41 %	21.58	+1.53 %	21.91	-10.06 %
Ca_{width} [% wt]	24.36	+28.46 %	3.25	-5.23 %	3.08	21.74 %
Ca_{low} [%]	5	+941 %	52.05	-1.67 %	51.18	+923.6 %
Ca_{high} [%]	5	-90.6 %	0.47	+163.8 %	1.24	-75.2 %
Mechanical properties						
$E_{r, mean}$ [GPa]	21.16	-18.9 %	17.15	-1.52 %	16.89	-20.18 %
$E_{r, peak}$ [GPa]	21.49	-18.9 %	17.42	-1.03 %	17.24	-19.78 %
$E_{r, width}$ [GPa]	5.22	-26.4 %	3.84	-31.51 %	2.63	-49.62 %
$E_{r, low}$ [%]	5	+949 %	52.45	+25.2 %	65.66	+1213%
$E_{r, high}$ [%]	5	-94 %	0.29	-100 %	0	-100 %
Hardness properties						
H_{mean} [GPa]	0.66	-7.6 %	0.61	=	0.61	-7.6 %
H_{peak} [GPa]	0.65	-4.6 %	0.62	-4.8 %	0.59	-9.2 %
H_{width} [GPa]	0.18	=	0.18	-22.2 %	0.14	-22.2 %
H_{low} [%]	5	+356.6 %	22.83	+3 %	23.52	+370.4 %
H_{high} [%]	5	-56 %	2.2	+71.8 %	3.78	-24.4 %

Table S5.1: Global properties of bone compared with the two mFC types (periosteal and insertional).

Parameter	Bone (Region I)	Δ(I-II)	Periosteal mFC (Region II)	Δ(II-III)	Insertional mFC (Region III)	Δ(I-III)
Ca_{mean} [% wt]	25.26	-9.2 %	22.94	-4.2 %	21.97	-13 %
Ca_{peak} [% wt]	25.15	-6.9 %	23.41	-1.1 %	23.15	-7.9 %
Ca_{width} [% wt]	3.68	+44.3 %	5.31	+6.4 %	5.65	+53.5 %
Ca_{low} [%]	5	+622.4 %	36.12	+35.5 %	48.93	+878.6 %
Ca_{high} [%]	5	-42.8 %	2.86	-11.5 %	2.53	-49.4 %

Table S5.2: Mineralization properties of bone compared with the periosteal and insertional mFC type (based on entire tissue region).

Parameter	Ca-E_r in E-mFC	Ca-H in E-mFC	Ca-E_r in P-mFC	Ca-H in P-mFC	Ca-E_r in bone	Ca-H in bone
a [% wt]	10.68	0.38	6.93	0.25	11	0.28
t-value for a [—]	32.94	20.66	22.36	21.53	21.62	21.07
b [GPa^{-1}]	0.02	0.02	0.04	0.04	0.03	0.03
t-value for b [—]	15.3	9.8	22.56	19.84	14.17	18.22

Table S5.3: Parameters of the exponential function fitting the relationship between calcium content and mechanical properties (Ca = a * e$^{(b\,E_r)}$ or Ca = a * e$^{(b\,H)}$) and corresponding t-values.

Parameter	E-uFC — E-mFC	Resin — Bone	P-uFC — P-mFC
α [% wt]	19.15	25.26	21.15
β [μm^{-1}]	0.792	1.55	0.78
$dist_0$ [μm]	1.912	1.54	0.45
Ca_0 [% wt]	2.11	0.03	0.26
TW [μm]	13.45	6.84	13.63

Table S5.4: Parameters of the sigmoid function fitting the non-mineralized to mineralized tissue transition Ca (dist) $= Ca_0 + \frac{\alpha}{1+e^{-\beta(\text{dist-dist}_0)}}$ and TW = dist(Ca = 0.995 * α + Ca_0) - dist(Ca = 0.005 * α + Ca_0).

Bibliography

[1] VC Mow, WY Gu, and FH Chen. "Structure and function of articular cartilage". In: *Basic orthopedic biomechanics and mechano-biology* 3 (2005), pp. 181–258.

[2] Lin Han, Alan J Grodzinsky, and Christine Ortiz. "Nanomechanics of the cartilage extracellular matrix". In: *Annual review of materials research* 41 (2011), pp. 133–168.

[3] I Zizak et al. "Characteristics of mineral particles in the human bone/cartilage interface". In: *Journal of structural biology* 141.3 (2003), pp. 208–217.

[4] M Benjamin and JR Ralphs. "Fibrocartilage in tendons and ligaments—an adaptation to compressive load". In: *The Journal of Anatomy* 193.4 (1998), pp. 481–494.

[5] Adam C Abraham and Tammy L Haut Donahue. "From meniscus to bone: a quantitative evaluation of structure and function of the human meniscal attachments". In: *Acta biomaterialia* 9.5 (2013), pp. 6322–6329.

[6] Alexander J Boys et al. "Understanding the stiff-to-compliant transition of the meniscal attachments by spatial correlation of composition, structure, and mechanics". In: *ACS applied materials & interfaces* 11.30 (2019), pp. 26559–26570.

[7] KN Hauch et al. "Nanoindentation of the insertional zones of human meniscal attachments into underlying bone". In: *Journal of the mechanical behavior of biomedical materials* 2.4 (2009), pp. 339–347.

[8] Andrew D Waggett et al. "Characterization of collagens and proteoglycans at the insertion of the human Achilles tendon". In: *Matrix Biology* 16.8 (1998), pp. 457–470.

[9] L Rossetti et al. "The microstructure and micromechanics of the tendon–bone insertion". In: *Nature materials* 16.6 (2017), pp. 664–670.

[10] Jeffrey P Spalazzi et al. "Quantitative mapping of matrix content and distribution across the ligament-to-bone insertion". In: *PLoS One* 8.9 (2013), e74349.

[11] Avihai Yosef Uzan et al. "Principles of elastic bridging in biological materials". In: *Acta Biomaterialia* 153 (2022), pp. 320–330.

[12] Alexandra Tits and Davide Ruffoni. "Joining soft tissues to bone: Insights from modeling and simulations". In: *Bone Reports* 14 (2021), p. 100742.

[13] Helen H Lu and Stavros Thomopoulos. "Functional attachment of soft tissues to bone: development, healing, and tissue engineering". In: *Annual review of biomedical engineering* 15 (2013), p. 201.

[14] S Thomopoulos, GR Williams, and LJ Soslowsky. "Tendon to bone healing: differences in biomechanical, structural, and compositional properties due to a range of activity levels". In: *Journal of biomechanical engineering* 125.1 (2003), pp. 106–113.

[15] Stavros Thomopoulos et al. "Variation of biomechanical, structural, and compositional properties along the tendon to bone insertion site". In: *Journal of orthopaedic research* 21.3 (2003), pp. 413–419.

[16] Mikhail Golman et al. "Toughening mechanisms for the attachment of architectured materials: The mechanics of the tendon enthesis". In: *Science advances* 7.48 (2021), eabi5584.

[17] Claire Camy et al. "Effects of hindlimb unloading and subsequent reloading on the structure and mechanical properties of Achilles tendon-to-bone attachment". In: *FASEB Journal* 36.10 (2022).

[18] HS Gupta et al. "Two different correlations between nanoindentation modulus and mineral content in the bone–cartilage interface". In: *Journal of structural biology* 149.2 (2005), pp. 138–148.

[19] Sara E Campbell, Virginia L Ferguson, and Donna C Hurley. "Nanomechanical mapping of the osteochondral interface with contact resonance force microscopy and nanoindentation". In: *Acta biomaterialia* 8.12 (2012), pp. 4389–4396.

[20] Kamel Madi et al. "In situ characterization of nanoscale strains in loaded whole joints via synchrotron X-ray tomography". In: *Nature biomedical engineering* 4.3 (2020), pp. 343–354.

[21] Micheal Benjamin and Dennis McGonagle. "The anatomical basis for disease localisation in seronegative spondyloarthropathy at entheses and related sites". In: *The Journal of Anatomy* 199.5 (2001), pp. 503–526.

Bibliography

[22] Amy S Kehl, Maripat Corr, and Michael H Weisman. "Enthesitis: new insights into pathogenesis, diagnostic modalities, and treatment". In: *Arthritis & rheumatology (Hoboken, NJ)* 68.2 (2016), p. 312.

[23] Jean-François Kaux et al. "Effects of platelet-rich plasma (PRP) on the healing of A chilles tendons of rats". In: *Wound Repair and Regeneration* 20.5 (2012), pp. 748–756.

[24] Jean-François Kaux et al. "Eccentric training improves tendon biomechanical properties: a rat model". In: *Journal of Orthopaedic Research* 31.1 (2013), pp. 119–124.

[25] Alexandra Tits et al. "Local anisotropy in mineralized fibrocartilage and subchondral bone beneath the tendon-bone interface". In: *Scientific Reports* 11.1 (2021), pp. 1–17.

[26] P Roschger et al. "Validation of quantitative backscattered electron imaging for the measurement of mineral density distribution in human bone biopsies". In: *Bone* 23.4 (1998), pp. 319–326.

[27] Markus A Hartmann et al. "Quantitative Backscattered Electron Imaging of bone using a thermionic or a field emission electron source". In: *Calcified Tissue International* 109.2 (2021), pp. 190–202.

[28] Paschalis Roschger et al. "Bone mineralization density distribution in health and disease". In: *Bone* 42.3 (2008), pp. 456–466.

[29] A Shipov et al. "Unremodeled endochondral bone is a major architectural component of the cortical bone of the rat (Rattus norvegicus)". In: *Journal of structural biology* 183.2 (2013), pp. 132–140.

[30] Fiona Linnea Bach-Gansmo et al. "Calcified cartilage islands in rat cortical bone". In: *Calcified tissue international* 92.4 (2013), pp. 330–338.

[31] Shmuel Roth and Isaac Freund. "Second harmonic generation in collagen". In: *The Journal of chemical physics* 70.4 (1979), pp. 1637–1643.

[32] Rebecca M Williams, Warren R Zipfel, and Watt W Webb. "Interpreting second-harmonic generation images of collagen I fibrils". In: *Biophysical journal* 88.2 (2005), pp. 1377–1386.

[33] Xiyi Chen et al. "Second harmonic generation microscopy for quantitative analysis of collagen fibrillar structure". In: *Nature protocols* 7.4 (2012), pp. 654–669.

[34] Marie-Andrée Houle et al. "Analysis of forward and backward Second Harmonic Generation images to probe the nanoscale structure of collagen within bone and cartilage". In: *Journal of biophotonics* 8.11-12 (2015), pp. 993–1001.

[35] Tengteng Tang et al. "Shear deformation and fracture of human cortical bone". In: *Bone* 71 (2015), pp. 25–35.

[36] Eve Donnelly et al. "Effects of surface roughness and maximum load on the mechanical properties of cancellous bone measured by nanoindentation". In: *Journal of Biomedical Materials Research Part A: An Official Journal of The Society for Biomaterials, The Japanese Society for Biomaterials, and The Australian Society for Biomaterials and the Korean Society for Biomaterials* 77.2 (2006), pp. 426–435.

[37] MS Bobji and SK Biswas. "Estimation of hardness by nanoindentation of rough surfaces". In: *Journal of Materials Research* 13.11 (1998), pp. 3227–3233.

[38] Warren Carl Oliver and George Mathews Pharr. "An improved technique for determining hardness and elastic modulus using load and displacement sensing indentation experiments". In: *Journal of materials research* 7.6 (1992), pp. 1564–1583.

[39] J Burkey. "LOWESS, Locally Weighted Scatterplot Smoothing for linear and non-linear data (enhanced)". In: *MATLAB Central File Exchange* (July 2020).

[40] Jill E Shea, Rhett K Hallows, and Roy D Bloebaum. "Experimental confirmation of the sheep model for studying the role of calcified fibrocartilage in hip fractures and tendon attachments". In: *The Anatomical Record: An Official Publication of the American Association of Anatomists* 266.3 (2002), pp. 177–183.

[41] Ingomar Jäger and Peter Fratzl. "Mineralized collagen fibrils: a mechanical model with a staggered arrangement of mineral particles". In: *Biophysical journal* 79.4 (2000), pp. 1737–1746.

[42] Ronald Seidel et al. "Mechanical properties of stingray tesserae: high-resolution correlative analysis of mineral density and indentation moduli in tessellated cartilage". In: *Acta Biomaterialia* 96 (2019), pp. 421–435.

[43] Virginia L Ferguson, Andrew J Bushby, and Alan Boyde. "Nanomechanical properties and mineral concentration in articular calcified cartilage and subchondral bone". In: *Journal of Anatomy* 203.2 (2003), pp. 191–202.

[44] Tengteng Tang et al. "Sub-canalicular nanochannel volume is inversely correlated with calcium content in human cortical bone". In: *Journal of Bone and Mineral Research* (2022).

[45] Davide Ruffoni et al. "The bone mineralization density distribution as a fingerprint of the mineralization process". In: *Bone* 40.5 (2007), pp. 1308–1319.

[46] Carolin Lukas et al. "Mineralization kinetics in murine trabecular bone quantified by time-lapsed in vivo micro-computed tomography". In: *Bone* 56.1 (2013), pp. 55–60.

[47]   Davide Ruffoni et al. "Effect of temporal changes in bone turnover on the bone mineralization density distribution: a computer simulation study". In: *Journal of bone and mineral research* 23.12 (2008), pp. 1905–1914.

[48]   Andreas Roschger et al. "The contribution of the pericanalicular matrix to mineral content in human osteonal bone". In: *Bone* 123 (2019), pp. 76–85.

[49]   Andreas Roschger et al. "Newly formed and remodeled human bone exhibits differences in the mineralization process". In: *Acta Biomaterialia* 104 (2020), pp. 221–230.

[50]   Mahdi Ayoubi et al. "3D interrelationship between osteocyte network and forming mineral during human bone remodeling". In: *Advanced healthcare materials* 10.12 (2021), p. 2100113.

[51]   Wenbo Zhu et al. "Determination of collagen-proteoglycan interactions in vitro". In: *Journal of biomechanics* 29.6 (1996), pp. 773–783.

[52]   Takashi Taguchi and Mandi J Lopez. "An overview of de novo bone generation in animal models". In: *Journal of Orthopaedic Research®* 39.1 (2021), pp. 7–21.

[53]   Andrea G Schwartz et al. "Mineral distributions at the developing tendon enthesis". In: *PloS one* 7.11 (2012), e48630.

[54]   MH Badi. "Calcification and ossification of fibrocartilage in the attachment of the patellar ligament in the rat." In: *Journal of Anatomy* 112.Pt 3 (1972), p. 415.

[55]   Hang Ping et al. "Mineralization generates megapascal contractile stresses in collagen fibrils". In: *Science* 376.6589 (2022), pp. 188–192.

[56]   Admir Masic et al. "Osmotic pressure induced tensile forces in tendon collagen". In: *Nature communications* 6.1 (2015), pp. 1–8.

[57]   Johnathan L Sevick et al. "Fibril deformation under load of the rabbit Achilles tendon and medial collateral ligament femoral entheses". In: *Journal of Orthopaedic Research®* 36.9 (2018), pp. 2506–2515.

[58]   Julian Sartori and Heiko Stark. "Tracking tendon fibers to their insertion–a 3D analysis of the Achilles tendon enthesis in mice". In: *Acta Biomaterialia* 120 (2021), pp. 146–155.

[59]   Julian Sartori et al. "Gaining insight into the deformation of achilles tendon entheses in mice". In: *Advanced Engineering Materials* 23.11 (2021), p. 2100085.

[60]   Maria Pierantoni et al. "A quality optimization approach to image Achilles tendon microstructure by phase-contrast enhanced synchrotron micro-tomography". In: *Scientific reports* 11.1 (2021), pp. 1–14.

[61]   Stavros Thomopoulos et al. "Collagen fiber orientation at the tendon to bone insertion and its influence on stress concentrations". In: *Journal of biomechanics* 39.10 (2006), pp. 1842–1851.

[62]   Dovina Qu et al. "Compositional mapping of the mature anterior cruciate ligament-to-bone insertion". In: *Journal of Orthopaedic Research* 35.11 (2017), pp. 2513–2523.

[63]   Lijuan Zhang et al. "A coupled fiber-matrix model demonstrates highly inhomogeneous microstructural interactions in soft tissues under tensile load". In: *Journal of biomechanical engineering* 135.1 (2013), p. 011008.

[64]   Kristen L Moffat et al. "Characterization of the structure–function relationship at the ligament-to-bone interface". In: *Proceedings of the national academy of sciences* 105.23 (2008), pp. 7947–7952.

[65]   Alix C Deymier-Black et al. "Allometry of the tendon enthesis: mechanisms of load transfer between tendon and bone". In: *Journal of biomechanical engineering* 137.11 (2015).

[66]   Alix C Deymier et al. "Micro-mechanical properties of the tendon-to-bone attachment". In: *Acta biomaterialia* 56 (2017), pp. 25–35.

[67]   Alix C Deymier et al. "The multiscale structural and mechanical effects of mouse supraspinatus muscle unloading on the mature enthesis". In: *Acta biomaterialia* 83 (2019), pp. 302–313.

[68]   Guy M Genin et al. "Functional grading of mineral and collagen in the attachment of tendon to bone". In: *Biophysical journal* 97.4 (2009), pp. 976–985.

[69]   A Aghaei et al. "Assessing the effective elastic properties of the tendon-to-bone insertion: a multiscale modeling approach". In: *Biomechanics and Modeling in Mechanobiology* 20.2 (2021), pp. 433–448.

[70]   Lester J Smith et al. "Tunability of collagen matrix mechanical properties via multiple modes of mineralization". In: *Interface focus* 6.1 (2016), p. 20150070.

[71]   Yanxin Liu et al. "Modelling the mechanics of partially mineralized collagen fibrils, fibres and tissue". In: *Journal of The Royal Society Interface* 11.92 (2014), p. 20130835.

[72]   Yanxin Liu et al. "Mechanisms of bimaterial attachment at the interface of tendon to bone". In: *Journal of engineering materials and technology* 133.1 (2011).

[73]   Wolfgang Wagermaier, Klaus Klaushofer, and Peter Fratzl. "Fragility of bone material controlled by internal interfaces". In: *Calcified tissue international* 97.3 (2015), pp. 201–212.

[74] Ashley M Torres et al. "Material heterogeneity in cancellous bone promotes deformation recovery after mechanical failure". In: *Proceedings of the National Academy of Sciences* 113.11 (2016), pp. 2892–2897.

[75] Naiara Rodriguez-Florez, Michelle L Oyen, and Sandra J Shefelbine. "Insight into differences in nanoindentation properties of bone". In: *Journal of the mechanical behavior of biomedical materials* 18 (2013), pp. 90–99.

[76] S Hengsberger, A Kulik, and PH Zysset. "Nanoindentation discriminates the elastic properties of individual human bone lamellae under dry and physiological conditions". In: *Bone* 30.1 (2002), pp. 178–184.

[77] Shahrouz Amini et al. "The role of quasi-plasticity in the extreme contact damage tolerance of the stomatopod dactyl club". In: *Nature materials* 14.9 (2015), pp. 943–950.

[78] Jakob Schwiedrzik et al. "In situ micropillar compression reveals superior strength and ductility but an absence of damage in lamellar bone". In: *Nature materials* 13.7 (2014), pp. 740–747.

[79] Davide Carnelli et al. "Nanoindentation testing and finite element simulations of cortical bone allowing for anisotropic elastic and inelastic mechanical response". In: *Journal of biomechanics* 44.10 (2011), pp. 1852–1858.

[80] Igor Zlotnikov, Emil Zolotoyabko, and Peter Fratzl. "Nano-scale modulus mapping of biological composite materials: Theory and practice". In: *Progress in Materials Science* 87 (2017), pp. 292–320.

[81] Megan L Killian et al. "The role of mechanobiology in tendon healing". In: *Journal of shoulder and elbow surgery* 21.2 (2012), pp. 228–237.

[82] Peter Fratzl and Richard Weinkamer. "Nature's hierarchical materials". In: *Progress in materials Science* 52.8 (2007), pp. 1263–1334.

Chapter 6

Bone-fibrocartilage crosstalk and osteocyte lacuno-canalicular behavior at the tendon-bone insertion

[a] Mechanics of Biological and Bioinspired Materials Laboratory, Department of Aerospace and Mechanical Engineering, University of Liège, Liège, Belgium ; [b] Ludwig Boltzmann Institute of Osteology at Hanusch Hospital of OEGK and AUVA Trauma Centre Meidling, 1st Medical Department Hanusch Hospital, Vienna, Austria ; [c] Department of Biomaterials, Max Planck Institute of Colloids and Interfaces, 14476 Potsdam, Germany ; [d] Department of Physical Medicine and Sports Traumatology, University of Liège and University Hospital of Liège, Liège, Belgium ; [e] Experimental Surgery unit, GIGA & Credec, University of Liege, Liege, Belgium ; [f] Department of Mechanical Engineering, KU Leuven, Leuven, Belgium.

ABSTRACT

Interactions among cells are crucial to the maintenance of proper tissue functions. Mineralized fibrocartilage, a fibrous form of cartilage typically found at entheses, is sandwiched between tendon and bone. Both tissues are characterized by cells (tenocytes in tendons and osteocytes in bone) which have extensive communication abilities thanks to their underlying dense networks (nanotubes in tendons and nanochannels in bone) connecting the corresponding cells. In bone, this network is referred to as the osteocyte lacuno-canalicular network (OLCN). These networks serve multiple functions: in addition to communication, nanotubes in tendon are believed to provide biomechanical stability while the OLCN is directly involved in bone mechanoresponsiveness and mineralization. Here, we explore the behavior of fibrochondrocytes (the

cells of fibrocartilage) and their possible crosstalk with bone functional porosity at the interface between the two tissues. At the specific investigated enthesis, namely the Achilles tendon insertion into calcaneus, a periosteal fibrocartilage is additionally present to facilitate tendon sliding. This anatomical feature is exploited to investigate the impact of loading environment on cell interactions. At the enthesis, we identified a connection path between trabecular bone marrow space and fibrocartilage through the anisotropic subchondral channel network, perforating the interface at several locations. Crosstalk between cells is indirect: the OLCN seems to stop or bend at the cement line separating tissues, but exhibits a high connectivity with perforating channels, the latter coming in close contact with the anisotropic fibrochondrocyte rows. The absence of such connections at the periosteal region is striking and suggests that different level of crosstalk between bone and fibrocartilage may be required to maintain healthy enthesis also depending on the fibrocartilage morphology (such as thickness) and biomechanical task.

6.1 Introduction

Cell-cell communication is a fundamental process to maintain the integrity of musculoskeletal tissues. Direct cell-cell coupling within the same tissue as well as communication mechanisms across multi-tissue interfaces are attracting increasing attention to better understand physiology, regeneration and aging. In living bone, osteocytes connect to other osteocytes through nanoscale channels called canaliculi ($\sim$ 100 - 300 nm in diameter) and form, together with osteocyte lacunae, an intricate and highly organized porous network, called the osteocyte lacuno-canalicular network (OLCN) [1, 2]. This high density network contributes to approximately 2 % to the global porosity of bone and provides, in the human skeleton, an inner surface as large as 200 m^2 [3, 4]. The OLCN serves important functions, including the control of bone remodeling and the regulation of mineral homeostasis [1, 5]. The mechanoresponsivness of bone, i.e. the ability to adapt its mass and architecture to changes in the loading environment [6], is mainly attributed to osteocytes sensing load-induced flow within the OLCN [7, 8]. The assumed decreased mechanoresponsivness in aged individuals may be due to changes in transduction pathways, as well as in network morphology [7]. Recent studies have demonstrated that the architecture of the OLCN influences the fluid flow pattern and, consequently, the process of bone remodeling [2, 9].

Long range cell-cell communication is also present in soft tissues: tendon cells (tenocytes), are believed to form a three-dimensional network characterized by thin cellular processes called nanotubes and connecting tenocytes over a distance much longer than cell dimensions [10–12]. This network should enable cellular crosstalk and may also contribute to the biomechanical stabilization of the tissue, since not all nanotubes seem to have gap junctions with other tenocytes [10, 12]. In cartilage, the usual picture that chondrocytes are isolated cells that communicate mainly through diffusion, is being refined by new evidence of direct cell-cell connection through gap junctions [13]. Cartilage anchors to bone through a layer of mineralized cartilage. In this tissue, as well as in subchondral bone, a network of nanochannels ($\sim$ 10 - 50 nm in diameter) smaller than bone canaliculi has been recently discovered [14], having a possible contribution in

molecular and ion transport.

The crosstalk between bone and cartilage has been attracting considerable attention, also owning to its critical role in osteoarthritis [15]. Not only the interface between the subchondral bone and mineralized cartilage contains some vascular channels but there is also evidence of molecular transport across the interface [16, 17], which seems to increase in pathological conditions [15]. The communication between bone and tendon is far less explored. Similarly to articular cartilage, tendon attaches to bone through an intermediate layer of fibrocartilage, which is not mineralized close to tendon and mineralized close to bone. In mineralized fibrocartilage (mFC), fibrochondrocytes are located inside fibrochondrocytes lacunae, arranged in rows or clusters and surrounded by a mineralized matrix. These cells are "sandwiched" between the three-dimensional networks of tenocytes and osteocytes. At some locations, like the Achilles tendon insertion into calcaneus, in addition to the "anchoring" enthesis fibrocartilage (mainly sustaining tensile stresses), a periosteal fibrocartilage is present, which facilitates tendon sliding (and should be loaded by compressive and shear forces). We have previously shown that these two types of fibrocartilage exhibit specific microstructural and material characteristics reflecting different loading conditions [18]. In the present work, we explore the possible crosstalk between bone and mFC as well as the properties of the OLCN within subchondral bone. To which extent do fibrocartilage and bone communicate? Which is the morphology of the OLCN when approaching the interface with fibrocartilage? Do the different loading environments present at enthesis and periosteal regions influence cell-cell communication? To tackle those questions, we combined micro-computed tomography (micro-CT), quantitative backscattered electron imaging (qBEI), second harmonic generation (SHG) imaging and confocal laser scanning microscopy (CLSM) on the same locations to highlight the functional porosity of bone and mFC and its relationship with the surrounding fibrous collagen matrix.

6.2 Materials and methods

6.2.1 Sample preparation and imaging

Sample extraction, embedding and micro-computed tomography (micro-CT)
Achilles tendon-calcaneus bone samples were extracted from the posterior legs of 3-month-old male Sprague-Dawley rats (n = 2, weight of 530 g) and stored in 70 % ethanol. Animals were available at the Liège University Hospital in the framework of an organ donation program (ethical approval: ULg-IACUC-21-2340). Whole tendon-bone specimens maintained in 70 % ethanol solution were first scanned with micro-CT at a nominal isotropic voxel size of 2 μm. In brief, the scanner (μCT 50, SCANCO Medical AG, Brüttisellen, Switzerland) was operated at tube voltage of 55 kV and current of 72 μA, in combination with a 0.5 mm thick aluminum filter. The samples were rotated over 180 ° with a rotation step of 0.12 ° (corresponding to 1500 projections), with an exposure time of 1500 ms and a frame averaging of 3, leading to a scan time of approximately 10.2 h. Following the scan, samples were dehydrated in a graded series of alcohol and

acetone and subsequently embedded in polymethylmetacrylate (PMMA). Before embedding, the samples were stained with rhodamine (rhodamine-6G, 0.02 % ethanol), which is a nanometer sized molecule that can penetrate all the accessible porosities and attach to free surfaces. When excited with a confocal laser, this molecule allows to visualize the OLCN [19]. After PMMA hardening, samples were trimmed with a diamond saw (Buehler Isomet 1000) to expose representative cross-sections of the tendon-bone insertion ([18] and Chapter 5, Section 5.2). Sample surface was sanded with a succession of abrasive papers and finally polished with diamond suspension to obtain plane, parallel and smooth surfaces. The grinding and polishing procedure was performed in absence of water by using diethylene glycol to avoid crack formation.

Confocal laser scanning microscopy (CLSM)

The prepared sections were imaged using a Leica TCS SP5 (Leica Microsystems, Wetzlar, Germany) CLSM, with a 63x oil immersion lens (HCX PL APO CS 63x 1.40 OIL), operating at a wavelength of 543 nm to ensure rhodamine excitation. Fluorescence signal was then measured between 553 and 705 nm. The imaged volume of a single CLSM stack was 1024 x 1024 x (approximately) 250 pixels with a pixel size of about 0.24 μm. Since the field of view was smaller than the regions of interest, four to six image stacks were acquired at the insertion and periosteal areas respectively, and then stitched using the ImageJ software tool BigStitcher [20].

Quantitative backscattered electron imaging (qBEI)

For qBEI, samples were coated with carbon to provide a conducting surface. As described previously (Chapter 5, Section 5.2), a Field Emission Scanning Electron Microscope (FESEM, Supra40, Zeiss) was used to quantify mineral content, using 20 kV voltage, a working distance of 10 mm and a scan speed of 90 s per frame [21]. Using a magnification of 130x, the resulting pixel size was 0.88 μm. Field of view being 1024 x 768 pixels, several images were taken and stitched together with ImageJ in order to characterize the entire sample.

Second harmonic generation (SHG) imaging

SHG imaging was used as previously described (Chapter 5, Section 5.2) to reveal the collagen fibrils organization [22, 23]. A SP8 confocal microscope (Leica Microsystems, Wetzlar, Germany) was used with a 910 nm wavelength Ti:Sa laser and the backward direction signal within the 450-460 nm range was acquired. The 40x oil immersion objective (HC PL APO 40×/1.30 OIL) lead to a nominal isotropic pixel size of about 0.38 μm. Several windows of 1024 x 1024 pixels were analyzed and stitched together such to cover the entire specimen.

6.2.2 Image processing and quantitative morphometry

Extraction of subchondral bone channels from micro-computed tomography scans

Micro-CT scans covered the whole volume of the samples and were exploited to extract the entire network

of subchondral bone channels, following a previously developed protocol [18]. Briefly, a preliminary re-alignment of the virtual bones along their three principal axes of inertia was performed using the software BoneJ (v.1.4.3), a module of ImageJ. mFC was eroded from the region of interest with a morphological operator and bone porosity was highlighted by inverting the image and then classified with a despeckle filter. Objects with an area smaller than 20 pixels (a diameter of about 10 μm in two-dimensional cross-sections) were considered to be either noise or osteocyte lacunae and discarded. Renderings of the channel network were then generated using the software CTVox (v.3.3.0, Skyscan).

Binarization and segmentation of CLSM images

The CLSM dataset was binarized using an adaptive threshold and segmented into canaliculi and larger pores with the in-house Python Tool for Image and Network Analysis (TINA) (available in [24]). Since the CLSM field of view included mFC and subchondral bone, the pores segmented by TINA comprised osteocyte lacunae, subchondral bone channels and fibrochondrocyte lacunae. To segment mFC from bone, the reflection mode of the CLSM was exploited. In this imaging modality, which was acquired together with the fluorescence signal, mFC and bone were clearly distinguishable: the former appearing much darker in all cross-sections (till a depth of about 60 μm). For the cross-sections located at the top of the CLSM image stack, complementary information available from qBEI measurements (having a penetration depth of $\sim$ 1 μm) on the highly mineralized cement line separating bone from mFC (Chapter 5), confirmed the validity of the proposed approach (Fig. S6.1). This procedure was done with the software CTAn (v1.19.4.0, Skyscan). Ambiguous pores located close to the interface between the two tissues were classified as osteocyte lacunae if they showed canaliculi or as fibrochondrocyte lacunae otherwise. Further segmentation of bone porosity was performed with a size threshold: pores with a volume smaller than 1000 μm^3 (roughly corresponding to a diameter of 10 μm in two-dimensional cross-sections) were considered as osteocyte lacunae, while the larger objects were defined as subchondral channels. A final cleaning step was required to manually delineate and remove parts of unmineralized fibrocartilage (uFC) that were highly stained (bright). Three-dimensional renderings were then generated using the software CTVox (v.3.3.0, Skyscan).

Correlation of images from all imaging techniques

To correlate images from multiple techniques (micro-CT, CLSM, qBEI and SHG) we used the following approach. Firstly, to entire volume of the micro-CT had to be "browsed" using CTVox to retrieve the specific cross-sections analyzed with the other imaging modes. SHG and qBEI were overlaid manually, using porosities as visual guidance. To visualize the OLCN architecture and fibrochondrocyte lacunae within the mineralized matrix, a z-projection of the CLSM was considered and overlaid onto qBEI images, as previously done [25]. Specifically, ten slices of CLSM (approximately corresponding to the penetration depth of qBEI and SHG), were projected from 3D to 2D using a standard deviation projection tool in ImageJ, and further binarized with a fixed global threshold. We used again bone porosity (osteocyte lacunae), to superimpose CLSM images with qBEI.

Quantification of osteocyte lacuno-canalicular network

After segmentation of osteocytes and canaliculi from the CLSM image stack, osteocyte lacunar (OL.N/TV) and canalicular (C.V/TV) densities were assessed with CTAn considering the "effective" bone volume (obtained by subtracting from the available bone volume the subchondral channel before computing osteocyte lacunar density and by subtracting both subchondral channel and lacunar volume before computing canalicular density). Densities were characterized in two regions: the entire subchondral bone as well as a smaller zone comprising bone located up to 100 μm away (Euclidean distance) from the bone-mFC interface. Measurements on individual lacunae were conducted with CTAn and included lacunar sphericity (OL.Sph), volume (OL.V) and centroid (center of mass). The sphericity was measured as the ratio between the surface area of a sphere of equivalent volume to the surface area of the object (e.g., OL.Sph = 1 indicates a perfectly spherical lacuna). To assess the spatial evolution of those properties, each lacuna centroid was used to determine its shortest (Euclidean) distance to the interface with mFC.

6.3   Results

6.3.1   Qualitative observations of bone-fibrocartilage crosstalk

The potential interaction between bone and fibrocartilage is explored at enthesis (Fig. 6.1 and S6.2) and periosteal (Fig. 6.2 and S6.3) regions using 3D renderings of the CLSM dataset. At the insertion, several fibrochondrocyte lacunae, despite being fully buried into a mineralized matrix, are reached by rhodamine and get stained (Fig. 6.1a). Those cells are typically arranged into characteristic rows which are entirely stained. Comparing the fluorescent and the reflective signal (Fig. 6.1e, f) highlights the fraction of fibrochondrocytes lacunae which are accessible to rhodamine. A closer look at the bone-mFC interface (Fig. 6.1b, c) reveals the presence of channels running through the interface. A central observation is that these channels, in bone, are decorated by numerous osteocytes and connected with them by a dense canalicular network (see segmented data in Fig. 6.1d, but also in Fig. S6.4 and S6.5). When reaching mFC, the channels are then located in the vicinity of stained fibrochondrocyte lacunae. These observations demonstrate a possible direct coupling between bone and mFC at enthesis.

Conversely, at the periosteal region (Fig. 6.2), only a few individual fibrochondrocyte are visible in the CLSM images. Again, the comparison between fluorescent and reflective modes (Fig. 6.2d, e) further indicates that many fibrochondrocytes are present within periosteal FC but only a small fraction of them are reached by the fluorescent molecules. Magnified view at the bone-mFC interface (Fig. 6.2b) and corresponding segmentation (Fig. 6.2c, but also in Fig. S6.4 and S6.5) confirm the reduced interplay between the two tissues at the periosteal location.

Combining CLSM with micro-CT reconstructions of the entire caudal part of the calcaneus (Fig. 6.3) allows to follow the channels even outside the volume analyzed by CLSM (Fig. 6.3, white triangles). This data
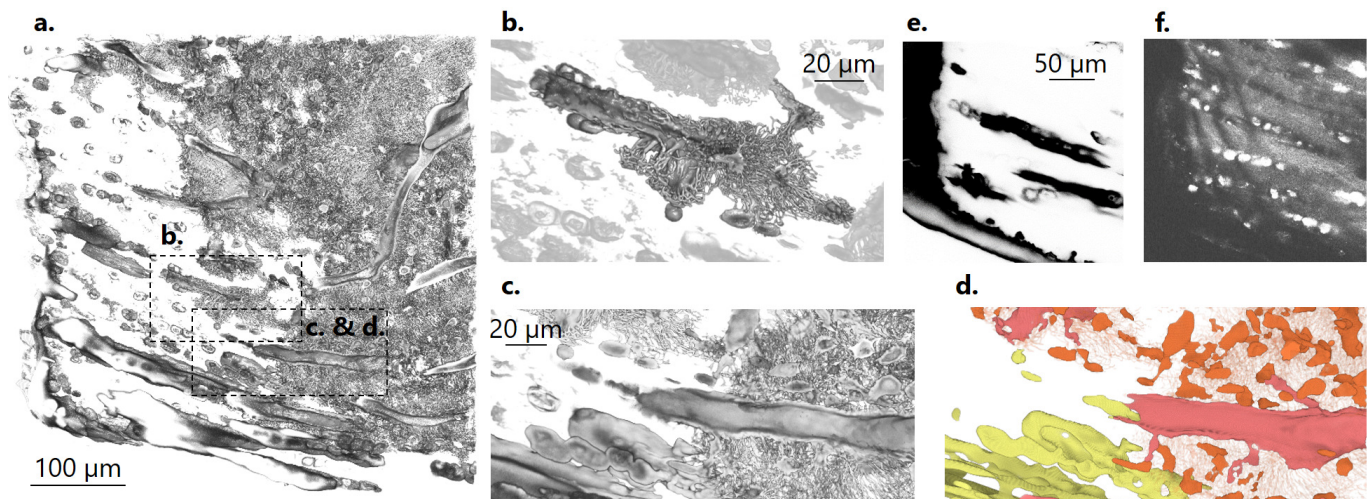
Figure 6.1: (a) Overview of functional porosity at the enthesis from a three-dimensional rendering of confocal laser scanning microscope (CLSM) images. (b, c) Magnified views of CLSM data illustrating the complex interaction between channels, osteocyte lacuno-canalicular network and fibrochondrocyte rows. (d) Colored segmentation of magnified view from (c), depicting channels (pink), osteocyte lacunae and their canaliculi (orange and light orange, respectively) and fibrochondrocyte lacunae (yellow). Illustration of one cross-section acquired with (e) excitation and (f) reflective mode showing that some fibrochondrocytes are stained (appearing dark in (e) and bright in (f)), but others are not (appearing bright in (f) only).
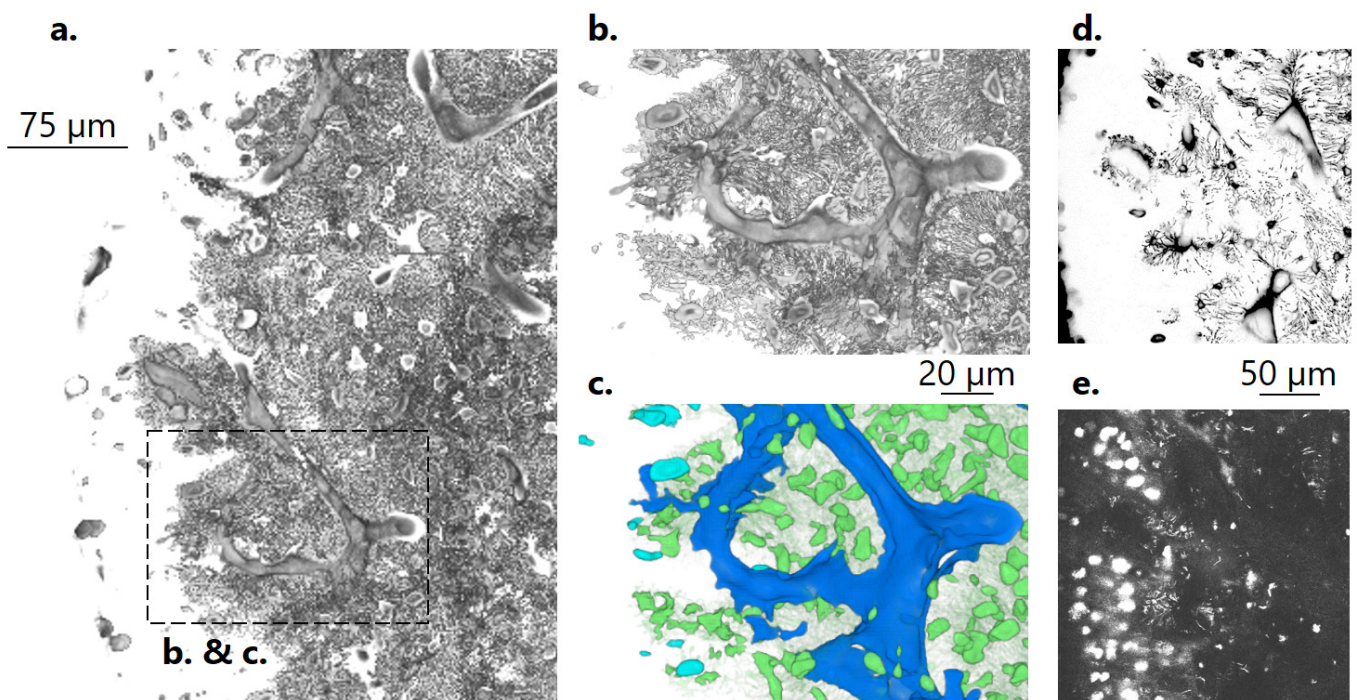
Figure 6.2: (a) Overview of functional porosity at the periosteal area from a three-dimensional rendering of confocal laser scanning microscope (CLSM) images. (b) Magnified views of CLSM data illustrating that, contrary to the insertion site, interactions between bone and mineralized fibrocartilage (mFC) is minimal. (c) Colored segmentation of magnified view from (b), depicting bone channels (dark blue), osteocyte lacunae and their canaliculi (green and light green, respectively) and fibrochondrocyte lacunae (light blue). Illustration of one cross-section imaged with excitation (e) and reflective (f) mode, confirming that only a small fraction of the available lacunae is reached by rhodamine.
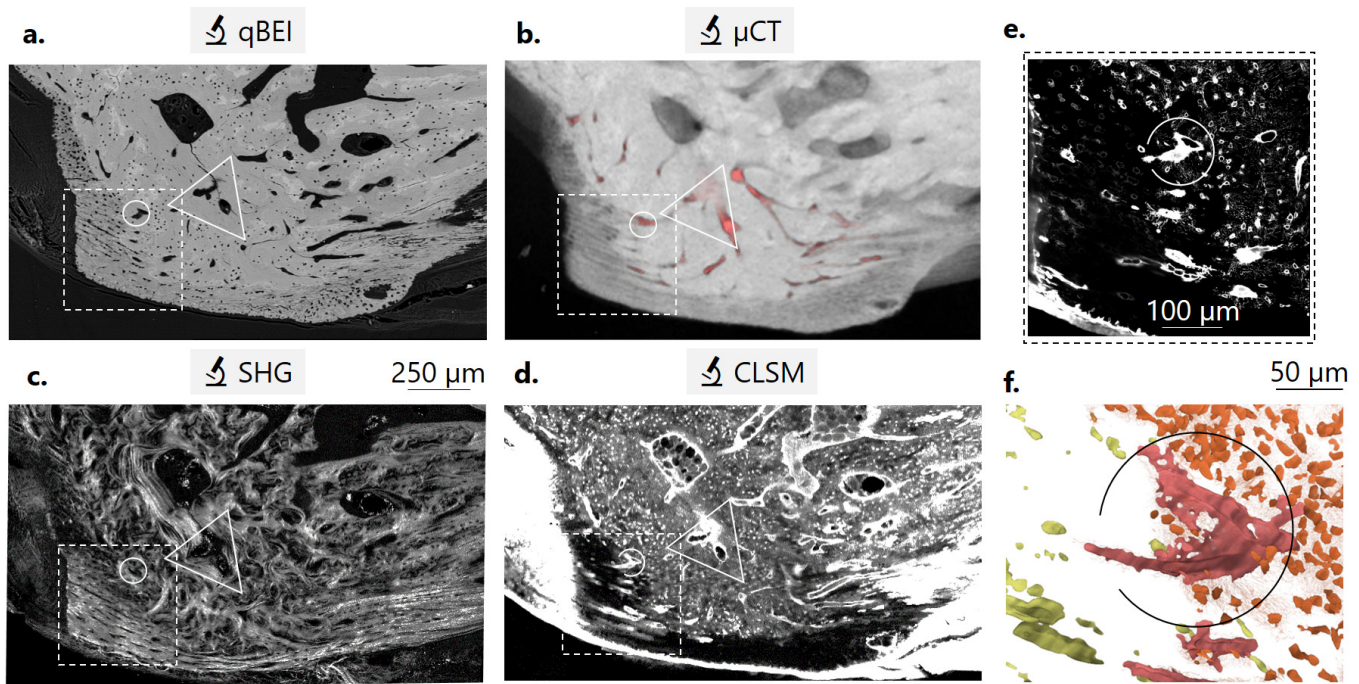
Figure 6.3: Correlation of (a) quantitative backscattered electron imaging (qBEI), (b) micro-computed tomography (μCT), (c) second harmonic generation imaging (SHG) and (d) low-resolution overview of the CLSM at the same position at enthesis. (e) CLSM representative cross-section of the dashed-line frame shown in a-d. (f) Magnified 3D view of the segmented microporosity, emphasizing the large channel encircled in all the images.

indicates possible paths followed by rhodamine to reach the enthesis, traveling through subchondral bone channels and it may also suggest long range interactions between bone and mFC. SHG imaging (Fig. 6.2c) emphasizes the previously observed a high degree of alignment of collagen fibers at enthesis (Chapter 5), which are oriented parallel to the rows of fibrochondrocyte lacunae. At the inferior side of the calcaneus, some fibers even run continuously from the Achilles tendon insertion towards the plantar fascia, attaching on the opposite side of the tuberosity.

6.3.2 Specificities of osteocytes lacuno-canicular network (OLCN)

The behavior of the OLCN and more specifically of the canaliculi is examined in Fig. 6.4 by combining qBEI, CLSM and SHG information on the same sections. At both enthesis and periosteal sites, mFC is demarcated by a thin ($\sim 2 \ \mu$m) highly mineralized cement line, visible in qBEI images (white line in Fig. 6.4a, d) and indicated by the dashed yellow line on CLSM (Fig. 6.4b, e) and SHG (Fig. 6.4c, f) images. The pattern of the cement line is more interdigitated and irregular at the enthesis than at periosteal locations, as observed previously (Chapter 5). Yet common to both regions is the central observation that a few osteocytes sit very close to the interface between bone and mFC and that some canaliculi of these osteocytes are directed towards the interface, reaching it at an almost right angle. All canaliculi stop either at the interface or even a few micrometers before it (see also Fig. S6.6). A high density of canaliculi is also observed around channels (especially at enthesis).
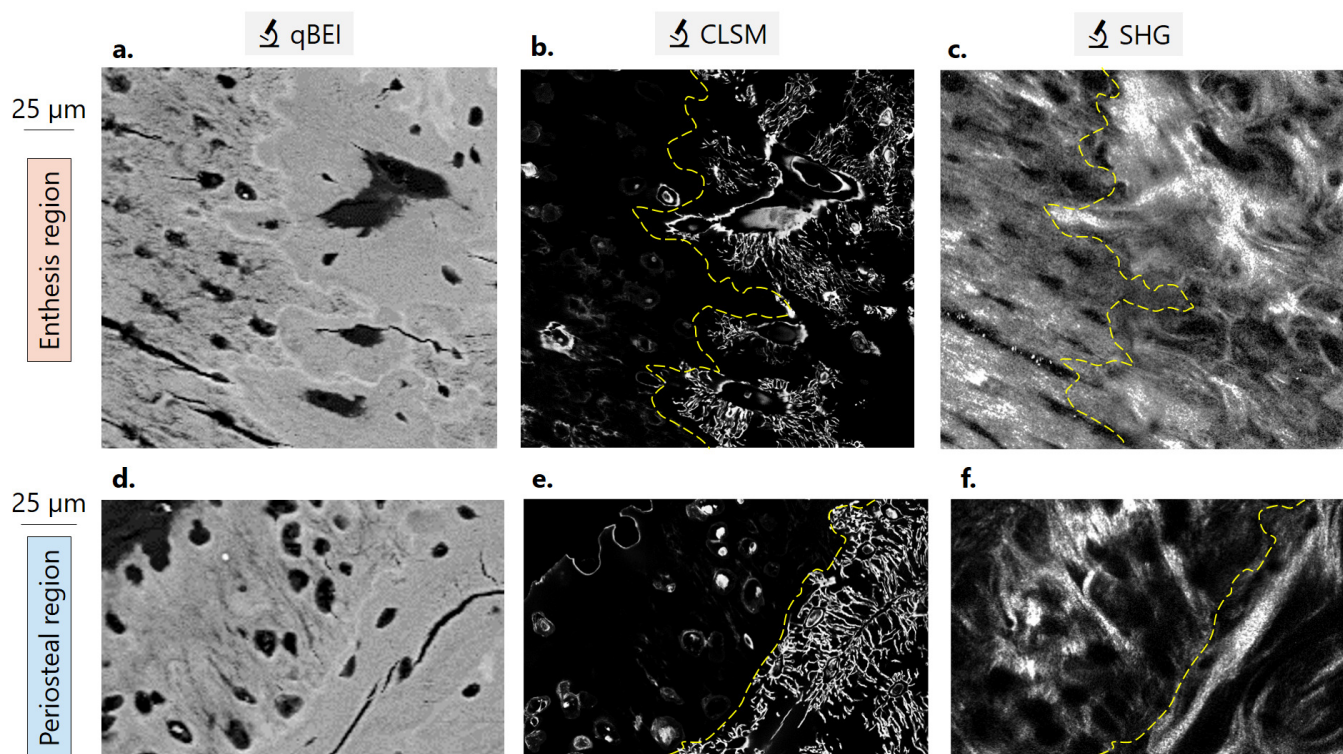
Figure 6.4: Investigation of the osteocyte lacuno-canalicular network at the interface between bone and mFC at (a-c) enthesis and (d-e) periosteal area, with qBEI, CLSM and SHG images taken at the same position. The yellow dashed line represents the interface between mFC and bone, delineated by superimposing CLSM or SHG with qBEI images.

Specific behaviors of the OLCN can also be spotted further away from the interface in trabecular bone. Some regions are characterized by a high SHG signal, indicating the presence of in-plane and well-oriented collagen fibers. In contrast with such uniform SHG signal, there is heterogeneity in the architecture of the OLCN: some areas (highlighted by the continuous yellow line in Fig. 6.5) have canaliculi well aligned in the image plane and oriented at a right angle with a large channel, whereas close by, a region of canaliculi coming out from plane is recognizable (dashed yellow line in Fig. 6.5). In between these two locations, cartilaginous islands, known features of rat bone [18, 26], are visible in qBEI and show no canaliculi.

The resulting densities of osteocytes (OL.N/TV) and canaliculi (C.V/TV) are reported in Table 6.1, considering entire periosteal and enthesis areas, as well as a 100 μm wide region of interest close to the interface between bone and mFC. Both osteocytes and canalicular densities seem to be higher within periosteal subchondral bone (P-SB) in comparison to enthesis subchondral bone (E-SB). In the former, a higher number of osteocytes and canaliculi are observed close to the interface. Within E-SB, canalicular density tends to be lower close to the interface than far from it. Overall, osteocyte connectivity at both sites is decreasing at the interface.
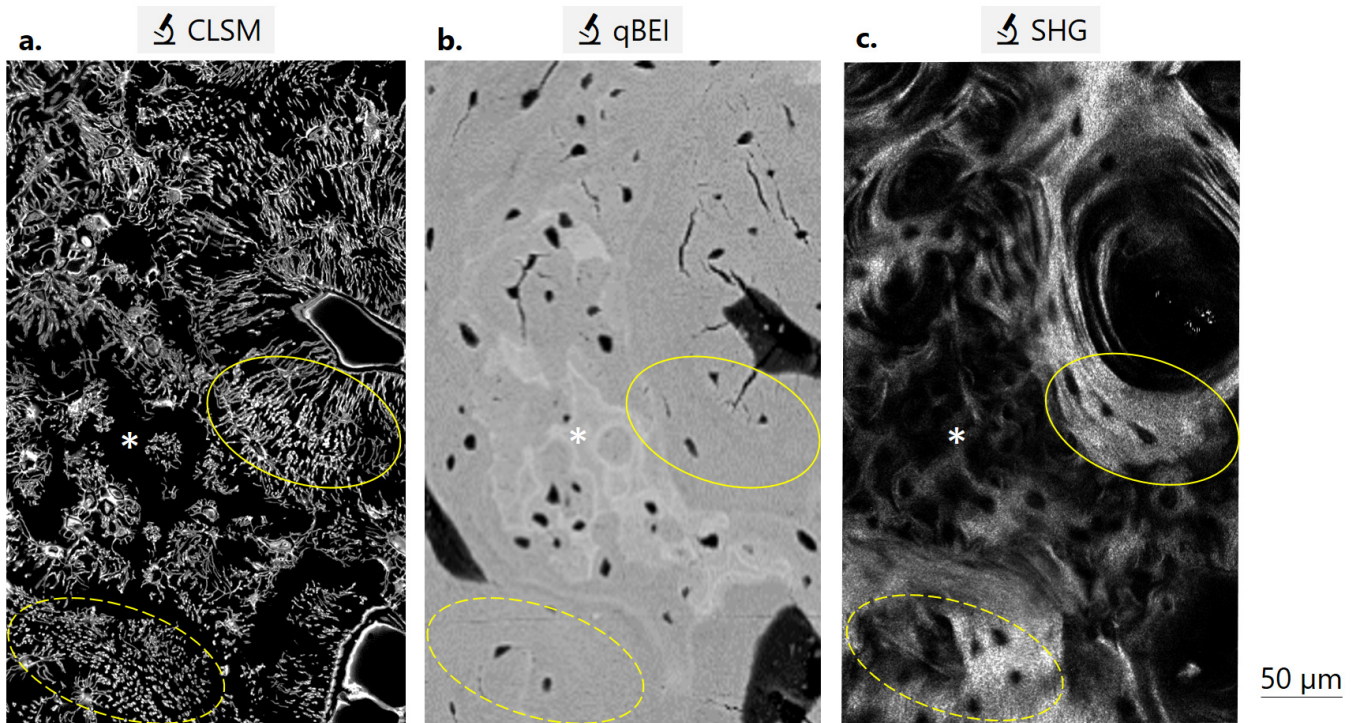
Figure 6.5: (a) Specific behavior of the OLCN in subchondral bone and corresponding (b) local mineral content (measured by qBEI) and (c) collagen finer orientation (characterized by SHG).

	OL.N/TV [10^3 OC/mm^3]		C.V/TV [%]	
	In the entire region	At the interface	In the entire region	At the interface
Enthesis SB	102.16 ± 20.09	103.62 ± 27.72	2.67 ± 1.13	2.34 ± 0.71
Periosteal SB	112.92 ± 37.8	129.51 ± 39.27	3.41 ± 1.05	3.67 ± 0.63

Table 6.1: Osteocyte lacunar and canalicular properties at the enthesis and periosteal subchondral bone (SB).
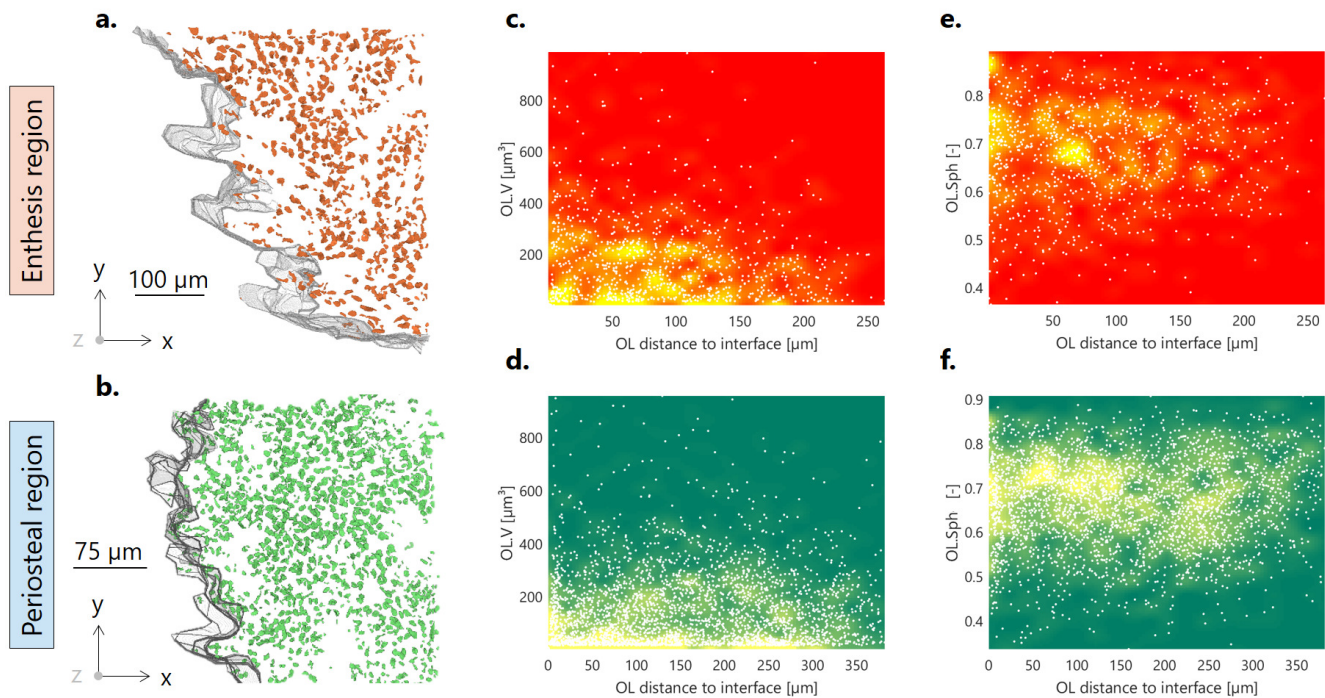
Figure 6.6: Osteocyte lacunar morphology at (a, c, e) insertion and (b, d, f) periosteal areas. (a, b) Overview of the segmented lacunae and extracted interface with mFC (grey lines) at both sites. (c, d) Lacunar volume (OL.V) and (e, f) sphericity (OL.Sph) as a function of the distance to the interface with mFC. Scatter plots are superimposed with density plots, brighter color implying higher density of measured points.

Osteocyte morphology, in terms of osteocyte volume (OL.V) and sphericity (OL.Sph), is quantified as a function to the distance from the bone-mFC interface within E-SB (Fig. 6.6a, c, e) and P-SB (Fig. 6.6b, d, f). The two morphological indicators have similar values in the two regions but seems to be slightly less scattered within E-SB. Contrary to osteocyte density, no clear trend is detected in osteocyte morphology when reaching the bone-mFC interface.

6.4 Discussion

Potential communication pathways between bone and mFC were explored by combining several high-resolution imaging techniques at two regions contiguous but sustaining specific mechanical loadings. Using rhodamine as an infiltrating fluorescent molecule, we demonstrated the staining of some rows of fibrochondrocytes lacunae located inside mFC at the enthesis (Fig. 6.1). Correlating CLSM data with micro-CT reconstructions of the entire caudal portion of the calcaneus, we could clarify the possible path followed by rhodamine: channels were identified originating from the trabecular bone marrow space, traveling through subchondral bone and, in some locations, perforating the bone-mFC interface (Fig. 6.3). The crucial role of vasculature is further emphasized by the presence of osteocytes and canaliculi interacting with channels before they enter mFC, ultimately connecting the OLCN with fibrochondrocytes (Fig. 6.1). Although bone growth should be limited given the age of the rats, it is known that during this process as well as during

133

endochondral ossification (Chapter 2), blood vessel invasion inside hyaline cartilage is observed and enables osteoblasts and osteoclasts to reach and transform cartilage matrix into bone [27, 28]. Much less lacunae were reached by rhodamine at the periosteal site (Fig. 6.2), indicating fewer interactions between the two tissues. From a biomechanical viewpoint, enthesis mFC should sustain a more challenging loading environment, characterized by higher stresses than periosteal mFC [29], perhaps requiring more crosstalk between the two tissues. One other influencing factor might be the thickness of mFC, which is higher at the insertion and therefore may require direct connection with bone also to transport nutrients and waste products.

The presence of osteocyte lacunae and, specifically, of canaliculi, directed towards the bone-mFC interface is an interesting finding, also considering that the canaliculi stop either before or right at the cement line anchoring bone to mFC (Fig. 6.4). Such abrupt interruption of the OLCN at the cement line has been reported as well at the osteochondral interface [14]. In the work by Tang and colleagues, a new structural network of nanochannels (much smaller than canaliculi), was revealed within calcified cartilage and bone, but was practically absent inside the cement line. The cement line may, therefore, be considered as an impermeable layer, hampering direct cartilage-bone interaction. Somewhat at odds with this finding are the results of Pouran and coworkers [17], reporting nanopores crossing the interface between calcified cartilage and subchondral bone, although the authors did not specifically focused on the cement line and analyzed regions much smaller than those characterized by Tang. Cement lines are also found at the outer boundary of osteons, but opinions on the permeability are diverging. Some studies have shown that the cement line is indeed a strict barrier disrupting the OLCN [19, 30, 31] as well as the nanochannel network [32], while others suggest age-dependent connections among osteons and between osteons and interstitial bone through canaliculi crossing the cement line [33–35]. Using focused ion beam-SEM, a recent study has shown that canaliculi within the cement sheath (a 3D denomination for the cement line) were preferentially parallel the cement sheath boundary [36], whereas canaliculi from the lamellar bone side reached the cement sheath boundary at a right angle, which is similar to our findings (Fig. 6.4).

From a material viewpoint, the structural anisotropy of the enthesis (Fig. 6.3c) [18] (see also Chapter 5) was not reflected in specific osteocyte lacunae morphology: bone lacunar properties, with the exception of a slight increase in osteocyte density close to the periosteal region, did not show specific behavior close to the interface (Fig. 6.6 and Table 6.1). Ongoing work focuses on the skeletonization of the OLCN in order to quantify the local orientation of individual canaliculi for all the osteocytes bordering the interface with mFC.
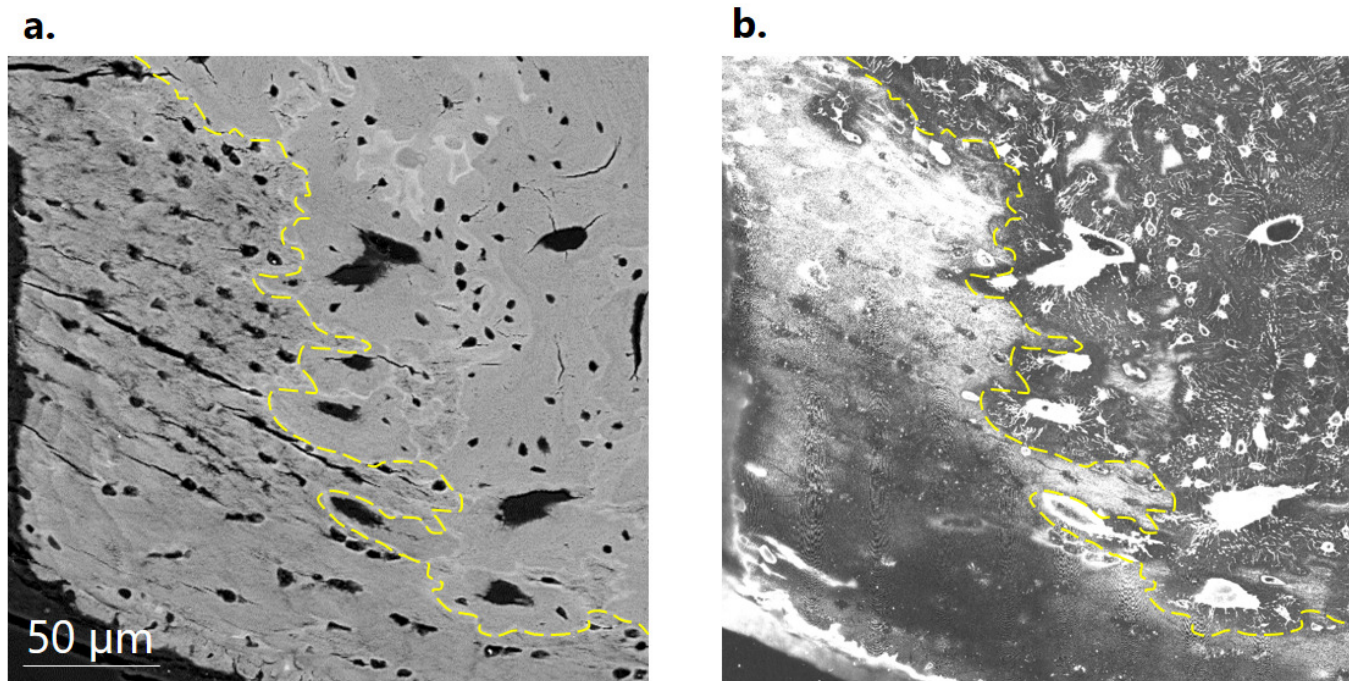
To underline the importance of the crosstalk between bone and mFC, it is instructive to move away from the enthesis, and to consider the connection between bone and articular cartilage. Recent findings have questioned the former vision of the calcified cartilage-bone interface as an impermeable barrier, specifically in the context of osteoarthritis (OA) [15, 37, 38]. Increased vascularization from subchondral bone into cartilage and microcracks formation at the bone-cartilage interface are modifications typically seen in OA joints.

Although still not proved in vivo, those changes are believed to increase communication between tissues through the transport of small molecules (up to 376 Da) [16], perhaps bringing such molecular exchange to unhealthy levels. At the same time, besides being linked to potential OA initiation and progression, some degree of crosstalk across the osteochondral interface is believed to be necessary to maintain joint health [15]. A similar cell-cell communication may be required at the tendon-bone insertion. The illustrated communication paths between fibrocartilage and bone at the insertion site could be further explored by quantifying the permeability of the interface through fluid flow simulations [9, 17]. Increasing our understanding of the crosstalk between both compartments in healthy, but also clinically relevant scenarios, may suggest new ways to deliver medications to fibrocartilage for example to treat rheumatic pathologies which are still considered an unsolved medical problem.

Acknowledgements

6.5 Supplementary Figures

a.

b.


50 µm

Figure S6.1: Illustration of the procedure followed to segment fibrocartilage from bone, showing the reference qBEI image (a) and the sum of both reflective and fluorescent CLSM modes at low depth at the exact same region (b). The yellow dashed line follows the cement line and is obtained by superimposing CLSM with qBEI images. A good correspondence can be observed between the cement line and the darker appearance of bone.
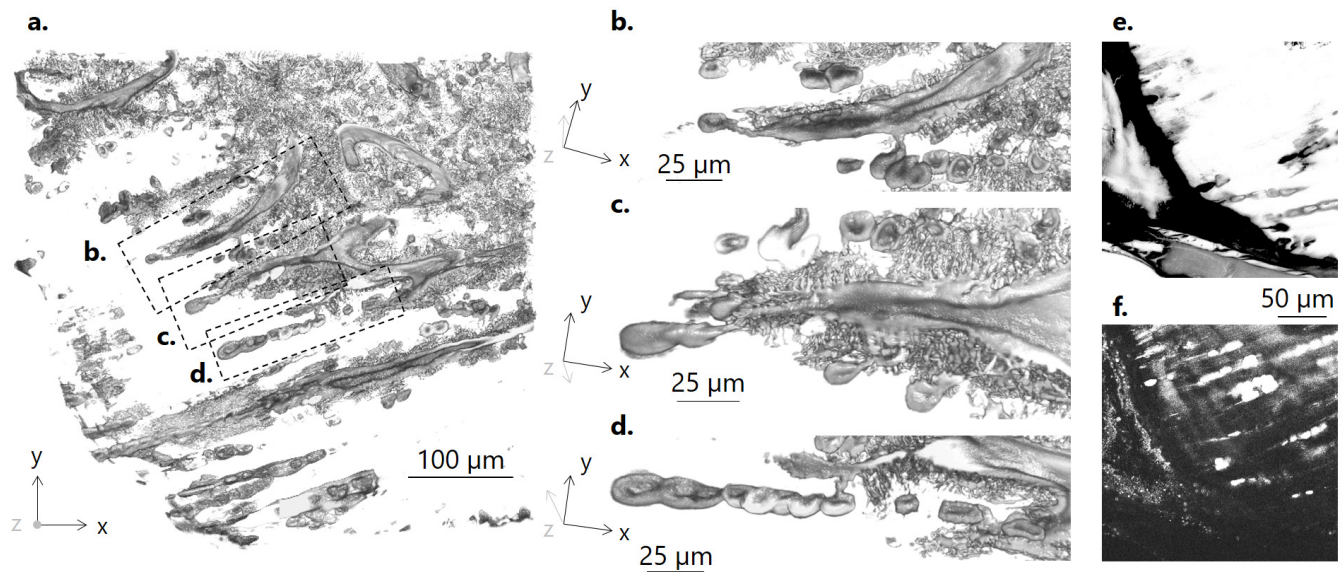
Figure S6.2: Equivalent to Figure 6.1 for the second analyzed sample. (a) Overview of functional porosity at the enthesis from a three-dimensional rendering of confocal laser scanning microscope (CLSM) images. (b, c, d) Magnified views of CLSM data illustrating the complex interaction between channels, osteocyte lacuno-canalicular network and fibrochondrocyte rows. (e) Illustration of one cross-section acquired with (e) excitation and (f) reflective mode showing that some fibrochondrocytes are stained (appearing dark in (e) and bright in (f)), but others are not (appearing bright in (f) only).
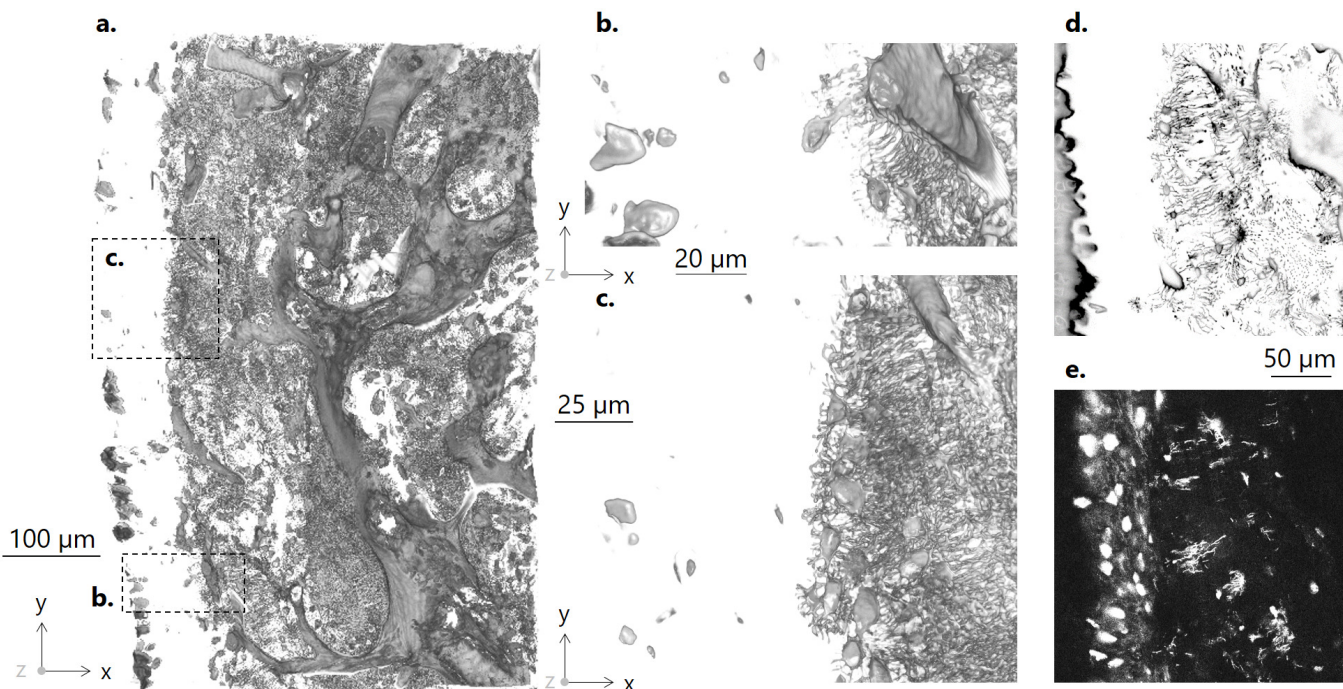

Figure S6.3: Equivalent to Figure 6.2 for the second analyzed sample. (a) Overview of functional porosity at the periosteal area from a three-dimensional rendering of confocal laser scanning microscope (CLSM) images. (b, c) Magnified views of CLSM data illustrating that, contrary to the insertion site, interactions between bone and mFC is minimal. Illustration of one cross-section imaged with excitation (e) and reflective (f) mode, confirming that only a small fraction of the available lacunae is reached by rhodamine.
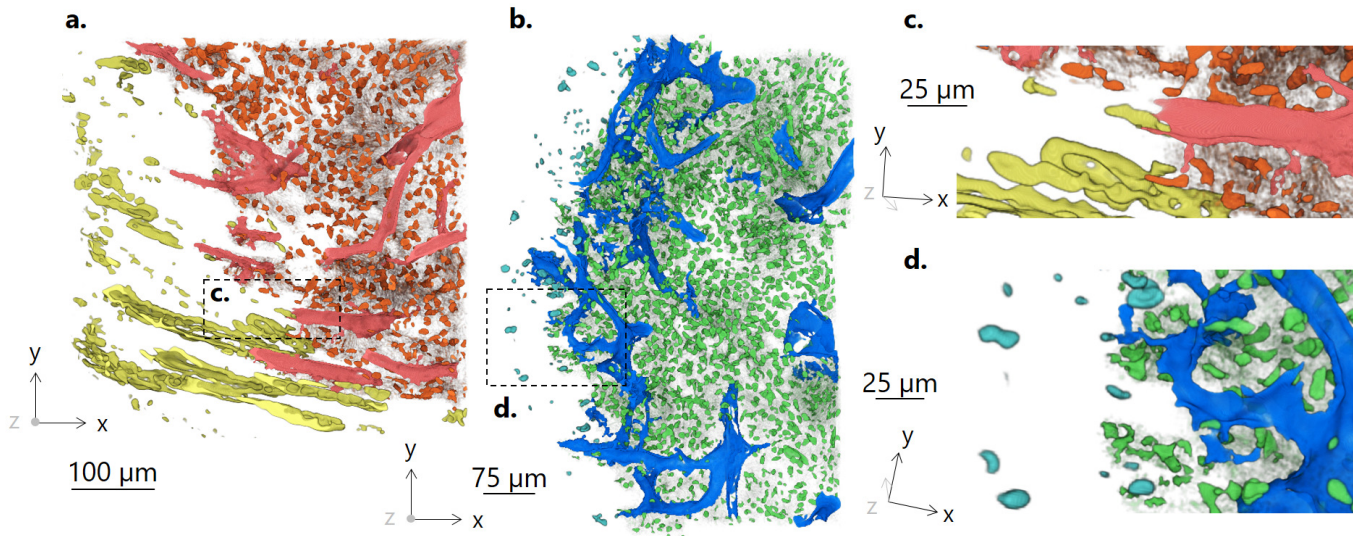
Figure S6.4: Colored segmentation of the overall functional porosity at the enthesis (a) and periosteal (b) areas for the sample presented in the main manuscript. (c, d) Magnified views from the depicted dashed frame illustrating the differences in the bone-fibrocartilage interactions at both sites.
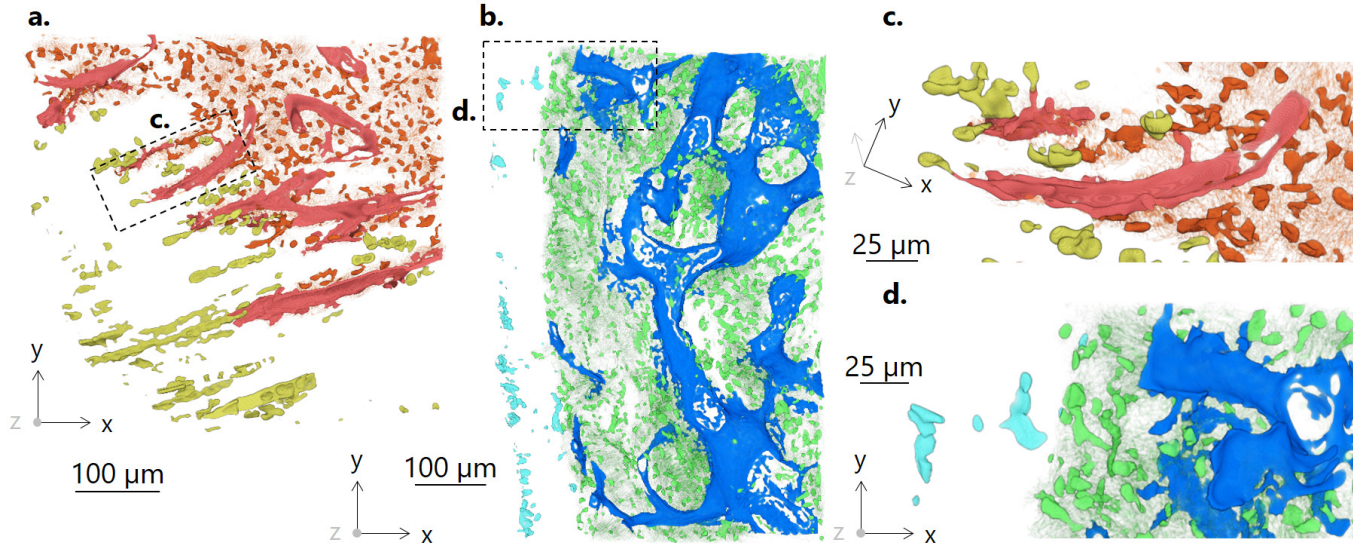
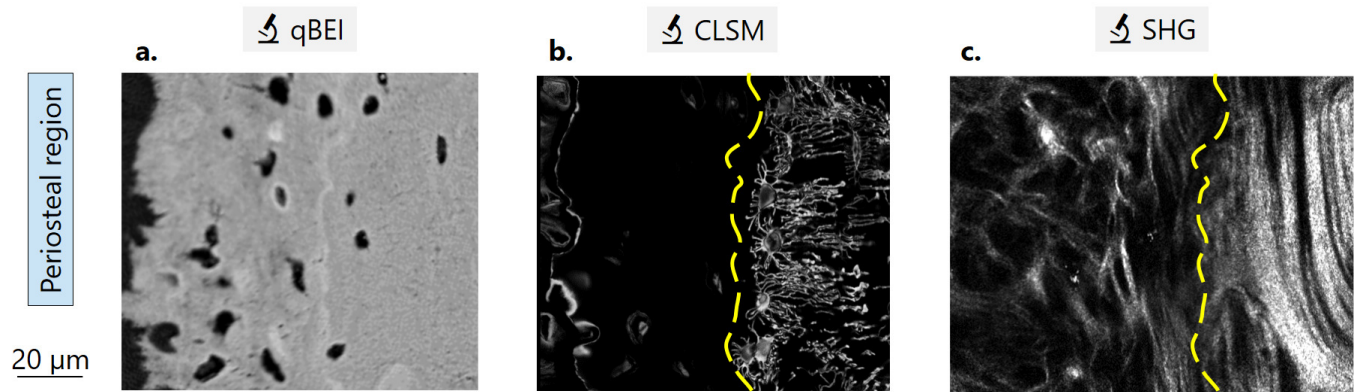**Figure S6.5:** Colored segmentation of the overall functional porosity at the enthesis (a) and periosteal (b) areas for the second sample. (c, d) Magnified views from the depicted dashed frame illustrating the differences in the bone-fibrocartilage interactions at both sites.

Figure S6.6: Additional illustration of the osteocyte lacuno-canalicular network at the interface between bone and mFC within the periosteal area, with qBEI, CLSM and SHG images taken at the same position. The yellow dashed line represents the interface between mFC and bone, delineated by superimposing CLSM or SHG with qBEI images.

Bibliography

[1] Felix Repp et al. "Coalignment of osteocyte canaliculi and collagen fibers in human osteonal bone". In: *Journal of Structural Biology* 199.3 (2017), pp. 177–186.

[2] Alexander F van Tol et al. "Network architecture strongly influences the fluid flow pattern through the lacunocanalicular network in human osteons". In: *Biomechanics and modeling in mechanobiology* 19.3 (2020), pp. 823–840.

[3] Luis Cardoso et al. "Advances in assessment of bone porosity, permeability and interstitial fluid flow". In: *Journal of biomechanics* 46.2 (2013), pp. 253–265.

[4] Pascal R Buenzli and Natalie A Sims. "Quantifying the osteocyte network in the human skeleton". In: *Bone* 75 (2015), pp. 144–150.

[5] Mahdi Ayoubi et al. "3D interrelationship between osteocyte network and forming mineral during human bone remodeling". In: *Advanced healthcare materials* 10.12 (2021), p. 2100113.

[6] Friederike A Schulte et al. "Local mechanical stimuli regulate bone formation and resorption in mice at the tissue level". In: *PloS one* 8.4 (2013), e62172.

[7] Haniyeh Hemmatian et al. "Aging, osteocytes, and mechanotransduction". In: *Current osteoporosis reports* 15.5 (2017), pp. 401–411.

[8] Sheldon Weinbaum, Stephan C Cowin, and Yu Zeng. "A model for the excitation of osteocytes by mechanical loading-induced bone fluid shear stresses". In: *Journal of biomechanics* 27.3 (1994), pp. 339–360.

[9] Alexander Franciscus van Tol et al. "The mechanoresponse of bone is closely related to the osteocyte lacunocanalicular network architecture". In: *Proceedings of the National Academy of Sciences* 117.51 (2020), pp. 32251–32259.

[10] Monika Egerbacher et al. "Tenocytes form a 3-D network and are connected via nanotubes". In: *Journal of anatomy* 236.1 (2020), pp. 165–170.

[11] JR Ralphs, AD Waggett, and M Benjamin. "Actin stress fibres and cell–cell adhesion molecules in tendons: organisation in vivo and response to mechanical loading of tendon cells in vitro". In: *Matrix biology* 21.1 (2002), pp. 67–74.

[12] CM McNeilly et al. "Tendon cells in vivo form a three dimensional network of cell processes linked by gap junctions." In: *Journal of anatomy* 189.Pt 3 (1996), p. 593.

[13] Maria D Mayan et al. "Articular chondrocyte network mediated by gap junctions: role in metabolic cartilage homeostasis". In: *Annals of the rheumatic diseases* 74.1 (2015), pp. 275–284.

[14] Tengteng Tang et al. "A 3D Network of Nanochannels for Possible Ion and Molecule Transit in Mineralizing Bone and Cartilage". In: *Advanced NanoBiomed Research* (2022), p. 2100162.

[15] David M Findlay and Julia S Kuliwaba. "Bone–cartilage crosstalk: a conversation for understanding osteoarthritis". In: *Bone research* 4.1 (2016), pp. 1–12.

[16] Jun Pan et al. "In situ measurement of transport between subchondral bone and articular cartilage". In: *Journal of Orthopaedic Research* 27.10 (2009), pp. 1347–1352.

[17] Behdad Pouran et al. "Topographic features of nano-pores within the osteochondral interface and their effects on transport properties–a 3D imaging and modeling study". In: *Journal of Biomechanics* 123 (2021), p. 110504.

[18] Alexandra Tits et al. "Local anisotropy in mineralized fibrocartilage and subchondral bone beneath the tendon-bone interface". In: *Scientific Reports* 11.1 (2021), pp. 1–17.

[19] Michael Kerschnitzki et al. "The organization of the osteocyte network mirrors the extracellular matrix orientation in bone". In: *Journal of structural biology* 173.2 (2011), pp. 303–311.

[20] David Hörl et al. "BigStitcher: reconstructing high-resolution image datasets of cleared and expanded samples". In: *Nature methods* 16.9 (2019), pp. 870–874.

[21]   Paschalis Roschger et al. "Bone mineralization density distribution in health and disease". In: *Bone* 42.3 (2008), pp. 456–466.

[22]   Xiyi Chen et al. "Second harmonic generation microscopy for quantitative analysis of collagen fibrillar structure". In: *Nature protocols* 7.4 (2012), pp. 654–669.

[23]   Marie-Andrée Houle et al. "Analysis of forward and backward Second Harmonic Generation images to probe the nanoscale structure of collagen within bone and cartilage". In: *Journal of biophotonics* 8.11-12 (2015), pp. 993–1001.

[24]   Felix Repp. "Tool for Image and Network Analysis (TINA)". In: *Bitbucket, https:// bitbucket.org/refelix/tina* (July 2017).

[25]   Victoria Schemenz et al. "Heterogeneity of the osteocyte lacuno-canalicular network architecture and material characteristics across different tissue types in healing bone". In: *Journal of structural biology* 212.2 (2020), p. 107616.

[26]   Fiona Linnea Bach-Gansmo et al. "Calcified cartilage islands in rat cortical bone". In: *Calcified tissue international* 92.4 (2013), pp. 330–338.

[27]   Hans-Peter Gerber et al. "VEGF couples hypertrophic cartilage remodeling, ossification and angiogenesis during endochondral bone formation". In: *Nature medicine* 5.6 (1999), pp. 623–628.

[28]   Carolina A Moreira, David W Dempster, and Roland Baron. "Anatomy and ultrastructure of bone–histogenesis, growth and remodeling". In: *Endotext [Internet]* (2019).

[29]   Albano Malerba et al. "A computational investigation of the tendon-to-bone insertion: the role of tissue-level properties". In: *Master thesis at Politecnico di Milano* (2022).

[30]   Vincent Ebacher et al. "Sub-lamellar microcracking and roles of canaliculi in human cortical bone". In: *Acta biomaterialia* 8.3 (2012), pp. 1093–1100.

[31]   S Weinbaum. "Models to solve mysteries in biomechanics at the cellular level; a new view of fibre matrix layers". In: *Ann. Biomed. Eng.* 26 (1998), pp. 1–17.

[32]   Tengteng Tang et al. "Sub-canalicular nanochannel volume is inversely correlated with calcium content in human cortical bone". In: *Journal of Bone and Mineral Research* (2022).

[33]   Petar Milovanovic et al. "Osteocytic canalicular networks: morphological implications for altered mechanosensitivity". In: *ACS nano* 7.9 (2013), pp. 7542–7551.

[34]   Todd A Curtis, Shahid H Ashrafi, and Dennis F Weber. "Canalicular communication in the cortices of human long bones". In: *The Anatomical Record* 212.4 (1985), pp. 336–344.

[35]   Satoshi Hirose et al. "A histological assessment on the distribution of the osteocytic lacunar canalicular system using silver staining". In: *Journal of bone and mineral metabolism* 25.6 (2007), pp. 374–382.

[36]   Emeline Raguin et al. "Focused ion beam-SEM 3D analysis of mineralized osteonal bone: lamellae and cement sheath structures". In: *Acta Biomaterialia* 121 (2021), pp. 497–513.

[37]   XL Yuan et al. "Bone-cartilage interface crosstalk in osteoarthritis: potential pathways and future therapeutic strategies". In: *Osteoarthritis and cartilage* 22.8 (2014), pp. 1077–1089.

[38]   Tim J Lyons et al. "The normal human chondro-osseous junctional region: evidence for contact of uncalcified cartilage with subchondral bone and marrow spaces". In: *BMC musculoskeletal disorders* 7.1 (2006), pp. 1–8.

Chapter 7

Synthesis and perspectives

This thesis examines and quantifies mineralized fibrocartilage and underlying suchondral bone at the rat Achilles tendon insertion into calcaneus bone, with the global aim to characterize their role for integrating the tendon. Two regions, contiguous but sustaining distinct mechanical loadings, are extensively analyzed. Various aspects of those poorly investigated tissues are unraveled, including microstructure and microporosity, the interplay between mechanical and surrounding matrix properties, as well as possible communication pathways.

Anisotropy and interdigitations are key features for tendon insertion

We show that the calcaneus bone of rats presents a dedicated protrusion anchoring the tendon on one side and the plantar fascia on the other side. A spatially resolved analysis of the trabecular microstructure did not show significant changes when approaching the insertion, further suggesting that this tuberosity may localise adaptation and facilitate the force flow coming from the tendon towards the plantar fascia. Within this bony protrusion, a strong structural anisotropy is revealed. Indeed, fibrocartilage collagen fibers are highly aligned, with fibrochondrocyte lacunae forming elongated and oriented column-like structures, sandwiched in between collagen bundles. More surprising is that bone collagen fibers, despite a compositional switch from a mix of type II and III (in fibrocartilage) to pure collagen type I (in bone), maintain this high anisotropy. Microstructural anisotropy is also observed in the subchondral channel network, well oriented along a predominant direction pointing towards the attachment. Conversely, osteocyte lacunae did not show any specific trend in their morphology. Anisotropy has a pivotal impact on the enthesis local mechanical behavior. Indeed, anisotropic regions are associated with a close spatial correspondence between mineral content and tissue modulus and a remarkably constant spatial profile is observed when moving away from the bone-mineralized fibrocartilage interface. Overall, our results suggest that enthesis fibrocartilage should mainly enhance attachment strength. Moreover, roughness of the unmineralized to mineralized tissue transition is high at the enthesis, as well as the entanglement of the fibrocartilage to bone connection. Although the unmineralized to mineralized transition zone has been more extensively studied, we believe both interfaces are crucial for tendon insertion.

Fibrocartilage is a highly versatile and efficient transition tissue

Using cartilage as an intermediate tissue is a common strategy of the musculoskeletal system to "help" bone at mechanically challenging locations. Our work shows that fibrocartilage offers high versatility and efficiency. Although this tissue is less investigated than articular cartilage, it is probably equally important for proper joint functioning. Indeed, periosteal fibrocartilage, contiguous to the highly anisotropic enthesis region, exhibits large dissimilarities in its structure, porosity, and mechanical behavior. Overall, periosteal area has to sustain compressive and shear loading, probably of smaller intensity than the insertion site. Besides reduced waviness and interdigitations at transition interfaces, the tissue is more heterogeneous and displays an intricate fiber organization with isotropic related channel network and more randomly arranged fibrochondroycte lacunae. This heterogeneity may favor damage resistance and results in a gradual increase in tissue modulus that probably permits to better resist compressive loading. Moreover, both fibrocartilages attain their stiffness and hardness by using less mineral than subchondral bone would necessitate, further demonstrating the mechanical efficiency of those transition tissues.

Vasculature has a crucial role in bone-fibrocartilage crosstalk

At the enthesis, the subchondral channel network is connecting trabecular bone marrow space to fibrocartilage by perforating the interface. Crosstalk between osteocytes and fibrochondrocytes is not direct as canaliculi stop before reaching the cement line anchoring the two compartments. It rather occurs indirectly, thanks to the osteocyte lacuno-canalicular network decorating the channels right before they enter fibrocartilage and reach the anisotropic fibrochondrocyte rows. The necessity of such connection has to be clarified but could be required for the healthy functioning of the enthesis.

Limitations and future research

This study and its limitations left open some interrogations, leading to possible directions for future research. In addition to the perspectives proposed in the discussion of each paper, we are here reflecting on more global implications of our work. First and foremost, how does our results expand to humans? To which extend can they be considered representative for other entheses of the musculoskeletal system? Can our findings lead to the development of new computational models integrating the uncovered enthesis features and how could they provide additional insights into their biomechanical function and force transmission mechanisms?

The similarities between humans and rodents in terms of bone architecture and musculoskeletal system is comforting the idea that the underlined anchoring strategies, namely anisotropy and interfacial waviness, should be preserved. The combination of high-resolution and large field of view attained in this thesis thanks to the small size of murine calcanei cannot be reached with human size samples. However, in collaboration

with Dr. Enrico Dall'Ara from the University of Sheffield, high-resolution peripheral quantitative computed tomography (HR-pQCT) scans of human calcanei are currently being investigated (Fig. 7.1). HR-pQCT has a much lower spatial resolution than micro-computed tomography (micro-CT), specifically 82 or 61 μm depending on the scanner, but also a much lower radiation dose, which makes it exploitable for a broader range of clinical applications [1]. Briefly, a total of ten cadaveric human feet were entirely scanned using HR-pQCT (XtremeCT I, Scanco Medical AG; Brüttisellen, Switzerland, isotropic 82 μm voxel size). Three-dimensional renderings (generated with CTVox, v.3.3.0, Skyscan) suggest that Achilles tendon and plantar fascia insert here as well in a bony protrusion of the calcaneus. A preliminary observation is that trabecular microstructure also seems to be exhibiting a preferential alignment close to the insertion, with trabeculae reaching the protrusion almost perpendicularly. A closer examination and quantification is currently in progress. Additionally, micro-CT scans of higher resolution are presently performed on a reduced field of view close to the attachment area.
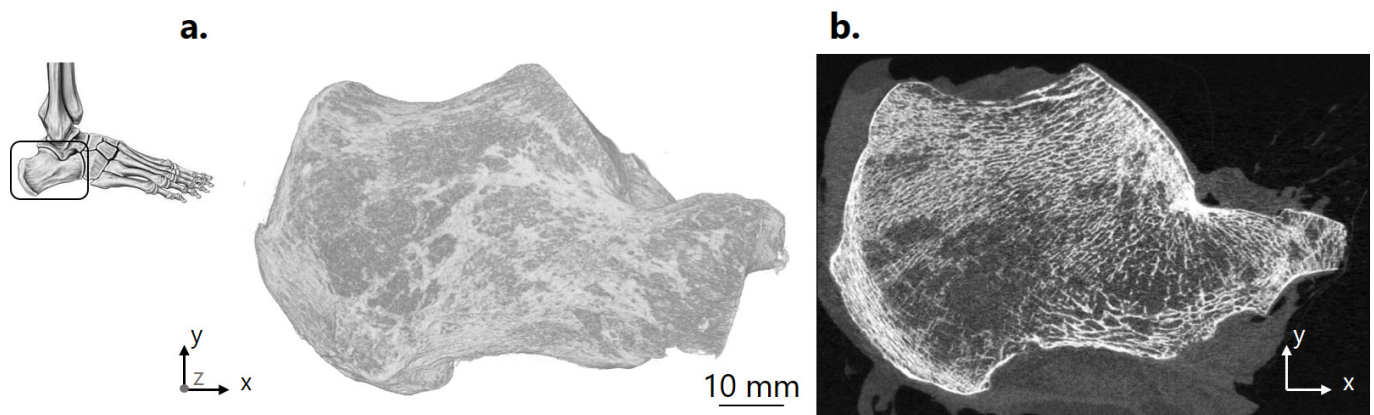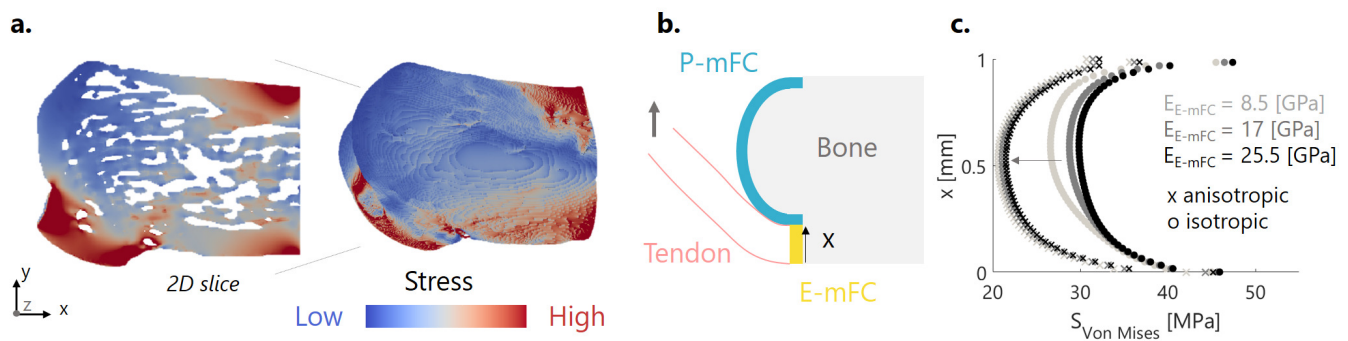

Figure 7.1: Volume rendering (a) and cross-section (b) of a representative human calcaneus sample, scanned with high-resolution peripheral quantitative computed tomography (HR-pQCT). Images courtesy of Dr Dall'Ara and Prof McCloskey.

The versatility of fibrocartilage translates inevitably into a high heterogeneity of entheses amongst the musculoskeletal system. Indeed, each enthesis being subjected to specific loading environment, our findings suggest that fiber architecture, microporosity and microstructure may be anatomical site-dependent. However, what can be extrapolated from our work is that entheses with a dominant tensile loading environment will probably feature fibrous anisotropic behavior with a highly entangled fibrocartilage-bone interface. Extending our analysis to other insertions potentially subjected to more complex environments, such as the many entheses of the knee joint or the rotator cuff group, would be extremely valuable.

In order to investigate the biomechanical implications of our findings, simplified finite element (FE) models are being used: one model with idealized material properties to highlight the role of microarchitecture (Fig. 7.2a), while the second has a simple two-dimensional (2D) geometry but includes specific material behaviors (Fig. 7.2b, c). The first micro-FE model, has a geometry based on micro-CT scans (5 μm pixel size, rescaled 20 times), simple linear elastic properties for bone, and was solved with the open-source software

ParOSol [2, 3] considering a horizontal force for the plantar fascia and a 45 ° force from the Achilles tendon side. This analysis was done in collaboration with Dr. Peter Varga (AO Foundation, Davos, Switzerland). Preliminary results show a considerable concentration of stresses within the tuberosity. The simplified 2D model was developed with Abaqus and considers layers of fibrocartilage at both sides with varying stiffness values and material models, including hard frictionless contact between tendon and bone. This work was done in collaboration with Prof. Pasquale Vena, in the context of the master thesis of Albano Malerba (Politecnico di Milano, Italy). Interestingly, using an anisotropic (specifically transverse isotropic elastic) model for the enthesis fibrocartilage layer instead of isotropy leads to a global stress reduction. Decreasing stiffness has a similar lowering impact on stress, but of much smaller amplitude than anisotropy (Fig. 7.2c). This preliminary result further clarifies the biomechanical impact of tissue anisotropy. Future research in this direction should consider including additional complexity to both models. On one hand, including failure properties could allow to demonstrate the increase in strength provided by fibrocartilage, and the observed trend should be explored with a three-dimensional model. On the other hand, the biomechanical advantage of concentrating stress flow within a dedicated protrusion should be clarified.

Figure 7.2: Preliminary finite element (FE) simulations highlighting the role of microarchitecture (a) and material properties (b, c). (a) Resulting stress distribution (volume rendering and representative cross-section) of a micro-FE model based on micro-CT scans, exhibiting a concentration of forces within the bony protrusion. Images courtesy of Dr P. Varga. (b) Schematic of the simulated two-dimension model with Abaqus. (c) Evolution of Von Mises stresses within the fibrocartilage layer as a function of material stiffness and model.

Conclusions

Attaching soft to hard is a challenge nature seamlessly tackles in many species. At entheses, it occurs through an intermediate and highly specialized tissue, measuring only a few hundred micrometers in width: fibrocartilage. Using cutting edge experimental and computational tools, this thesis shed the light on various aspects of its functioning. More importantly, our findings suggest that whether it is in the context of a reattachment surgery, an engineered bimaterial junction, a tissue-engineered implant or the development of a whole joint computational model, this tiny region and its interactions with surrounding tissues should be carefully considered to ensure an efficient and long-lasting attachment.

Bibliography

[1]   Louis M Metcalf et al. "Validation of calcaneus trabecular microstructure measurements by HR-pQCT". In: *Bone* 106 (2018), pp. 69–77.

[2]   Amelie Sas, An Sermon, and G Harry van Lenthe. "Experimental validation of a voxel-based finite element model simulating femoroplasty of lytic lesions in the proximal femur". In: *Scientific reports* 12.1 (2022), pp. 1–10.

[3]   Amelie Sas et al. "Fracture risk assessment and evaluation of femoroplasty in metastatic proximal femurs. An in vivo CT-based finite element study". In: *Journal of Orthopaedic Research®* (2022).

Chapter 8

Side projects

In this chapter two collaborative side projects that have been handled during the course of the PhD thesis are presented. Those studies have led to publications currently under review.

8.1 The mantis shrimp spike

A first collaborative side project was related to the thesis of a PhD student Yann Delaunois (Science Faculty, Laboratory of Functional and Evolving Morphology) and consisted in morphology quantification based on high resolution scans from a mantis shrimp spike.

The full paper: Yann Delaunois [1], Alexandra Tits [2], Quentin Grossman [2], Sarah Smeets [1], Cédric Malherbe [4], Gauthier Eppe [4], G. Harry van Lenthe [5], Davide Ruffoni [2*], Philippe Compère [1,3*], *Design Strategies of the Mantis Shrimp Spike: How The Crustacean Cuticle Became a Remarkable Biological Harpoon?*, can be found here: https://doi.org/10.22541/au.167199666.61851387/v1.

[1] Laboratory of Functional and Evolutionary Morphology, FOCUS Research Unit, Department of Biology, Ecology and Evolution, University of Liège, Liège, Belgium ; [2] Mechanics of Biological and Bioinspired Materials Laboratory, Department of Aerospace and Mechanical Engineering, University of Liège, Liège, Belgium ; [3] Center for Applied Research and Education in Microscopy (CAREM) and Interfaculty centre of biomaterials (CEIB), University of Liège, Liège, Belgium ; [4] Mass Spectrometry Laboratory, MolSys Research Unit, Department of Chemistry, University of Liège, Liège, Belgium. [5] Department of Mechanical Engineering, KU Leuven, Leuven, Belgium. * Equal supervision of the work.

ABSTRACT

Spearing mantis shrimps are aggressive crustaceans using specialized appendages with sharp spikes to capture fishes with a fast movement. Each spike is a biological tool that has to combine high toughness, as required by the initial impact with the victim, with high stiffness and strength, to ensure sufficient pene-

tration while avoid breaking. We performed a multimodal analysis to uncover the design strategies of this harpoon based on chitin. We found that the spike is a slightly hooked hollow beam with the outer surface decorated by serrations and grooves to enhance cutting and interlocking. The cuticle of the spike resembles a multilayer composite: an outer heavily mineralized, stiff and hard region (with average indentation modulus and hardness of 68 and 3 GPa), providing high resistance to contact stresses, is combined with a less mineralized region, which occupies a large fraction of the cuticle (up to 50 %) and features parallel fibers oriented longitudinally, enhancing stiffness and strength. A central finding of our work is the presence of a tiny interphase (less than 10 μm in width) based on helical fibers and showing a spatial modulation in mechanical properties, which has the critical task to integrate the stiff but brittle outer layer with the more compliant highly anisotropic parallel fiber region. We highlighted the remarkable ability of this helicoidal region to stop nanoindentation-induced cracks. Using three-dimensional multimaterial printing to prototype spike-inspired composites, we showed how the observed construction principles can not only hamper damage propagation between highly dissimilar layers (resulting in composites with the helical interphase absorbing 50 % more energy than without it) but can also enhance resistance to puncture (25 % increase in the force required to penetrate the composites with a blunt tool). Such findings may provide guidelines to design lightweight harpoons relying on environmentally friendly and recyclable building blocks.

Morphology and biomechanics of the entire spike

The raptorial appendage of the mantis shrimp *Lysiosquillina maculata* (Fig. 8.1A) features several spikes of increasing size (Fig. 8.1B). A first type of scan was performed with micro-computed tomography (micro-CT) at a low resolution of 15 μm to visualize the entire spike, including the dactyl (Fig. 8.1C). After resin embedding, the spikes were characterized with high-resolution micro-CT, using an isotropic voxel size of 2 μm, and further analyzed using with ImageJ (v.1.52a), Matlab (R2018a; The Mathworks, USA) and CTAn (v.1.19.4.0, Skyscan). Namely, several features of the spike cross-sections were quantified such as its main axes (illustrated in Fig. 8.1D) and eccentricity (see Fig. S2 of the full paper). The local curvature was measured along the spike (Fig. 8.1D). Principal moments of area about the minor (I_{min}) and the major (I_{max}) axis of each cross-section, corresponding approximately to dorso-ventral and lateral loadings, were also calculated based on Mohr's circle theory (Fig. 8.1F). Those measurements allowed to highlight interesting adaptive features of the spike morphology, as well as a first estimation of its bending rigidities.
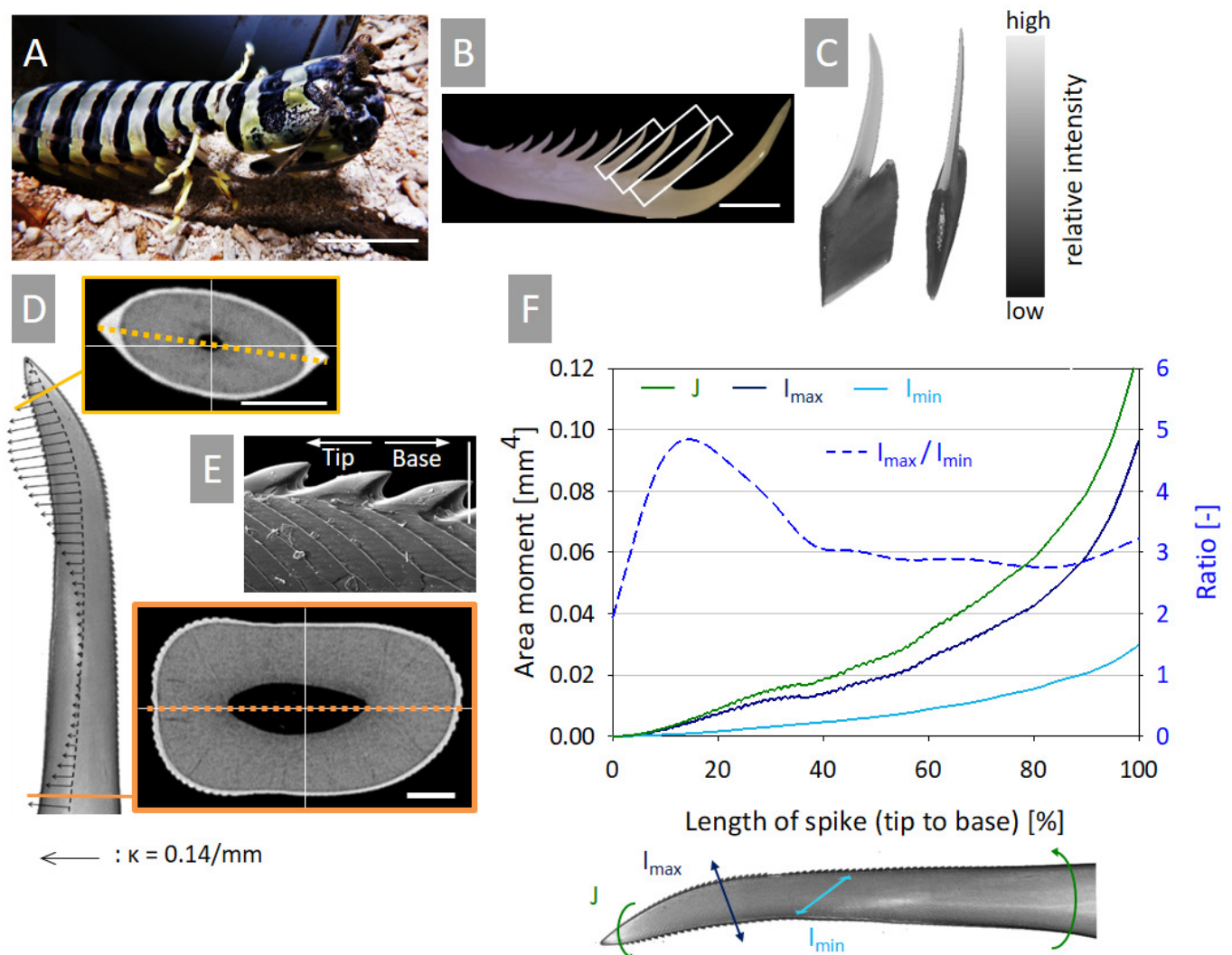
Figure 8.1: Morphology and biomechanics of a spike from the spearing mantis shrimp *L. maculata*. (A) Photograph of a specimen (scale bar: 5 cm) and (B) of a raptorial appendage showing, in the white boxes, the distal spikes characterized here (scale bar: 1 cm). (C) Micro-CT reconstruction of a distal spike attached to the dactyl. The gray levels give a qualitative indication of the heterogeneous density of the cuticle (increasing density from light gray to black). (D) Micro-CT reconstruction of a single spike showing the gross morphology. Superimposed to the micro-CT are arrows having length proportional to the local curvature κ of the spike (a representative arrow indicating a curvature of 0.14 mm^{-1} is shown at the bottom). The inserts (yellow and orange boxes) show two typical cross-sections at the base and near the tip of the spike (scale bars: 200 μm). By comparing the two cross-sections, a slight rotation (of about 15 deg) along the main axis of the spike is evident. (E) Side view of the lateral outer border of the spike in SE-SEM showing serrations and surface grooves. (F) Spatial variations of maximum (I_{max}) and minimum (I_{min}) second area moments as well as polar moment (J) of the spike cross-sections along its length.

8.2 Calcium carbonate biominerals

The second project was related to the characterization of biominerals mechanical behavior, in collaboration with Prof. P. Gilbert (University of Wisconsin, USA) and Prof. M. Buehler (MIT, Boston).

The full paper: Pupa Gilbert [1], Andrew Lew [2], Cayla Stifler [1], Alexandra Tits [3], Connor Schmidt [1], Emily Luffey [1], Andreas Scholl [4], Astrid Cantamessa [3], Laura Müller [3], Yann Delaunois [3], Philippe Compère [3], Davide Ruffoni [3], Markus Buehler [2], *Convergent, slightly misoriented crystals toughen corals and seashells*, can be found here: https://doi.org/10.21203/rs.3.rs-1879515/v1.

[1] University of Wisconsin-Madison, Madison, Wisconsin, United States ; [2] Massachusetts Institute of Technology, Cambridge, Massachusetts, United States ; [3] University of Liège, Liège, Belgium ; [4] Lawrence Berkeley National Laboratory, Berkeley, California, United States.

ABSTRACT

The hardest and toughest tissues formed by living organisms are organic-mineral composites termed biominerals. When they are crystalline, their mesostructure includes the nano- and micro-scale crystallite size, shape, arrangement, and orientation. Mesostructures vary enormously across marine $CaCO_3$ biominerals (aragonite, vaterite, calcite) because they result from divergent evolution: biominerals were formed long after organisms diverged from one another. Despite such diversity, $CaCO_3$ marine biominerals share a convergent character: adjacent crystals are similarly oriented. The reason for such convergence is unclear. Here, we show with quantitative, precise measurements at the nanoscale that the slight misorientation is consistently between 1 ° - 40 ° in diverse biominerals. Can this slight misorientation confer a desirable materials property and therefore an evolutionary advantage to the forming organisms? We test and confirm this hypothesis with nanoindentation in diverse biominerals, geologic aragonite, and in abiotic, slightly misoriented, synthetic spherulites. Molecular dynamics (MD) simulations of bicrystals reveal that aragonite, vaterite, calcite, exhibit toughness peaks when they are misoriented by 10 °, 20 °, 30 °, respectively, demonstrating that slight misorientation alone increases crack deflection and therefore fracture toughness. Slight misorientation, along with other previously known and co-existing toughening mechanisms, was selected repeatedly and convergently, during the course of evolution, to postpone fracture and thus provide organisms with competitive advantage. We anticipate slight misorientation-toughening to be a starting point for more sophisticated materials synthesis and additive manufacturing in many fields. Compared to previously known toughening mechanisms, in fact, the advantages of slight misorientation are that it can and does occur in synthetic materials, it requires one material only and no specific top46 down architecture, it is easily achieved by self-assembly of organic molecules (e.g. aspirin, chocolate), polymers, metals, and ceramics well beyond biominerals.

Toughness of slightly misoriented vs. single-crystalline aragonite crystals, measured by nanoin-dentation

Adjacent crystals within $CaCO_3$ biominerals were shown to be slightly misoriented. To investigate the relationship between this misorientation and fracture resistance, we measured and compared the local fracture toughness using nanoindentation on geologic (single-crystalline), synthetic and biogenic aragonites. Specifically, two sets of experiments were conducted using a Triboindenter TI-950 (Bruker, USA). The first set used low-load (1500 µN) indentations in order to measure local indentation elastic modulus E and hardness H using the classical Oliver-Pharr approach [1], further required for toughness measurement (see Equ. 8.1). Samples were then tested using higher loads (1 - 1500 mN) in order to induce a reasonable amount of detectable crackings (Fig. 8.2A to D), and then imaged with secondary electron microscopy (SEM) to measure the radius of the residual indent R_I, as well as of the damaged area R_D (Fig. 8.2A to D and F). To estimate indentation fracture toughness ((Fig. 8.2G), we fitted the correlation between crack length c (equal to damaged region R_D) and indentation load P (see Fig. S5 of the full paper) obtained by rewriting the fracture toughness equation as described in [2, 3]:

$$c = \frac{E}{H}^{1/3} \frac{\chi P}{K_c} \tag{8.1}$$

The resulting toughness, as well as the damage tolerance under high load (as visualized with SEM or through indentation curves, Fig. 8.2E) were then compared between samples to highlight the potential mechanical advantage of crystal misorientation.
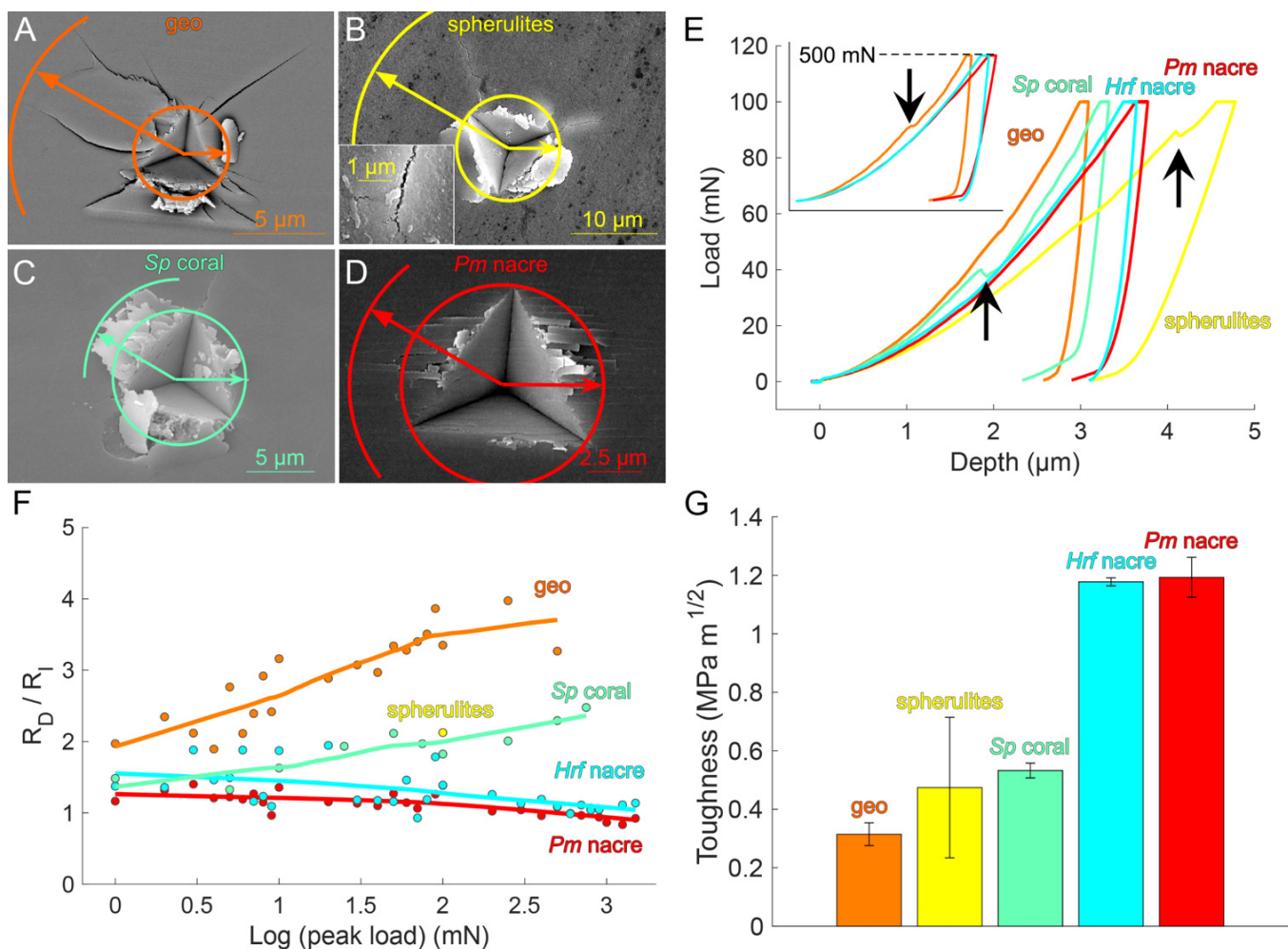
Figure 8.2: Indentation fracture toughness is greater in aragonite biominerals and synthetic spherulites, compared to single-crystalline geologic aragonite. A-D. SEM micrographs post indentation with peak load 100 mN. In A, B, and D the indentation direction was perpendicular to the aragonite c-axis, in C multiple crystals in coral skeleton have unknown orientations. A. Geologic aragonite crystals indented perpendicular to c-axis, B. synthetic spherulites (inset shows additional toughening mechanisms: crack deflection, microcracking, and crack branching), C. coral skeleton and D. *Pm* nacre (indented perpendicular to c-axis, that is, with nacre tablet layers horizontal in the image). *Hrf* nacre has a behavior qualitatively similar to *Pm* nacre (see Fig. S4C of the full paper). SEM images are used to extract the radius of the residual indent R_I and of the entire damaged area R_D by fitting the smallest possible circle centered on the indent. E. Typical indentation curves at a peak load of 100 mN: synthetic and coral aragonites show characteristics pop-in events (highlighted by arrows) associated with sudden damage beneath the contact surface. Geological aragonite also shows such discontinuities but at higher loads (see inset). Conversely, the indentation curve of *Pm* nacre is free from pop-in events, indicating a progressive damage accumulation. F. Ratio of damage radius (R_D) and indentation radius (R_I) plotted versus indentation peak load (trend lines are Locally Weighted Scatterplot Smoothing, LOWESS, regression fits with a smoothing factor of 0.8). This metric quantifies whether damage tends to localize around the indent (as in *Pm* nacre) or to propagate (as in Geo aragonite). Both coral and synthetic spherulites have intermediate behavior. G. Experimentally measured indentation fracture toughness (abbreviate toughness), obtained by fitting the correlation between damage radius (R_D, a measure of crack length) and indentation load (see methods and Fig. S5 of the full paper) [4, 5]. Data presented as mean ± SD over multiple locations within the same sample with the exception of the spherulites, where several samples are considered. Comparison of all samples demonstrates that slight misorientations, present in synthetic spherulites, coral skeleton, and nacre but absent from geologic aragonite, correspond to greater toughness.

Bibliography

[1] Warren Carl Oliver and George Mathews Pharr. "An improved technique for determining hardness and elastic modulus using load and displacement sensing indentation experiments". In: *Journal of materials research* 7.6 (1992), pp. 1564–1583.

[2] Ali Miserez et al. "Effects of laminate architecture on fracture resistance of sponge biosilica: Lessons from nature". In: *Advanced Functional Materials* 18.8 (2008), pp. 1241–1248.

[3] Zhifei Deng et al. "Black drum fish teeth: built for crushing mollusk shells". In: *Acta Biomaterialia* 137 (2022), pp. 147–161.

[4] Adam C Maloof et al. "The earliest Cambrian record of animals and ocean geochemical change". In: *GSA bulletin* 122.11-12 (2010), pp. 1731–1774.

[5] Adolf Seilacher. "Fabricational noise in adaptive morphology". In: *Systematic Zoology* 22.4 (1973), pp. 451–465.

Curriculum Vitae

Alexandra Tits

Born 6th Augustus, in Liège, Belgium

Link to my ORBi profile: https://orbi.uliege.be/profile?uid=p176941

Education

2018 - 2022	**PhD Candidate in Biomedical Engineering** Mechanics of Biological and Bioinspired Materials research unit, University of Liege, Belgium, under the supervision of Prof. Davide Ruffoni.
2016 - 2018	**Master in Biomedical Engineering** University of Liege, Belgium. Graduated *summa cum laude* with congratulations of the jury members. Master Thesis at the Auckland Bioengineering Institute (New-Zealand) and at the University of Liege, under the shared supervision of Prof. Davide Ruffoni and Dr. Justin Fernandez.

Awards and honours

2022	ESB Student Award, European Society of Biomechanics (ESB), Porto, Portugal.
2022	Travel Award as a speaker at the Bones and Teeth Gordon Research Conference (GRC), Ventura, CA, United States.
2022	Jury prize at the ULiège selection of the outreach competition of "My Thesis in 180 seconds" – selected for the national final.
2018	Award of the best Master Thesis offered by the AiLg (Association des Ingénieurs de Liège).

Publications

2023	A. Tits, S. Blouin, M. Rummler, JF. Kaux, P. Drion, GH. van Lenthe, R. Weinkamer, MA. Hartmann, D. Ruffoni, *Bone-fibrocartilage crosstalk and osteocyte lacuno-canalicular behavior at the tendon-bone insertion*, in preparation.
2022	A. Tits, S. Blouin, M. Rummler, JF. Kaux, P. Drion, GH. van Lenthe, R. Weinkamer, MA. Hartmann, D. Ruffoni, *Structural and functional heterogeneity of mineralized fibrocartilage at the Achilles tendon-bone insertion*, under review in Acta Biomaterialia.
2021	A. Tits, E. Plougonven, S. Blouin, M.A. Hartmann, J-F. Kaux, P. Drion, J. Fernandez, GH Van Lenthe, D. Ruffoni, *Local anisotropy in mineralized fibrocartilage and subchondral bone beneath the tendon-bone interface*, Scientific Reports 2021; 11(1), 1-17.
2021	A. Tits and D. Ruffoni, *Joining soft tissues to bone: insights from modeling and simulations*, Bone Reports 2021; 100742.
2022	Y. Delaunois, A. Tits, Q. Grossman, S. Smeets, C. Malherbe, G. Eppe, GH. van Lenthe, D. Ruffoni, P. Compère, *Design Strategies of the Mantis Shrimp Spike: How The Crustacean Cuticle Became a Remarkable Biological Harpoon?*, under review in Natural Sciences.
2023	A. J. Lew, C. A. Stifler, A. Tits, C. A. Schmidt, E. L. Luffey, A. Scholl, A. Cantamessa, L. Müller, Y. Delaunois, P. Compère, D. Ruffoni, M. J. Buehler, P. U. P. A. Gilbert, *Slight misorientation of adjacent crystals toughens $CaCO_3$ biominerals, evolved convergently*, under rebuttal in PNAS.

Supervision

During the course of my PhD, I actively participated in the projects of the lab, and it specifically included the supervision of the following master theses:

2022 – 2023	V. Gaillard (in collaboration with E. Dall'Ara, University of Sheffield), *Adaptation to Achilles tendon insertion in human calcaneus bone samples*.
2021 – 2022	A. Malerba (in collaboration with P. Vena, Politecnico di Milano, Italy), *The impact of structural anisotropy and material properties on the biomechanical behavior of the tendon-to-bone attachment*.
2020 – 2021	L. Müller, *Ultra-structure and mechanical properties of the enameloid and cuticle of pacu and piranha with different diets*.
2019 – 2020	T. Volders, *Imaged-based mechanical analysis of the tendon-to-bone attachment*.
2018 – 2019	L. Riberio (in collaboration with GH. Van Lenthe, KU Leuven), *Biomechanical study of the effects of staining agents on cartilage samples*.

Conference presentations

Ventura, United States - 2022	**Gordon Research Conference** ǀ A. Tits, S. Blouin, M. Rummler, JF. Kaux, P. Drion, GH. van Lenthe, R. Weinkamer, MA. Hartmann, D. Ruffoni, *Biomechanical and biological aspects of mineralized fibrocartilage at the tendon-bone interface: a multimodal analysis.*
Porto, Portugal - 2022	**European Society of Biomechanics Conference** ǀ A. Tits, S. Blouin, M. Rummler, JF. Kaux, P. Drion, GH. van Lenthe, R. Weinkamer, MA. Hartmann, D. Ruffoni, *Biomechanics and mechanobiology of mineralized fibrocartilage at the tendon-bone attachment.*
Noordwijck, Netherlands - 2022	**International Workshop on Quantitative Musculoskeletal Imaging, in combination with 9th International Symposium on Ultrasonic Characterization of Bone** ǀ A. Tits, S. Blouin, M. Rummler, JF. Kaux, P. Drion, GH. van Lenthe, R. Weinkamer, MA. Hartmann, D. Ruffoni, *Combining high-resolution imaging techniques to reveal the structure and function of fibrocartilage at the tendon-bone insertion.*
Illmitz, Austria - 2021	**Ludwig Boltzmann Institute of Osteology Retreat** ǀ A. Tits, S. Blouin, M. Rummler, JF. Kaux, P. Drion, GH. van Lenthe, R. Weinkamer, MA. Hartmann, D. Ruffoni, *A multimodal investigation of mineralized fibrocartilage at the tendon-bone insertion.*
Online - 2021	**European Society of Biomechanics Conference** ǀ A. Tits, S. Blouin, M. Rummler, J-F. Kaux, P. Drion, GH. van Lenthe, R. Weinkamer, MA. Hartmann, D. Ruffoni, *Microstructural anisotropy and material gradients in mineralized fibrocartilage at the tendon-bone insertion.*
Online - 2020	**European Calcified Tissue Society Digital Masterclass** ǀ A. Tits, P. Varga, T. Volders, J-F. Kaux, E. Plougonven, J Fernandez, P Drion, G H van Lenthe, D Ruffoni, *Soft-to-hard biological interfaces: microstructural and micromechanical investigation of the tendon-bone attachment.*
Vienna, Austria - 2019	**European Society of Biomechanics Conference** ǀ A. Tits, J-F. Kaux, J. Fernandez, P. Drion, GH. van Lenthe, D. Ruffoni, *Structural and mechanical analysis of calcaneus bone at the Achilles tendon insertion site.*